ISSN No. 0737-5352-13

MESOSCALE ANALYSIS BY NUMERICAL MODELING COUPLED WITH SATELLITE-BASED SOUNDING

by Alan E. Lipton

NOAA Grant No. NA-85-RAH-05045 (53-1209)

Principal Investigators:

Thomas H. Vonder Haar
James F.W. Purdom

November, 1988

CIRA Cooperative Institute for Research in the Atmosphere

Colorado State University

MESOSCALE ANALYSIS BY NUMERICAL MODELING COUPLED WITH SATELLITE-BASED SOUNDING

by

Alan E. Lipton

Principal Investigators:
Thomas H. Vonder Haar
James F. W. Purdom

Research Supported by

National Oceanic and Atmospheric Administration
Grant NA–85–RAH–05045 (53-1209)

and in part by

Army Research Office Center for Geosciences
Grant DALL–03–86–K–9175

Cooperative Institute for Research in the Atmosphere
Colorado State University
Foothills Campus
Fort Collins, CO 80523

November, 1988

This paper was also submitted as a dissertation
in partial fulfillment of the requirements for
the degree of Doctor of Philosphy
Department of Atmospheric Science
Colorado State University
Fall, 1988

ABSTRACT OF DISSERTATION

MESOSCALE ANALYSIS BY NUMERICAL MODELING COUPLED WITH SATELLITE-BASED SOUNDING

This dissertation deals with the development of a system for time-continuous mesoscale analysis and its use in studying the mesoscale distribution of summertime convective cloud development in the Northeastern Colorado region. There were two basic components of the system — a version of the CSU Regional Atmospheric Modeling System (RAMS) and an algorithm for retrieving temperatures and water vapor concentrations from VISSR Atmospheric Sounder (VAS) data. The system was designed to avoid some of the problems that researchers have encountered when satellite-retrieved parameters have been input to models. The primary distinguishing feature of the new method is that there is an intimate coupling of the retrieval and modeling processes. Water vapor concentrations and ground surface temperatures were the foci of the analyses.

In preparation for analysis experiments we tested the sensitivity of a two-dimensional version of the model to various controls on the behavior of water vapor concentrations and surface temperatures. For water vapor mixing ratios, variations that might be caused by analysis errors had very little impact on the dynamics of circulations in the pre-convective stage. In contrast, ground surface temperature variations were shown to have a large impact on circulations, so analysis errors are very relevant to pre-convective dynamics.

The first comparisons of the coupled analysis method with other, related, methods was by means of two-dimensional simulations. Analyses in which surface temperatures were derived from satellite-retrievals were compared with the alternative of relying on energy balance computations. The energy balance computations were so sensitive to soil characteristics, which were simulated as unknown, that the satellite retrieval method gave better results even with cloud contamination. In water vapor analysis comparisons no single

method was superior in every respect, but the coupled method performed relatively well. Vertical gradients and horizontal gradients were well represented, and the method was relatively insensitive to a common problem in pre-convective analysis — contamination of satellite data by increasing amounts of small convective clouds.

Analysis methods were further compared in a three-dimensional case study for 21 August 1983. The horizontal and time variations of satellite-retrieved surface temperatures closely corresponded to the conventional shelter temperature observations, but had much greater detail. In contrast, the energy balance-based temperatures tended to increase too quickly during the morning and lacked some of the observed gradients. According to the retrievals, there can be very large mesoscale gradients in temperatures at the ground surface even on the relatively flat plains. In the case study water vapor analyses there were substantial differences among the results of the several methods that were intercompared. The study demonstrated that, when the first set of satellite data is less reliable than the later sets, some of the contamination lingers throughout the time-continuous coupled analysis results. However, the coupled method generally appeared to be the most valuable of the methods considered in this study because it exploited the major strengths of the numerical model and the satellite data while making it relatively easy to recognize any impacts of their weaknesses.

The results of this dissertation support the hypothesis that both ground surface temperatures and terrain variations can play important roles in pre-convective water vapor kinematics through their influences on vertical and horizontal winds. The development of convective clouds corresponded largely, but not exclusively, with convergence and deepening of low-level water vapor. The analysis system proved to be valuable for forecasting through the close correspondence between derived stability indices and later convective development. The new method is a step in the expanding capability of meteorologists to combine tools and sources of data for understanding and forecasting mesoscale phenomena.

Alan E. Lipton
Department of Atmospheric Science
Colorado State University
Fort Collins, Colorado 80523
Fall, 1988

ACKNOWLEDGEMENTS

I thank my adviser, Dr. T. H. Vonder Haar, for his guidance throughout my doctoral studies and for providing me the freedom, equipment, and excellent research environment that made this work feasible. Thanks go also to the other members of my advisory committee, Drs. S. K. Cox, R. A. Pielke, and C.-Y. She, for their valuable suggestions relating to my research.

Drs. Moti Segal, Ray Arritt, and Deborah Abbs assisted me in learning about the numerical mesoscale model used in this study and advised me on interpreting the model results. Without their help this study would have been much more difficult to accomplish. Dr. Don Hillger was greatly helpful in developing the VAS retrieval software, and John Weaver provided the stability analysis software. I appreciate the efforts of several SSEC personnel at the University of Wisconsin and of Deborah Lubich and Dr. Jim Purdom at the Cooperative Institute for Research in the Atmosphere (CIRA) at CSU for their help in obtaining VAS data. Dennis Rogers of NOAA/ERL in Boulder provided access to hardcopy satellite imagery. Mrs. Loretta Wilson skillfully assisted in preparation of the manuscript and Mrs. Judy Dunn drafted some of the figures. In addition, I thank Dr. H.-C. Kuo for the encouragement and insights he provided through scientific discussions.

This research was supported primarily by NOAA contract NA-85-RAH-05045 (53-1209) to CIRA and in part by ARO Geosciences Center contract DALL03-86-K-9175. A portion of the computations were done on facilities at the National Center for Atmospheric Research (NCAR) in Boulder. NCAR is sponsored by the National Science Foundation.

TABLE OF CONTENTS

		Page
	Signature Page	ii
	Abstract	iii
	Acknowledgements	v
	List of Tables	ix
	List of Figures	x
1.0	Introduction	1
	1.1 Background	1
	1.1.1 Conditions Favoring Deep Convection	1
	1.1.2 Terrain-Forced Mesoscale Circulations	2
	1.1.3 Summer Convection in Northeast Colorado	5
	1.2 Purpose and Objectives	5
2.0	Tools and Techniques	8
	2.1 VAS Characteristics	8
	2.2 Retrieval/Radiative Transfer Computation Methods	8
	2.3 Objective Analysis	11
	2.4 Numerical Model Formulation	12
	2.5 Mesoscale Water Vapor Analysis Methods	13
	2.5.1 Method 1: Stand-Alone Retrieval	13
	2.5.2 Method 2: Initialized Model Run	15
	2.5.3 Method 3: Modeled Initial Guess	15
	2.5.4 Method 4: Coupled	15
	2.6 Surface Temperature Coupling Method	17
3.0	Model Sensitivity Tests	20
	3.1 Water Vapor	20
	3.1.1 Control	20
	3.1.2 Radiative Effect	24
	3.1.3 Air Density Effect	29
	3.2 Surface Temperature	30
	3.2.1 Control	30
	3.2.2 Perturbation Experiments	32

Page

4.0 Simulated Analyses 37
4.1 Water Vapor 37
4.1.1 Simulated Observations 37
4.1.2 Stand-Alone Retrieval Results 39
4.1.3 Initialized Model Run Results 42
4.1.4 Modeled Initial Guess Results 42
4.1.5 Coupled Results 45
4.1.6 Cloud Contamination Effects 51
4.2 Surface Temperature 56
4.2.1 Simulated Observations 58
4.2.2 Analysis by Energy Balance 61
4.2.3 Coupled Analysis 61
4.2.4 Cloud-Contaminated Analysis 65
4.3 Summary 65

5.0 Case Study 67
5.1 Ground-Based Data 67
5.2 Satellite Data 82
5.2.1 Imagery 82
5.2.2 Sounding Strategy 89
5.3 Model Runs 94
5.3.1 Initial Data 94
5.3.2 Surface Temperature Handling 96
5.3.3 Surface Temperature Results 99
5.3.4 Wind Results 109
5.4 Water Vapor Analyses 123
5.4.1 Conventional Results 123
5.4.2 Stand-Alone Retrieval Results 123
5.4.3 Initialized Model Run Results 130
5.4.4 Modeled Initial Guess Results 130
5.4.5 Coupled Results 135
5.5 Water Vapor Kinematics 147
5.6 Factors in Convective Development 152
5.7 Summary 161

6.0 Conclusion 164
6.1 Sensitivity of Modeled Circulations 164
6.2 Analysis Method Performance 165
6.3 Application of Analysis Results 167
6.4 Principal Results and Implications for Future Research 168

Page

References 171
Appendix A – Retrieval Mechanisms 176
A.1 VAS Channel Usage 176
A.2 Temperature Profile Adjustment 177
A.3 Surface Temperature Adjustment 178
A.4 Water Vapor Profile Adjustment 178
A.5 Retrieval Procedures 180
Appendix B – Experiments with Initial/Boundary Conditions in Case-Study Modeling 183

LIST OF TABLES

		Page
Table 2.1	VAS Instrument Characteristics (VAS–E).	9
Table 3.1	Vertical grid levels for model runs.	22
Table 4.1	Spatially averaged relative differences in mixing ratio at 14 LST for various simulated analyses.	55
Table 5.1	VAS dwell sounder sping budget for 21 Aug 1983.	91
Table A.1	Surface emittances for case-study retrievals.	176

LIST OF FIGURES

		Page
Figure 2.1	Standard VAS weighting fuctions.	10
Figure 2.2	Schematic diagrams of procedures for producing mesoscale water vapor analyses.	14
Figure 2.3	A schematic diagram of the procedure for coupling surface temperature retrieval with mesoscale model integration.	19
Figure 3.1	The analysis domain for two-dimensional experiments, with the westerly wind component (m/s) for the sensitivity test control run at eight hours after sunrise (13 LST).	21
Figure 3.2	The temperature sounding used to initialize the two-dimensional experiments.	23
Figure 3.3	Initial soil temperature profiles.	25
Figure 3.4	Water vapor mixing ratios (g/kg) for the sensitivity test control run at sunrise (05 LST) and eight hours later (13 LST). . .	26
Figure 3.5	Initial (05 LST) water vapor mixing ratios (g/kg) for one of the noisy-field tests of sensitivity to radiative effects.	28
Figure 3.6	Model parameter values for the surface temperature sensitivity control run at 14 LST.	31
Figure 3.7	The westerly and vertical wind components for one of the noisy surface temperature model runs (N-1), at 14 LST.	33
Figure 3.8	Differences in model parameters between the noisy surface temperature run N-7 (as in Fig. 3.7) and the control run at 14 LST.	34
Figure 3.9	The westerly and vertical wind components for the warm–west, cool–east surface temperature perturbation run, at 14 LST. . . .	36
Figure 4.1	Water vapor mixing ratios (g/kg) in the reference atmosphere at three-hour intervals.	38

Page

Figure 4.2 Water vapor mixing ratios (g/kg) used as initial data for analysis simulations. 40

Figure 4.3 Water vapor mixing ratio analysis results (g/kg) from the stand-alone retrieval method. 41

Figure 4.4 As in Fig. 4.3, but from the initialized model run method. 43

Figure 4.5 Water vapor mixing ratios (g/kg) for the initial guess data for 14 LST modeled initial guess method retrievals, and the 14 LST modeled initial guess analysis results. 44

Figure 4.6 As in Fig. 4.3, but from the coupled analysis method. 46

Figure 4.7 Differences (%) between analysis results and the reference values of mixing ratio. 47

Figure 4.8 Water vapor mixing ratio analysis results (g/kg) at 08 LST for simulations with weakened background winds. 49

Figure 4.9 Differences as in Fig. 4.7, but corresponding to the analyses contoured in Fig. 4.8, respectively. 50

Figure 4.10 Water vapor mixing ratio analysis results (g/kg) at 14 LST for two methods of transferring retrieval output to the model grid in coupled analysis. 52

Figure 4.11 Water vapor mixing ratio analysis results (g/kg) at 14 LST for low and high clouds using the modeled initial guess method and the coupled method. 53

Figure 4.12 As in Fig. 4.11, but for high clouds introduced at 14 LST only. 57

Figure 4.13 Surface temperature differences at three-hour intervals. 59

Figure 4.14 The a) westerly and b) vertical wind components at 14 LST from the reference conditions for surface temperature analysis simulation. 60

Figure 4.15 Surface temperature differences at 14 LST from the analysis by energy balance, coupled analysis, and cloud-contaminated analysis. 62

Page

Figure 4.16 The westerly and vertical wind components from the surface temperature analysis simulation by energy balance. 63

Figure 4.17 As in Fig. 4.16, but from the coupled surface temperature analysis simulation. 64

Figure 4.18 As in Fig. 4.16, but from the coupled surface temperature analysis simulation with cloud-contaminated satellite data. 66

Figure 5.1 The case study domain. 68

Figure 5.2a The 70-kPa analysis for 12 UTC (05 MST) 21 Aug 1983. 69

Figure 5.2b As in Fig. 5.2a, but for 50 kPa. 70

Figure 5.2c As in Fig. 5.2a, but for 30 kPa. 71

Figure 5.3 A skew-T/log-p plot of the 12 UTC (05 MST) 21 Aug 1983 rawinsonde report for Denver, Colorado and North Platte, Nebraska. 72

Figure 5.4a The 04 MST 21 Aug 1983 surface observations of temperatures and dewpoint temperatures. 74

Figure 5.4b As in Fig. 5.4a, but for 07 MST. 75

Figure 5.4c As in Fig. 5.4a, but for 10 MST. 76

Figure 5.4d As in Fig. 5.4a, but for 13 MST. 77

Figure 5.5a The 04 MST 21 Aug 1983 surface observations of wind. 78

Figure 5.5b As in Fig. 5.5a, but for 07 MST. 79

Figure 5.5c As in Fig. 5.5a, but for 10 MST. 80

Figure 5.5d As in Fig. 5.5a, but for 13 MST. 81

Figure 5.6a The GOES-5 infrared image from 22 MST 20 Aug 1983. 83

Figure 5.6b As in Fig. 5.6a, but for 04 MST 21 Aug. 83

Figure 5.6c As in Fig. 5.6a, but for 07 MST 21 Aug. 84

Figure 5.6d The GOES-5 visible image from 0930 MST 21 Aug 1983. 84

Page

Figure 5.6e As in Fig. 5.6d, but for 1130 MST. 85

Figure 5.6f As in Fig. 5.6d, but for 1230 MST. 85

Figure 5.6g As in Fig. 5.6a, but for 13 MST 21 Aug. 86

Figure 5.6h As in Fig. 5.6a, but for 16 MST 21 Aug. 86

Figure 5.6i As in Fig. 5.6a, but for 1730 MST 21 Aug. 87

Figure 5.6j As in Fig. 5.6a, but for 2030 MST 21 Aug. 87

Figure 5.7 Isohyets at intervals of 5 mm for the period 17 MST 20 Aug through 04 MST 21 Aug. 88

Figure 5.8 Locations of sounding fields of view for atmospheric soundings. . . 92

Figure 5.9 Locations of sounding fields of view for surface temperature retrieval. 93

Figure 5.10 A schematic outline of the computer runs used in the case study. 95

Figure 5.11 The background geostrophic wind speed and direction for the case study model runs. 97

Figure 5.12 A plot of surface temperature splines for the grid point at the center of the domain. 98

Figure 5.13 Ground surface temperatures at 04 MST from the two model runs with coupled water vapor analyses. 100

Figure 5.14 As in Fig. 5.13, but at 07 MST. 102

Figure 5.15 As in Fig. 5.13, but at 10 MST. 103

Figure 5.16 As in Fig. 5.13, but at 13 MST. 104

Figure 5.17 Air temperatures at 15 m above ground at 04 MST from the two model runs with coupled water vapor analyses. 106

Figure 5.18 As in Fig. 5.17, but at 07 MST. 107

Figure 5.19 As in Fig. 5.17, but at 10 MST. 108

Page

Figure 5.20 Horizontal winds at 10 m above ground at 04 MST from the two model runs with coupled water vapor analyses. 110

Figure 5.21 An east/west cross section through 40°N of horizontal winds at 04 MST from the model run with coupled water vapor analysis and energy balanced-based surface temperatures. 111

Figure 5.22 As in Fig. 5.20, but at 07 MST. 112

Figure 5.23 Horizontal winds, as in Fig. 5.20, but at 250 m above ground and at 07 MST. 114

Figure 5.24 Vertical velocities at 250 m above ground at 07 MST from the energy balance-based and satellite retrieval-based model runs. . . 115

Figure 5.25 As in Fig. 5.20, but at 10 MST. 116

Figure 5.26 Horizontal winds, as in Fig. 5.20, but at 500 m above ground and at 10 MST. 117

Figure 5.27 Vertical velocities, as in Fig. 5.24, but at 500 m above ground and at 10 MST. 118

Figure 5.28 Vertical velocity differences at 500 m above ground at 10 MST from the two model runs. 120

Figure 5.29 As in Fig. 5.20, but at 13 MST. 121

Figure 5.30 Vertical velocities at 1350 m above ground at 13 MST from the energy balanced-based and satellite retrieval-based model runs. 122

Figure 5.31 Mixing ratios at 10 m above the ground from the analysis of conventional data for 04, 07, and 10 MST. 124

Figure 5.32 Mixing ratios at 04 MST from the stand-alone analysis. 126

Figure 5.33 The GOES-5 water vapor channel (channel 10) image from 0430 MST 21 Aug 1983. 127

Figure 5.34 As in Fig. 5.32, but at 07 MST. 128

Figure 5.35 As in Fig. 5.32, but at 10 MST. 129

Figure 5.36 Mixing ratios at 04 MST that apply to the initialized-model-run, modeled-initial-guess, and coupled analysis sequences with energy balance-based surface temperatures. 131

Figure 5.37 Mixing ratios at 07 MST from the initialized-model-run analysis. 132

Figure 5.38 As in Fig. 5.37, but at 10 MST. 133

Figure 5.39 Mixing ratios at 07 MST from the modeled-initial-guess analysis with energy balance-based surface temperatures. 134

Figure 5.40 As in Fig. 5.39, but at 10 MST. 136

Figure 5.41 Mixing ratios at 04 MST that apply to the modeled-initial-guess and coupled analysis sequences with satellite retrieval-based surface temperatures. 137

Figure 5.42 As in Fig. 5.39, but with satellite retrieval-based surface temperatures. 138

Figure 5.43 As in Fig. 5.40, but with satellite retrieval-based surface temperatures. 139

Figure 5.44 Mixing ratios at 07 MST from the coupled analysis with energy balance-based surface temperatures. 140

Figure 5.45 As in Fig. 5.44, but at 10 MST. 142

Figure 5.46 As in Fig. 5.44, but from the 13 MST "forecast." 143

Figure 5.47 As in Fig. 5.44, but with satellite retrieval-based surface temperatures. 144

Figure 5.48 As in Fig. 5.45, but with satellite retrieval-based surface temperatures. 145

Figure 5.49 As in Fig. 5.46, but with satellite retrieval-based surface temperatures. 146

Figure 5.50 Integrated water vapor from 60 kPa to the surface just before the 07 MST coupled adjustment, and the integrated water vapor adjustment at 07 MST. 148

Page

Figure 5.51 As in Fig. 5.50, but at 10 MST. 149

Figure 5.52 Integrated water vapor from 60 kPa to the surface from the coupled analyses with energy balance-based and satellite-based surface temperatures. 151

Figure 5.53 The change in total precipitable water from 10 to 13 MST from the runs with energy balance-based and satellite retrieval-based surface temperatures. 153

Figure 5.54 Integrated water vapor from 60 kPa to the surface at 13 MST from the coupled analyses with energy balance-based and satellite-based surface temperatures. 154

Figure 5.55 Integrated buoyant energies from the modeled-initial-guess analysis with satellite-based surface temperatures at 10 MST. . . 156

Figure 5.56 As in Fig. 5.55, but from the coupled analysis. 157

Figure 5.57 Positive buoyancy from the modeled-initial-guess analysis with energy balanced-based surface temperatures at 10 MST. . . 158

Figure 5.58 As in Fig. 5.57, but from the coupled analysis. 159

Figure 5.59 As in Fig. 5.55, but from the coupled analysis that began with 07 MST water vapor retrievals. 160

Figure 5.60 As in Fig. 5.57, but from the coupled analysis at 13 MST. 162

Figure 5.61 Positive buoyancy from the coupled, satellite-based analysis at 13 MST. 163

Figure B.1 Wind components of two-dimensional initialization parameter tests at 17 MST. 184

Figure B.2 As in B.1, but for 23 MST. 186

Figure B.3 As in B.2, but for a case with background geostrophic winds at 0.5 m/s from the south. 187

Figure B.4 A microscopic view of temperature differences at 23 MST caused by differing background geostrophic winds. 188

1.0 INTRODUCTION

This dissertation deals with the development and application of a system for time-continuous mesoscale analysis. The new method is an advancement in the intensively researched topic of combining analysis tools to better understand and forecast mesoscale meteorological phenomena. A mesoscale numerical model and an algorithm for retrieving temperatures and water vapor concentrations from satellite sounder data comprise the basic components of the system. The primary distinguishing feature is that these two components are intimately coupled. The method has been applied to the initiation and mesoscale distribution of summertime convection in the Northeastern Colorado region in two-dimensional (in space) simulations and a three-dimensional case study.

1.1 Background

1.1.1 Conditions Favoring Deep Convection

This discussion focuses on the thermodynamic conditions that favor deep convective cloud formation and how those conditions arise. The essential condition is a large enough temperature lapse rate and sufficient water vapor that a lifted parcel of air will accelerate upward — realization of potential convective instability. Particularly favorable conditions occur when the necessary lifting is small and the acceleration is large (Darkow, 1986).

If the low-level air that feeds lifted parcels has high humidity then saturation occurs relatively close to the ground and latent heat release makes a large contribution to parcel buoyancy. One result is that the nature and intensity of convective development is sensitive to varying water vapor concentrations (Modahl, 1979; Mahrt, 1977). Water vapor is a particularly important factor in localizing cloud development since water vapor concentrations tend to vary greatly over small scales of space and time (Barnes and Lilly, 1975).

Local increases in water vapor concentrations and temperature lapse rates can be readily achieved by the lifting that results from low-level convergence (Beebe and Bates, 1955). In the absence of strong differential advection, convergence appears to discriminate mesoscale regions of weak and strong convective development. Ulanski and Garstang (1978) found that convective rainfall was virtually always preceeded by mesoscale convergence during the Florida Area Cumulus Experiment. Chen and Orville (1980) shed some light on the role of convergence via numerical modeling. They found that in the presence of convergence there was a greater upward moisture flux by eddies and clouds tended to be broader and deeper.

An important aspect of a convergent mesoscale circulation is that it tends to deepen the layer of high humidity adjacent to the ground. This is especially relevant to the development of deep cumulus as they are growing and entraining air from their environment. When the entrained air has a low humidity there is a reduction of buoyancy and cloud growth is hindered (Austin, 1948). This has been shown to be a particularly important factor in tropical easterly waves, where convergence-induced deepening of moisture distinguishes between regions of shallow and deep cumulus (Cho and Ogura, 1974).

1.1.2 Terrain-Forced Mesoscale Circulations

Variations in terrain characteristics can have a substantial impact on circulations at the mesoscale. The following is a brief review of the terrain-forced circulations that are most relevant to convective cloud development near the Rocky Mountains in summer.

Thermal effects of varying terrain height can be so strong as to dominate circulations in local areas, as pointed out by Defant (1951) in his review of local winds. Wagner (1938) recognized that the observed mountain/valley wind systems arise from related forcing mechanisms that act on a range of scales. On the smallest scale is the basic gravity current that results from the heating or cooling of air overlying sloping surfaces. These upslope and drainage flows force larger scale flows through the evacuation or pooling of mass in enclosed valleys, while nearby plains are relatively undisturbed. The theory of the interaction of the slope flow with the valley/plains flow was advanced by Defant (1949), who also provided an illuminating graphical depiction of this phenomenon.

Aircraft observations (Braham and Draginis, 1960) verified that slope flows can be intense enough to initiate cumulus clouds above mountain peaks. Orville (1964, 1965, 1968) expanded on the information available from observations by numerically modeling how varying characteristics of the terrain and the atmosphere affect the intensity of slope flows and the initiation of clouds. Later observations and modeling (Banta, 1982) revealed a mechanism by which these cumulus clouds can grow and propagate after initiation.

The thermally-induced effects of varying terrain elevation extend far beyond mountain peaks and valleys. Over broad sloping surfaces a mesoscale component of the geostrophic wind is induced that interacts with turbulent mixing effects to give a diurnal variation in the wind. Holton (1967) provided the basic theory of this phenomenon as an explanation for the observed nocturnal low-level jet over the Great Plains. The theory was advanced by Bonner and Paegle (1970) and further insight was derived through numerical modeling (McNider and Pielke, 1981).

Either in the presence or absence of sloping terrain there can be forcing of mesoscale circulations by variations in soil wetness, vegetation, or cloudiness. Pielke and Segal (1986) called these "nonclassical mesoscale circulations" to distinguish them from circulations whose forcing is related to mountains, water bodies, or cities.

Soil wetness has a greater impact than any other soil characteristic on ground surface temperatures (McCumber and Pielke, 1981). It plays the dual roles of regulating soil thermal conductivity and the flux of latent heat to the atmosphere, with the latter generally being more important. Zhang and Anthes (1982) evaluated the effects of several surface characteristics on boundary layer development in a one-dimensional model and found that soil wetness had the greatest impact and surface roughness was secondary. Ookouchi, *et al.* (1984) modeled the effects of contrasts in soil wetness in two dimensions. Mesoscale winds of a few meters per second were typical under a variety of contrast magnitudes and terrain geometries. Later two-dimensional modeling demonstrated that this type of circulation can give rise to clouds and rain (Yan and Anthes, 1988). For a moist band surrounded by dry soil, a wider band corresponded to a stronger circulation and more rain, up to the maximum width of 216 km. There were no clouds or rain for band widths of 48 km or less.

Vegetation affects the transfer of both heat and momentum between the ground and the atmosphere. Anthes (1984) reviewed the physical basis and some observational evidence for the effects of varying vegetation on precipitation at the mesoscale. Segal, *et al.* (1988a) used a numerical model to evaluate vegetation effects on the generation and modification of mesoscale circulations. They concluded that, under favorable conditions, circulations with an intensity close to that of a sea breeze can develop when very dense vegetation is adjacent to a region with bare soil. Direct observations of vegetation-related mesoscale forcing were made by Segal, *et al.* (1988b) with aircraft flights over northeastern Colorado in July. At 180 m above ground they observed substantial contrasts in temperature ($\sim$5 K) and water vapor mixing ratio ($\sim$5 g/kg) over a distance of 25 km between irrigated cropland and dry grassland. Wind effects were evident but appeared to be distorted by other terrain- induced mesoscale circulations.

Stratiform clouds can have a large impact on surface temperatures by altering shortwave and longwave radiative fluxes. In Purdom (1982) is a dramatic example of how thunderstorm locations and intensities can be effected by cloud cover-related differential heating and its induced circulation.

The growth of deep convective clouds can also be affected by mountain-forced gravity waves. In Tripoli's (1986) numerical simulation, a mountain wave was an important factor in the growth of a convective cloud system over the Rocky Mountains. Durran (1986) reviewed the theory of mountain waves at the mesoscale, giving examples of their effect on cloudiness. According to linear theory waves may be either vertically propagating or trapped, depending on atmospheric stability and the variation of wind with height (Scorer, 1949). For vertically propagating waves the disturbance does not extend far from the mountain and the wavelength tends to be longer (>25 km). Durran points out that wide mountain ranges, such as the Front Range of the Rockies in Colorado, tend to force vertically propagating waves. Mountain waves may achieve large amplitudes at times, with one possible reason being the reflection of wave energy in the presence of varying stability (Klemp and Lilly, 1975). Another possibility is that breaking of a mountain wave induces a critical layer, which traps wave energy and gives rise to strong winds at the surface (Clark and Peltier, 1977; Peltier and Clark, 1979).

1.1.3 Summer Convection in Northeast Colorado

There has been a particular focus of mesoscale analysis on the northeastern Colorado region, where terrain plays an important role in the mesoscale organization of weather events. Dirks *et al.* (1967, 1969) deduced from early satellite pictures that there are significant variations in cloudiness at the mesoscale. He reported that there is commonly a cloud-free band about 100 km wide along the highest plains, with extensive cloudiness to either side. Toth and Johnson (1985) documented an upslope/downslope diurnal circulation cycle that dominates the surface flow in summer. They found that the locations of convergence maxima correlate well with areas favored for deep convective development, as revealed by satellite (Klitch, *et al.*, 1985) and radar (Henz, 1974) data. Abbs and Pielke (1986) shed light on this relationship with a climatologically-oriented modeling study that focused on low-level convergence and destabilization patterns. The study of Segal, *et al.* (1988b) indicated that, in addition to terrain slopes, contrasts of land use are very relevant in this region. Large variations of water vapor concentrations are common and play an important role in determining the nature of convective development (Modahl, 1979; Mahrt, 1977). These studies did not address how synoptic and mesoscale gradients of atmospheric and surface characteristics interact with terrain features to organize convective activity on any given day.

1.2 Purpose and Objectives

The effects of varying terrain elevation are relatively easily accounted for in mesoscale analysis and forecasting because elevations do not change (within time scales of interest) and are readily observed. Propagating or cloud-related forcings, however, are transient and spatially irregular and generally have not been well observed or documented. There is a need for improved understanding of their importance within the contexts of a variety of meteorological settings. For short-range forecasting, procedures are needed to quantitatively incorporate these factors into forecast systems (Pielke and Segal, 1986).

Few mesoscale observations of either surface or atmospheric characteristics currently impact operational forecasting, and lack of data is only part of the problem. Forecasters

are already bombarded with information, so it is essential that mesoscale observations reach the forecasters in a readily useable form. Since numerical models are a primary forecasting tool it is particularly valuable for data to be accessible as a model initialization (Smith, *et al.*, 1986).

Satellite sounders have been turned to as a source of mesoscale data because of the poor temporal and spatial resolution of radiosonde soundings. Hillger and Vonder Haar (1981) and Mostek, et al. (1986) showed that infrared sounder data can be used to detect variations in low-level water vapor concentrations and consequently they are useful for assessing the potential for deep convection over the Great Plains. The use of sounders for observing surface characteristics has been focused on the monitoring of sea surface temperatures (Njoku, *et al.*, 1985; Bates and Smith, 1985). The VISSR Atmospheric Sounder (VAS) can be operated at high resolution in horizontal space and in time (Menzel, et al., 1983), so it has particular potential as a mesoscale analysis tool. However, the VAS (and other present-day satellite sounders) is limited in that the retrieved profiles are of mediocre absolute accuracy and poor vertical resolution. In addition, clouds are a major obstacle to retrievals from infrared data. Microwave sounders are much less sensitive to clouds, but they have other limitations.

Mesoscale numerical models are useful for analyzing and forecasting regions of destabilization, and are particularly well suited to situations in which terrain variations strongly force atmospheric circulations (Pielke, 1984). When used for analysis, the model complements the observational data by filling in gaps between observations (in space and time) and providing estimates of parameters that were not measured. Synoptically forced (Anthes, *et al.*, 1983) and ground-surface forced (Segal and Pielke, 1981) weather events have been studies by these means.

Data for initialization and updating of models can be retrieved from satellite sources provided that clouds do not give rise to large data gaps and that the retrieved data are consistent with other characteristics of the model atmosphere (Cram and Kaplan, 1985). In four-dimensional initialization and forecast experiments (Cram and Kaplan, 1985; Aune,

et al., 1987) VAS data were used to retrieve profiles of atmospheric parameters, and the retrievals were input to the models. This approach constitutes a one-way flow of information from the satellite to the models.

The author believes that there are significant disadvantages to the approaches that have been used to apply satellite soundings to mesoscale numerical modeling, in which the retrieval operation has been largely separate from the modeling. One problem is that the constraints on the retrievals are not optimal for the particular times and locations at which the retrievals are performed. Baker *et al.* (1987, as attributed to J. Susskind) discussed why it is advantageous to use model output in the constraints, within the context of a synoptic scale assimilation problem. Input from a model can enhance the vertical resolution of satellite soundings, and error reduction in terms of vertical structure leads to reduction of errors in the horizontal structure at any given altitude. A second problem is that there is a tendency for some of the modeled atmospheric features to be needlessly and detrimentally altered in the process of introducing retrieved data. Gal-Chen *et al.* (1986) addressed one aspect of this problem using variational analysis.

The research reported in this dissertation was motivated in part by the prospect of enhancing mesoscale analysis capabilities by alleviating these problems to the maximum possible extent. The chosen approach was to intimately couple the numerical interpretation of satellite sounder data with numerical modeling. Hayden (1973) and Kreitzberg (1976) proposed a merger of technologies such as this for synoptic and mesoscale applications, respectively.

The principal objectives of the research reported in this dissertation were to demonstrate the feasibility and value of using a coupled satellite/ model approach to mesoscale analysis, and to explore the kinematics of the mesoscale pre-convective environment over the Northeastern Colorado region in summer. Two parameters were the foci of this study — water vapor concentrations and ground surface temperatures. Air temperatures could also be included in coupled analysis, but an elaborate initialization procedure would be needed to avoid exciting spurious gravity waves in the model. It was preferable, at this stage of the research, to work with parameters that only slowly influence the modeled dynamics.

2.0 TOOLS AND TECHNIQUES

2.1 VAS Characteristics

The VAS radiometers on the GOES geostationary platforms are used for both imaging and sounding of the atmosphere and ground surface. Each instrument includes one visible channel with a ground resolution of about 1 km and twelve channels that detect radiation in filter-selected bands between 3.7 and 15 μm with 7- or 14-km resolution. Spin scanning provides spatial coverage, and in the dwell sounding mode each field of view can be viewed repeatedly to allow for averaging out a portion of the measurement noise. In addition, it is intended that some spatial averaging of adjacent fields of view be done to bring noise levels down sufficiently that profiles of atmospheric temperature and water vapor can be retrieved (Menzel, *et al.*, 1983).

Several characteristics of the VAS sounder channels are summarized in Table 2.1, and weighting functions computed for the U.S. Standard Atmosphere (1976) are shown in Fig. 2.1 (Chesters and Robinson, 1983).

2.2 Retrieval/Radiative Transfer Computation Methods

VAS data were used to simultaneously retrieve three parameters: ground surface temperature, atmospheric temperature profile, and water vapor mixing ratio profile. The solutions for all parameters were mutually dependent. The retrieval procedure was iterative, starting with initial guess values of the parameters and altering them systematically so that the radiances computed from the parameterized atmosphere would approach the radiances observed by the VAS system. For retrieval it was necessary to have methods for computing atmospheric transmittances and integrating the radiative transfer equation. The same methods also were used for simulating VAS data within idealized analysis experiments. The required transmittances and Plank radiance integrals were computed by an efficient scheme based

Table 2.1 VAS Instrument Characteristics (VAS-E)

Channel	Central Wavelength (μm)	Principal Purpose	Inflight Single Sample Noise (mW m^{-2} sr^{-1} cm)	Specified Acceptable Noise for Sounding ϵ_L [1]	ϵ_T [2]
1	14.7	Temperature	2.8	0.25	0.3
2	14.5	"	1.5	0.25	0.3
3	14.3	"	1.1	0.25	0.3
4	14.0	"	0.9	0.25	0.2
5	13.3	"	0.8	0.25	0.2
6	4.5	"	0.023	0.004	0.1
7	12.7	H_2O	0.8	0.25	0.2
8	11.2	Surface	0.2	0.25	0.2
9	7.3	H_2O	0.6	0.15	0.4
10	6.7	H_2O	0.2	0.10	0.5
11	4.4	Temperature	0.027	0.004	0.3
12	3.9	Surface	0.007	0.004	0.1

[1] ϵ_L – radiance units (mW m^{-2} sr^{-1} cm)
[2] ϵ_T – brightness temperature units (K)

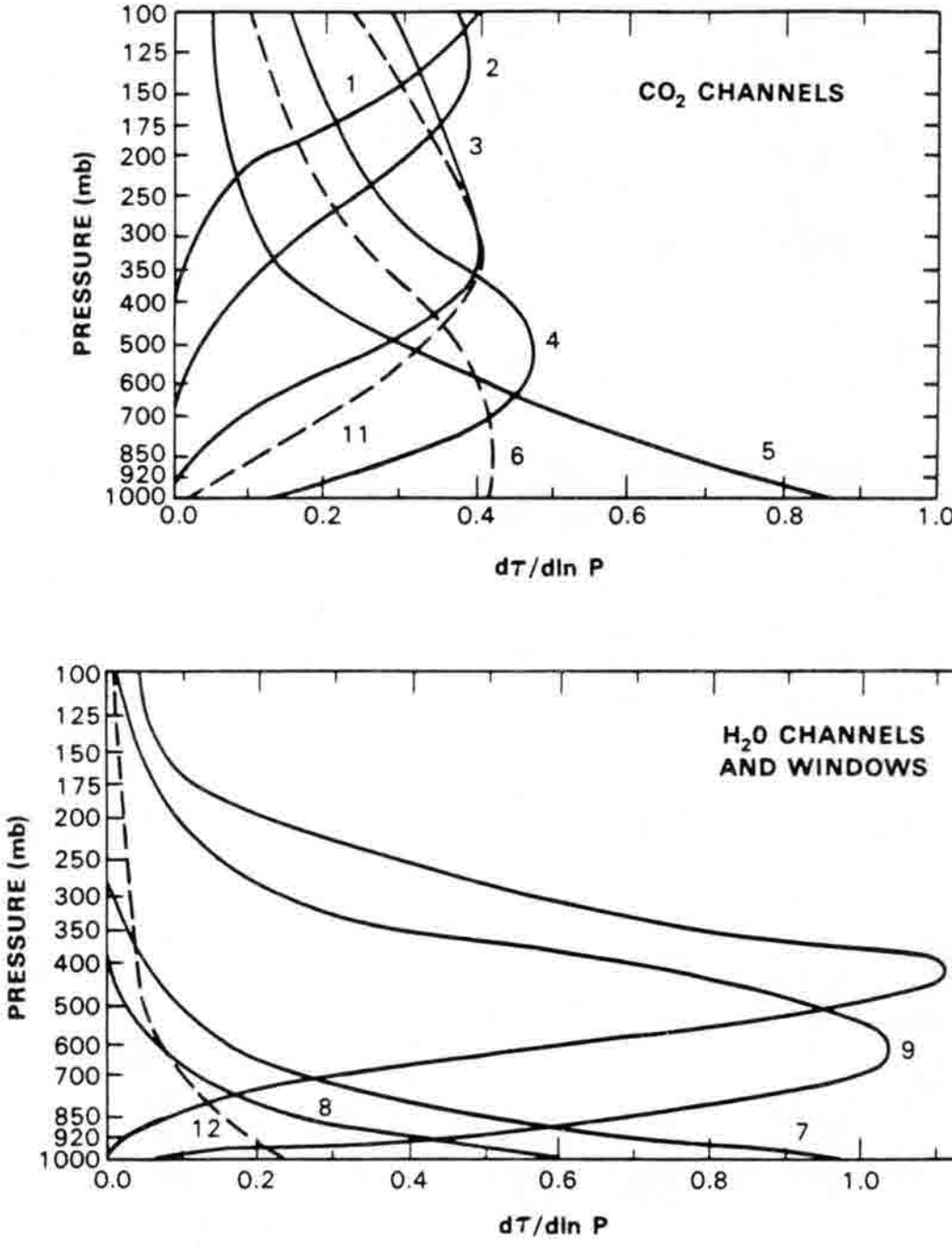

Figure 2.1 Standard VAS weighting functions (Chesters and Robinson, 1983).

on empirical modeling (Smith, *et al.*, 1974; Weinreb and Neuendorffer, 1973; McMillin and Fleming, 1976; and Fleming and McMillin, 1977).

In Appendix A the formulae used to adjust the retrieved parameters are described and the retrieval procedure is outlined. The procedure included an option to retrieve only surface temperature by assuming that the atmospheric component of surface channel radiances could be accounted for adequately via the initial guess profiles. This will be referred to as "quick" surface temperature retrieval. Also, there was an option to either iterate until the water vapor profile appeared to converge, or to stop iterating when the computed radiances (or equivalent blackbody temperatures) agreed with the VAS-observed values within the expected instrument noise.

2.3 Objective Analysis

Horizontal interpolation was needed in the case study to transfer data between the model grid and the satellite sounding locations. The Lipton and Hillger (1982) method was tailored specifically to use with satellite data, but a few modifications were made for application to this research project.

To avoid tight packing of gradients between widely spaced data points the interpolation weighting function was altered to decrease less rapidly at great distances. The new function W is

$$W = \begin{cases} \exp(-aS^2), & W \geq 0.1; \\ bS^{-2}, & W \leq 0.1; \end{cases}$$

where S is distance, a is determined by least squares (as before), and b is chosen such that the function is continuous at $W = 0.1$. In addition, a maximum was put on a to avoid problems when data are noisy.

The criterion for identifying data gaps was altered so that a gap is present if the radius of consideration is greater than $2d_m$, where d_m is the median distance from each data point to its closest neighboring data point. For this study, the radius of consideration remained circular even in data gaps.

2.4 Numerical Model Formulation

Atmospheric processes were modeled with a version of the Colorado State University Regional Atmospheric Modeling System. The formulation was hydrostatic and incompressible, with a rectangular, staggered grid in the horizontal and a terrain following, staggered grid in the vertical (Pielke, 1974; Mahrer and Pielke, 1977). The lateral boundary conditions specified zero gradients perpendicular to the boundaries for all parameters except the vertical velocity, which was diagnosed from the horizontal wind. The upper boundary included a momentum-absorbing layer to control wave reflection (Mahrer and Pielke, 1978; Klemp and Lilly, 1978). Water vapor concentrations were computed, but no phase changes were included within the atmosphere and clouds were not represented explicitly. Boundary layer processes (McNider and Pielke, 1981) and solar and longwave radiation (Mahrer and Pielke, 1977) were parameterized.

At the ground surface, the modeled fluxes of momentum, sensible heat, water, and radiation depended on the surface temperature. One method used to determine the surface temperature was solution of an energy balance equation, which depended on specified values of soil characteristics (Mahrer and Pielke, 1977). An alternative was to use retrievals from VAS data to prescribe the surface temperature at each grid point at every time step. An option allowed computing surface fluxes from a weighted average of the energy-balance and satellite-derived temperatures, recognizing that both values are subject to errors. While both surface temperatures were carried separately in the computer, the energy-balance value was somewhat dependent on the satellite value (when one was used) since some terms of the energy equation included atmospheric parameters that are sensitive to the history of surface temperatures. For example, air temperatures depend on forcing by the surface and they feed back into energy balance computations, since sensible heat fluxes depend in part on air/surface temperature contrasts.

An option was built into the model to allow for updating the water vapor concentrations at any stage of the model run. This made it possible to directly insert satellite-retrieved data at each VAS observation time. No elaborate initialization procedure was needed because alteration of water vapor had such a slow and small effect on modeled winds that gravity

wave excitation was of no concern. Experiments on model sensitivity to water vapor are discussed in Chapter 3.

Atmospheric temperatures and winds were initialized by starting with horizontally homogeneous fields and then allowing the flow to interact with the terrain until approximate balance was reached. During this dynamic initialization period radiative forcing and ground temperatures were held constant. Soil temperatures were initialized with the same profile at every grid point. Values were specified in terms of differences from temperatures of the air just above the terrain surface, so they varied with terrain elevation whenever the atmosphere was not isothermal.

2.5 Mesoscale Water Vapor Analysis Methods

Satellite-based sounders and mesoscale models can be used in a variety of ways to produce water vapor analyses. The possible methods range from using the two technologies separately to an intimate coupling of the two, while several intermediate options exist. Four schemes are introduced below, with results presented in Chapters 4 and 5.

2.5.1 Method 1: Stand-Alone Retrieval

The initial guess sounding for iterative retrieval methods generally is obtained from nearby radiosondes (Hillger, 1984), a climatology, or operational synoptic-scale model output (Smith, 1983). The guess reflects little, if any, mesoscale information in terms of space and time variation. Retrieval results at consecutive observation times are largely independent of one another. Figure 2.2a diagrams an example in which VAS data at four observation times are used to retrieve mesoscale water vapor fields, each based on an initial guess field. The small arrows depict the flow of information, which is vertical. The initial guess can have a large or small impact on the final retrieval depending on the iterative adjustment procedure. In the stand-alone approach the impact should be relatively small since little mesoscale information can be lost in deviating from the initial guess, while the mesoscale information in the VAS data should be fully utilized.

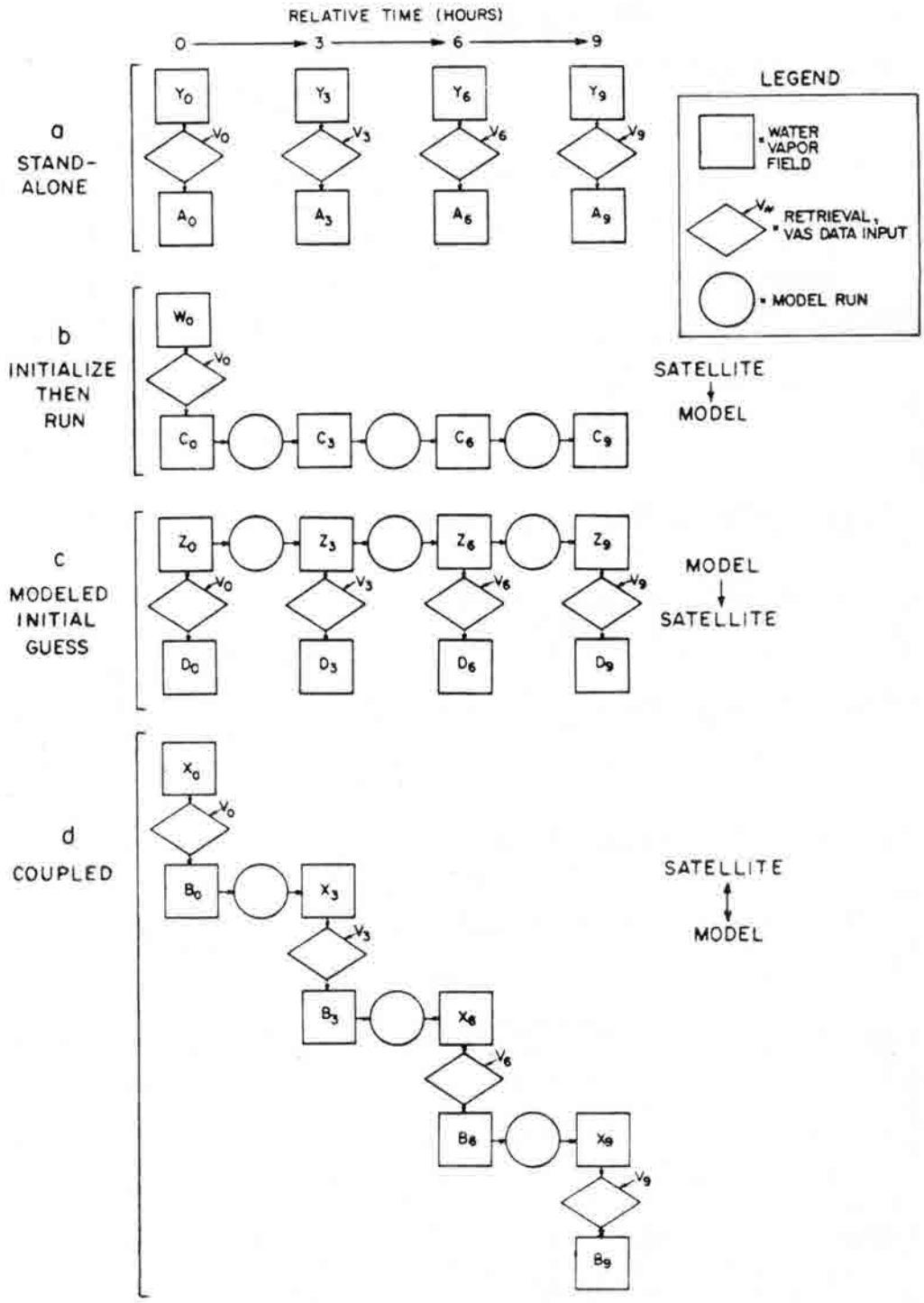

Figure 2.2 Schematic diagrams of procedures for producing mesoscale water vapor analyses. Symbols are defined in the legend. Arrows indicate the flow of data. Subscripts identify the relative time corresponding to the data, with the assumption that VAS data are available at three-hour intervals. Diagrams are for a) stand-alone retrieval, b) initialized model run, c) modeled initial guess, and d) coupled analysis.

2.5.2 Method 2: Initialized Model Run

The traditional approach to using mesoscale models in weather analysis is shown in Figure 2.2b. In this case VAS retrievals provide the initial model field and the flow of information is primarily horizontal (over time). Each analysis depends entirely on the previous analysis along with the model's simulation of intervening atmospheric processes.

2.5.3 Method 3: Modeled Initial Guess

Figure 2.2c depicts the use of mesoscale model output to provide initial guesses for retrieval. This analysis scheme has the advantage that the initial guesses contain some mesoscale information, and should therefore be closer to the true atmospheric profiles than the ones in scheme 1. The modeled fields reflect variations in boundary layer development and its influence on vertical sounding structure. Also, the model can simulate the effect of mesoscale flows on the synoptic scale features present in the original analysis (Z_0, Fig. 2.2c).

2.5.4 Method 4: Coupled

The coupled analysis scheme (Fig. 2.2d) is a cross between methods 2 and 3. The final analysis (B_9) contains information from three short model runs and four sets of VAS data. The coupled approach includes the advantages of method 3, but also allows for the interaction of VAS-detected mesoscale features with mesoscale circulations. In coupled retrieval the initial guess should have a substantial impact on the retrieved profiles so that mesoscale modeled information is retained. In practice, iteration was halted as soon as the computed brightness temperatures agreed with the observed values within the expected noise levels at each of times 3, 6, and 9 (Fig. 2.2d). At time 0, iteration was continued to convergence.

Coupling offers the potential to minimize problems caused by small areas of missing VAS data (for example, data transmission failures or interference by clouds). The retrieval/adjustment process might be done only where VAS data are present, while in data

gaps the intial guess may be retained unaltered. There would be little detrimental effect on the analysis as long as the gap does not persist through every set of VAS data.

The transfer of water vapor analyses between the retrieval program and the model is a potential source of problems whenever the satellite provides model input at more than one time. There is a danger that any strong horizontal or vertical gradients produced by the model could be smoothed out during interpolation from satellite retrieval points to the model grid. For example, Cram and Kaplan (1985) found VAS water vapor data assimilation to be detrimental to their model forecasts because of a smoothing problem. Gal-Chen *et al.* (1986) dealt with smoothing in the vertical dimension by adjusting forecast temperature profiles according to deep-layer average temperatures from VAS instead of adjusting to the smooth VAS-retrieved profiles that comprised their data set.

This study employed an interpolation procedure that does no unwanted smoothing of model-generated gradients during a retrieval step, but still incorporates virtually all of the vertical and horizontal structure that can be resolved in VAS soundings. First, data were interpolated linearly in the vertical from model grid levels to VAS retrieval levels. Then (in 3-dimensional analyses) the data were interpolated horizontally to VAS sounding locations. Retrievals were done using the interpolated data as initial guesses. At this point some smoothing had taken place, but it had little effect on retrieval accuracy since the model resolution was finer than the retrieval resolution. The retrieval results were not directly interpolated back to the model grid. Instead, the *difference* between the retrieval and the intial guess was interpolated vertically, and then horizontally back to the model grid. Then the difference was added to the original model output values. The result is an updated analysis that is just an adjustment of the model field to bring it into closer agreement with the VAS radiance observations.

Schemes related to the one introduced here have been used at the synoptic scale by O'Lenic (1986) and Douglas and Warner (1987). In their studies a model provided initial guess data for retrievals, which were in turn used to initialize a numerical forecast. One distinction is that our method has multiple sets of satellite data influencing a single time-continuous analysis. In addition, their retrievals were directly interpolated to the model grid,

along with observations from non-satellite sources. For their synoptic scale applications it may not have been very important to avoid smoothing on interpolation.

2.6 Surface Temperature Coupling Method

A problem in using satellite retrievals of surface temperature as model input is that values must be specified at every grid point at every time step. Water vapor concentrations are simpler to input because they are an initial condition, while surface temperatures are a time-dependent boundary condition. The model used for this study generally requires time steps of one to two minutes, whereas the VAS typically makes observations at a frequency of three hours. Temporal interpolation is needed for model runs intended as analyses, and for forecasts it is necessary to extrapolate or use data from other sources (e.g. revert to energy balance computations). Furthermore, spatial interpolation may be complicated by the presence of cloudy regions where retrievals are not possible. Cloud-shaded areas tend to be cooler than clear ones, so interpolations from clear to cloudy areas are subject to exceptional error. The method used for surface temperature input was designed to accommodate these problems.

Surface temperature retrieval results were transferred from retrieval locations to the model grid in an adjustment process identical to the one used for water vapor coupling, except that no vertical interpolation is needed since this is done on a single terrain-following surface. As with water vapor adjustment, gradients resolved by the satellite data are not smoothed. In addition, gradients stemming from variations in terrain elevations are retained even in data-free gaps. At this stage it was possible to assign each gridded value a quality factor based on the distance to the nearest retrieval locations, the presence or absence of cloud cover at the grid site, and any other factors that affect retrieval accuracy. The definition of the quality factors can be tailored for any given situation, but they must have values ranging from zero to one.

Time interpolation was done independently at each grid point by fitting a cubic spline through the values at all available observation times. The spline parameters and quality factors were model input. Surface temperatures were computed at each time step from the splines, and quality factors were interpolated linearly between observation times. The

quality factors were the weights used in averaging satellite-derived surface temperatures with energy balance values (see Sec. 2.4). By using splines and weights the time-dependent surface temperatures were controlled directly, and there was no need to employ nudging methods (Hoke and Anthes, 1976).

Figure 2.3 is an illustration of the scheme for incorporating surface temperature retrieval with coupled water vapor analysis, and is an extension of Fig. 2.2d. The choice of design was inspired by a desire to maximize accuracy of the surface temperature estimates while minimizing the amount of computation involved in retrieval. Here, surface temperatures are a relevant part of the input and output of the retrieval program and the model. Two retrieval options are employed, full and "quick" retrieval (see Sec. 2.2). For a given observation time, the estimates of surface temperatures improve each time "quick" retrieval is performed, due to improved initial guess data. When the model run catches up to that observation time, a full retrieval provides the best and final estimate of surface temperatures while also retrieving water vapor values.

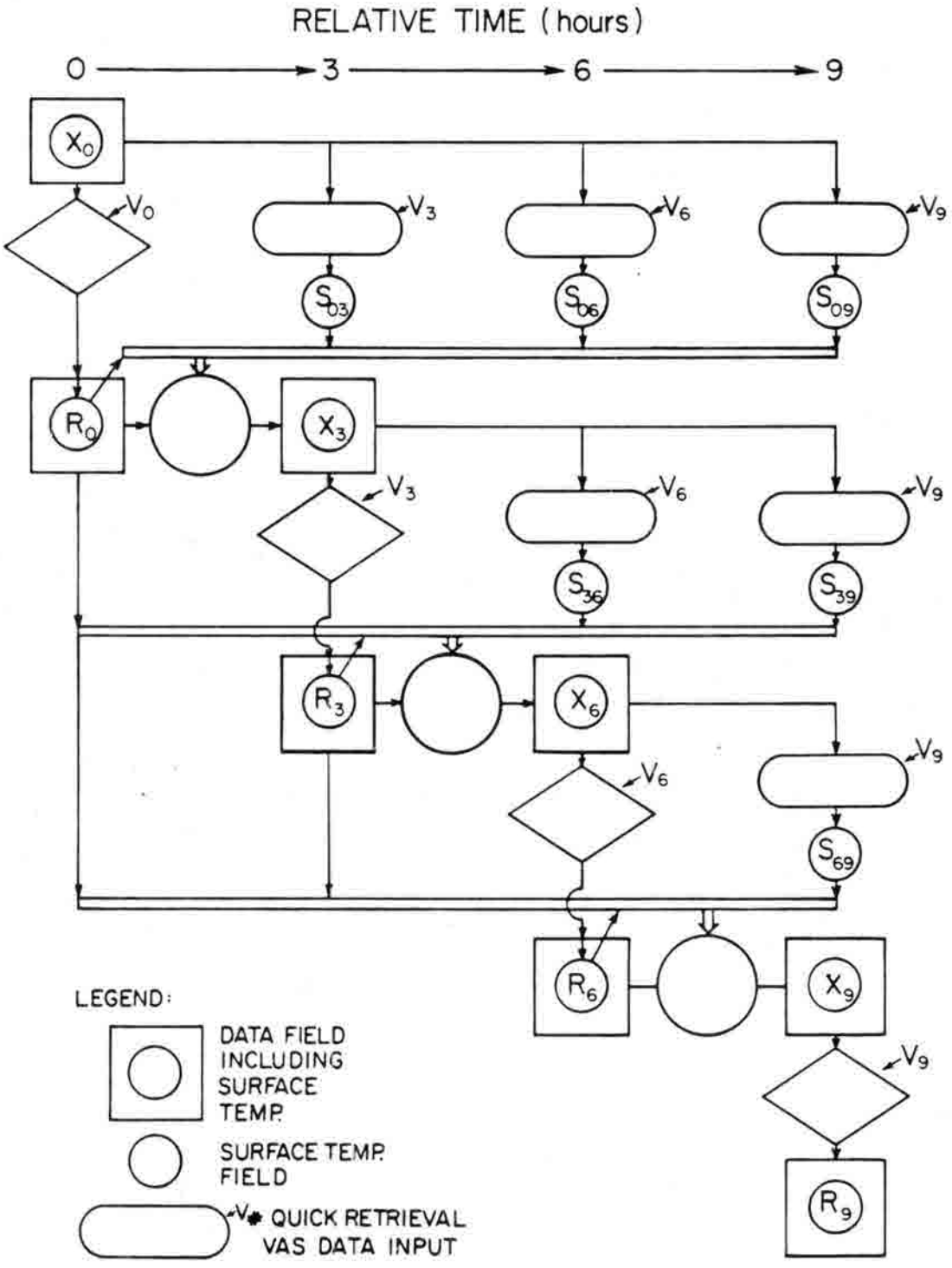

Figure 2.3 A schematic diagram of the procedure for coupling surface temperature retrieval with mesoscale model integration. Symbol definitions are the same as in Fig. 2.2, except as noted in the legend. The double lines denote assembly of surface temperatures and spline fitting.

3.0 MODEL SENSITIVITY TESTS

Experiments were conducted to test the sensitivity of the numerical model to various controls on the behavior of the water vapor concentrations and the surface temperatures. The goals were to 1) make sure that changes in the model formulation would not give rise to serious computational problems, 2) determine the extent to which virtual temperature could be replaced by temperature in the model equations, and 3) determine the impacts of perturbations of water vapor and surface temperature on modeled wind fields.

3.1 Water Vapor

There are two primary ways in which water vapor concentrations can affect modeled winds. Longwave and shortwave radiative fluxes are sensitive to water vapor, and they in turn affect winds by way of air temperatures. In addition, air density depends on the water vapor mixing ratios. This effect is generally accounted for by using virtual temperatures in place of actual temperatures in the appropriate model equations.

3.1.1 Control

Sensitivity tests were performed with a two-dimensional version of the numerical model, using a domain that was a highly simplified east–west cross-section through the mountains and high plains of northeastern Colorado. The domain (Fig. 3.1) consisted of a horizontal region spanning 705 km at a grid spacing of 15 km and a vertical grid with 26 levels from 10 to 13,500 m above ground level (Table 3.1). The model was run under mid-summer conditions, and was initialized at sunrise (05 LST) with a July average temperature sounding from Denver, Colorado (Fig. 3.2) and a uniform geostrophic wind of 0.5 m/s from the south. The run duration was eight hours, with a 120-s time step. For surface energy balance computations, the parameter values were:

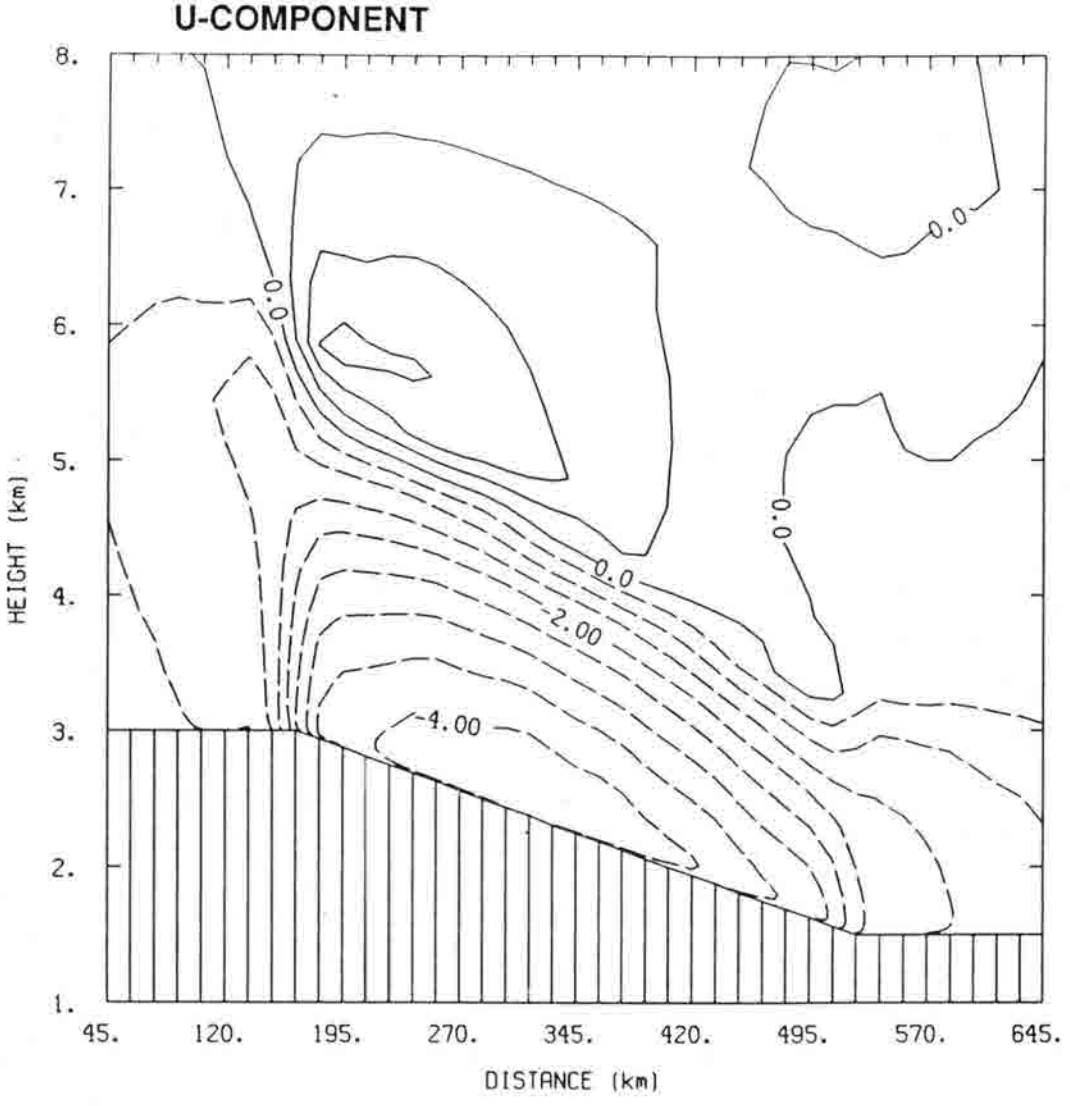

Figure 3.1 The analysis domain for two-dimensional experiments, with the westerly wind component (m/s) for the sensitivity test control run at eight hours after sunrise (13 LST). At sunrise the westerly wind components were less than 0.5 m/s throughout the domain. Contours are at intervals of 0.5 m/s, with dashed lines for negative (easterly) winds. Horizontal distance is relative to the western boundary of the model grid, and height is relative to sea level. Vertical hatching denotes the terrain, with the lines at model grid points.

Table 3.1 Vertical grid levels for model runs.

Level	Height (m)	Level	Height (m)
1	10.	14	2750.
2	20.	15	3250.
3	30.	16	3750.
4	50.	17	4250.
5	90.	18	4750.
6	150.	19	5500.
7	250.	20	6500.
8	500.	21	7500.
9	750.	22	8500.
10	1000.	23	9500.
11	1350.	24	10,500.
12	1750.	25	11,500.
13	2250.	26	13,500.

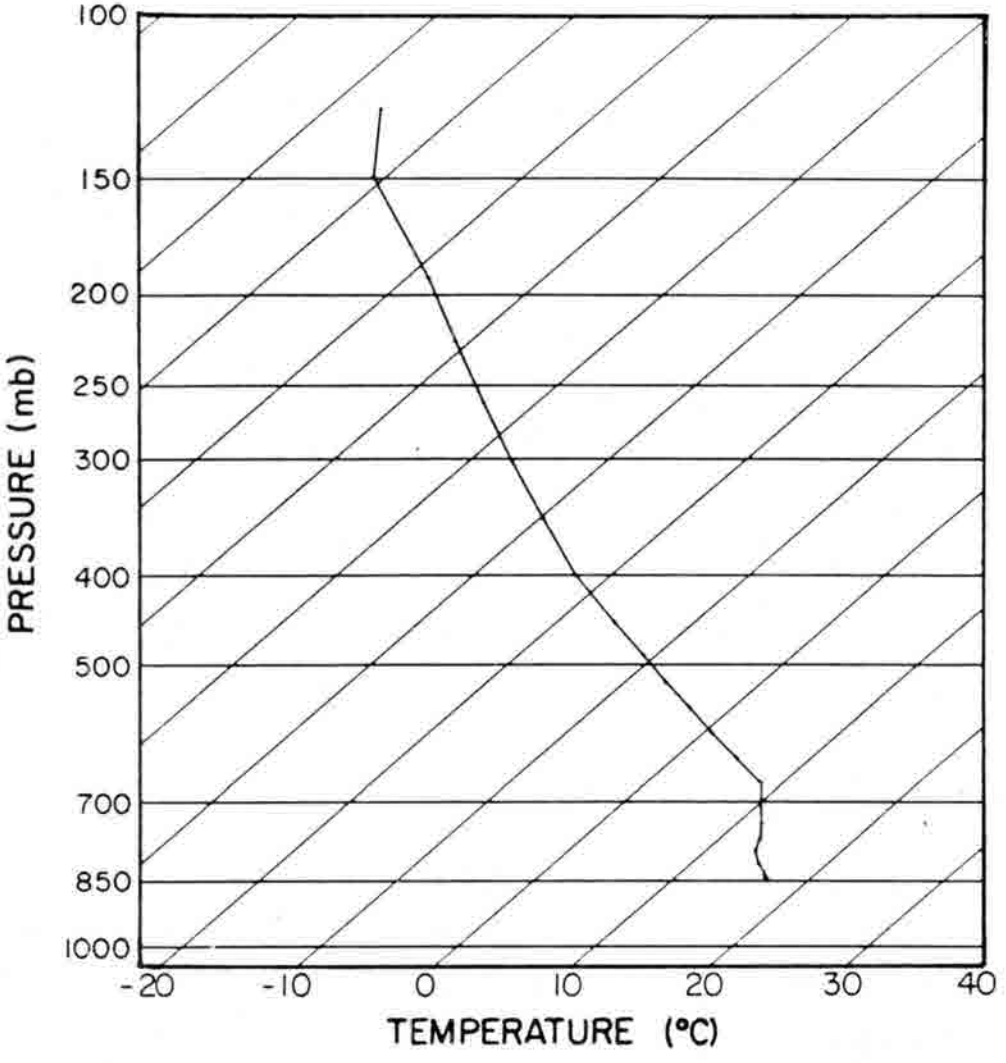

Figure 3.2 The temperature sounding used to initialize the two-dimensional experiments.

soil thermal conductivity	3.0×10^{-7} m^2 s^{-1}
soil density	1.5×10^3 kg m^{-3}
soil specific heat	1.25×10^3 J kg^{-1} K^{-1}
soil wetness	0.04.

The surface roughness length was 0.03 m, the surface albedo was 0.2, and the initial soil temperature profile was as in Fig. 3.3.

For this control run, water vapor concentrations were initialized with a uniform field in the horizontal along lines of constant height (Fig. 3.4a). Surface temperatures were determined by energy balance computations.

The control wind and water vapor fields (Figs. 3.1, 3.4) were heavily influenced by solar heating of the sloping terrain. Throughout the day the well-mixed layer deepened and the low-level flow accelerated upslope. A mid-level return flow appeared as a zone of westerlies. The water vapor concentrations reflected the boundary layer growth and the vertical motions associated with the local circulation.

3.1.2 Radiative Effect

The impact of water vapor concentration changes on wind speed was investigated with a model formulation that did not account for water vapor's density effect; that is, the difference between virtual temperatures and actual temperatures was neglected. For these experiments the model was initialized with conditions identical to those in the control run, except that water vapor concentrations were perturbed. The run durations were eight hours past sunrise.

First, noise was added to the mixing ratio values as follows. Mixing ratio perturbations were computed independently for each horizontal grid point at pressure levels of 10, 30, 40, 50, 70, and 85 kPa. The perturbations were normally-distributed products of a random-number generator, with magnitudes that varied with pressure level. The perturbation standard deviations for each of the above levels were 0.01, 0.02, 0.2, 0.6, 1.6, and 2.2 g/kg, respectively. The perturbations were then interpolated vertically to the vertical grid heights and added to the grid values of mixing ratio. This approach provides for some vertical coherence of the noise and accounts for the fact that mixing ratios, and mixing ratio variabilities, tend to decrease sharply with height. An example of a noisy water vapor

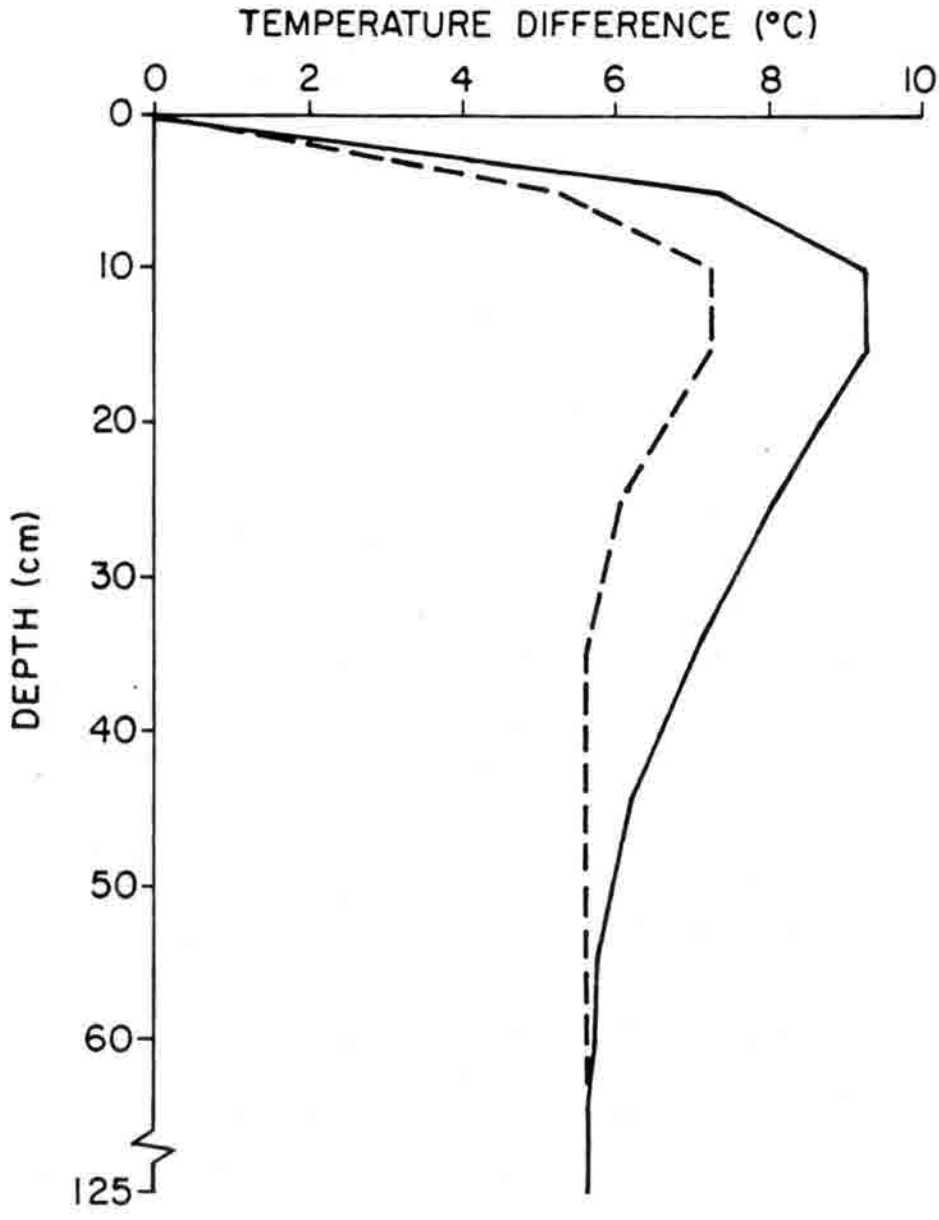

Figure 3.3 Initial soil temperature profiles, given as a difference from the temperature at the bottom of the atmosphere at any given grid location. The dashed line is for the altered initialization (Sec. 4.2.1). The solid line is for all other simulations and sensitivity tests.

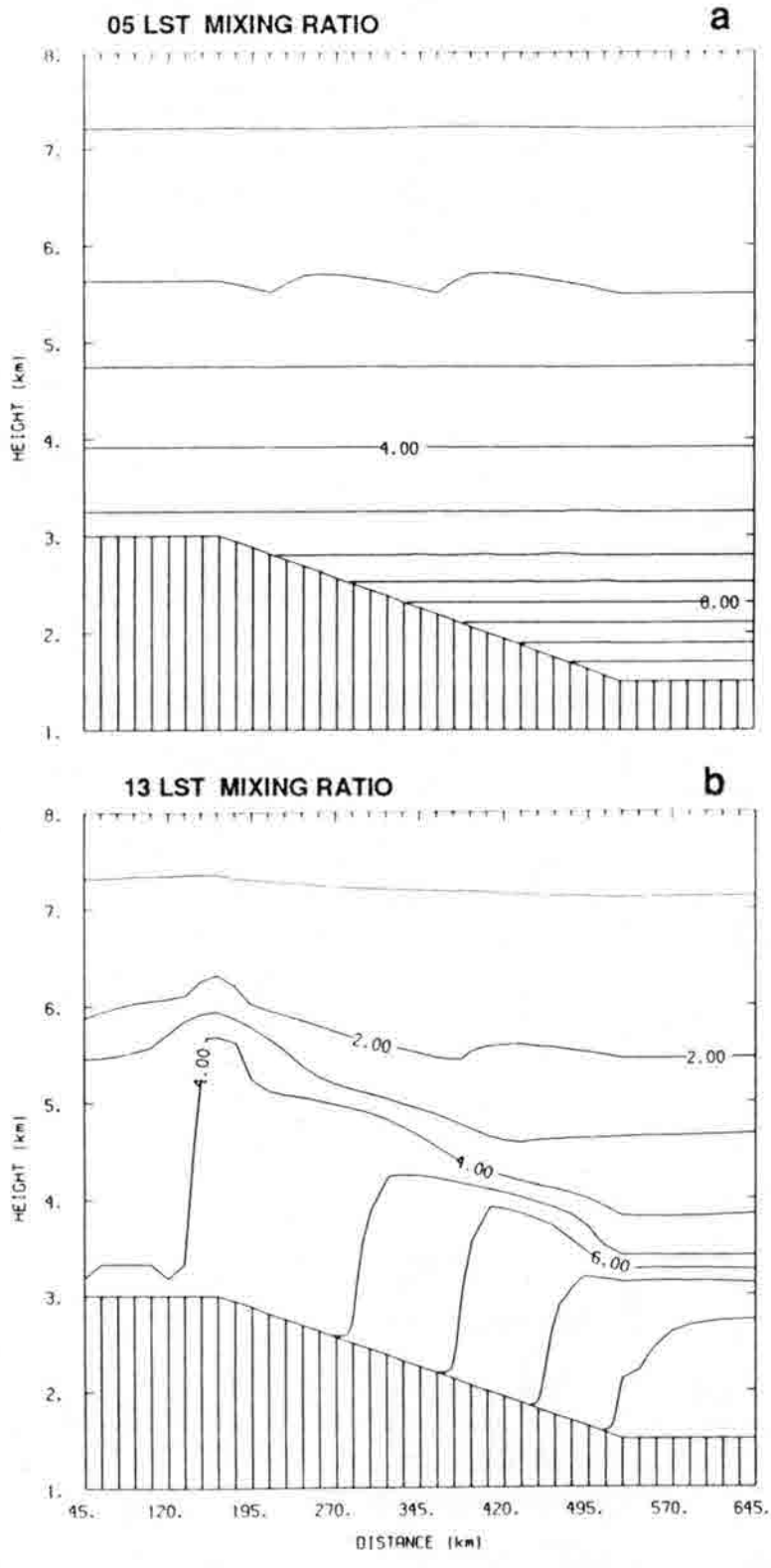

Figure 3.4 Water vapor mixing ratios (g/kg) for the sensitivity test control run at a) sunrise (05 LST) and b) eight hours later (13 LST). Contours are at intervals of 1 g/kg.

field is diagramed in Figure 3.5. An ensemble of ten such fields were produced and each was used to initialize a model run.

The winds produced in the noise tests (not shown) were not significantly different from the control winds. Positions of the upslope and downslope speed maxima were essentially unchanged. The magnitude of the upslope maximum changed by 1.7% in the most extreme of the ten cases. Horizontal wind speed differences were typically less than 0.1 m/s. Thus, the addition of noise to the modeled water vapor values did not have any detrimental impact on model performance in terms of the effect on the pressure gradient force.

The next water vapor perturbation was a ten percent increase in mixing ratio values over the entire field. This change had a small impact on several of the terms in the surface energy balance computations, with downwelling longwave radiation being the dominant factor. The net effect on the winds was a negligible (less than 1%) increase in the intensity of the upslope/downslope circulation.

An experiment was run with water vapor concentrations decreased from the control values by ten percent in the eastern half of the domain and increased by ten percent in the western half. The downwelling longwave radiation at the surface was again the dominant factor, giving rise to a decrease in heating of the high terrain and the converse for the low terrain. The result was a decrease in the upslope wind speed maximum of about 2%.

Another experiment involved perturbing water vapor concentrations by a sudden change in their values from one time step to the next. This was done because the proposed scheme for coupled water vapor analysis called for altering the gridded values at each satellite observation time, making model "shock" a possibility. For this test all fields were identical to the control fields until two hours after sunrise, when the water vapor concentrations were perturbed. Noise was added to the mixing ratios, as described above, and then the values were decreased by 10% in the eastern half-domain and increased by 10% in the western half. After making the perturbations model integration was resumed and carried to the eight-hour point. The modeled wind speeds gradually reacted to the perturbations, with no evidence of "shock".

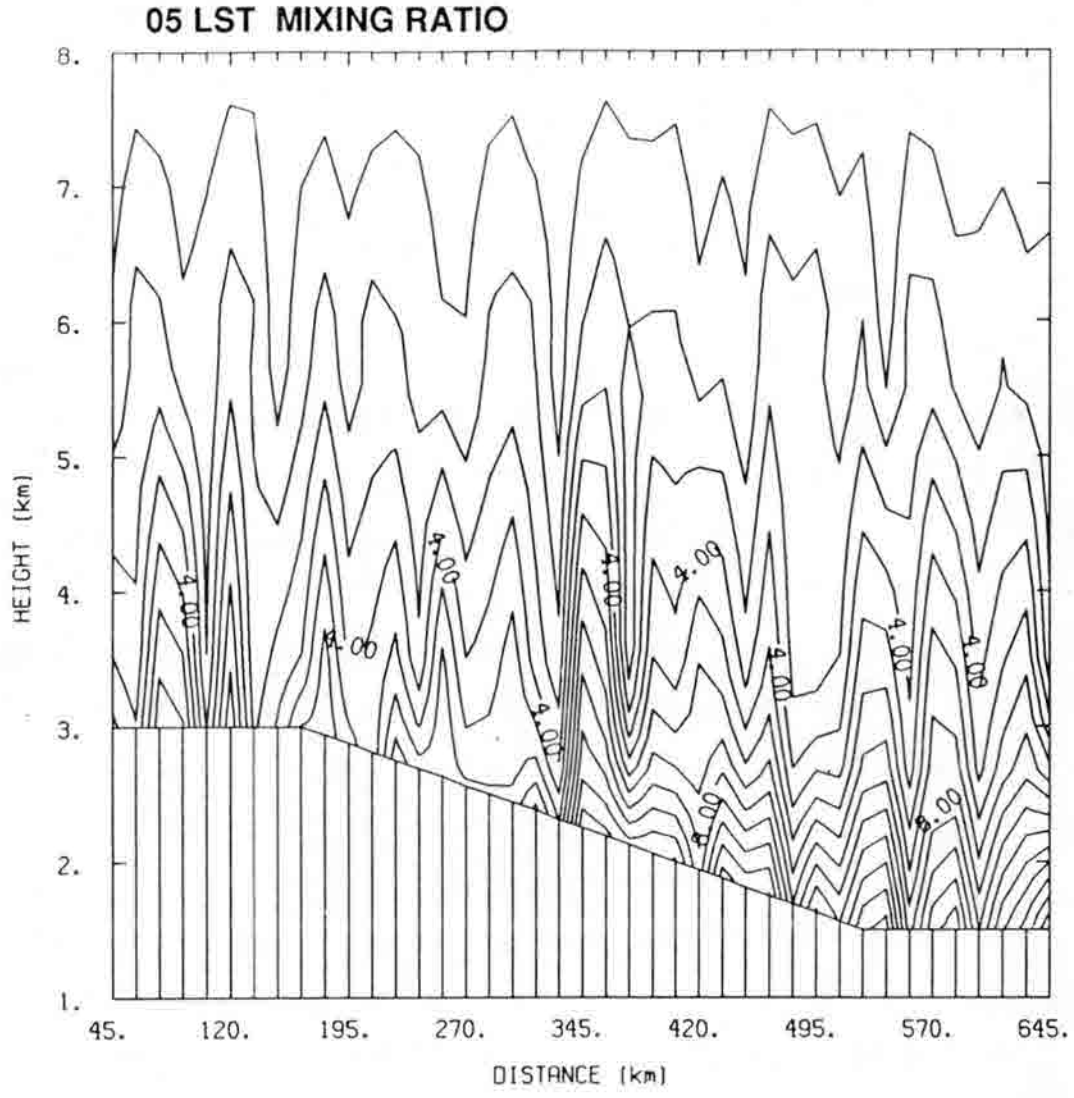

Figure 3.5 Initial (05 LST) water vapor mixing ratios (g/kg) for one of the noisy-field tests of sensitivity to radiative effects. Contours are at 1 g/kg intervals.

3.1.3 Air Density Effect

Water vapor concentrations affect modeled atmospheric flows via density-related terms in several equations, primarily the hydrostatic equation, the horizontal momentum equations, and the equation for boundary layer depth (Mahrer and Pielke, 1977).

A non-uniform water vapor field was used for these experiments, since the pressure gradient force depends on horizontal density gradients. Here, initial mixing ratios were increased from the control values by 10% in the lower 2 km of the eastern half of the domain. Values were decreased by 10% elsewhere. The initial geostrophic wind field was changed to 3 m/s from the east, for applicability to later experiments. The same initial conditions were used for all density-related experiments.

Comparisons were made between results of model runs with 1) temperatures, and 2) virtual temperatures used in all the above-noted equations. At nine hours after sunrise (14 LST) the boundary layer depth was about 4% greater with virtual temperatures than with temperatures. The wind (and water vapor) differences were greatest near the boundary layer top because the locations of strong vertical gradients were displaced. For example, east–west wind velocity differences were as great as 0.7 m/s near the boundary layer top ($\sim$ 17% of the circulation magnitude) but were generally less than 0.2 m/s elsewhere.

To isolate the effect of the boundary layer height computation, the model was run with virtual temperature in that equation and temperature in all others. Results were compared to the all-virtual temperature run at 14 LST. The greatest differences occurred near the intersection of the horizontal water vapor gradient and the boundary layer top, with a maximum east–west velocity difference of 0.25 m/s ($\sim$ 6% of the circulation magnitude). The differences were typically less than 0.1 m/s.

There were no substantial errors caused by neglecting the water vapor effect on density in all terms but the boundary layer depth computation, but there are advantages in neglecting it. When water vapor concentrations have very little effect on the model flows, then water vapor can be treated as an inert substance, and it is straightforward to interpret results of analysis/retrieval experiments. The boundary layer depth computation is not very sensitive to water vapor retrieval, since the depth depends on a vertical gradient that has a scale finer

than scales impacted by retrieval. Hence it was decided that virtual temperature would be used nowhere but the boundary layer depth computation for all later work.

Based on the results of the experiments on radiative and density effects, it was reasonable to treat water vapor as an essentially inert substance in subsequent experiments covering the pre-convective period.

3.2 Surface Temperature

3.2.1 Control

The control model run for surface temperature sensitivity studies was the same as the one used for testing water vapor sensitivity, with a couple of exceptions. The initial condition included the same water vapor distribution and 3 m/s easterly geostrophic wind as were used in the air density experiments (Sec. 3.1.3).

First, the model was run to nine hours after sunrise using the energy–balance computation of surface temperature. At each grid point, the modeled surface temperatures were sampled at three-hour intervals and the four values were fit with a spline in the time dimension. Each spline was clamped at the sunrise point to a temperature tendency of zero, and was free at the nine hour point. In mathematical notation these boundary conditions are $\frac{\partial S}{\partial t}(t{=}0 \text{ hr}) = 0$ and $\frac{\partial^2 S}{\partial t^2}(t{=}9 \text{ hr}) = 0$, where S is the value of the spline. A second model run was made using the splines to specify surface temperatures in place of the energy balance values.

The results of the second run (Fig. 3.6) were nearly identical to those of the first, demonstrating that three-hourly data were sufficient for resolving a smooth diurnal surface temperature cycle. This finding was encouraging, because it supported the idea of using three-hourly VAS data to specify surface temperatures. This also set the stage for surface temperature sensitivity experiments by making it possible to arbitrarily specify perturbations in time-dependent surface temperatures. The three-hourly values could be perturbed before spline fitting, and the model run results could be compared with results from the run with unperturbed values.

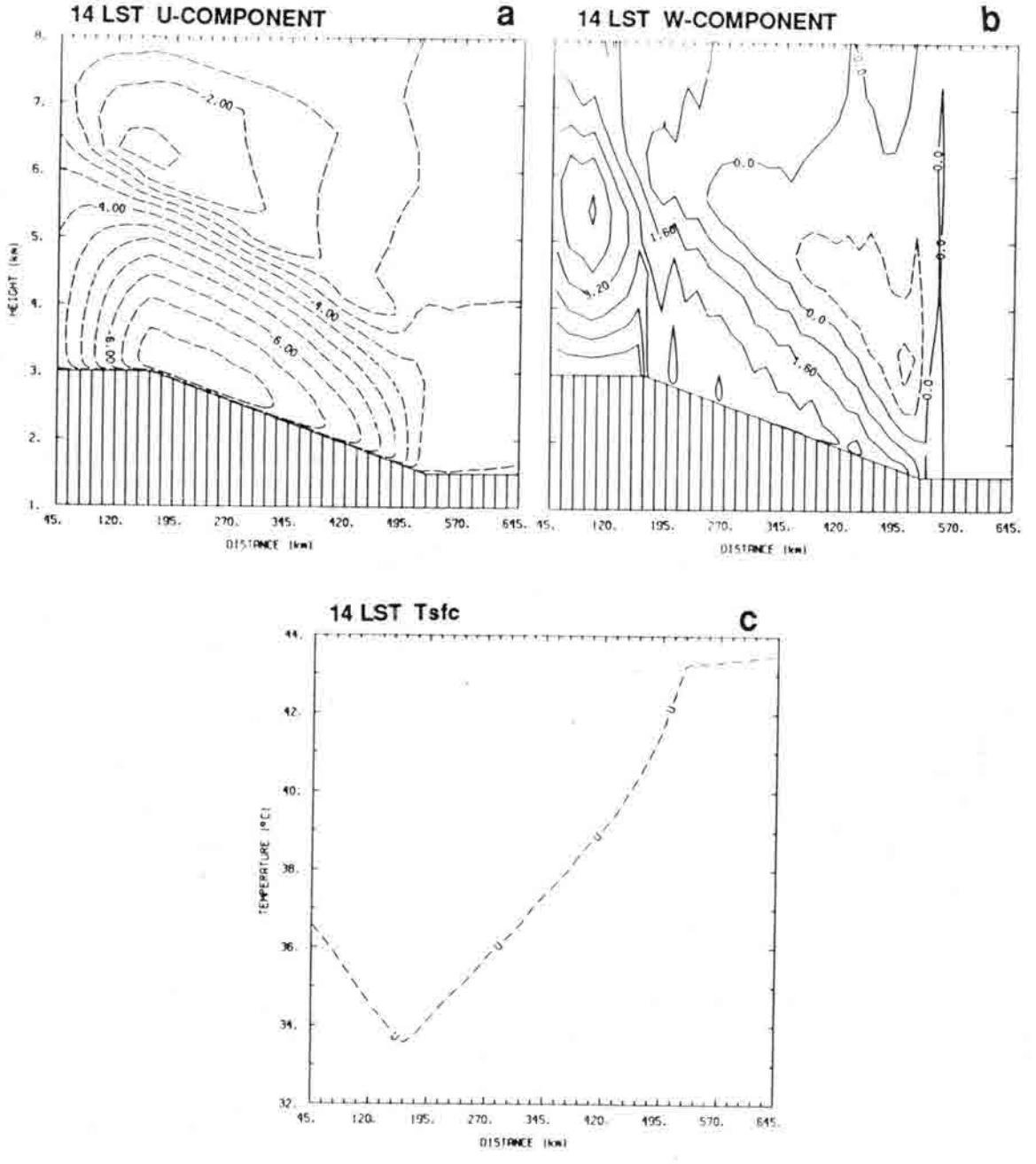

Figure 3.6 Model parameter values for the surface temperature sensitivity control run at 14 LST: a) westerly wind component (m/s) with contours at 0.5 m/s, b) vertical wind component (cm/s) with contours at 0.8 cm/s, and c) surface temperature. A large portion of the high-frequency feature in the vertical winds was found to be caused by small 2-grid length scale variations in terrain height, but the variations had no significant impact on overall flow characteristics.

3.2.2 Perturbation Experiments

The first perturbation experiment involved addition of noise to the surface temperatures. The perturbations were actually done in terms of surface *potential* temperatures for computational convenience. A perturbation of 1 K in potential temperature corresponds to about 0.90–0.95 K in temperature for the range of surface pressures in the domain.

At each three-hourly interval, random noise was added to the gridded values of surface potential temperature. The noise had a normal distribution with a standard deviation of 1 K. This resulted in temperature variations on scales down to $2\Delta x$, where Δx is the grid length. It would be inappropriate to force the model at scales that are very poorly resolved, so the potential temperatures were smoothed according to

$$\theta'_s(x_i) = [\theta_s(x_{i-1}) + 2\theta_s(x_i) + \theta_s(x_{i+1})]/4,$$

where θ_s is surface potential temperature, θ'_s is the smoothed value, and x_i is the location of point i in the horizontal grid. With this smoother applied to a harmonic θ_s the resultant θ'_s is damped by the factor $1 - \sin^2 \frac{\pi \Delta x}{L}$ (Haltiner and Williams, 1980, pp 392-3). This completely eliminates variations of scale $L = 2\Delta x$ and the damping effect decreases for larger scales. A temporal spline was fit through the smoothed values at each grid point, and the spline values were used as forcing in a model run.

An ensemble of ten runs were made with noisy surface temperatures. The impact of surface temperature noise on the wind fields (Figs. 3.7, 3.8) was substantial, with the basic flow features being distorted. The differences had a well-defined cellular structure (see Fig. 3.8b) with preferred scales of about five to ten grid lengths. Sizes appear to correspond to advection speeds over hot and cold spots. Over the ensemble of runs the average greatest vertical wind speed difference (3.1 cm/s) was 64% of the maximum control value, while the most extreme difference (5.1 cm/s) was 104% of the control maximum. Horizontal winds were less sensitive. The average greatest horizontal wind speed difference was 12% of the control's relative wind speed maximum, and the average difference in total horizontal kinetic energy was 0.8%.

In addition to the tests with noisy surface temperatures, experiments were run with surface (potential) temperatures uniformly increased by 1 K and decreased by 2 K. The

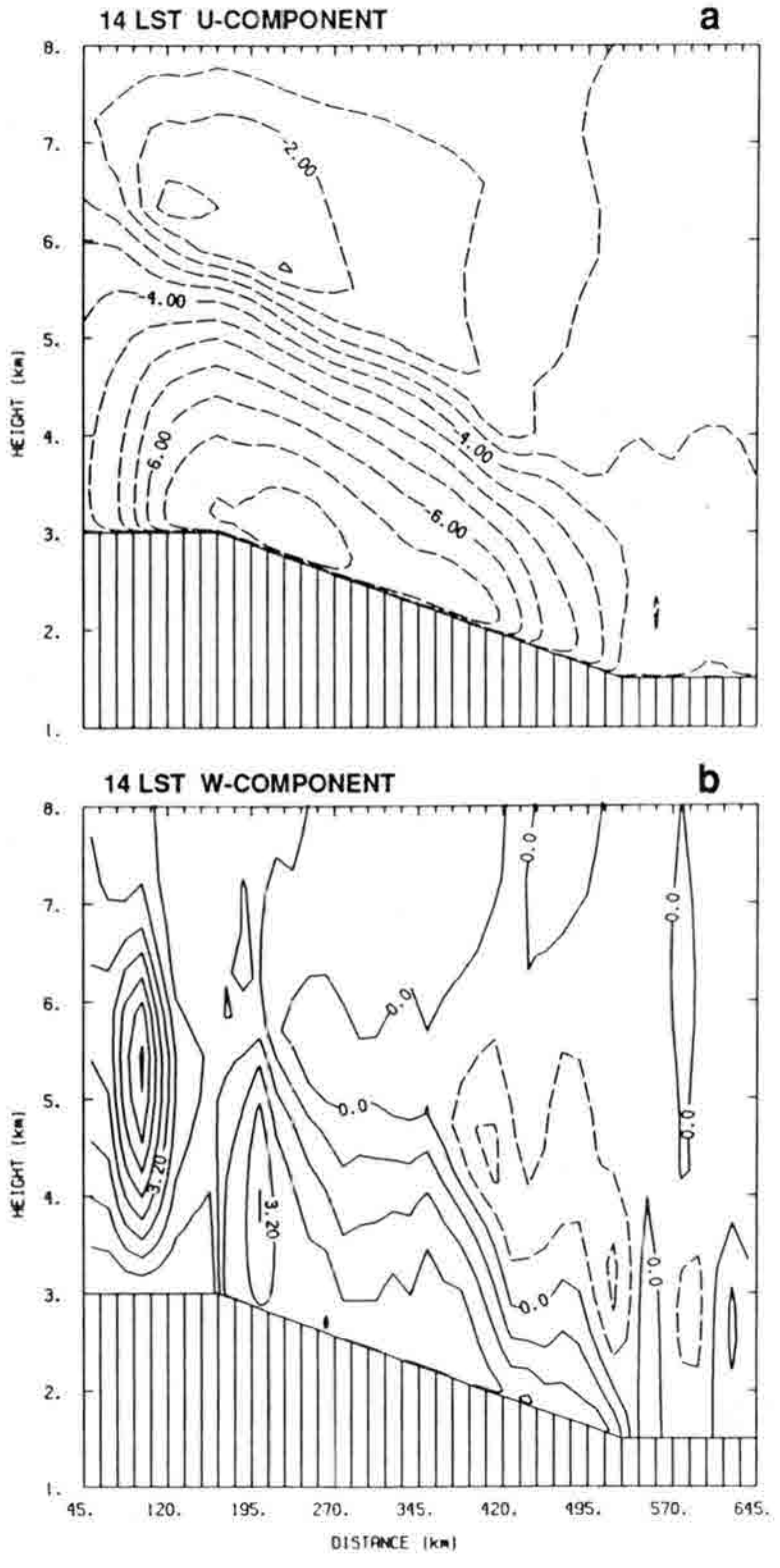

Figure 3.7 The a) westerly and b) vertical wind components for one of the noisy surface temperature model runs (N-1), at 14 LST. Contours are as in Fig. 3.6.

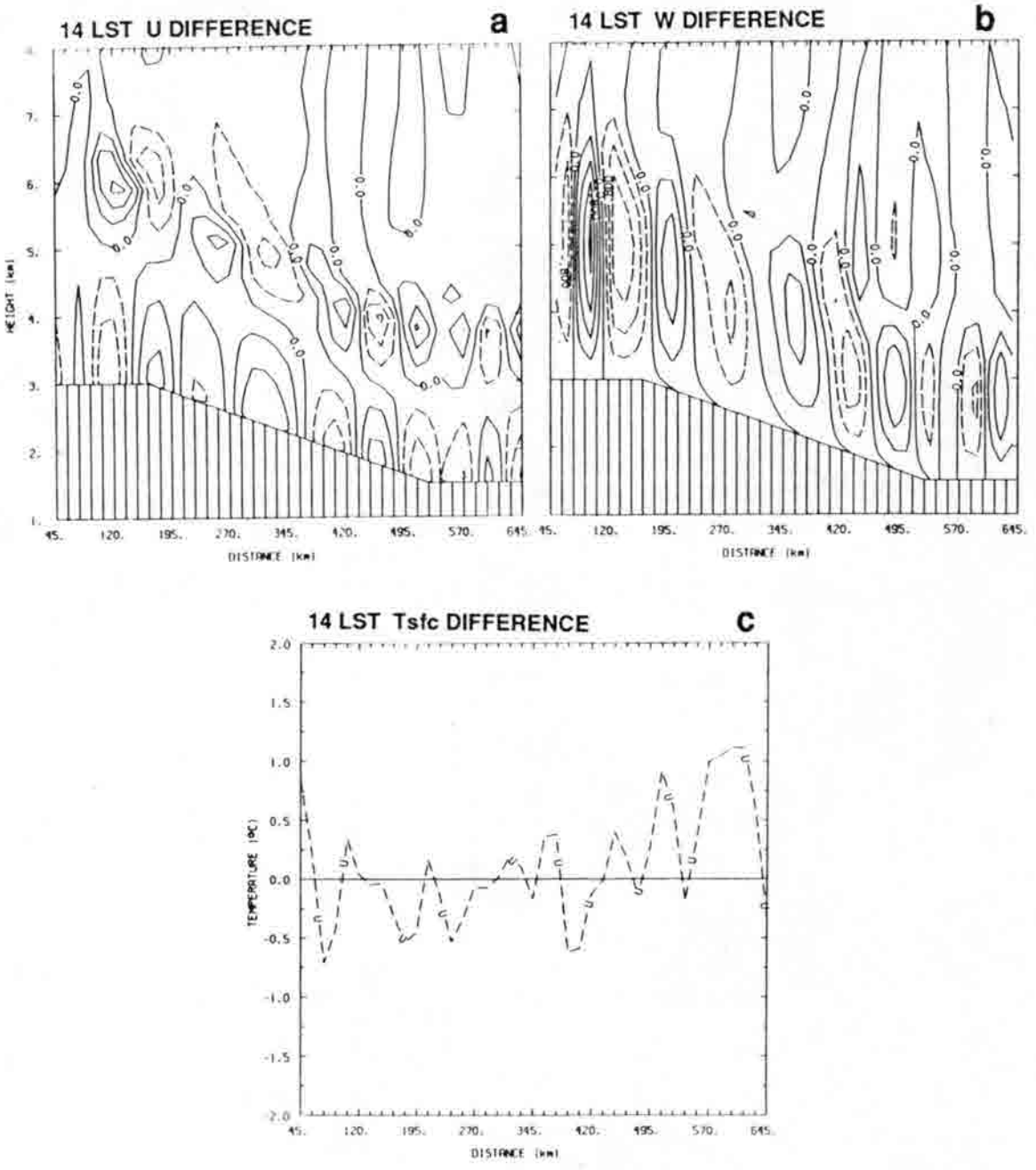

Figure 3.8 Differences in model parameters between noisy surface temperature run N-1 (as Fig. 3.7) and the control run at 14 LST: a) westerly wind component (m/s), b) vertical wind component (cm/s) contoured at 0.4 cm/s, and c) surface temperature.

perturbation mechanism was the same as for adding noise, but no smoothing was done. The results of these two runs were very symmetrical about the control — changes from the control caused by the 2 K decrease tended to be opposite in sign and double the magnitude of changes caused by the 1 K increase. Only the results of the 2 K decrease will be discussed further.

The surface temperature decrease weakened the forcing of the solenoidal circulation, and gave rise to a 0.2 m/s (5%) decrease in the intensity of the local upslope circulation. The other effect of the change was a decrease in depth of the boundary layer of about 0.25 km. Correspondingly, there were large differences in several model parameters between the two runs at heights near the boundary layer top, where strong vertical gradients were shifted.

Other experiments were run with surface (potential) temperatures increased by 1 K in the western half of the domain and decreased by 1 K in the eastern half, and vice versa. Again, the results were very symmetrical about the control, and only the warm–west, cool–east results will be discussed further.

In this latter experiment the 14 LST maximum upslope wind component (Fig. 3.9a) was increased relative to the control by 0.6 m/s and was displaced toward the domain center. The upslope minimum in the return flow was also distorted significantly. The greatest difference in upslope wind component was a speed increase of 0.7 m/s just downwind of the warm/cool interface. The vertical winds (Fig. 3.9b) were correspondingly altered, with an up–down couplet near the interface of magnitude up to 1.4 cm/s. Other differences in the modeled parameters were directly related to changes in the boundary layer depth.

The tests of sensitivity to surface temperature perturbations provided a scaling of how sensitive the modeled atmospheric features are to the types of errors that could be present in satellite-based surface temperature retrievals — namely noise, global biases, and systematic regional biases. Similarly, these tests indicate model sensitivity to surface temperature features that might exist in nature, but go unaccounted for in surface energy balance computations.

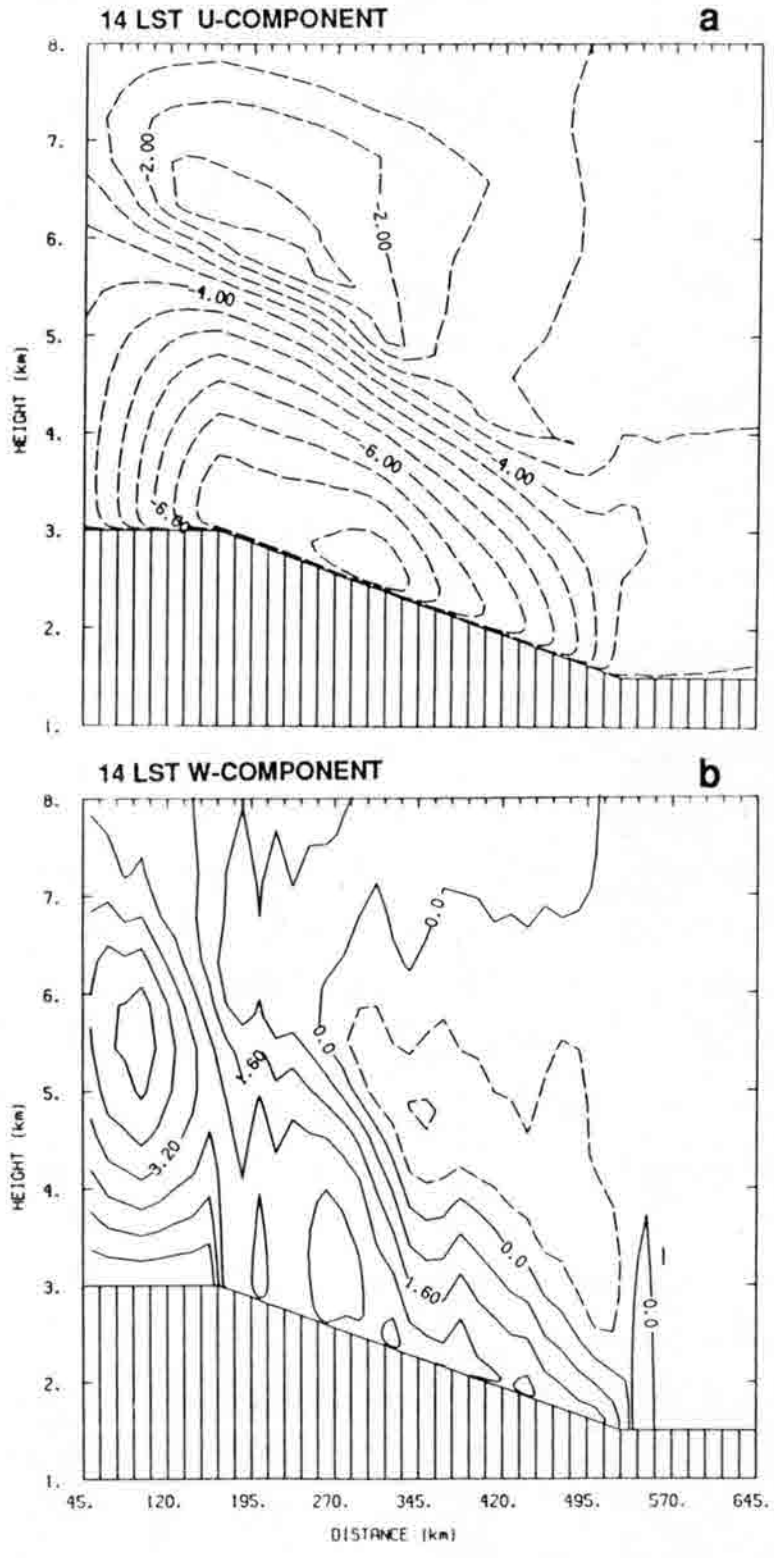

Figure 3.9 The a) westerly, and b) vertical wind components for the warm–west, cool–east surface temperature perturbation run, at 14 LST. Contours are as in Fig. 3.6.

4.0 SIMULATED ANALYSES

Analysis methods for water vapor and surface temperature were tested in two-dimensional simulation experiments. The purposes were to determine the accuracy of coupled analysis results under controlled conditions and to compare the strengths and weaknesses of the coupled scheme with those of other analysis schemes. The experimental domain was the same as for the model sensitivity tests.

4.1 Water Vapor

The four water vapor analysis methods introduced in Sec. 2.5 were tested under cloud-free conditions, and two of them were tested for the effects of cloudiness. The results are discussed in this subsection.

4.1.1 Simulated Observations

A numerical model run defined a set of atmospheric conditions to serve as the subject for analysis. This will be referred to as the "reference" atmosphere. Gridded model output comprised a perfect set of "observations" of the atmosphere and ground surface. The model was integrated over nine hours, starting at sunrise. The conditions were as described in Sec. 3.1.1, but with a background geostrophic wind of 3 m/s from the east. The winds and surface temperatures at the nine hour point were nearly identical to those for the surface temperature sensitivity test control (Fig. 3.6).

Water vapor concentrations were initialized with anomalously high values in the lower eastern portion of the domain, as described in Sec. 3.1.3. The values changed through the simulation period (Fig. 4.1) in response to boundary layer development, the local circulation, and the background flow.

Once the reference atmosphere had been defined, the next step was to simulate the data that would result from observing that atmosphere with the VAS instrument. VAS

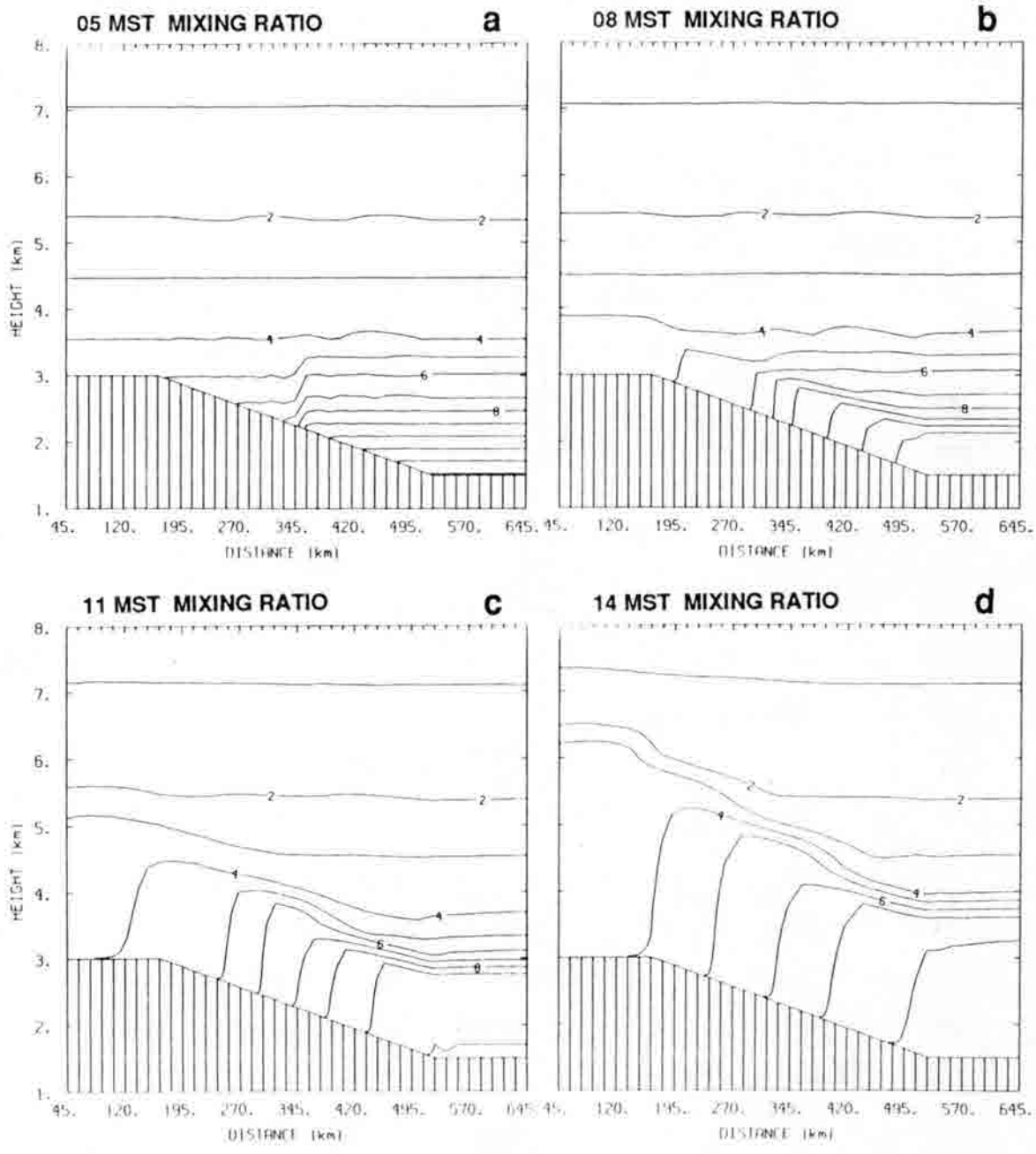

Figure 4.1 Water vapor mixing ratios (g/kg) in the reference atmosphere at three-hour intervals. Times (LST) for each frame are in the upper left corner. Contours are at intervals of 1 g/kg.

brightness temperatures were computed at three-hour intervals in the simulation, since that was the interval at which data were available for a case study (Chap. 5). The brightness temperatures resulted from taking vertical profiles of model parameters at each grid point, adding climatological data for altitudes above the highest grid level, and performing radiative transfer computations. Normally distributed random noise was added to the brightness temperatures, with standard deviations equal to ϵ_T (Table 2.1). The sounding field of view resolution was taken to be equal to the model grid resolution (15 km), which is finer than the current VAS instruments can achieve (Chesters, *et al.*, 1982) but is within the capabilities of future geostationary instruments (Schwalb, 1985).

The challenge to the analysis schemes was to reproduce the reference water vapor fields (Fig. 4.1) using only indirect information, namely the simulated VAS data and the numerical model formulation.

4.1.2 Stand-Alone Retrieval Results

Retrievals were performed at each horizontal grid point at 05, 08, 11, and 14 LST, all using the same initial guess water vapor profile. The profile was composed of July-average data from Denver (Fig. 4.2) with climatological data appended to the top. Referring to the diagram of Fig. 2.2a, this is the case in which fields Y_0, Y_3, Y_6, and Y_9 are all represented by Fig. 4.2. Even though water vapor mixing ratios were the only parameters utilized from retrieval results, it was still necessary to have initial guess temperatures. The 05 LST reference temperatures were used.

The analyses (Fig. 4.3) were impacted by the noise in the VAS data, and had poor vertical resolution. In particular, the strong gradient at the top of the reference boundary layer (see Fig. 4.1) was not reproduced. The 5- and 6-g/kg contours in Fig. 4.3 demonstrate that a horizontal gradient in low-level water vapor was detected near the center of the domain. The time changes in these contours indicate an upslope flux at low levels. At upper levels, the east-to-west gradient that developed by 14 LST in the reference run was coarsely reproduced in the retrievals. The difference at 14 LST between the stand-alone analysis and the reference field (Fig. 4.7a) is characteristic of a vertical resolution deficiency.

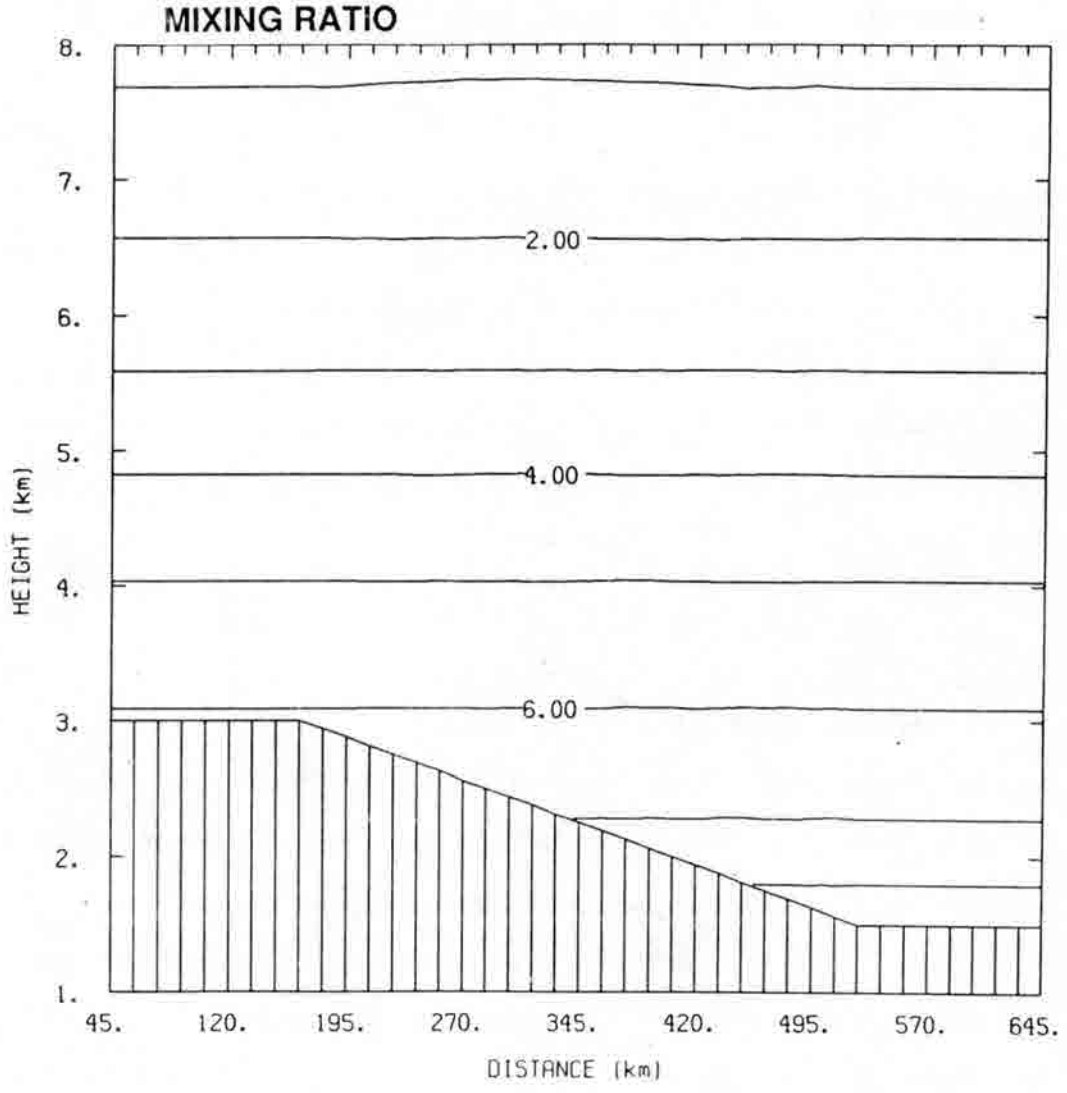

Figure 4.2 Water vapor mixing ratios (g/kg) used as initial data for analysis simulations. Contours are at intervals of 1 g/kg.

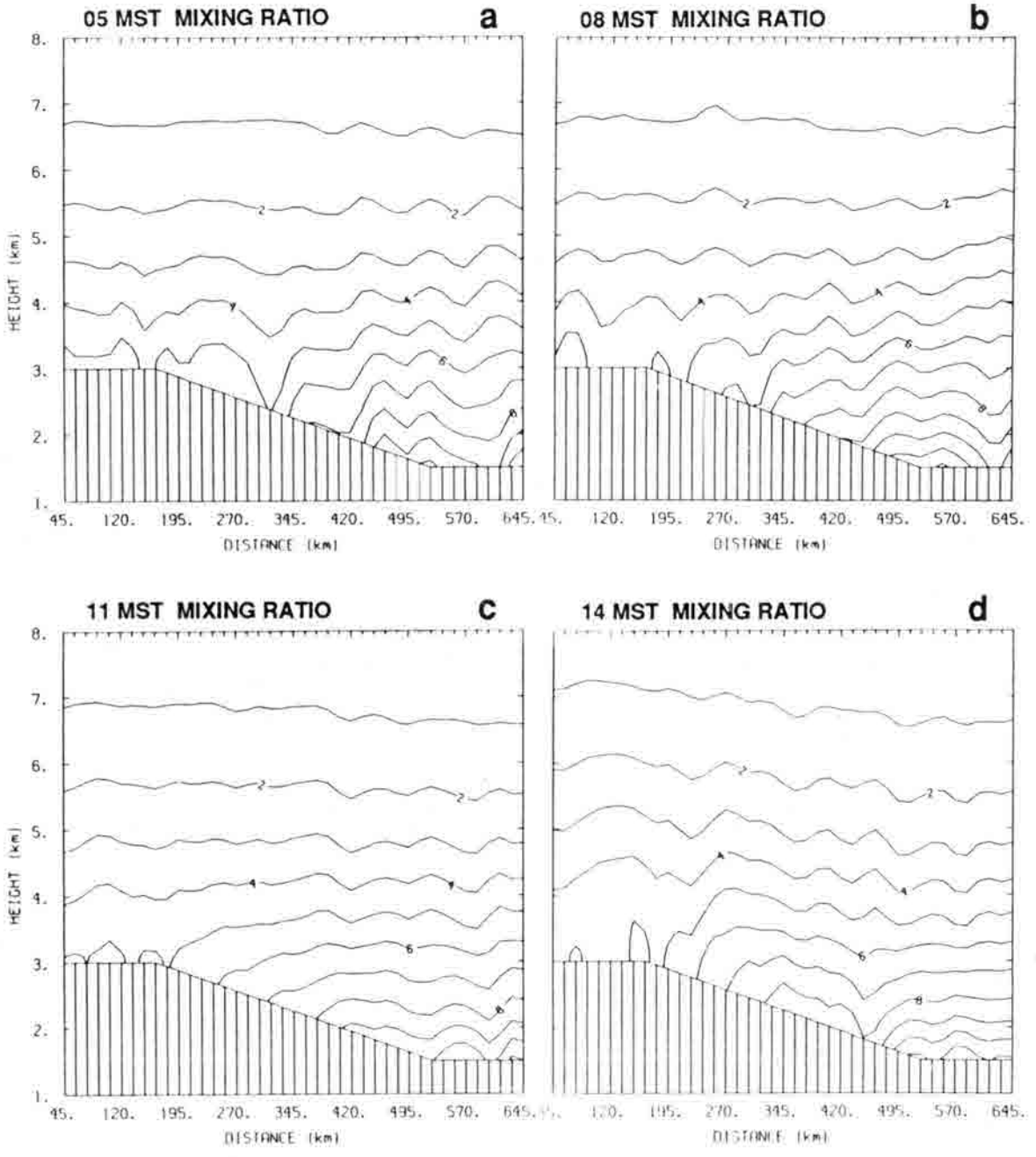

Figure 4.3 Water vapor mixing ratio analysis results (g/kg) from the stand-alone retrieval method, with slight smoothing for presentation clarity. Times (LST) for each frame are in the upper left corner. Contours are at intervals of 1 g/kg.

4.1.3 Initialized Model Run Results

For this experiment, the initial water vapor field was the stand-alone retrieval result for 05 LST. Referring to Fig. 2.2, fields Y_0 and A_0 were identical to W_0 and C_0, respectively. The initial guess temperatures were the 05 LST reference values. The model formulation in this simulation was the same as the one used to generate the reference atmosphere, which is equivalent to having a numerical model that depicts the flow of the real atmosphere perfectly. Differences between the 05 LST retrievals and the reference values at 05 LST were the only possible causes of differences at later hours.

The analyses (Fig. 4.4) appear very similar to the reference fields (Fig. 4.1). The fields became less noisy within the first few hours of simulation because of the model's horizontal diffusion, which selectively damps features at the shortest scales. Differences relative to the 14 LST reference values (Fig. 4.7b) were much smaller than in the stand-alone case. By that stage of the simulation, atmospheric processes had redistributed water vapor to such an extent that vertical gradients in the lower troposphere were brought into approximate agreement with reference gradients. The larger differences in the upper portion of the domain were due to vertical resolution problems. The vertical structure of the initial guess profile at upper levels was quite different from the reference atmosphere structure.

An interesting feature of the difference plot is the region of negative values in the lower eastern corner. This resulted from noise-induced retrieval error on the upwind model boundary. The error propagated freely into the analysis domain since no water vapor information was introduced to the analysis system after initialization.

4.1.4 Modeled Initial Guess Results

For this experiment the model initialization field (Z_0 in Fig. 2.2) was comprised of the same data used for initial guesses in stand-alone retrieval (Y_0). After integrating the model to 14 LST, but performing no retrievals, the water vapor field (Z_9) was as shown in Fig. 4.5a. This is the analysis that would result from ignoring VAS data altogether and relying solely on the numerical model and the July-average Denver sounding data.

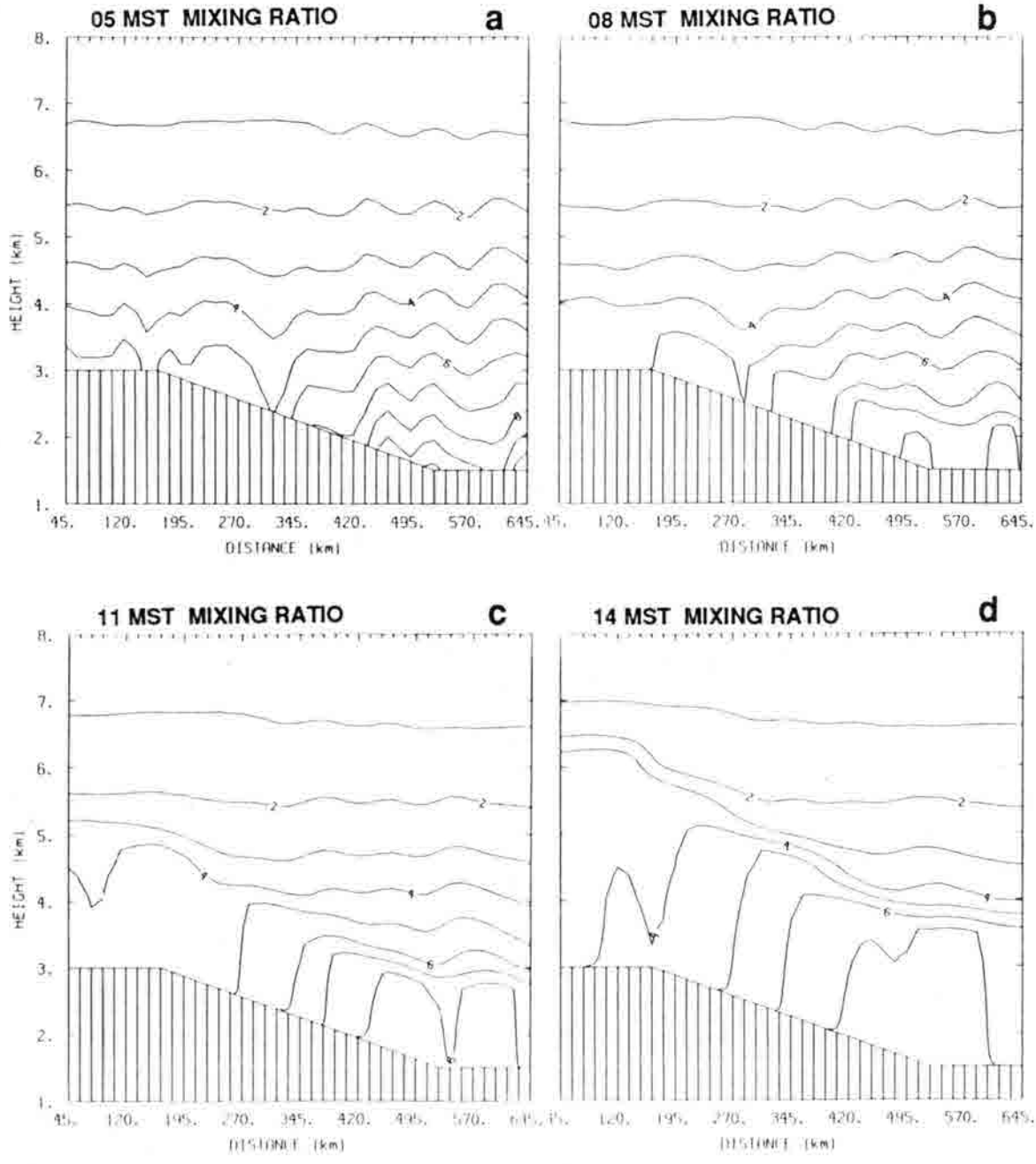

Figure 4.4 As in Fig. 4.3, but from the initialized model run method. Only frame 'a' data was smoothed.

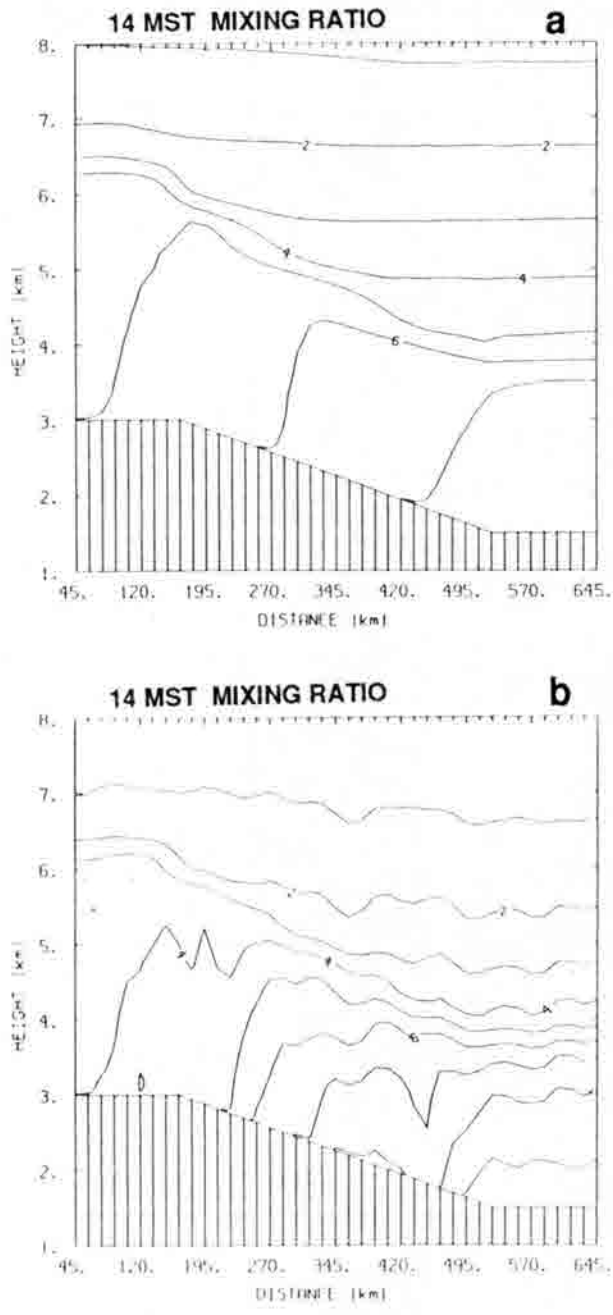

Figure 4.5 Water vapor mixing ratios (g/kg) for a) initial guess data for 14 LST modeled initial guess method retrievals, and b) the 14 LST modeled initial guess analysis results, slightly smoothed. Contours are at intervals of 1 g/kg.

Only the 14 LST analysis (D_9) was retrieved from the initial guess model run. Initial guess temperatures were taken from the model data, and thus were very similar to the reference values. The results (Fig. 4.5b) are considerably more similar to the reference values than the stand-alone results were, but the vertical gradients were not reproduced very well. The vertical structure shown in Fig. 4.5a was not preserved through the retrieval step since there was no constraint to preserve it, while a large mixing ratio adjustment was called for. The 14 LST difference field for this experiment (Fig. 4.7c) indicates that the vertical resolution deficiency was less than in the stand-alone case.

4.1.5 Coupled Results

The first step of the coupled analysis was the same as the first segment of stand-alone retrieval. That is, X_0 and B_0 (Fig. 2.2) were identical to Y_0 and A_0, respectively. The model parameters, aside from mixing ratios, were the same as in the other simulation experiments and were not adjusted during the water vapor adjustment steps. Modeled temperature values were used in retrieval initial guesses.

The analysis results (Fig. 4.6) included gradients and magnitudes very similar to the reference field features. The relative differences at 14 LST (Fig. 4.7d) were very small over much of the analysis domain, but reflected the same upper-level bias as was found in the initialized-model-run results.

One purpose of conducting this experiment was to determine whether the random brightness temperature errors would tend to cancel each other out when four sets of VAS data were used in succession. If so, the final coupled analysis (B_9) would be more similar to the reference field than the final initialized analysis (C_9) was.

A brief inspection of Figures 4.7b and 4.7d reveals that the coupled results were actually less accurate, in general, than the initialized-model-run results. One possible reason for this is that the model did a perfect job of depicting the advection of water vapor, so there was no tendency for the initialized-model-run analyses to degrade over time. Also, the model smooths out fine-scale water vapor variations over three hours of integration, so each new application of VAS data can, at best, cancel out only larger scale noise-related features.

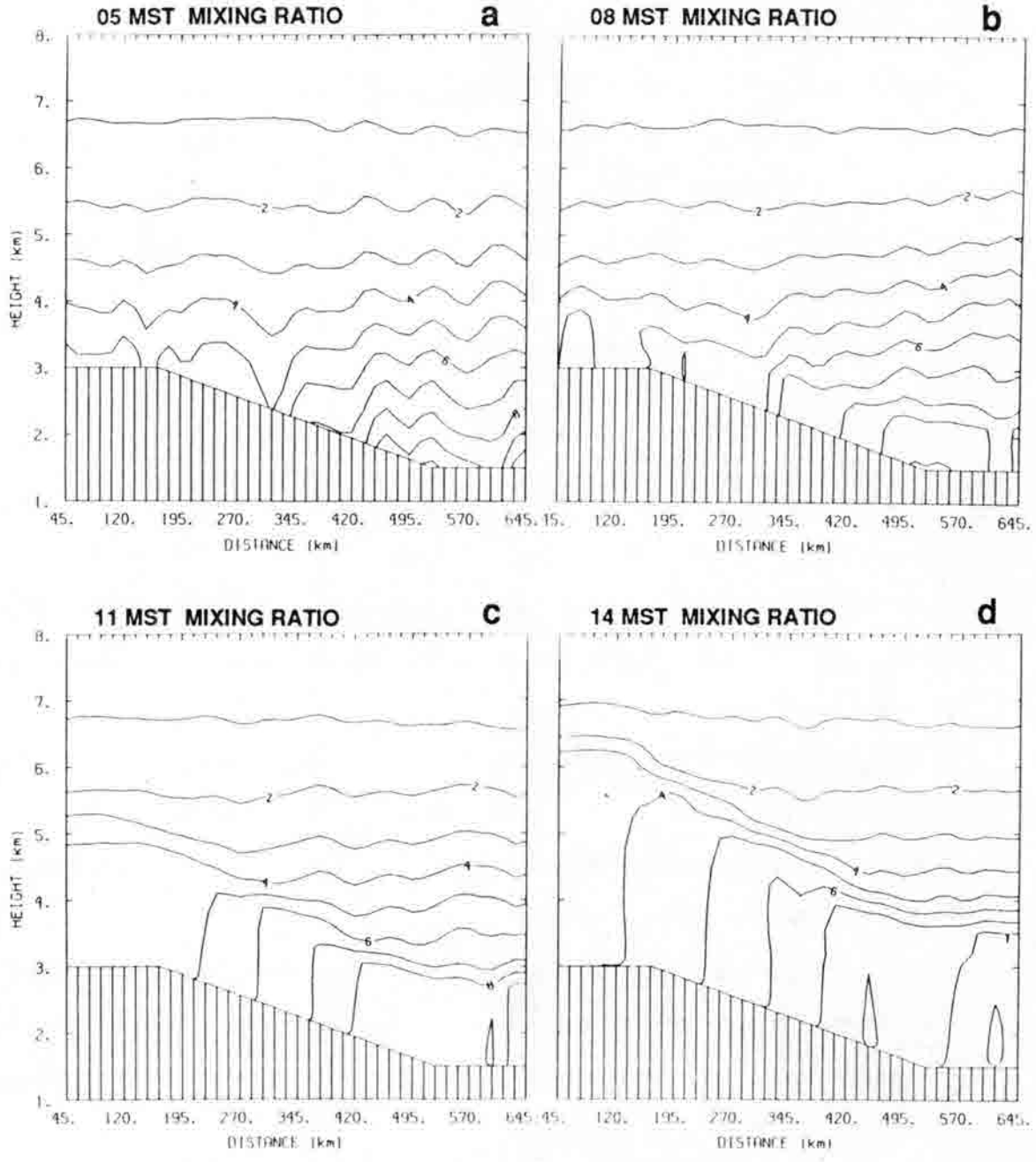

Figure 4.6 As in Fig. 4.3, but from the coupled analysis method.

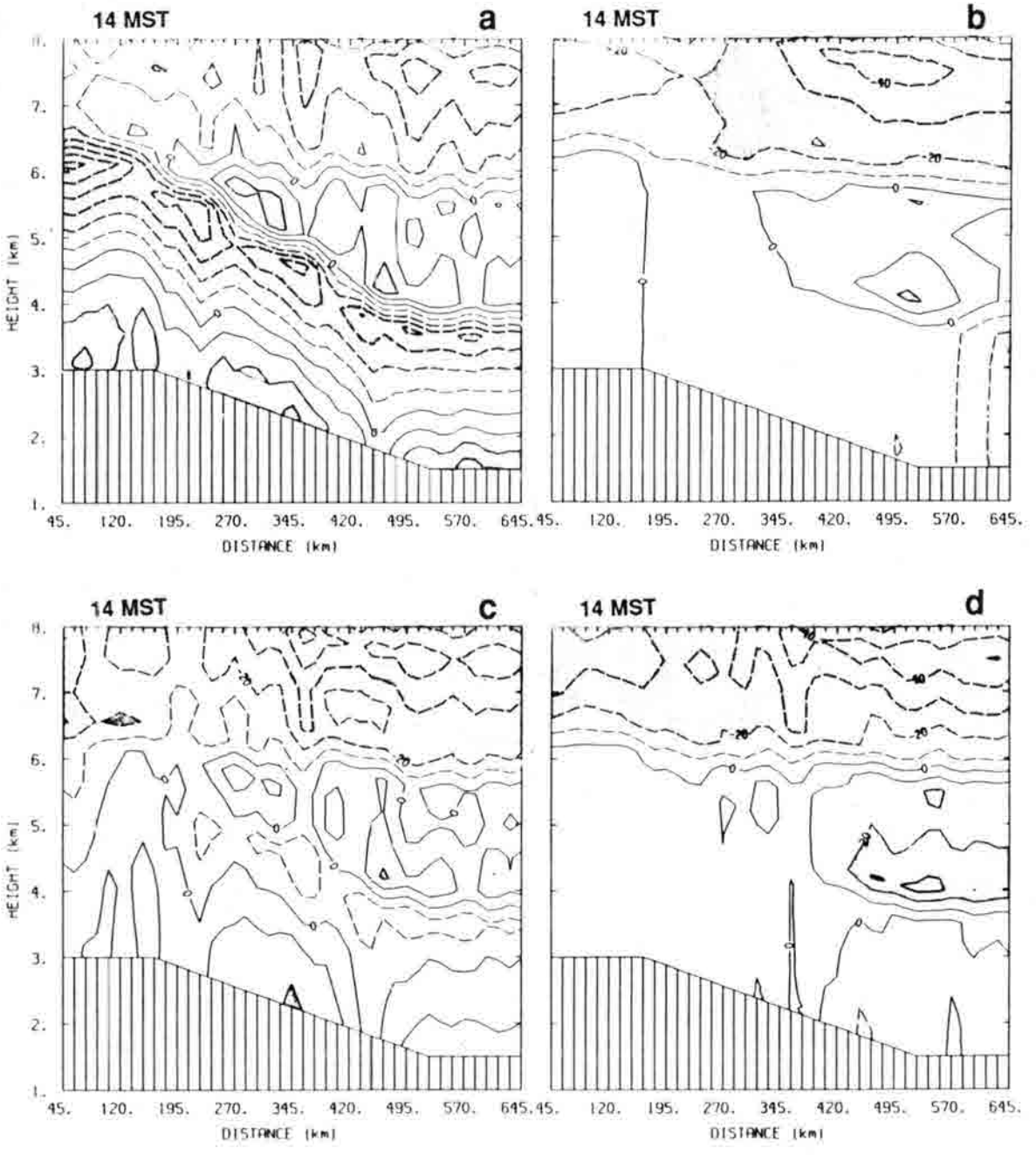

Figure 4.7 Differences (%) between analysis results and the reference values of mixing ratio, computed at each grid point by subtracting the reference value from the analysis value and dividing the result by the average of the two values. Frames are for a) stand-alone retrieval, b) initialized model run, c) modeled initial guess, and d) coupled. All are for 14 LST. Contours are at intervals of 10%, and stippling indicates absolute values greater than 20%.

Another experiment was conducted to focus on the differences between the coupled and initialized-model-run methods by examining in detail the effects of repeated adjustments to the water vapor concentrations. A coupled analysis was run through just the first three hours of simulation, with all conditions as before except that the background geostrophic wind was changed from the "true" value of 3 m/s to an erroneous value of 0.1 m/s from the east. In this case the advection of the east-west gradient was too weak, so the second retrieval step was challenged with correcting the degraded analysis. Note that, after only three hours of simulation, field X_3 (Fig. 2.2) is equivalent to an initialized-model-run analysis.

The initialized-model-run analysis at 08 LST (Fig. 4.8a) had a wavy character due to the noise in the initialization retrievals at 05 LST. Given a horizontal wind error of 3 m/s, gradients should be misplaced by about two grid lengths after three hours. The differences relative to the reference field (Fig. 4.9a) in fact include a large negative difference just downwind of the strongest low-level gradient, although there are many other large differences as well. After the retrieval step (Fig. 4.8b) the waviness was diminished, and the low-level gradient was intensified and shifted westward (downwind). The differences (Fig. 4.9b) were not consistently larger or smaller than before retrieval.

The patterns of Figs. 4.8 and 4.9 were interpreted subjectively in an effort to better understand the effect of repeated adjustment. The adjustment step appeared to make the "true" water vapor features more coherent, while noise-induced features either stayed about the same, were weakened, or were reversed. In an analysis with real data, the features that show up consistently through repeated adjustments can be recognized as reliable. This demonstrates an important advantage of the coupled method, since the major purpose of mesoscale analysis is to accurately resolve mesoscale features. On the other hand, the second adjustment brought an increase in systematic differences that resulted from vertical resolution deficiencies.

The coupled analysis simulations included one other enlightening comparison. This illustrated the importance of the interpolation method that was part of the coupled analysis system. For contrast with the adjustment-interpolation method described in Sec. 2.5.4 an alternative coupled analysis was made, in which the transfer of retrieval output data to the model grid was done by a conventional, direct interpolation. The resulting 14 LST

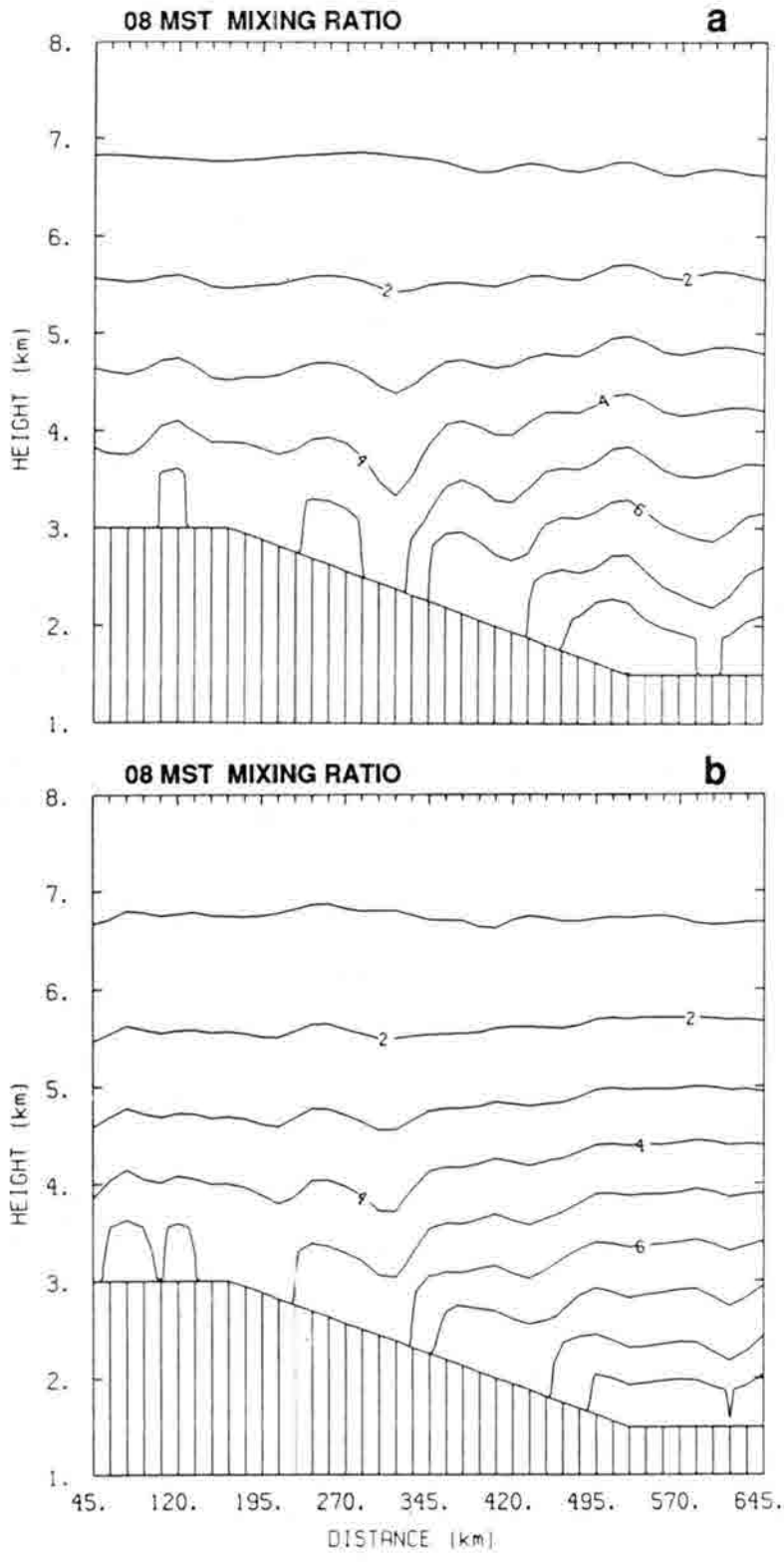

Figure 4.8 Water vapor mixing ratio analysis results (g/kg) at 08 LST for simulations with weakened background winds. Frames are for a) initialized model run, and b) coupled analysis with results slightly smoothed before contouring. The contour interval is 1 g/kg.

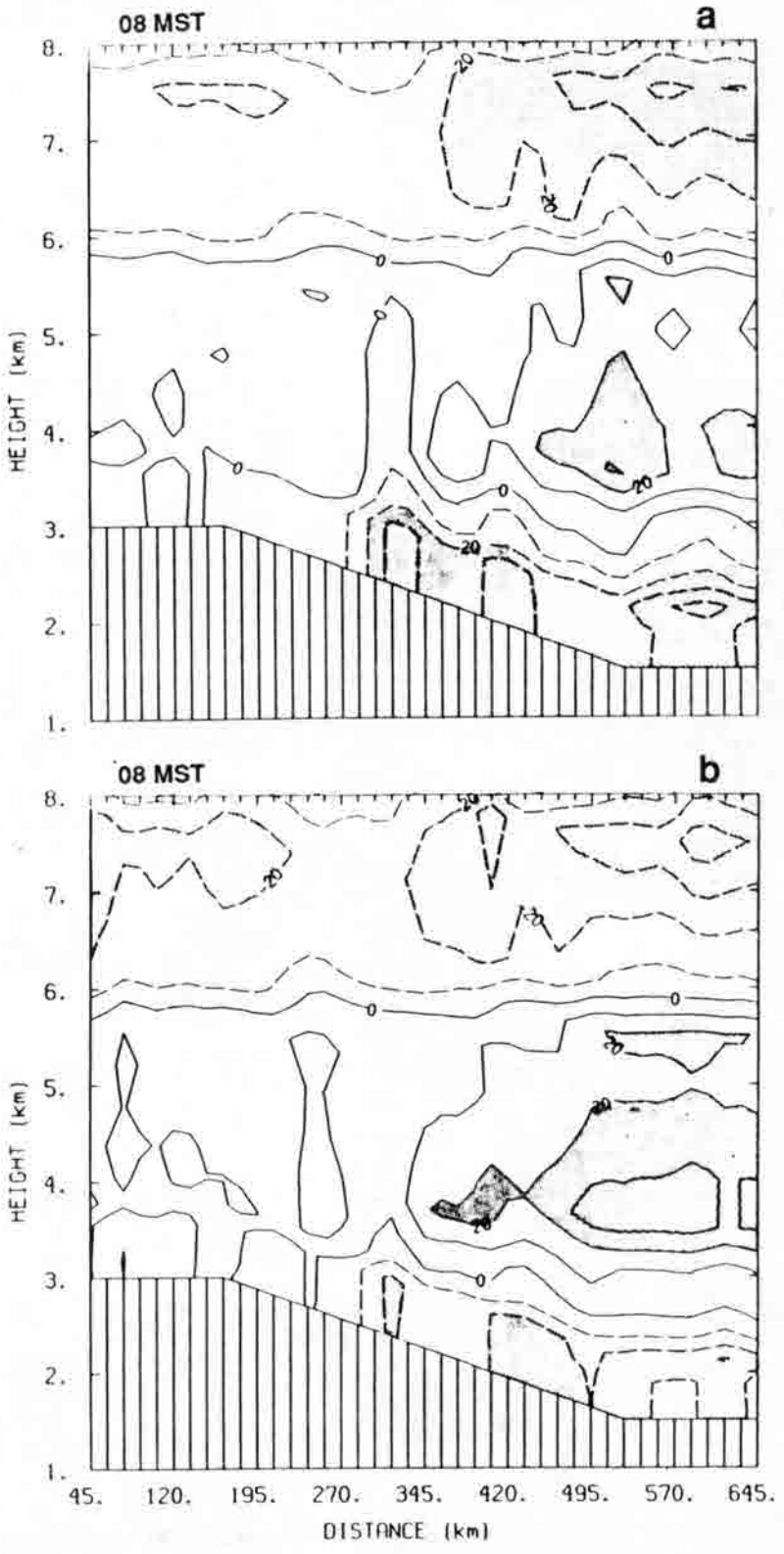

Figure 4.9 Differences as in Fig. 4.7, but corresponding to the analyses contoured in Fig. 4.8, respectively.

analysis is presented in Fig. 4.10 along with the results of applying the adjustment method of transfer. The gradient near the top of the boundary layer was faithfully maintained when the adjustment method was used, but it was smoothed when direct interpolation was used.

4.1.6 Cloud Contamination Effects

Experiments were performed to determine what would be the impact on analysis accuracy if the satellite data were cloud-contaminated. Contamination here refers to a situation in which there are enough clouds within a sounding field of view that the VAS brightness temperatures are significantly different from clear-atmosphere values, but the cloudiness is not extensive enough to be recognized and accounted for.

Contaminated VAS data were simulated for each specified field of view by computing a clear-sky radiance and a cloud-covered radiance, taking a weighted average of the two, converting to brightness temperature, and adding noise. Weighting was based on the effective cloud emittance, which was set at 5%. This value can be interpreted as the product of the actual cloud emittance and the fraction of the field of view covered by cloud. In radiance computations, the cloud temperature was taken to be equal to the ambient atmospheric temperature at the pressure level of the cloud top.

Separate experiments were run with low and high clouds. The low cloud case was intended to simulate a developing cumulus field, so cloud tops were at the top of the reference boundary layer. Thus, the contamination became worse with time as the cloud grew higher and colder. The progression of boundary layer depths is evident in Fig. 4.1 from the band of strong vertical gradients of mixing ratios. In the high cloud case the cloud tops were fixed at 150 mb throughout the simulations. For simplicity, cloud-related physics did not feed back to modeled flows in any way.

Clouds were arbitrarily specified in two regions of the experimental domain, as indicated in Fig. 4.11. The western region was stationary, while the eastern region drifted westward two grid lengths per three-hour interval. The eastern group of clouds moved approximately with the mean wind, so the motion of air relative to the clouds was westward below the cloud tops and eastward above them. There was a relative westward flux of air both above

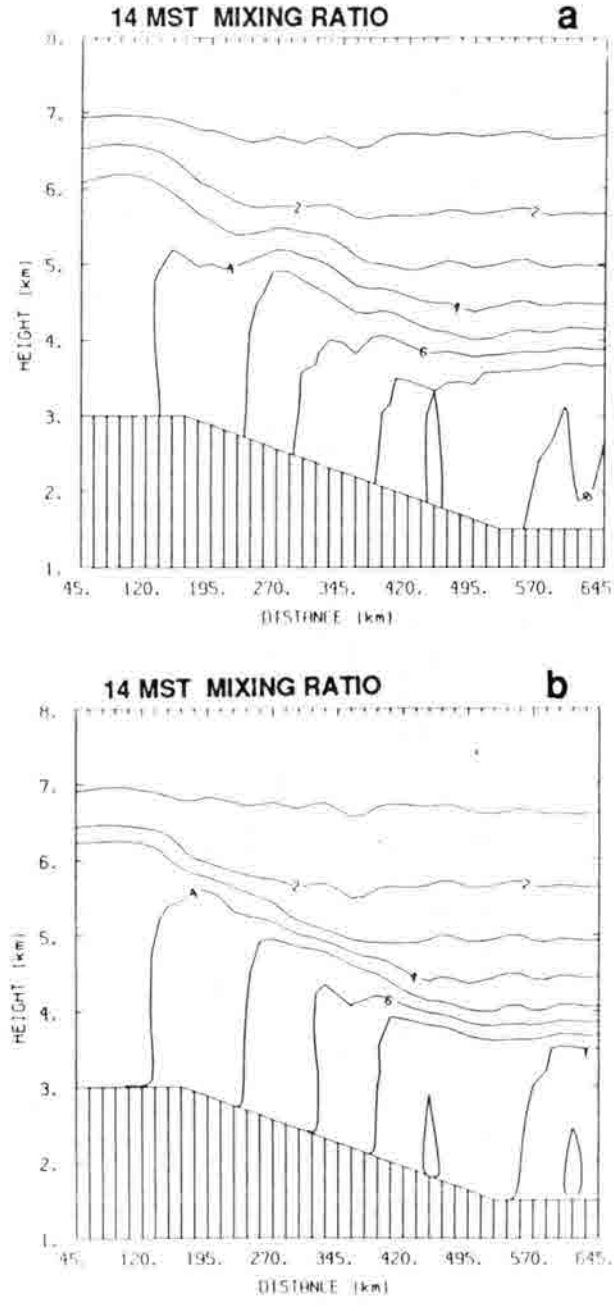

Figure 4.10 Water vapor mixing ratio analysis results (g/kg) at 14 LST for two methods of transferring retrieval output to the model grid in coupled analysis: a) direct interpolation and b) adjustment. Contours are at 1 g/kg intervals.

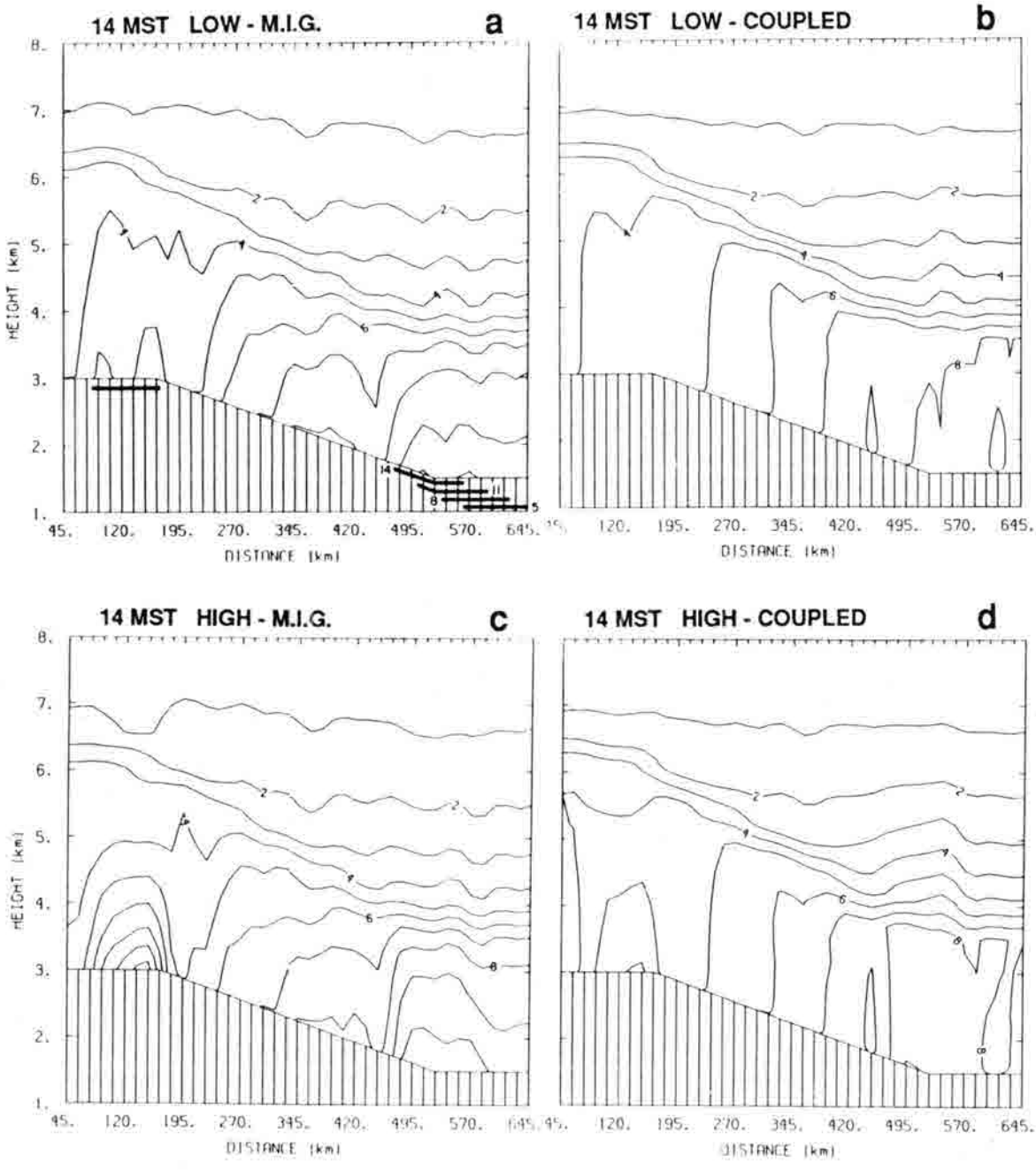

Figure 4.11 Water vapor mixing ratio analysis results (g/kg) at 14 LST for low (a and b) and high (c and d) clouds using the modeled initial guess method (a and c) and the coupled method (b and d). Results were slightly smoothed. Horizontal lines below the terrain surface in frame 'a' denote regions of cloud contamination. The position of the eastern cloud region is given as a function of LST.

and below the western group of clouds. With air parcels entering and exiting cloudy regions in a variety of ways, the coupled analysis program had to cope with diverse challenges.

Results at the nine hour point (14 LST) were evaluated for the modeled initial guess method and the coupled method to determine which was more susceptible to cloud contamination effects. Stand-alone analyses were not considered because they were expected to be affected very similarly to modeled initial guess analysis; the only difference is in the quality of the initial guess profiles for retrievals. Initialized-model-run analysis tests would not be very useful either, since the results would depend heavily on whether contamination was worse at the initialization time or the final analysis time.

The impact of low clouds was noticeable but not large, as can be seen by comparing Figs. 4.11a and b with Figs. 4.5b and 4.6d, respectively. The high clouds had an obvious impact on the analyses (Figs. 4.11c and d).

Statistics were computed to highlight the susceptibility to cloud-induced errors. Mixing ratio absolute differences, relative to the reference values, were averaged over grid points 4–44 (the plotting domain) in the horizontal and at points 4, 8, 10–17 in the vertical. Some of the lower grid levels were omitted to avoid biasing the results in favor of regions with tight grid spacing.

In Table 4.1 is a list of the average absolute differences and the proportional increases in differences caused by cloud contamination. For low clouds, the coupled analysis was less sensitive to cloud contamination than the modeled initial guess analysis was (8 versus 11% increase); however, there was no sensitivity difference for high clouds. One hypothesis for the difference in low-cloud response of the two methods is that coupled retrievals do not respond fully to patches of cloudiness. At an upwind cloud edge (in relative motion) high-quality initial guess data are advected into a region of contaminated VAS data. The updated analysis at that location should not fully reflect the contamination since mixing ratios are adjusted only to the VAS noise-level criterion instead of adjusting to convergence (see Sec. 2.5.4). On the other hand, at locations just downwind of clouds, contaminated initial guess data are degrading retrievals where uncontaminated VAS data are available. The net effect depends on the relative importance of these two processes. Neither process exists in the modeled initial guess analysis method. This hypothesis is refuted by the results

Table 4.1 Spatially averaged relative differences in mixing ratio at 14 LST for various simulated analyses.

	Relative Differences (%)		
	Clear	Cloud Contaminated	Cloud-Induced Change (%)
Low Cloud:			
Modeled I.G.	10.5	11.7	11
Coupled	10.0	10.8	8
High Cloud:			
Modeled I.G.	10.5	15.4	47
Coupled	10.0	14.7	47
High Cloud 14 LST only:			
Modeled I.G.	10.5	15.4	47
Coupled	10.0	12.9	29

of the high cloud experiments (no sensitivity difference), since the patchiness effect should have been similar for low and high clouds.

A second hypothesis is that the sensitivity difference depended on the fact that low cloud contamination *increased* during the analysis period as cloud tops became colder. In the coupled experiment the mixing ratios were adjusted to convergence only at initialization (05 LST), when contamination of the VAS data was negligible. At the three later retrieval stages (08, 11, 14 LST) adjustment went only as far as was dictated by the noise-level criterion. At these times retrievals depended more heavily on initial guesses, and each given batch of initial guess data was not as badly contaminated as its corresponding batch of VAS data. Thus, time continuity was the key. The final coupled analysis resulted from a succession of adjustments with less-contaminated historical data and more-contaminated current data, while the modeled initial guess analysis resulted from only the more-contaminated data. This effect would not apply to the high cloud case because cloud temperatures were constants in that case.

The second hypothesis was tested with an extreme situation. The radiances were non-contaminated for the first three retrieval times, and then high clouds were introduced only at 14 LST. This could occur if clouds formed or drifted over the domain within the last three hours of the analysis period. Since the modeled initial guess analysis at 14 LST depends only on 14 LST VAS data, it would be identical to the constant high cloud analysis. The coupled analysis results are given in Fig. 4.12 and are summarized in the last row of Table 4.1. In this case the coupled method was considerably less susceptible to cloud contamination than the modeled initial guess method was (29 versus 47% increase). These results strongly support the second hypothesis. It should be kept in mind that, if the clouds had been present at any retrieval stage other than 14 LST, then they would have affected the 14 LST coupled analysis but not the modeled initial guess analysis.

4.2 Surface Temperature

Simulations were conducted to determine the relative benefits of specifying surface temperatures by VAS retrievals versus energy balance computations.

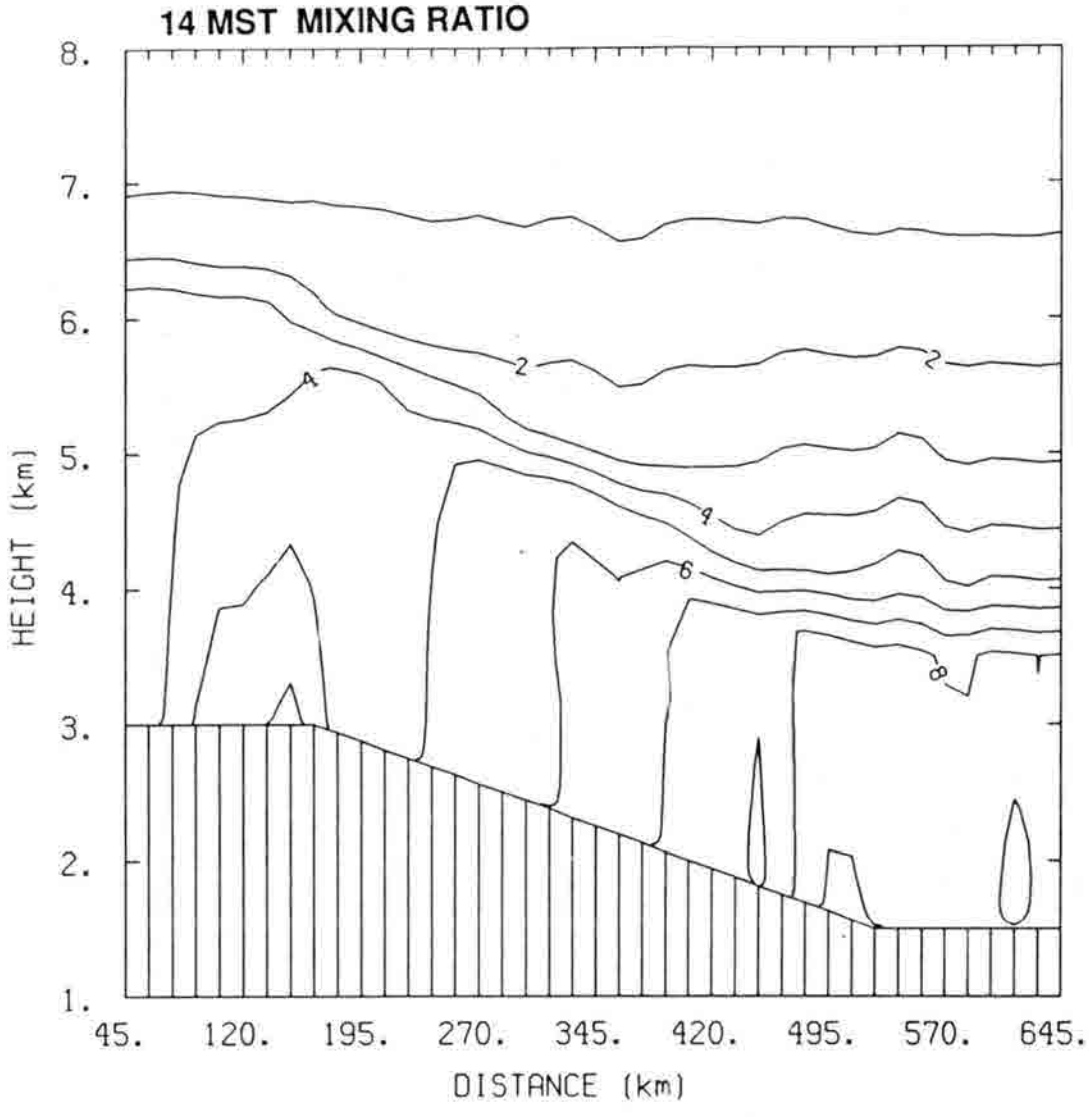

Figure 4.12 As in Fig. 4.11, but for high clouds introduced at 14 LST only.

4.2.1 Simulated Observations

For surface temperature analysis evaluations a second reference atmosphere was generated. The only difference between this one and the one used for the water vapor studies was in the specification of soil characteristics, which influence surface temperatures via energy balance computations. In the water vapor reference case soil characteristics were uniform over the domain, with the values given in Sec. 3.1.1. For the second reference case two characteristics varied in the horizontal. In the western third of the domain the initial soil profile temperatures were reduced as shown in Fig. 3.3. The soil moisture was increased to 0.20 in the eastern third of the domain and remained at 0.04 elsewhere. Such a condition might be present if on the previous day clouds had persisted over the high terrain and convective rain moistened the low terrain.

An increase in soil moisture causes an increase in evaporation rate, and thus has a cooling effect on soil temperatures. Given that the choice of soil moisture values was somewhat arbitrary, a secondary factor was ignored — that increasing moisture is generally accompanied by increasing thermal conductivity of the soil (de Vries, 1963). A conductivity increase would only enhance the cooling effect during the daytime, when heat flows downward from the surface. The simulation results confirmed that the conduction effect was of secondary importance. The latent heat fluxes from the ground increased so much with the change in soil moisture that they would have dominated a conductivity change even if soil conduction were doubled.

The initial profile temperature change had little impact on the evolution of surface temperatures, but the soil moisture increase strongly retarded surface heating (Fig. 4.13). The surface temperature changes, in turn, had a substantial impact on the winds by 14 LST (Fig. 4.14). For reference, the winds without the changes in soil characteristics were approximately as in Fig. 3.6. The wind differences were greatest near the soil moisture gradient.

VAS data were simulated for the second reference atmosphere by the means described in Sec. 4.1.1.

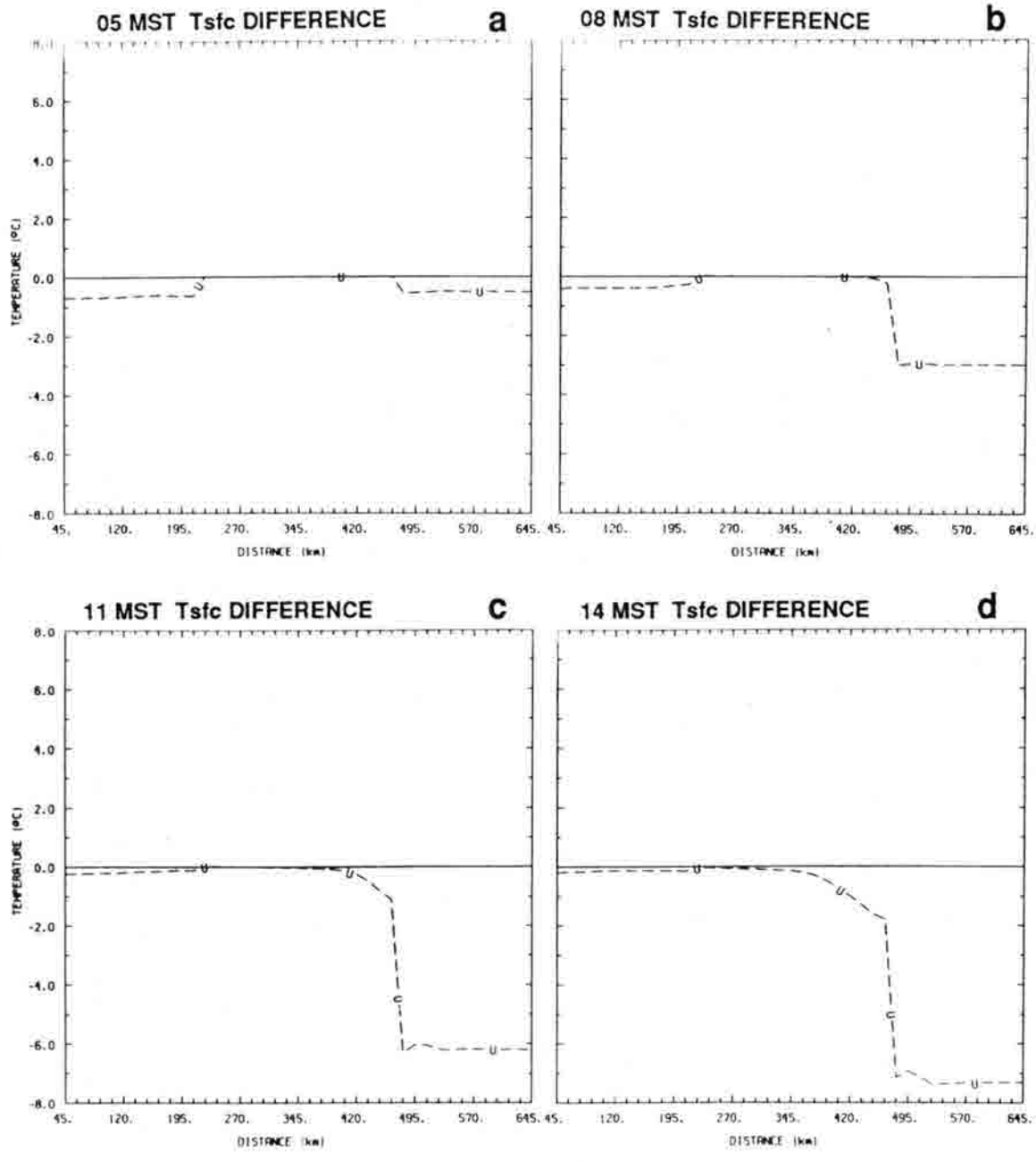

Figure 4.13 Surface temperature differences at three-hour intervals, with times (LST) in the upper left corners. Differences are values from the surface temperature reference conditions minus approximate values from the water vapor reference conditions. The horizontal axis is as in Fig. 3.1.

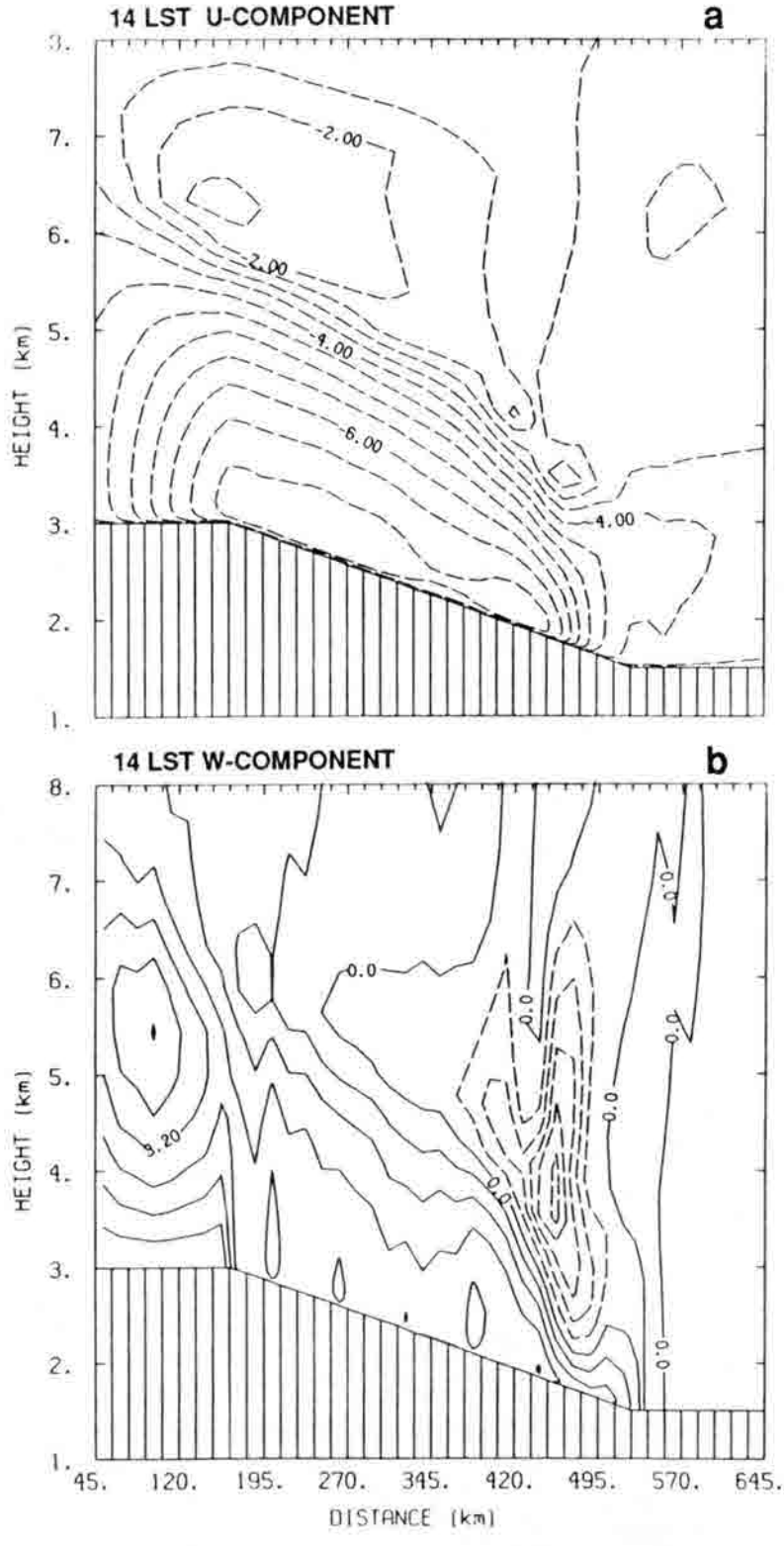

Figure 4.14 The a) westerly and b) vertical wind components at 14 LST from the reference conditions for surface temperature analysis simulation. Contours are as in Fig. 3.6.

4.2.2 Analysis by Energy Balance

It is common in mesoscale modeling studies to use energy balance computations to estimate surface temperatures. One problem with this approach is that mesoscale data on soil characteristics are generally not available. This situation was simulated with a model run in which all factors were essentially the same as in the reference run, except that all soil characteristics were uniform horizontally. The initial soil temperature profile was the one used in the previous simulations and the soil moisture was set to 0.08. These conditions are relatively favorable for matching with the reference since it is assumed that the energy balance computation method is perfect, that most soil characteristics are known perfectly, and that averages of the two unknown characteristics (initial soil temperature and soil moisture) have been well estimated.

The surface temperature differences, relative to the reference values, were as great as about 5°C at 14 LST (Fig. 4.15a). The winds at 14 LST (Fig. 4.16) were weaker than the reference winds in general. Differences near the soil moisture gradient were as great as 1.6 m/s for the westerly component and 3 cm/s for the vertical component.

4.2.3 Coupled Analysis

An analysis was done using the procedure for determining surface temperatures via satellite data, as described in Sec. 2.6. In this simulation VAS data were the only source of surface temperatures; no energy balance products were weighted in. Otherwise, the model parameters were the same as in the reference run.

The surface temperature retrievals in this simulation were highly accurate, as can be seen from the difference plot for 14 LST (Fig. 4.15b). The largest differences, at two adjacent points, were caused by the smoothing of retrieval data across the strong gradient before the data were input to the model. The corresponding winds (Fig. 4.17) were very similar to the reference values.

Real-world retrievals of surface temperature generally would not be as accurate as those presented here, even though data noise was included. Additional errors would be caused by uncertainties in surface emittances and atmospheric transmittances. It is largely guesswork

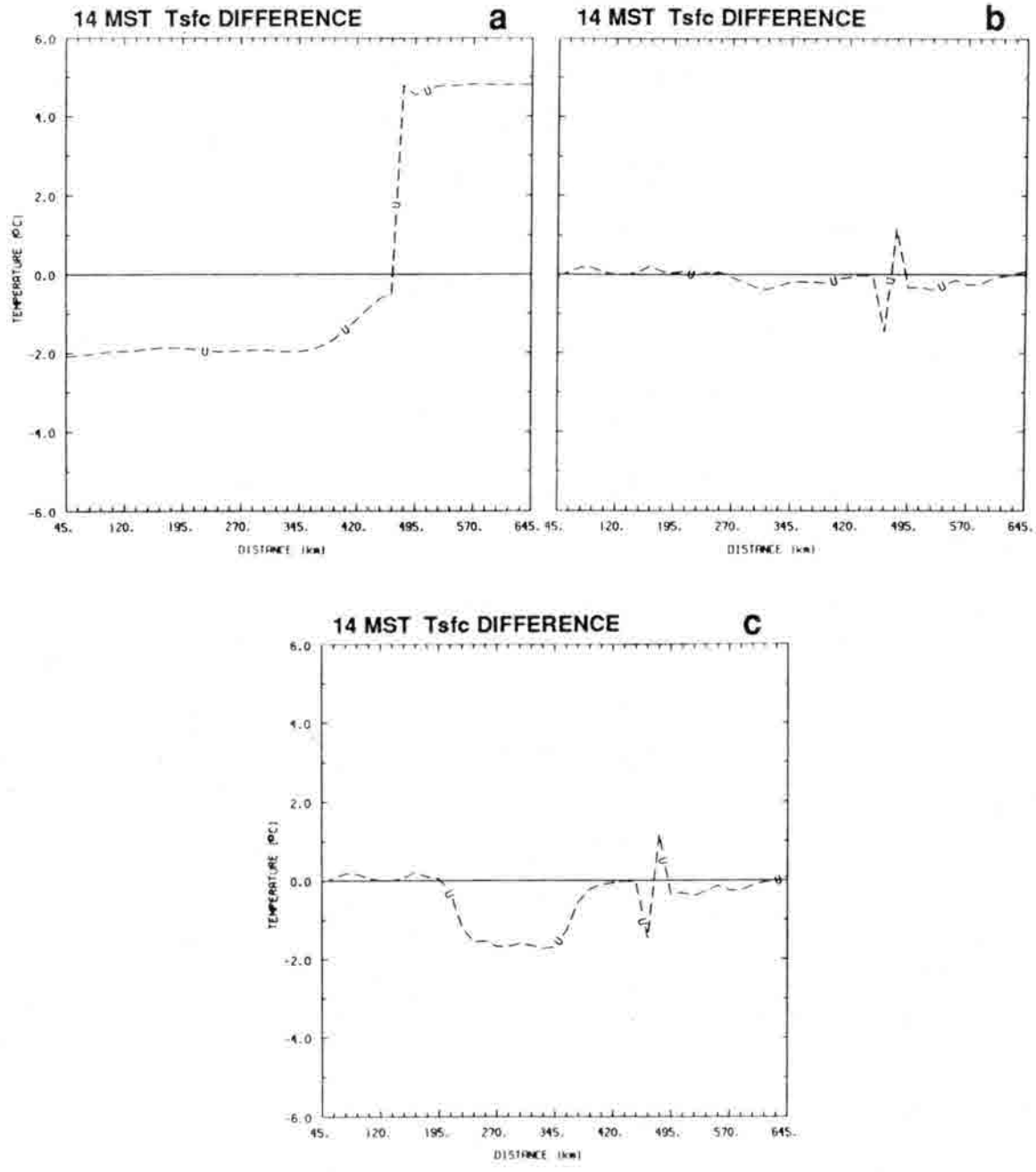

Figure 4.15 Surface temperature differences at 14 LST from the a) analysis by energy balance, b) coupled analysis, and c) cloud-contaminated analysis. Each difference is relative to the reference values.

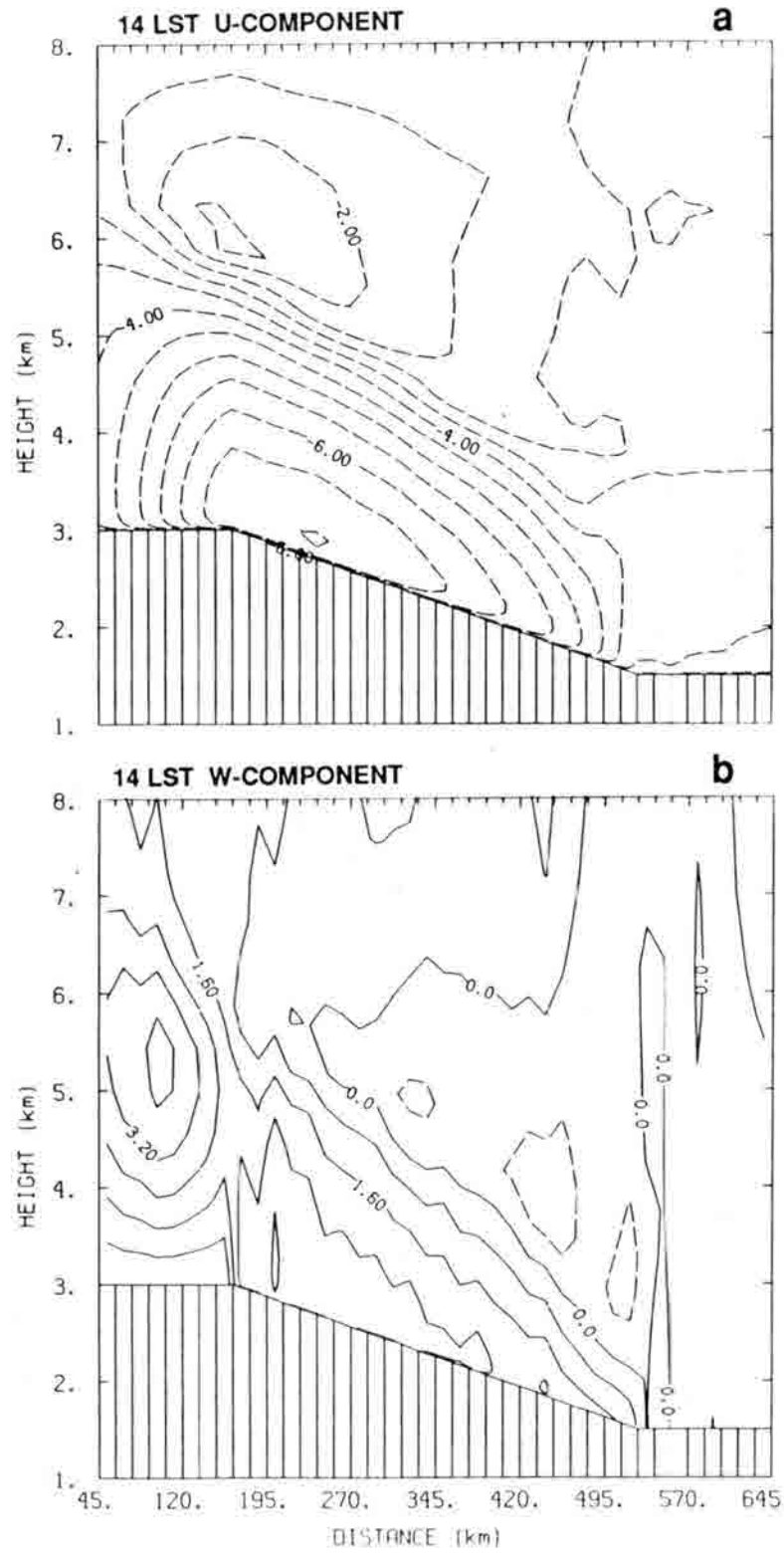

Figure 4.16 The a) westerly and b) vertical wind components from the surface temperature analysis simulation by energy balance. Contours are as in Fig. 3.6.

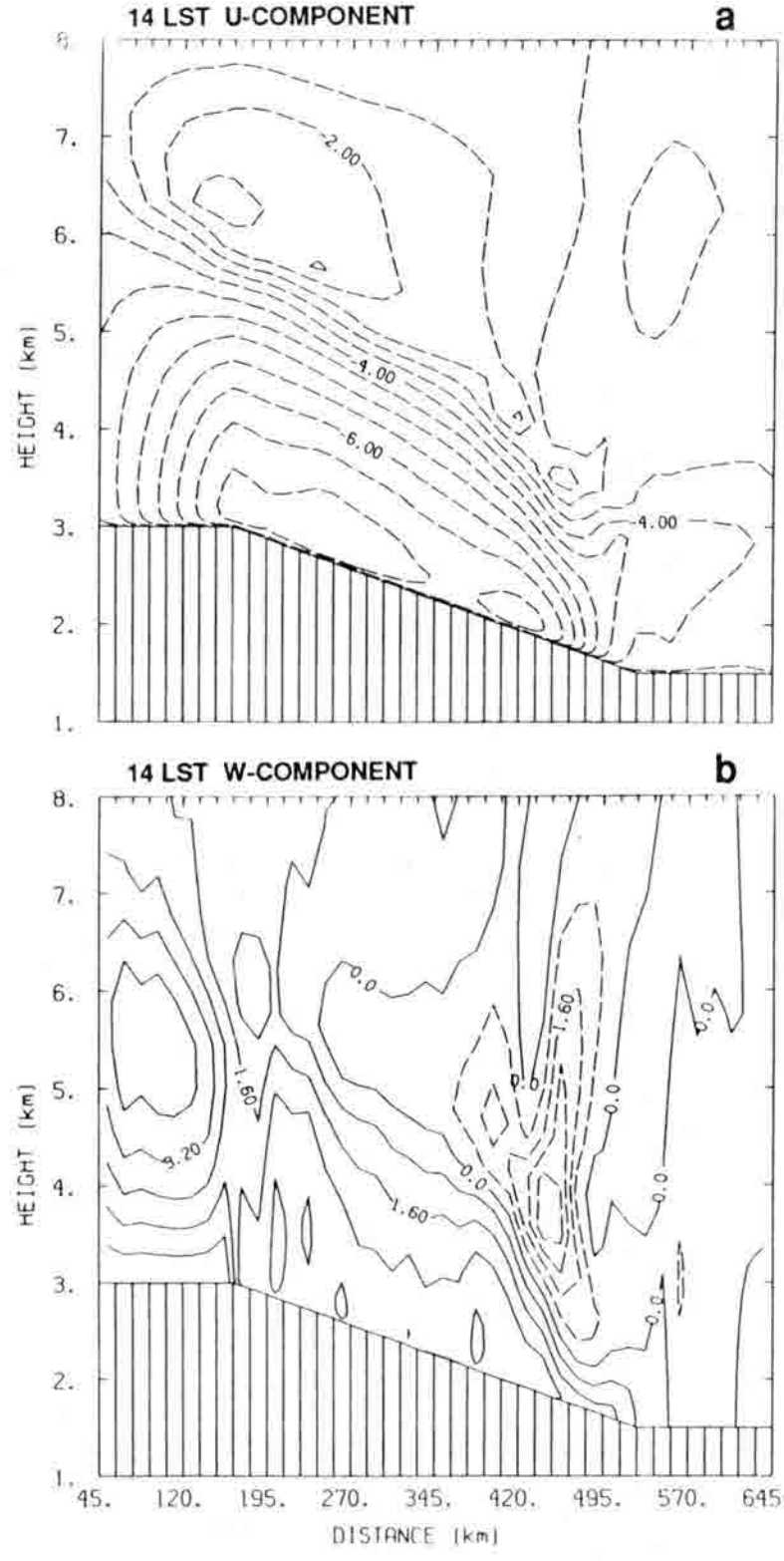

Figure 4.17 As in Fig. 4.16, but from the coupled surface temperature analysis simulation.

to estimate realistic error magnitudes for the simulated situations since emittance data are rare, particularly for terrain scenes the size of a VAS field of view. Based on some indirect information (Link, 1979; Taylor, 1979; Liu, *et al.*, 1987), it seems reasonable that erroneous temperature variations in a mesoscale domain would not exceed a few degrees Celsius.

4.2.4 Cloud-Contaminated Analysis

To add another element of reality to the study, a coupled analysis was run with cloud-contaminated VAS data. The cloud heights were based on the boundary layer depth, as described previously (Sec. 4.1.6). The contamination region was as designated in Fig. 4.18, with an effective emittance of 5%.

The surface temperature differences for this experiment (Fig. 4.15c) were much smaller than those for the analysis by energy balance. Accordingly, the wind differences were also smaller, with maximum differences of 0.5 m/s and 1.5 cm/s for westerly and vertical components, respectively. The circulations (Fig. 4.18) reflected the impact of cool-biased surface temperatures in the cloudy area.

Given the conditions imposed on these simulations, coupled surface temperature analysis was preferable to relying on energy balance computations, even when the satellite data were contaminated by clouds.

4.3 Summary

These simulation experiments demonstrated that applying coupled mesoscale analysis is technologically feasible and, under some circumstances, is superior to the alternatives. However, simulations are not sufficient to thoroughly assess the value of an analysis method. Some of the performance conclusions were sensitive to the values of experimental parameters. The values were somewhat arbitrary, even though the goal was to be realistic for the types of meteorological conditions that this study was intended to address.

These simulation results made it appear promising that the coupled analysis system would be a valuable tool for studying mesoscale weather events.

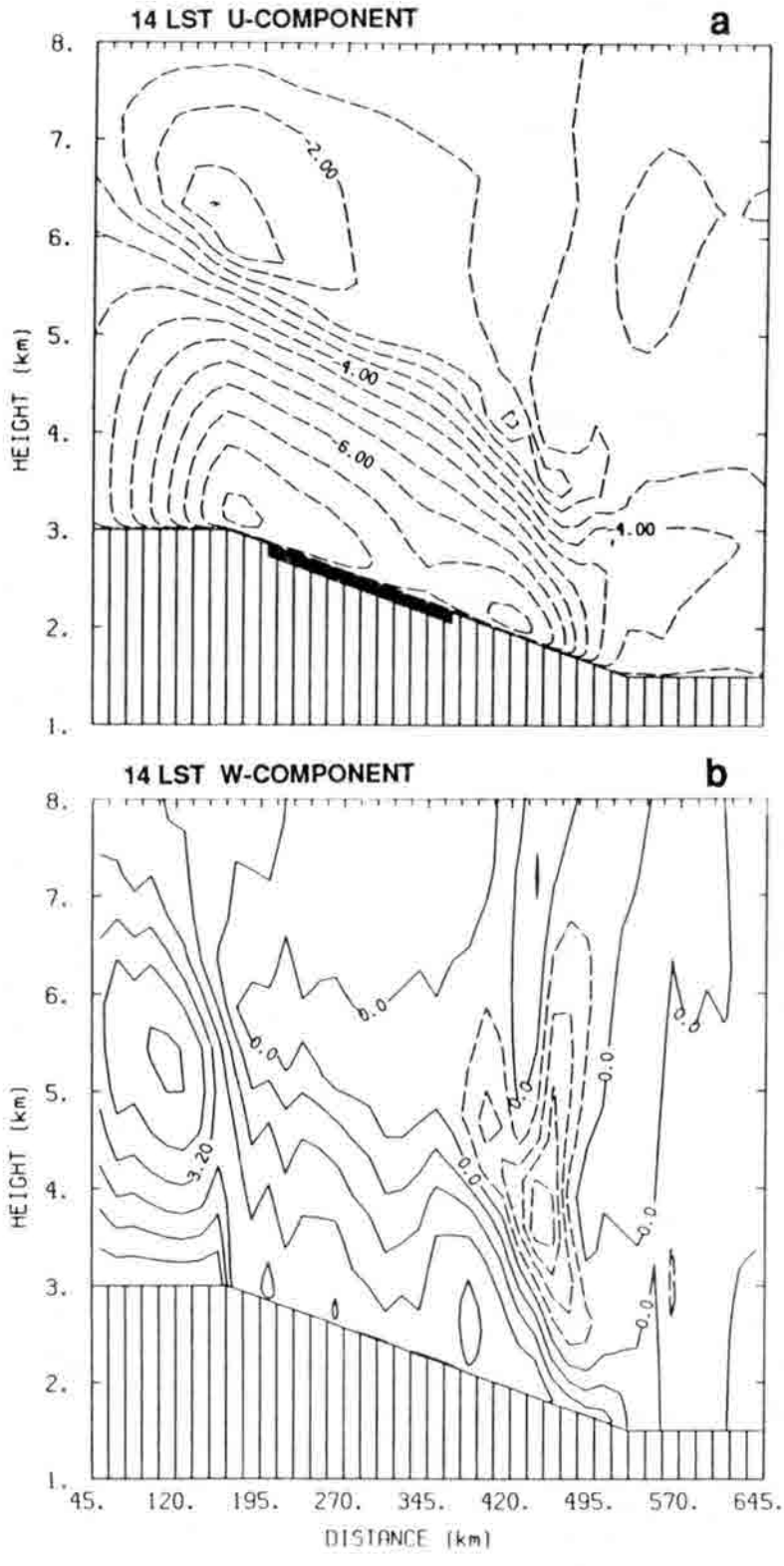

Figure 4.18 As in Fig. 4.16, but from the coupled surface temperature analysis simulation with cloud-contaminated satellite data. The cloud region is denoted by the horizontal line below the terrain surface in frame 'a'.

5.0 CASE STUDY

Several of the characteristics of Northeastern Colorado weather make the region favorable for the study of coupled mesoscale analysis. An additional advantage is that the Program for Regional Observing and Forecasting Services (PROFS: Beran and Little, 1979) operates a mesoscale surface observation network over part of the region. Summertime was preferred for study because convective storms are common even in the absence of strong synoptic-scale forcing. The case of 21 August 1983 was chosen because high-quality VAS data were available and the meteorological conditions were reasonably well-suited to a study of this kind. The analysis domain is depicted in Fig. 5.1.

5.1 Ground-Based Data

National Meteorological Center (NMC) radiosonde data were obtained from the archives at the National Center for Atmospheric Research (NCAR) and were plotted as constant-level maps (Fig. 5.2) and vertical soundings (Fig. 5.3). Synoptic scale features at upper levels generally were weak and relatively constant in space and time over the study area.

Winds at 50 kPa and above were uniformly southwesterly to westerly. Temperature gradients were very weak at all levels, while water vapor concentrations were more variable in space and time. Dry advection occurred over central Colorado and westward throughout the day. The soundings at Denver and North Platte (Fig. 5.3) detected a gradient of water vapor in the lower troposphere between the two stations. Another notable feature was a stable layer between 40 and 50 kPa.

Two sources of surface weather observations were used. Manual NMC observations were obtained from the National Climate Data Center. PROFS provided observations averaged over five-minute periods from automated mesonetwork stations. The PROFS stations were concentrated in the mountains and high plains of Northeastern Colorado. Analyses from the NMC and PROFS data combined are shown in Figs. 5.4 and 5.5.

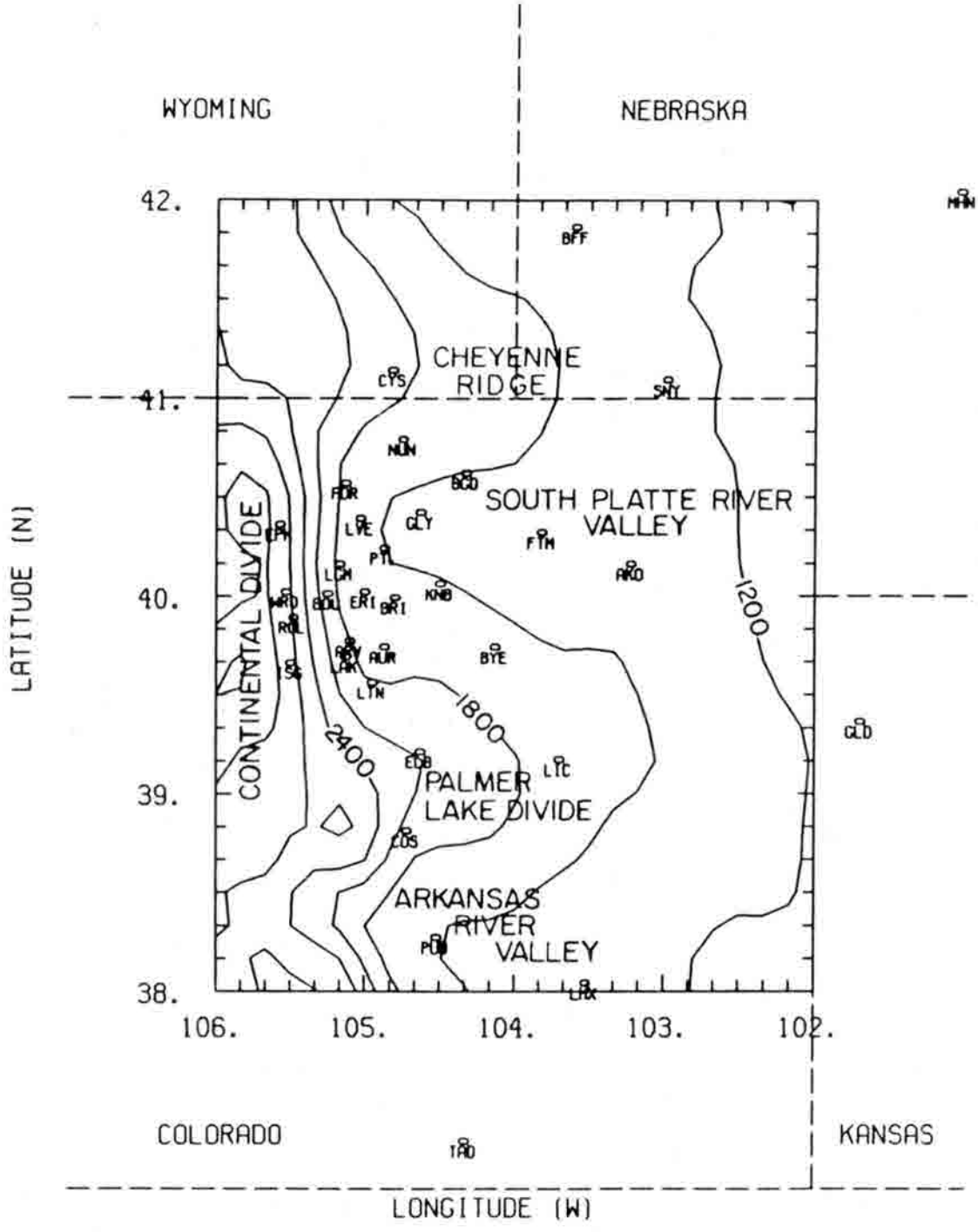

Figure 5.1 The case study domain. Tick marks denote horizontal grid locations, and state boundaries are dashed lines. Gridded terrain elevations are contoured at 300-m intervals, and major geographic features are labeled. The circles with three-letter identifiers denote surface observation locations.

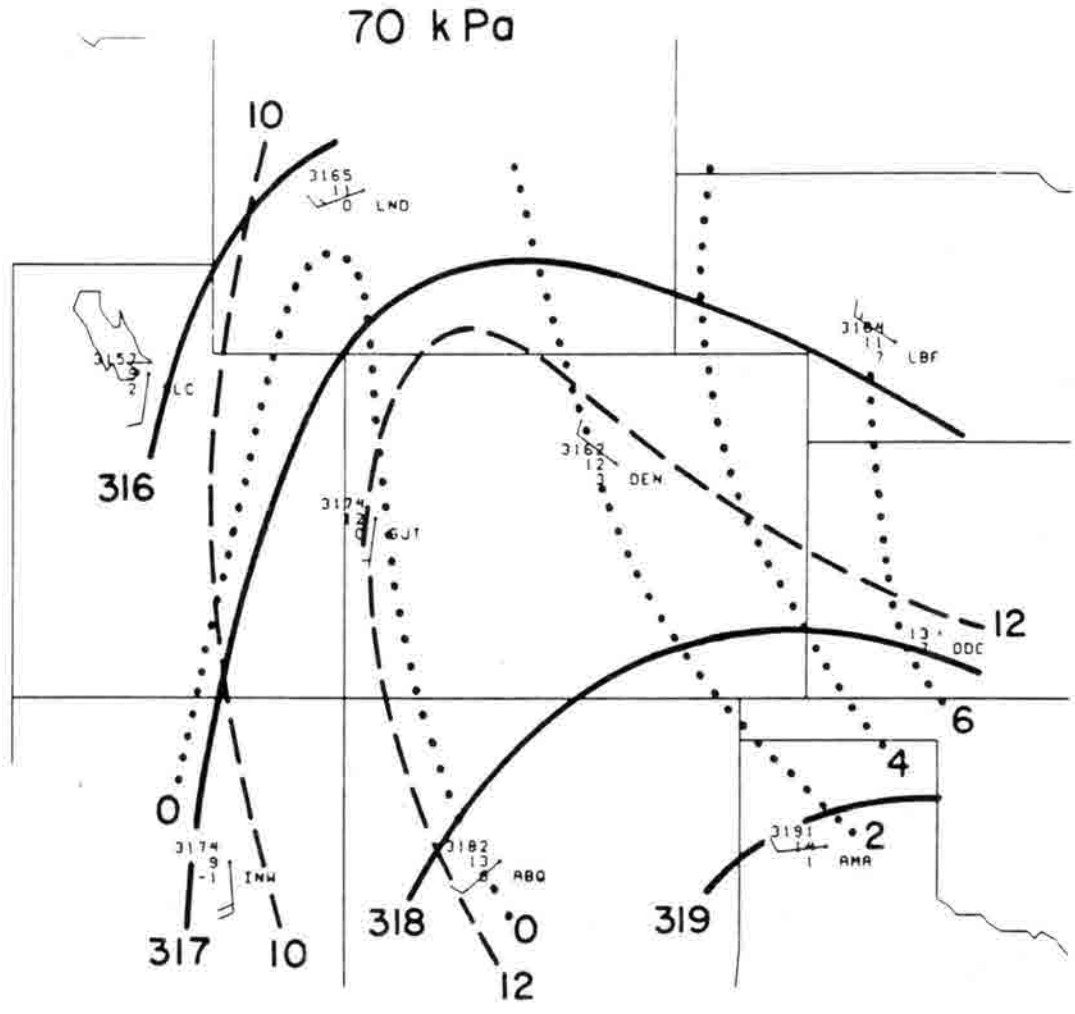

Figure 5.2a The 70-kPa analysis for 12 UTC (05 MST) 21 Aug 1983. Geopotential heights are contoured solid at 1-dam intervals and temperature lines are dashed and dewpoint temperature lines are dotted, both at 2°C intervals. One full wind barb represent 10 kt.

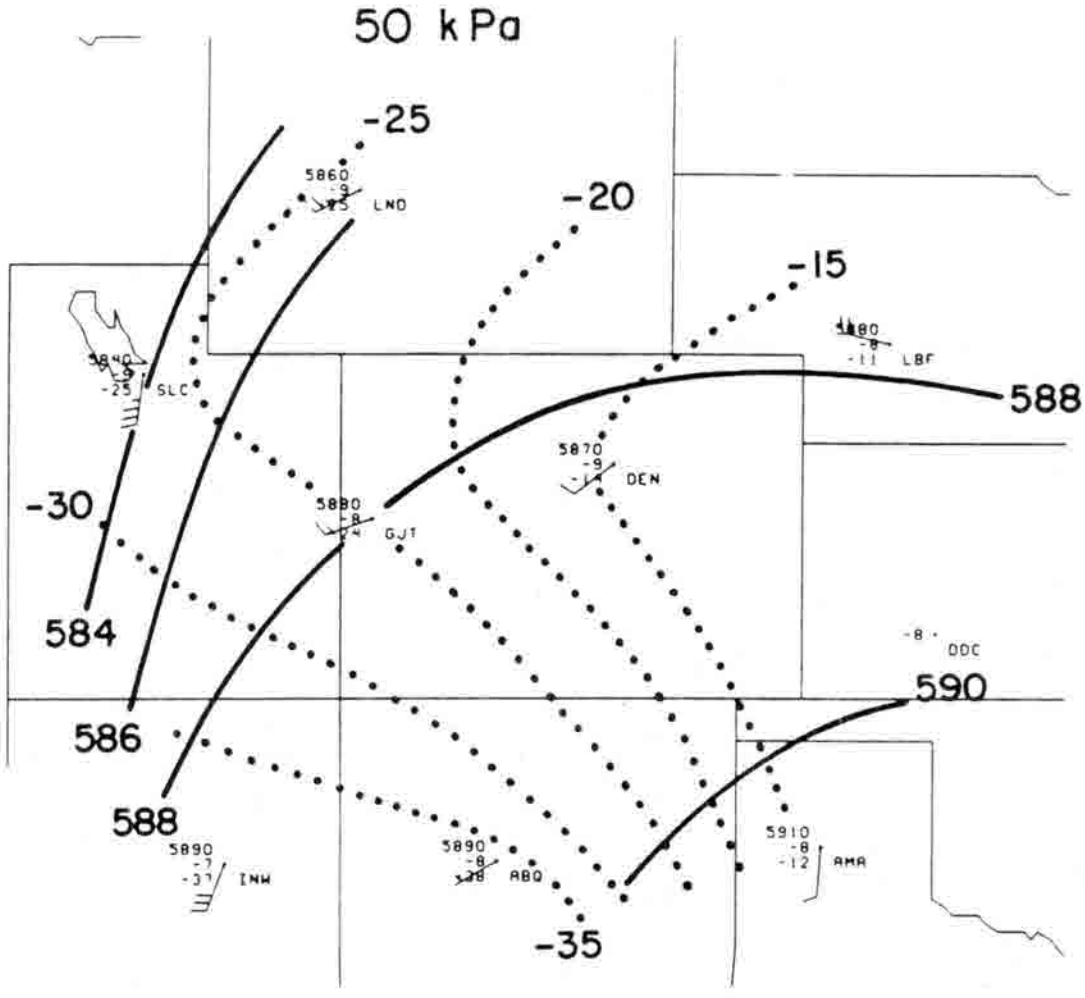

Figure 5.2b As in Fig. 5.2a, but for 50 kPa with 2-dam intervals on height contours. No temperature lines were drawn, since the field was nearly uniform.

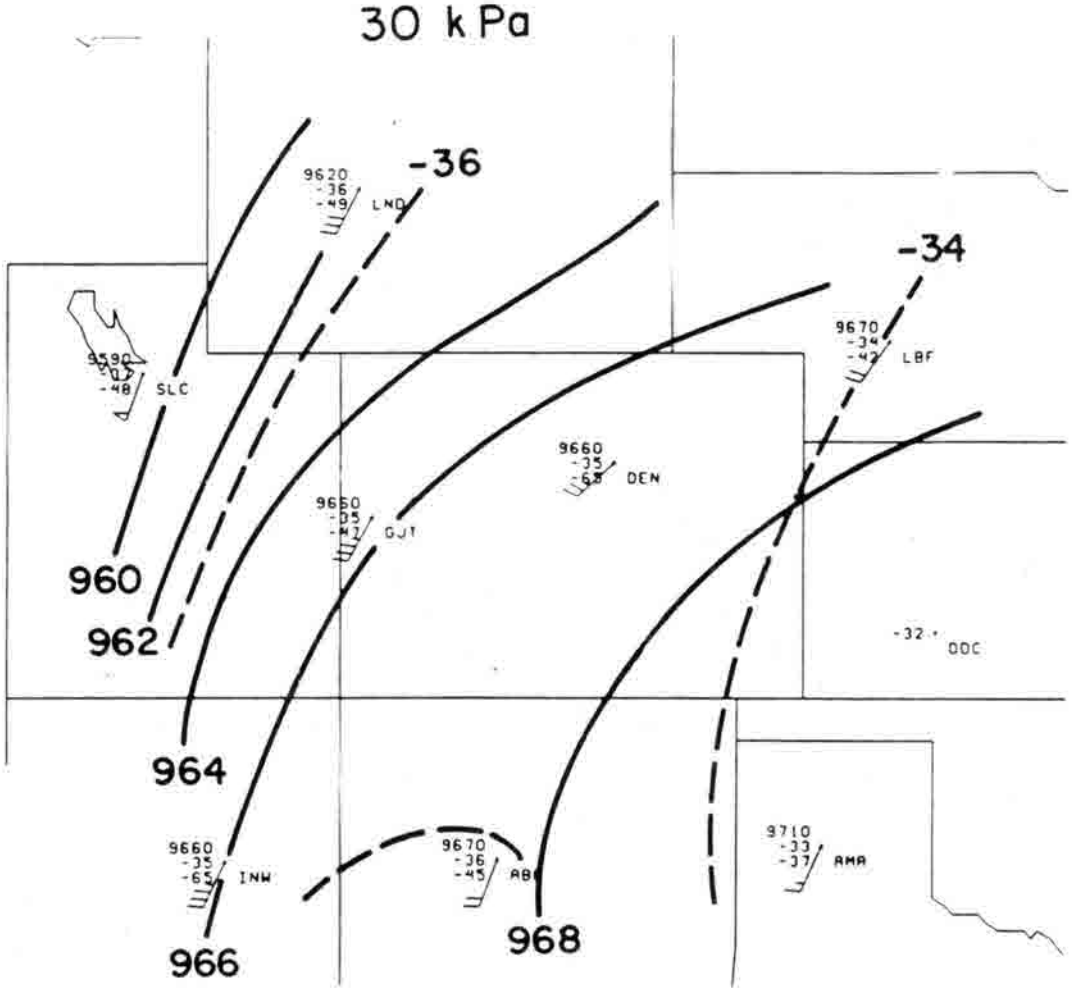

Figure 5.2c As in Fig. 5.2a, but for 30 kPa without dewpoint temperature contours and with 2-dam intervals on height contours.

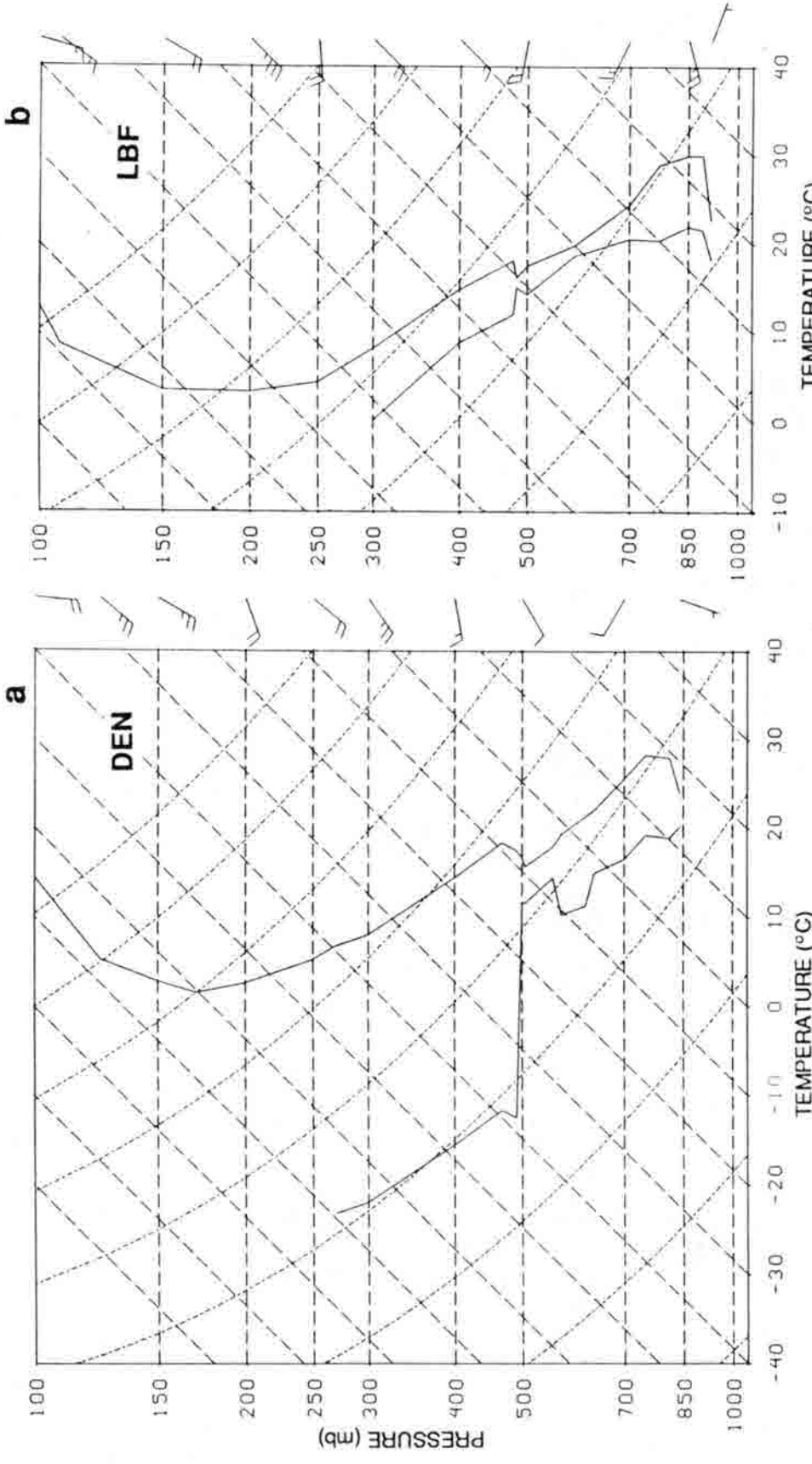

Figure 5.3 A skew-T/log-p plot of the 12 UTC (05 MST) 21 Aug 1983 rawinsonde report for a) Denver, Colorado and b) North Platte, Nebraska. Each full wind barb represent 10 kt. The plotted curves are temperature (right) and dewpoint temperature (left).

Temperature and water vapor analyses were restricted to regions east of the mountains. The early morning temperatures (Fig. 5.4a) roughly followed the terrain elevation, except for particularly warm air in the southeast. There was a sharp contrast between the ridges and valleys. Dewpoints were relatively high in the upper South Platte River Valley (stations GLY, PTL, KNB), and were particularly low on the upper Palmer Lake Divide. Those moisture features changed little through 07 MST (Fig. 5.4b). A small region near stations BRI and KNB was slow to warm during the early morning, relative to stations closer to the mountains. The result was a warm/cool hook in the contours for 07 MST. At 10 MST (Fig. 5.4c) there were local maxima and minima in the upper South Platte Valley forming a warm/cool/warm sequence. The cool spot centered on station KNB was also relatively moist, implying that evaporation from the ground may have held down the temperatures. The southeast region continued to be distinctly warm through this period while the dry region on the Palmer Divide spread eastward. The most prominent features at 13 MST (Fig. 5.4d) were the hot air in the southeast and the relatively large moisture values from the northeast extending into the South Platte Valley.

The winds (Fig. 5.5) had many features in common with Toth and Johnson's (1985) climatology from July 1981, including the directional reversal from downslope in the early morning to upslope in late afternoon. Synoptic-scale forcing resulted in a generally northwesterly flow over the eastern portion of the domain through most of the morning with speeds ranging from about 2 to 8 m/s. At 04 MST (Fig. 5.5a) there was downslope flow over the higher terrain, with southwesterlies from the Denver area (LAK, LTN) to as far northeast as BGD. The region of southwesterlies retreated toward the mountains by 07 MST (Fig. 5.5b), but weak downslope persisted at most of the higher stations. By 10 MST (Fig. 5.5c) most of the stations on the upper plains recorded upslope winds, while there was no consistent pattern in the mountains. Toward the east the winds had turned to almost northerly. The upslope flow region expanded by 13 MST (Fig. 5.5d) to include all of the mountain stations and some of the stations as far east as SNY (Sydney, Nebraska). Winds were still northwesterly, however, in the Arkansas Valley.

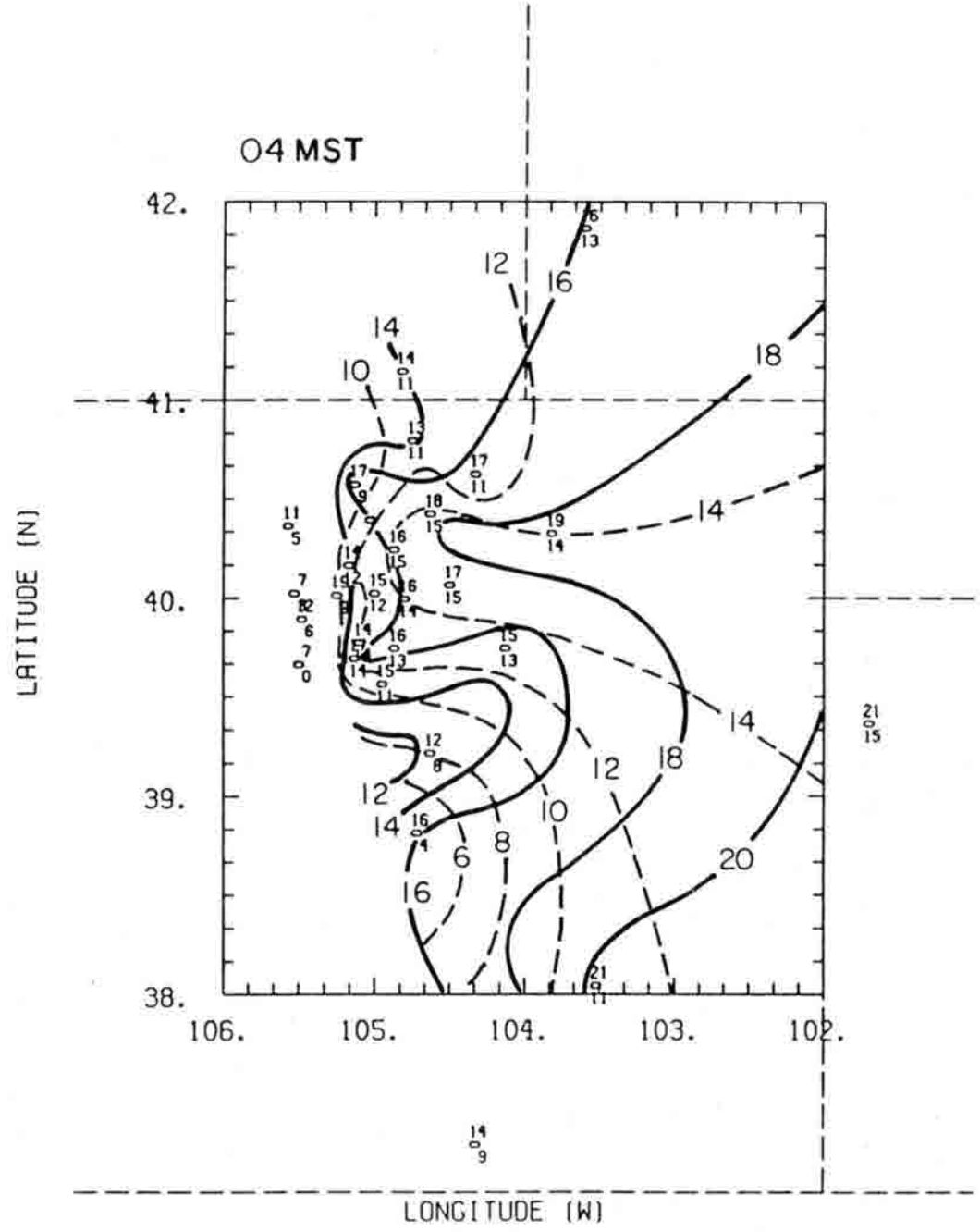

Figure 5.4a The 04 MST 21 Aug 1983 surface observations of temperatures (solid lines) and dewpoint temperatures (dashed lines), each contoured at intervals of 2°C. Stations outside the domain grid were used in the analysis.

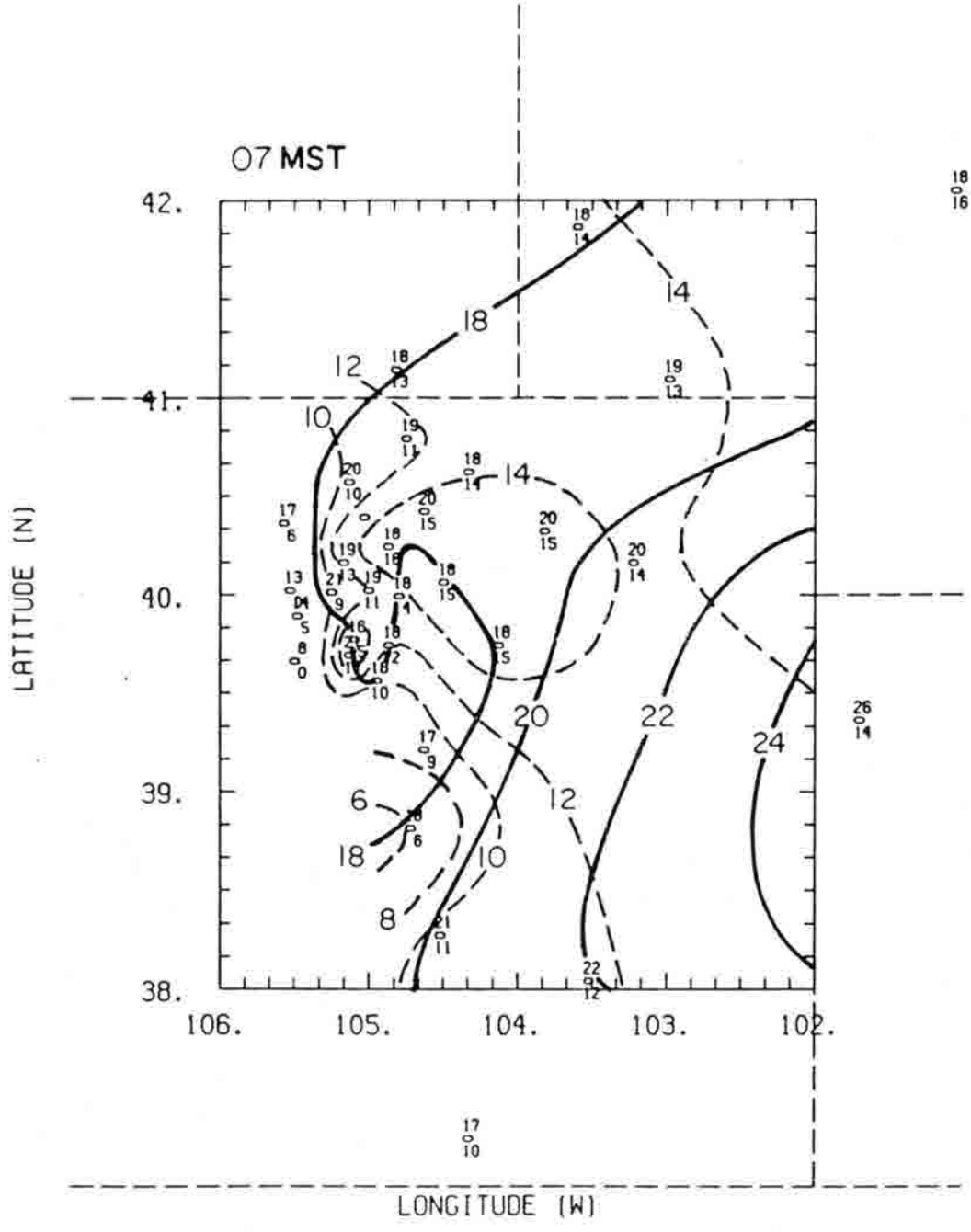

Figure 5.4b As in Fig. 5.4a, but for 07 MST.

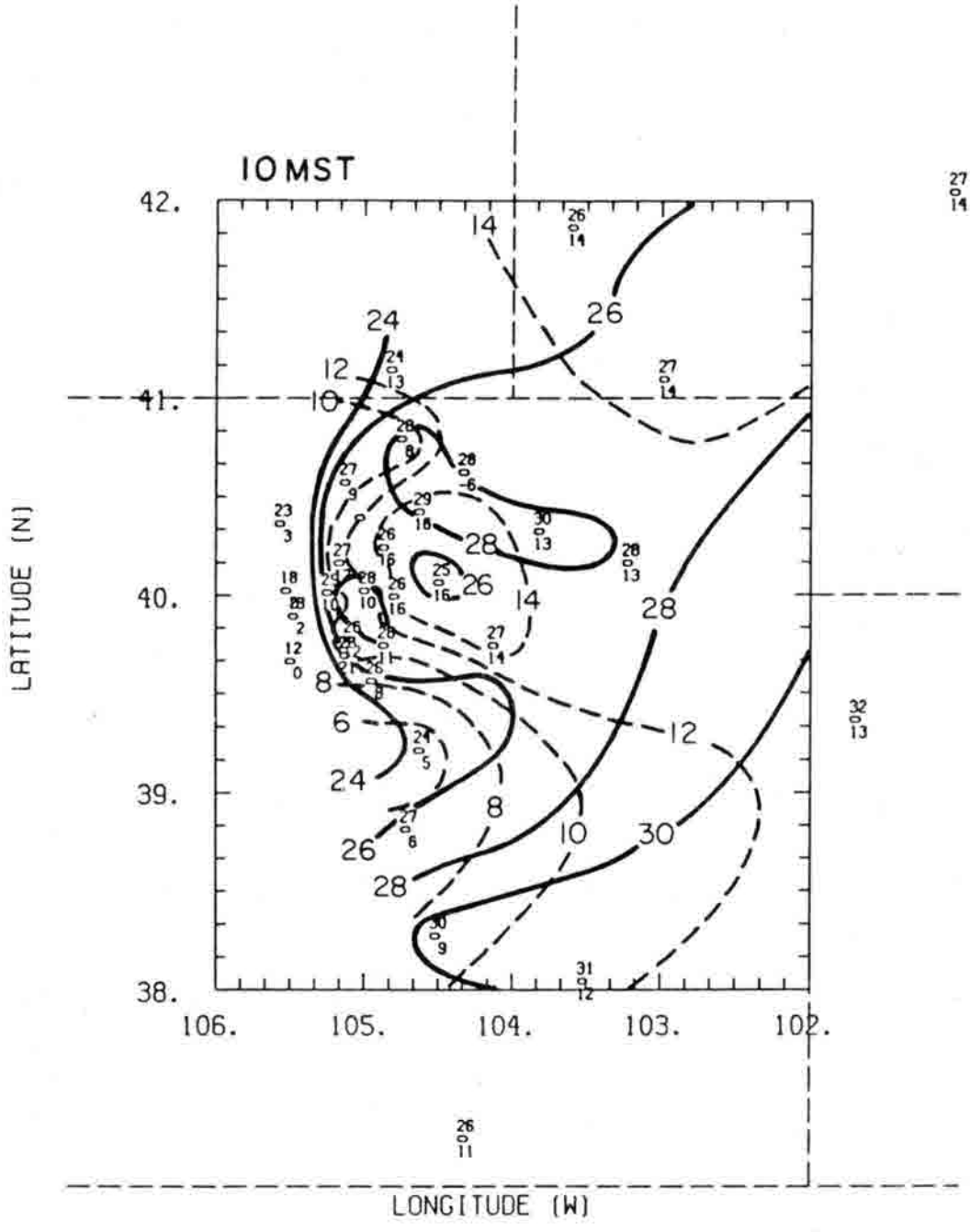

Figure 5.4c As in Fig. 5.4a, but for 10 MST.

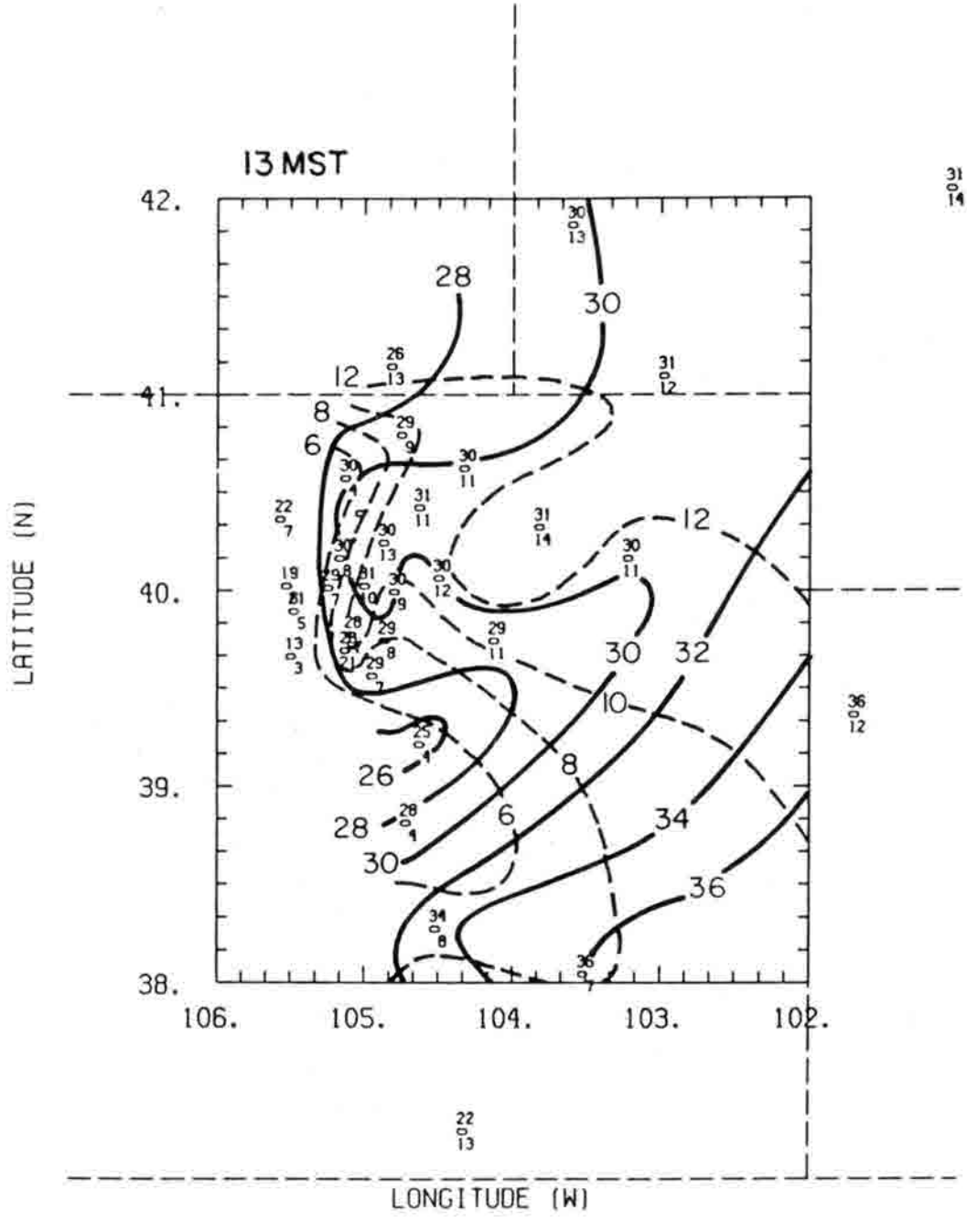

Figure 5.4d As in Fig. 5.4a, but for 13 MST.

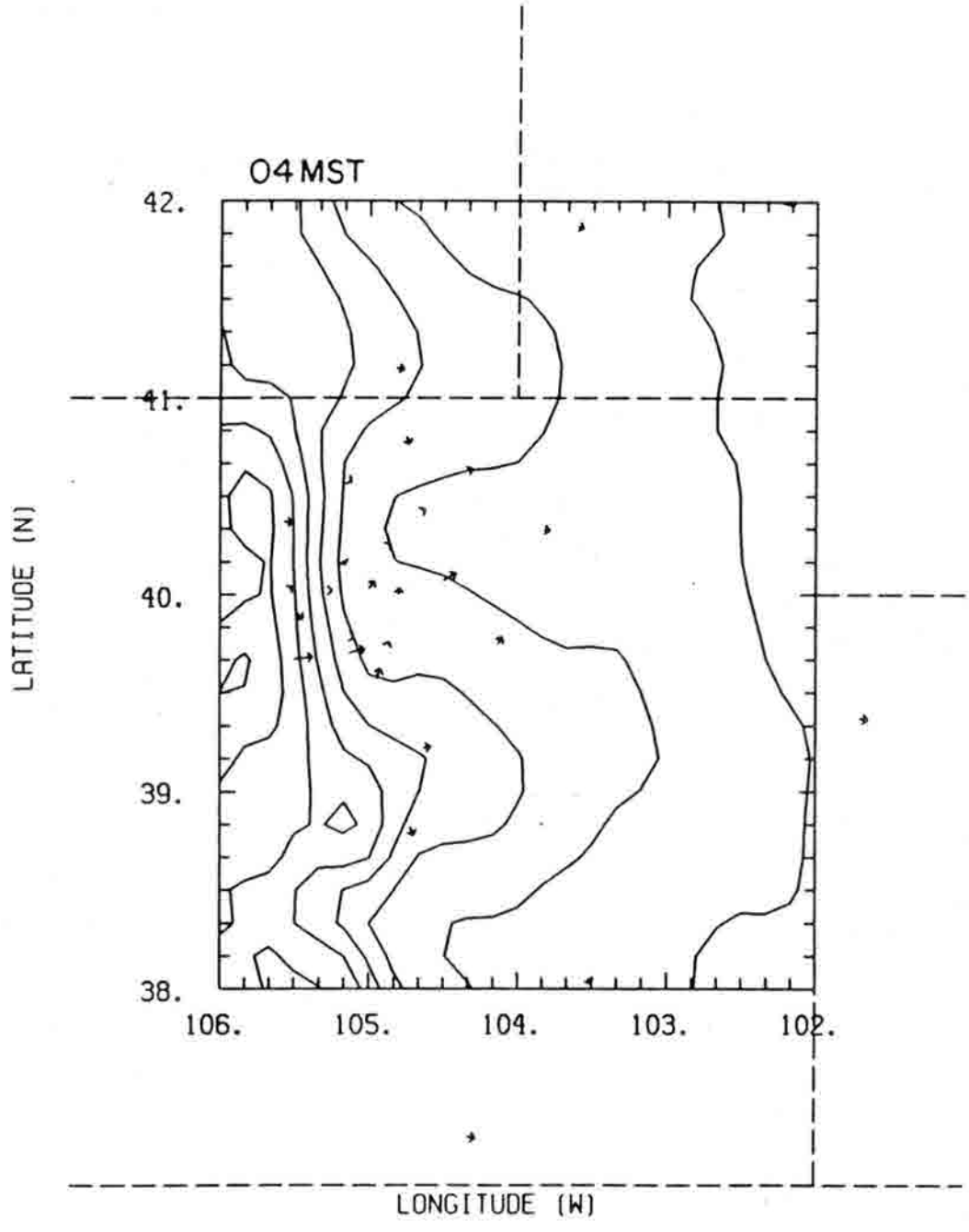

Figure 5.5a The 04 MST 21 Aug 1983 surface observations of wind. An arrow of length equal to one east-west grid interval represents a speed of 10 m/s. The background contours are terrain elevations.

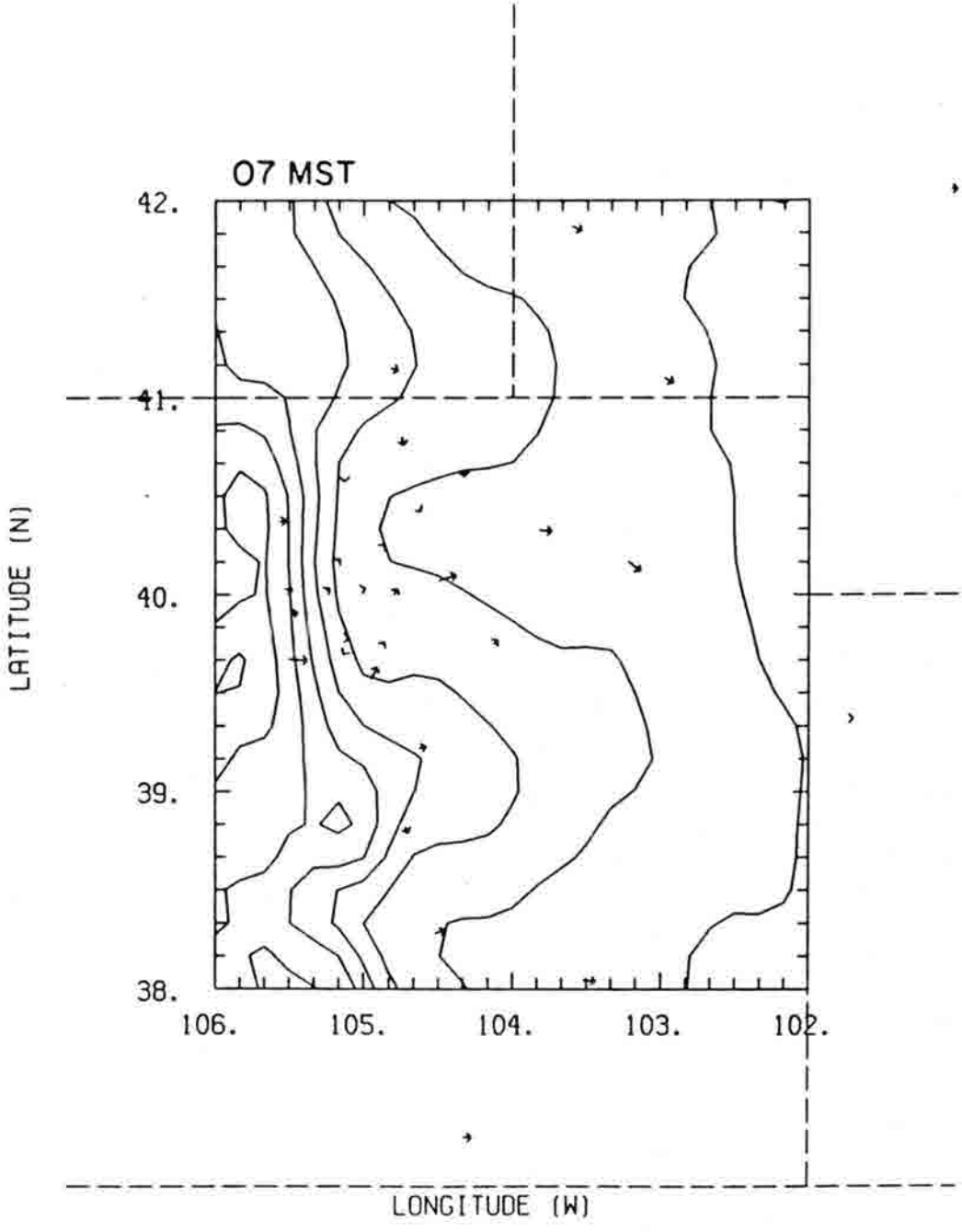

Figure 5.5b As in Fig. 5.5a, but for 07 MST.

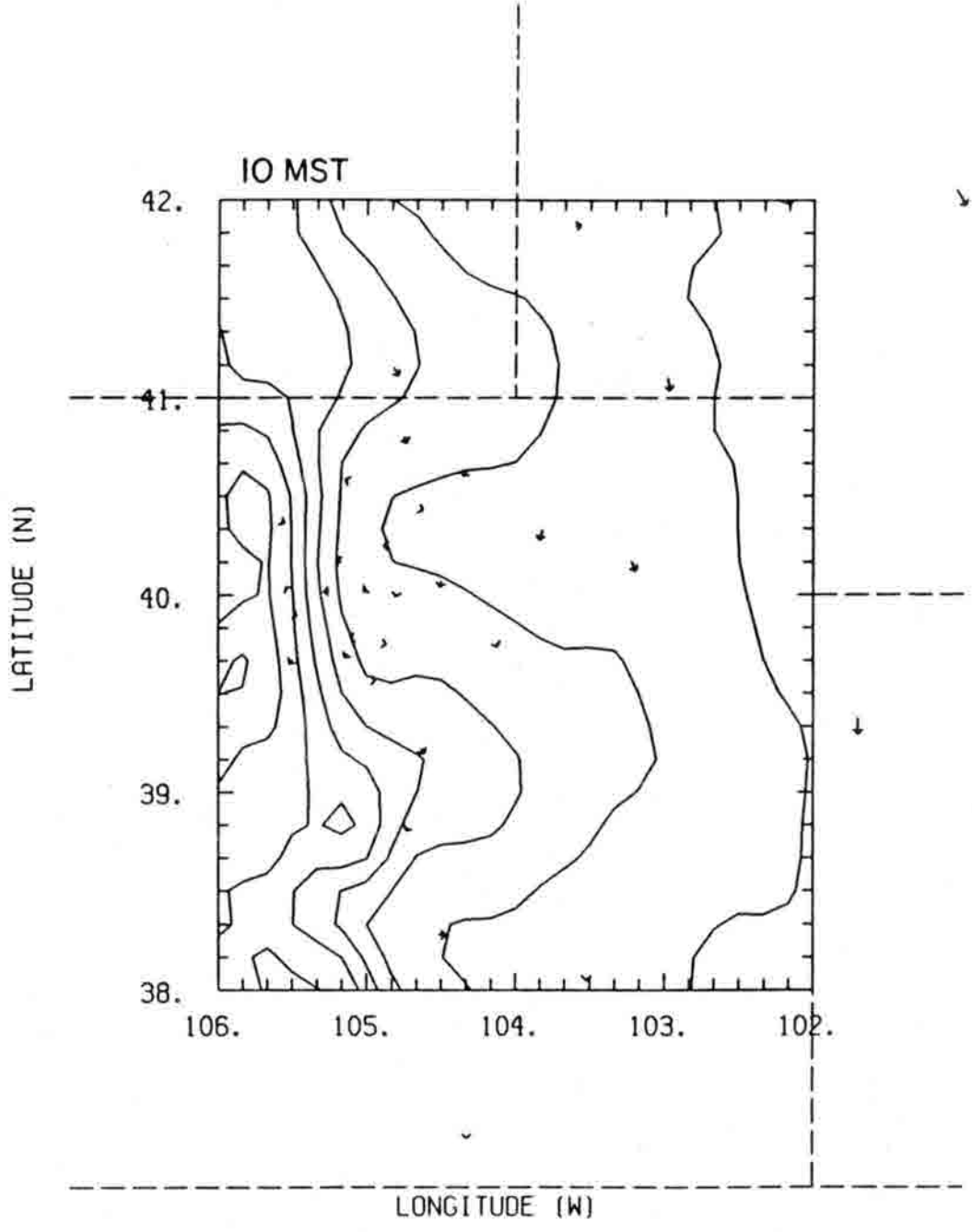

Figure 5.5c As in Fig. 5.5a, but for 10 MST.

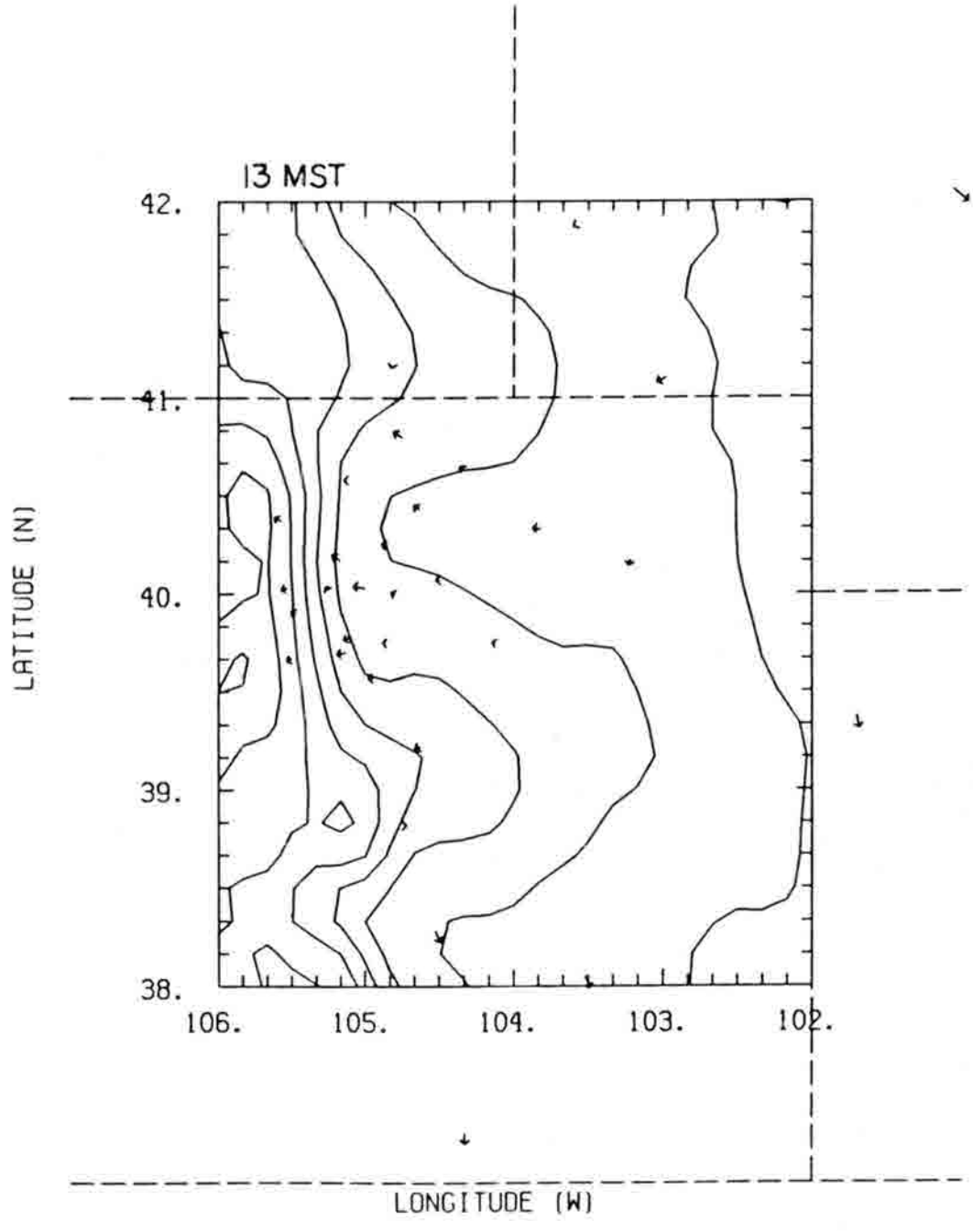

Figure 5.5d As in Fig. 5.5a, but for 13 MST.

5.2 Satellite Data

5.2.1 Imagery

Visible and infrared (channel 8) imagery from GOES-5 provided a record of cloud development within the case study domain from the evening of 20 August through the evening of 21 August. The images presented here are from the operational NOAA/NESDIS products.

The infrared image from 22 MST 20 Aug. (Fig. 5.6a) reveals a thunderstorm anvil cloud covering much of the upper South Platte Valley, with a minimum equivalent blackbody temperature of about -52°C. In Fig. 5.7 is an isohyet analysis based on mesonetwork observations for the period encompassing the storm. The region of significant rainfall corresponds with the cool, moist spot in the 10 MST 21 Aug. surface analysis (Fig. 5.4c), supporting the idea that evaporation was responsible for retarding heating in that area. By 04 MST, just after the first VAS sounding data were taken, the storm had dissipated and its remnants covered the northeastern portion of the analysis domain (Fig. 5.6b). Most of the domain was clear at 07 MST (Fig. 5.6c), as the storm remnants continued to drift eastward and low clouds developed along the Colorado/Kansas border.

By 0930 MST (Fig. 5.6d) the diurnal cycle of cloud development had begun, as the first convective clouds formed over the mountain peaks. Two hours later the convective cloudiness extended onto the upper plains, making a distinct C-shaped feature in the visible satellite image (Fig. 5.6e). The "arms" of the C covered the southern portion of the Cheyenne Ridge and the center of the upper Palmer Divide. Convective development was stronger in the Sangre de Cristo mountains running southward from the southern edge of the domain. At 1230 MST (Fig. 5.6f) cloudiness extended further eastward along the Palmer and Cheyenne ridges and closed in toward the center of the South Platte Valley. There was still a clear slot just east of the continental divide, which may be the type of feature that Dirks (1969) noted as a common occurrence in the satellite imagery he inspected.

By 13 MST (Fig. 5.6g) the cloud field matured to the point that thunderstorms were developing. The coldest cloud top in the domain was just west of Limon, Colorado (LIC), while storms appeared to be maturing near the southern Colorado border. The storm near Limon intensified over the following three hours and moved slowly eastward along the Palmer

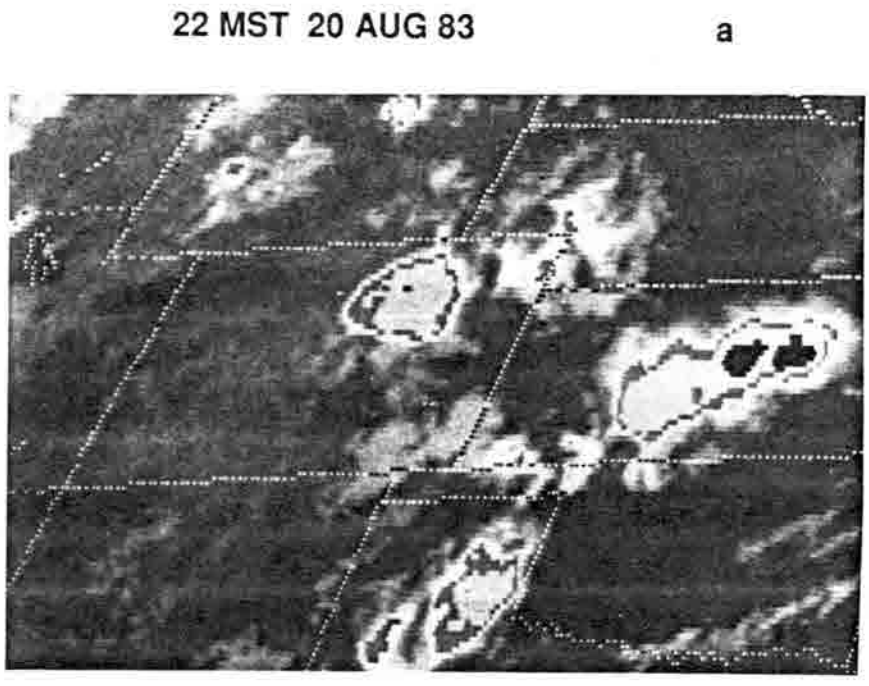

Figure 5.6a The GOES-5 infrared image from 22 MST 20 Aug 1983. State boundaries are denoted by dotted lines, with Colorado in the center. The NOAA/NESDIS operational MB enhancement was used, with colder regions represented by: medium gray (-32 to -41°C), light gray (-41 to -52°C), dark gray (-52 to -58°C), and black (-58 to -62°C).

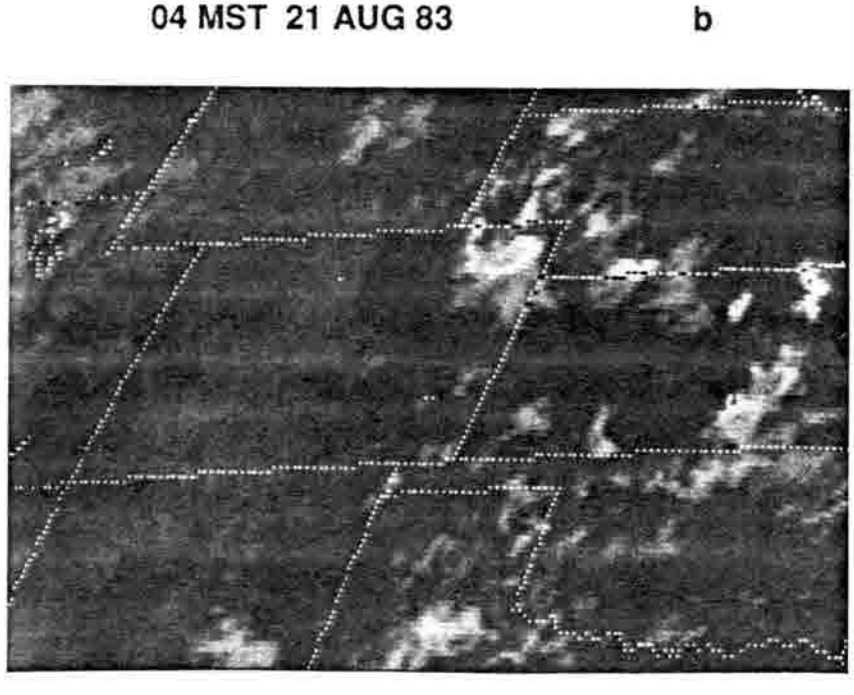

Figure 5.6b As in Fig. 5.6a, but for 04 MST 21 Aug.

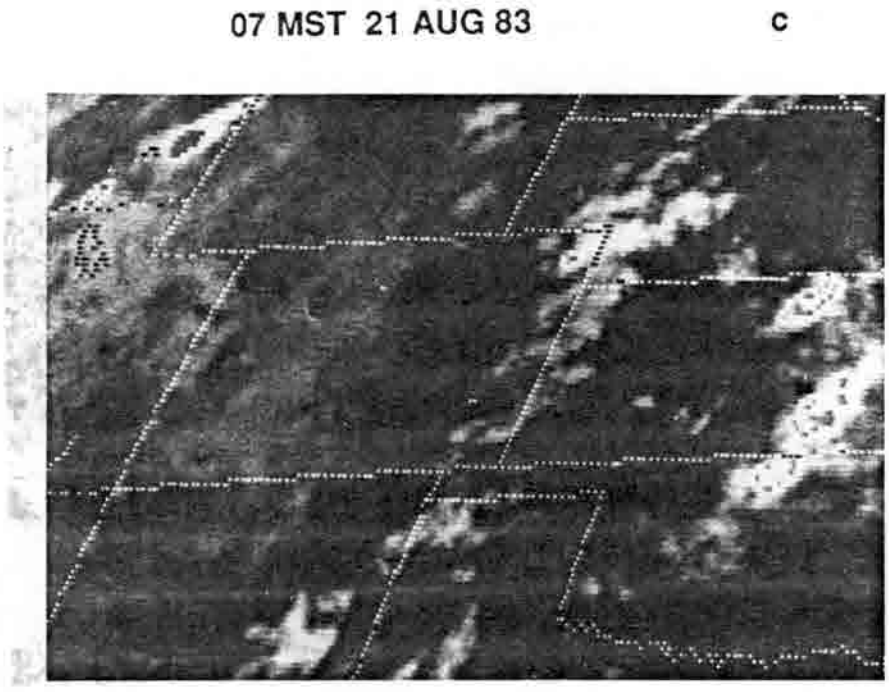

Figure 5.6c As in Fig. 5.6a, but for 07 MST 21 Aug.

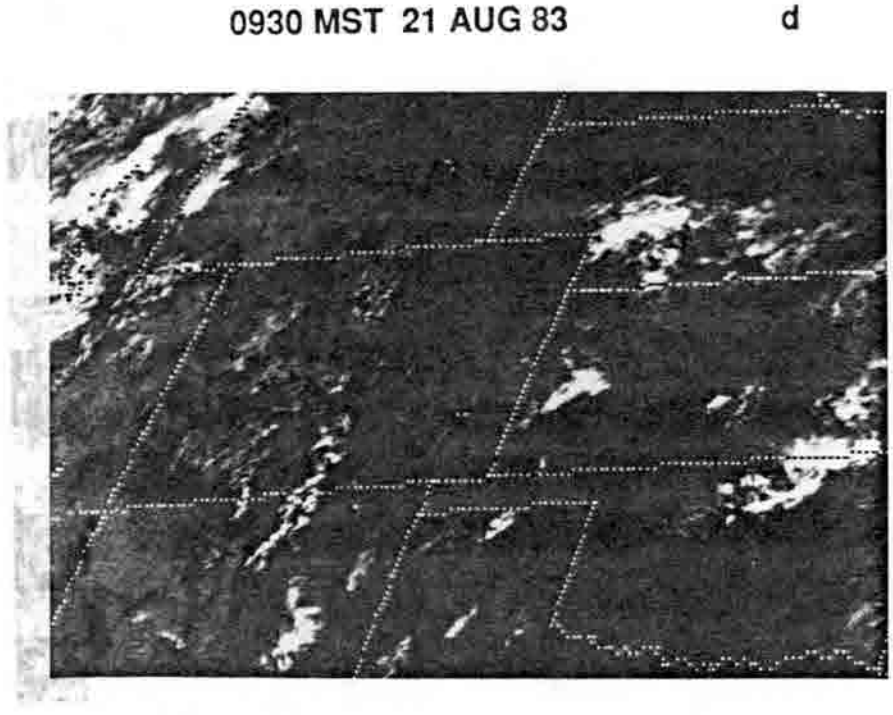

Figure 5.6d The GOES-5 visible image from 0930 MST 21 Aug. 1983, with state boundaries dotted.

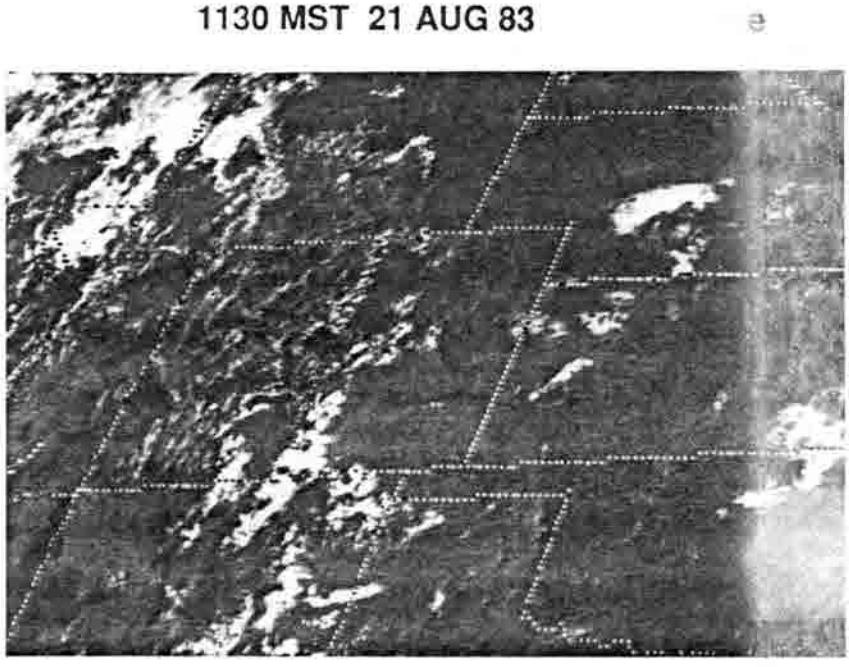

Figure 5.6e As in Fig. 5.6d, but for 1130 MST.

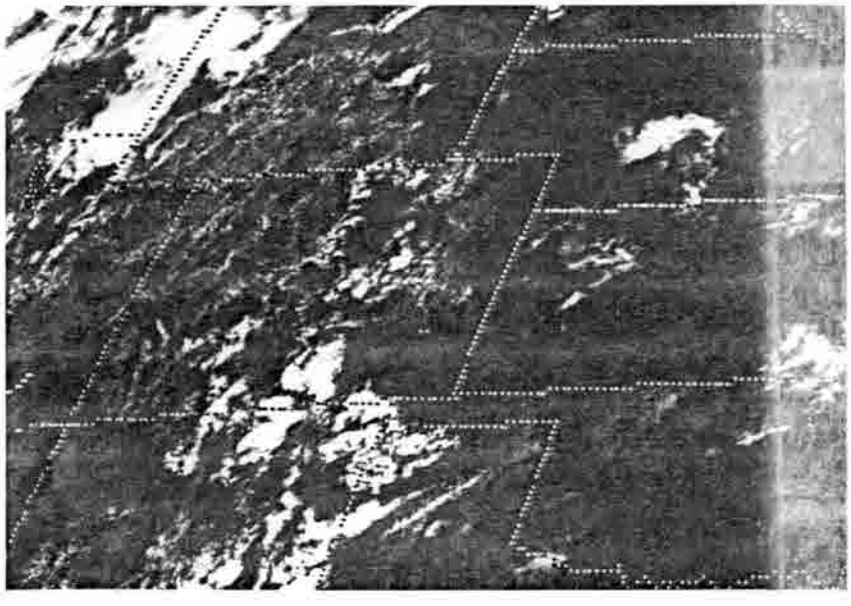

Figure 5.6f As in Fig. 5.6d, but for 1230 MST.

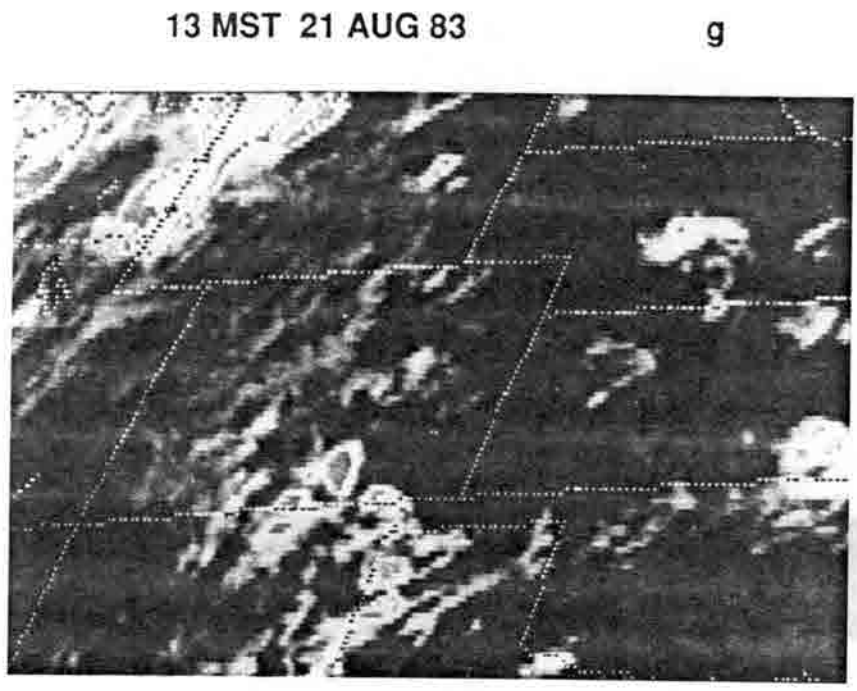

Figure 5.6g As in Fig. 5.6a, but for 13 MST 21 Aug.

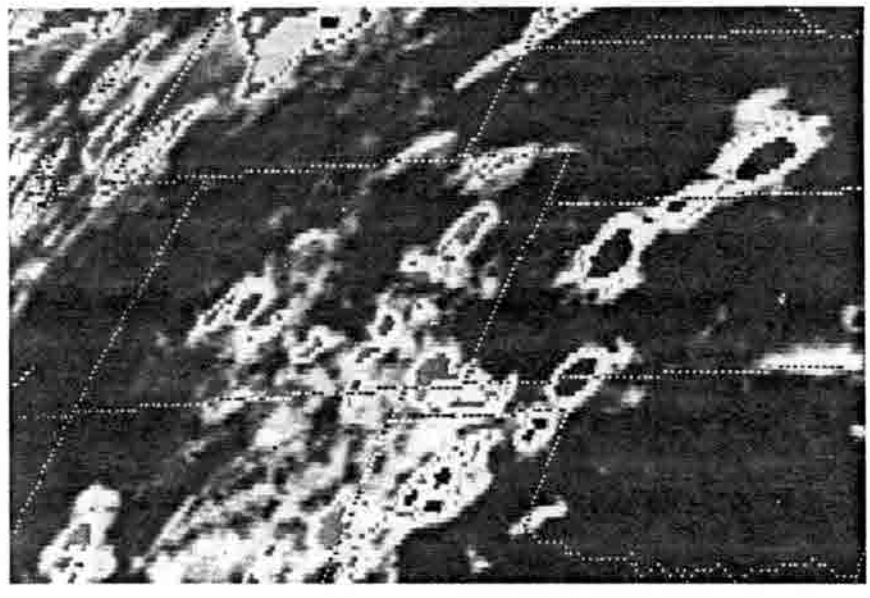

Figure 5.6h As in Fig. 5.6a, but for 16 MST 21 Aug.

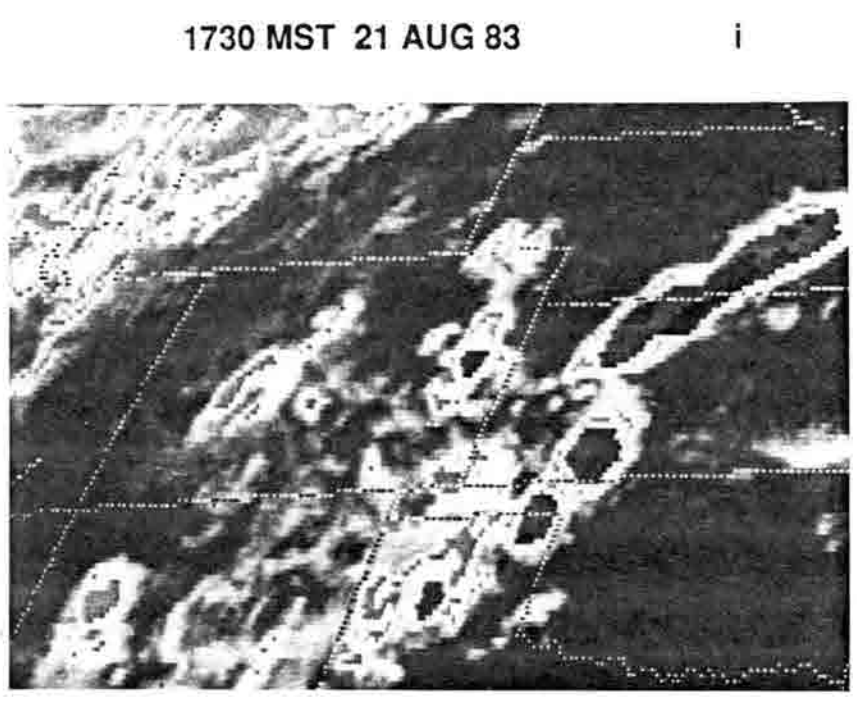

Figure 5.6i As in Fig. 5.6a, but for 1730 MST 21 Aug.

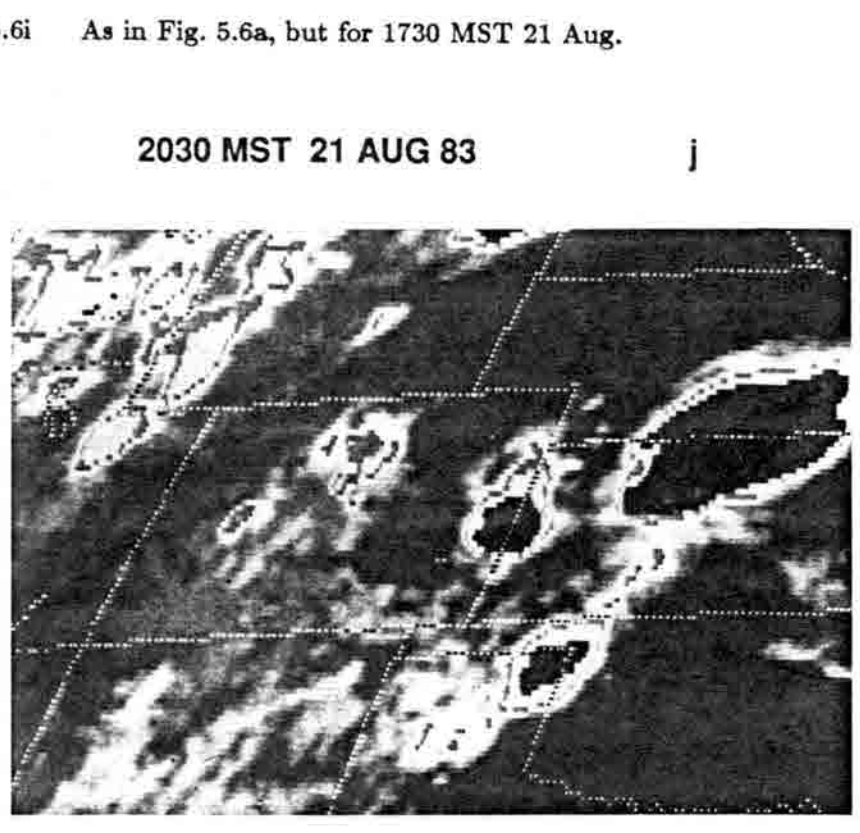

Figure 5.6j As in Fig. 5.6a, but for 2030 MST 21 Aug.

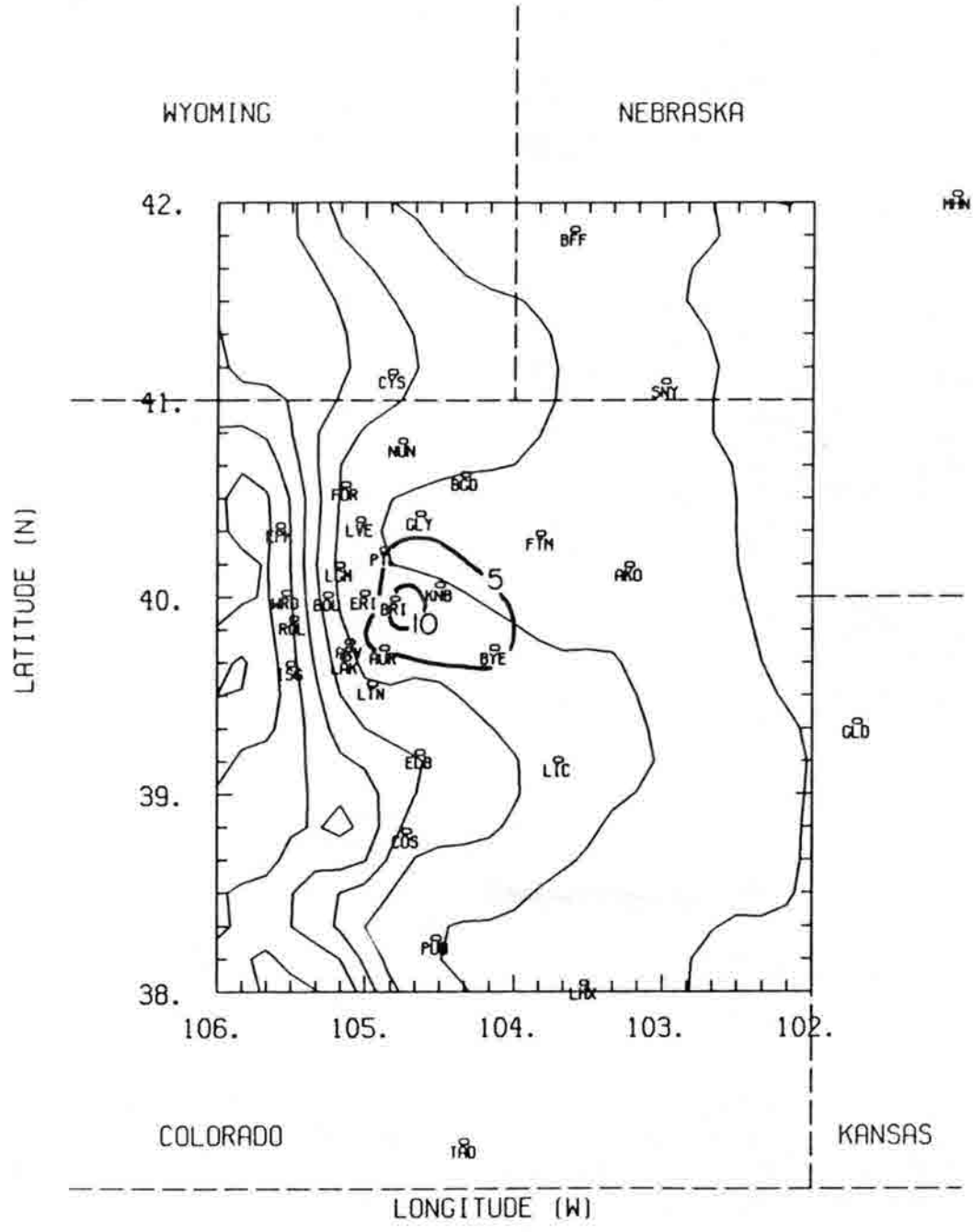

Figure 5.7 Isohyets at intervals of 5 mm for the period 17 MST 20 Aug. through 04 MST 21 Aug. Contours are based on data from the mesonetwork stations.

Divide (Fig. 5.6h). In addition, there were weaker cells to the north and south. To the west, over the high mountains of the domain, the clouds died out in place. Apparently, not all the ingredients required for propagation and intensification of the mountaintop clouds (Banta, 1982; Tripoli, 1986) were present on this day.

By 1730 MST (Fig. 5.6i) most of the clouds had deteriorated, with the prominent exception of the storm on the Palmer Divide. The storm moved southwestward through 2030 MST (Fig. 5.6j) and intensified, achieving cloud top brightness temperatures below -58°C. Meanwhile, a large convective system had developed along a surface pressure trough running northeast/southwest through Kansas and Nebraska, well outside the analysis domain.

The series of satellite images depicts several key features to be addressed by mesoscale analysis: the clear slot east of the high mountains, the decay of the mountain convection, and the intensification and propagation of the storm that originated near Limon.

5.2.2 Sounding Strategy

On 21 Aug. 1983 the VAS dwell sounder scanned all of the case study domain just before the hours of 04, 07 and 10 MST. Because the satellite's scan region drifts diurnally there was only partial coverage of the domain later in the day. At the later times there was a data-free gap running east/west across the domain, with a half-hour interval between data from the northern and southern subdomains. These factors complicate data processing. Since this study was focused on the pre-convective period and convective development was widespread by noon, only the morning sounding data were used.

The dwell sounder data were obtained from the VAS data archive at the University of Wisconsin Space Science and Engineering Center (SSEC) at a nominal resolution of 16 km. The SSEC also provided the corresponding visible imagery at 4-km resolution. The CSU Interactive Research Imaging System (IRIS) was used to manually flag cloudy regions through inspection of visible and infrared imagery. This approach was considered more reliable than automatic cloud detection procedures. Retrievals were performed only in the regions that appeared to be completely clear. The IRIS was also used to make manual corrections to automatic navigation programs provided by the SSEC.

On 21 Aug. the VAS dwell sounder operated with the spin budget given in Table 5.1. The data from SSEC had been averaged over the repeated measurements at each instantaneous field of view, but that averaging was not sufficient to meet the noise requirements for atmospheric sounding (Table 2.1). The radiances were spatially averaged to points centered at alternating lines and elements, resulting in nominal 32-km sounding resolution. For the troposphere-sensing channels (3-12) five adjacent 16-km pixels were averaged into each sounding field of view, while 25 pixels were averaged for the stratosphere-sensing channels (1 and 2). Thus, there was some overlap between neighboring sounding fields of view. Cloudy pixels were omitted from the averaging process, and a sounding field of view was rejected unless all tropospheric- and stratospheric-channel averages included at least 4 and 19 cloud-free pixels, respectively. The centers of the resulting sounding fields of view are plotted in Fig. 5.8.

Water vapor retrievals for the lower troposphere are unreliable over mountains because the background, as viewed from space, varies greatly in height and temperature within a sounding field of view. Accordingly, only upper troposphere retrievals (above the 50-kPa level) were used from mountain sites (surface pressure less than 79 kPa). Before water vapor retrievals could be made it was necessary to make some adjustments to the retrieval software to minimize domain-wide biases in the results. The radiative transfer routines include tuning parameters that compensate for differences between theoretical and real-world atmospheric transmittances. Parameter values were determined subjectively by comparing the Denver radiosonde observation with nearby satellite retrievals. Adjustments take the form

$$\tau_j{}' = \tau_j{}^{\gamma},$$

where $\tau_j{}'$ is the adjusted transmittance for channel j. The most extreme value of γ used in this study was 1.1.

For water vapor retrievals it would have been a waste of computer time to do retrievals at resolution finer than 32 km because of noise limitations (Chesters, *et al.*, 1986). On the other hand, surface temperature retrievals rely mostly on window channel radiances that have significant structure down to 16 km or less (Hillger and Vonder Haar, 1988). Therefore, surface temperatures were retrieved at the full 16-km resolution (Fig. 5.9). Channel

Table 5.1 VAS dwell sounder spin budget for 21 Aug 1983.

Channel	Number of Views
1	1
2	3
3	4
4	3
5	2
6	6
7	2
8	1
9	3
10	1
11	0
12	1

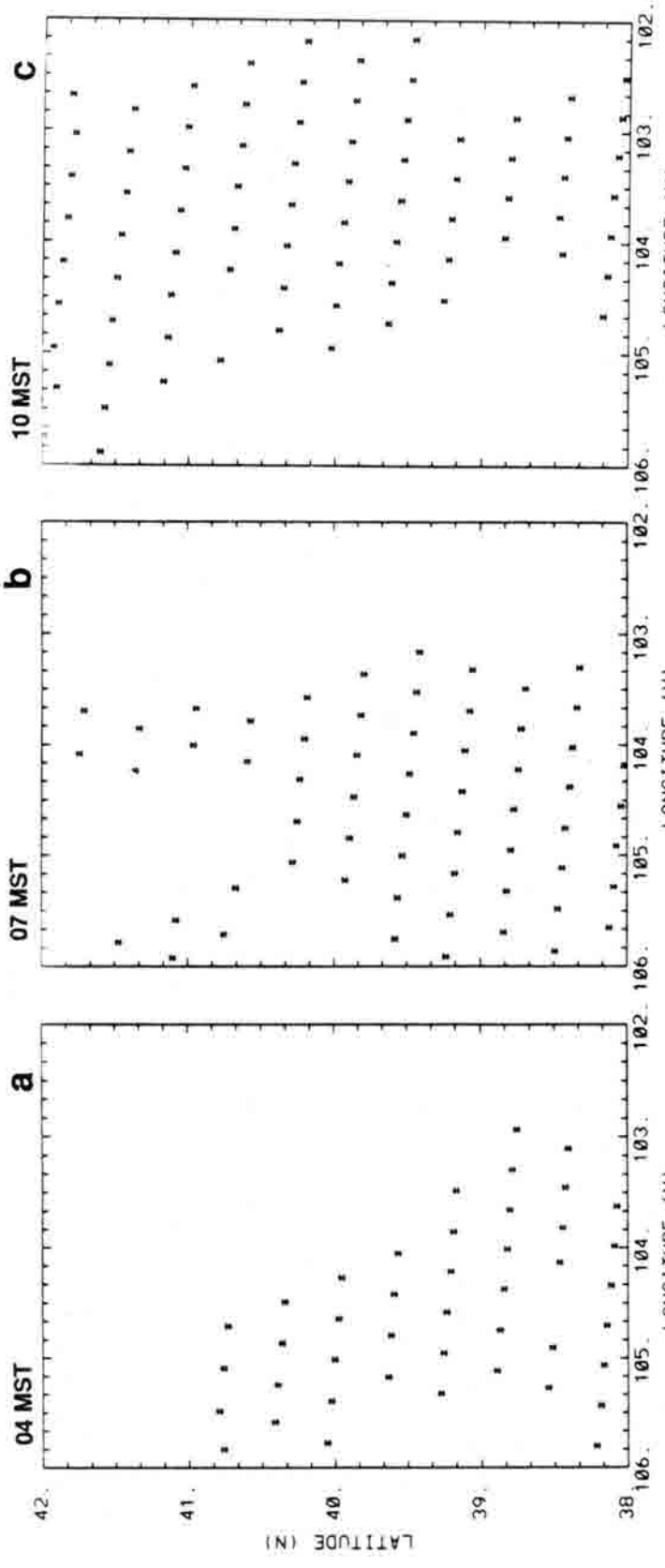

Figure 5.8 Locations of sounding fields of view for atmospheric soundings at a) 04, b) 07, and c) 10 MST.

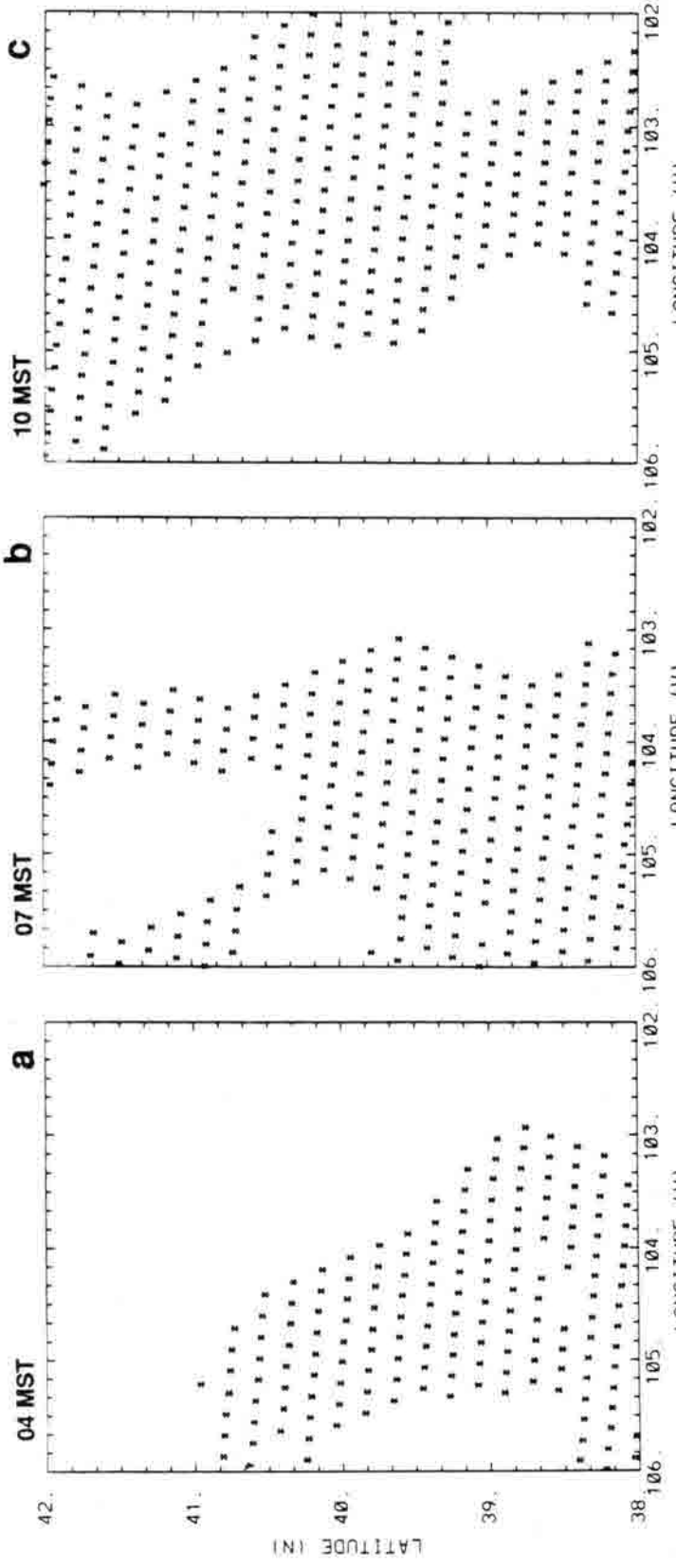

Figure 5.9 Locations of sounding fields of view for surface temperature retrieval at a) 04, b) 07, and c) 10 MST.

averaging was the same as for water vapor retrievals except that channel 8 radiances were not averaged at all. The increased resolution required a sacrifice of computer time. For "quick" retrievals that was a minor consideration, but surface temperature coupling also required full, iterative retrievals that are far more time consumptive. To alleviate this problem the full and "quick" retrieval schemes were linked. This way surface temperatures had full-retrieval accuracy and 16-km resolution at about the cost of 32-km full retrievals. Details are in Appendix A.

5.3 Model Runs

The numerical model runs made for this case study are outlined in Fig. 5.10. The time step was 90 s, and the vertical grid was as in the two-dimensional experiments. The horizontal grid length was 10′ latitude/longitude (about 17 km) within the 38–42°N, 102–106°W analysis domain, with a stretched grid surrounding it. All runs had common initial data, with six hours of dynamic initialization. Most segments of integration time were applied to more than one analysis. The primary differences in temperatures and winds depended on the source of surface temperature information. Accordingly, only two time-series' of temperature and wind results are presented below, one with energy balance-derived surface temperatures and the other with satellite-retrieved values. In both cases the results are from the runs with coupled water vapor analysis. Only those two runs were extended beyond 10 MST to make three-hour numerical "forecasts".

5.3.1 Initial Data

The model dynamic fields were initialized at 17 MST 20 Aug. so that there would be time for nocturnal drainage circulations to develop before the first analyses were done in the morning. The initial temperature profile was based on the radiosonde sounding at Denver at 05 MST 21 Aug. (Fig. 5.3a) with a slightly subadiabatic layer imposed near the ground to compensate for the time difference. Other, minor, adjustments were made at higher levels so that the modeled and observed soundings at Denver nearly matched at 05 MST. The surface pressure at Denver was 84 kPa. The background geostrophic wind profile was

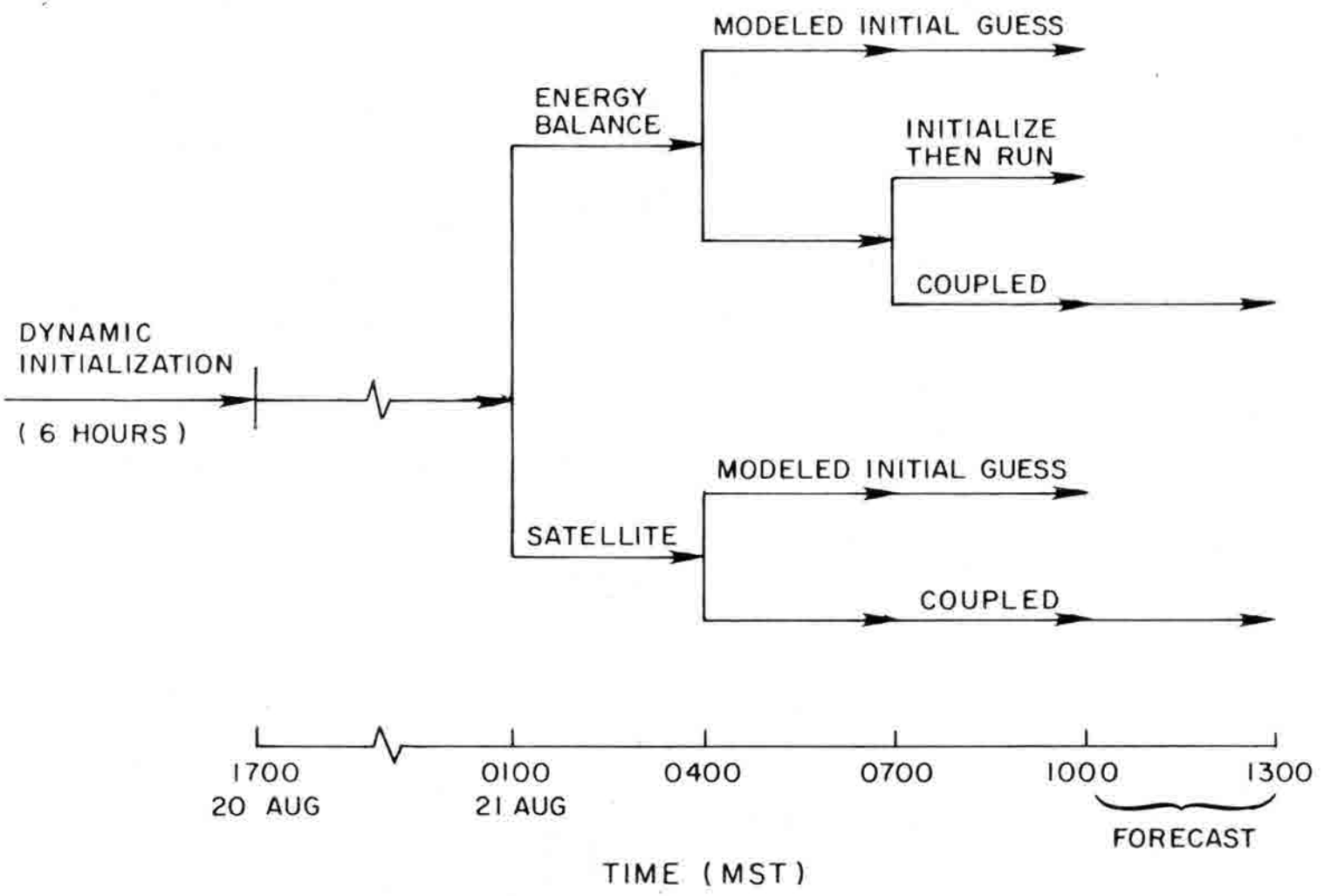

Figure 5.10 A schematic outline of the computer runs used in the case study. Lines are labeled according to the water vapor analyses for which they were used.

estimated from the 05 MST radiosonde reports of geopotential height. The height gradient across the domain was estimated manually, and values from the 84-kPa level were used at all lower levels (Fig. 5.11).

Soil characteristics were taken as constants across the model domain. The initial soil temperatures were based on 19 MST observations at the Fort Collins weather station as archived by the Colorado Climate Center. Initial values were set as differences from the air temperature at the lowest grid level. The other parameters used in surface energy balance computations were the same as in the model sensitivity tests and in Abbs and Pielke's (1986) study of the same area. The surface roughness was specified to increase from the plains to the mountains. This was appropriate since the mountains are mostly forested, with rugged terrain, and the plains are mostly grassland. Details of the roughness specification and an evaluation of its effects are in Appendix B. In brief, the variations in surface roughness have a significant impact on the wind speeds and directions within the lowest 1 km of the atmosphere.

5.3.2 Surface Temperature Handling

The effects of clouds on solar and infrared radiation were ignored in both the energy balance and satellite-derived surface temperature determinations. When model-gridded surface temperatures were adjusted in accordance with satellite retrievals the adjustments were interpolated from clear areas into cloudy ones. Virtually all of the study domain was clear during at least one of the three satellite observation periods, so some time-lagged cloud effects were accounted for indirectly.

For the model runs with retrieved surface temperatures there was a smooth transition over a three hour period between pure energy balance-based values and pure satellite-based values. Each time–interpolation spline was fit not only to the 04, 07 and 10 MST satellite-derived temperatures, but also to the energy balance-derived values at 01 MST. For integration from 01 to 04 MST the temperatures used for computing fluxes were based increasingly on the splines, going from weighting of zero at 01 MST to one at 04 MST.

Figure 5.12 is a record of surface temperature splines for one grid point. There were discontinuous changes whenever the retrievals were updated (see Sec. 2.6) since some of

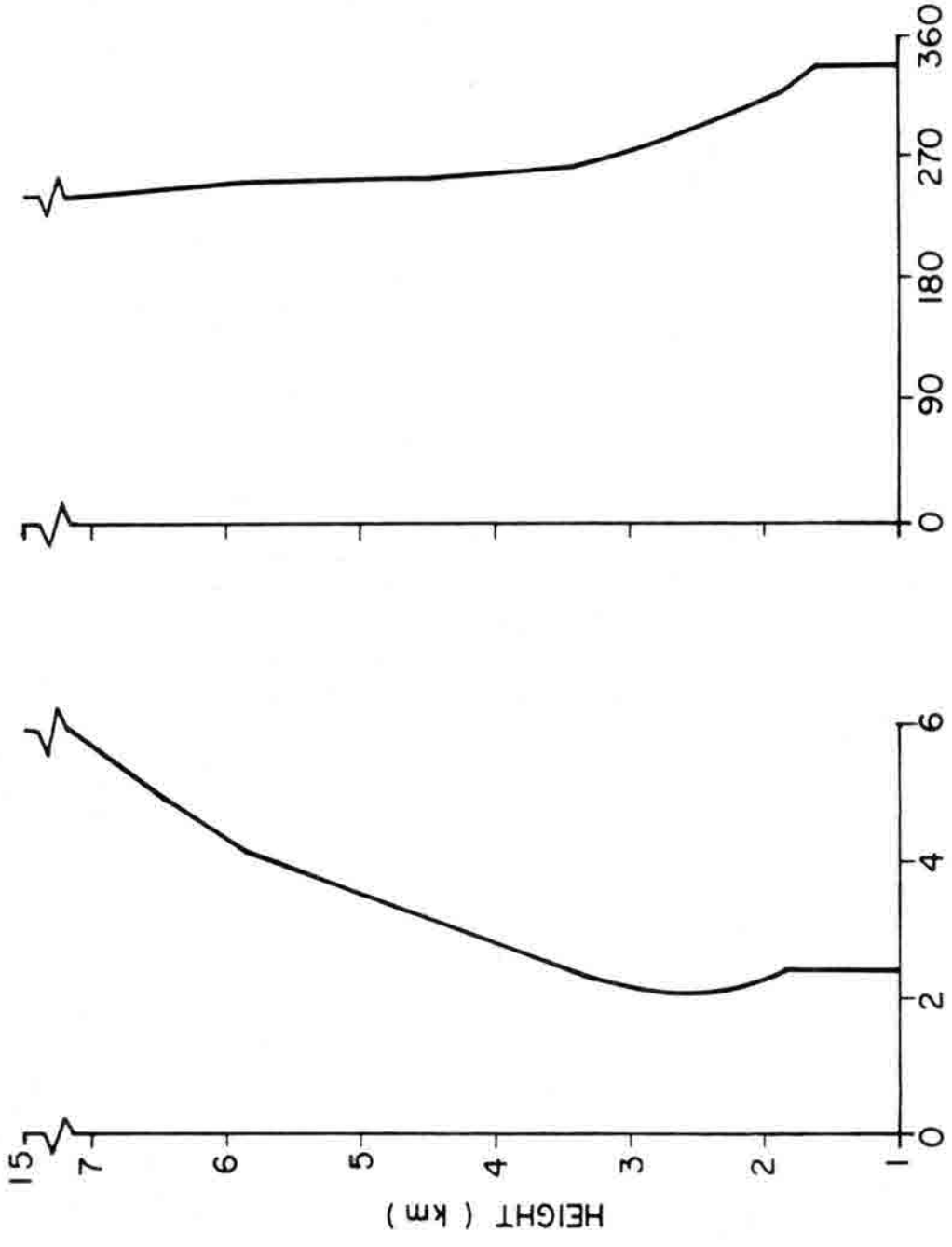

Figure 5.11 The background geostropic wind speed (a) and direction (b) for the case study model runs.

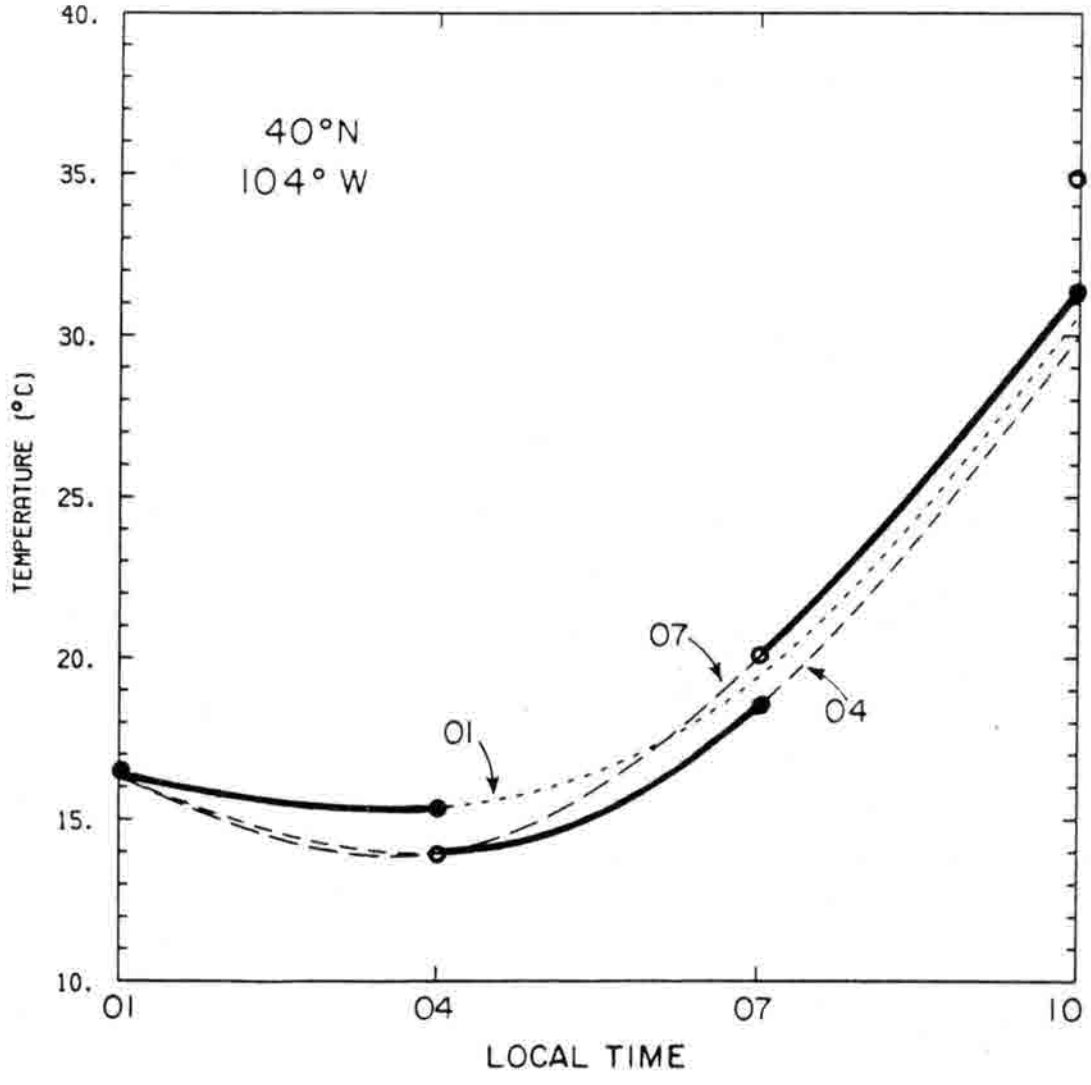

Figure 5.12 A plot of surface temperature splines for the grid point at the center of the domain. Each curve is labeled according to the model integration time at which the spline fit was made. The heavy, broken curve denotes the temperatures used at each time step. The open circles ('exclusive' end points) indicate the final retrieved values.

the preliminary estimates of surface temperatures differed significantly from the final, and most reliable, estimates. The changes were generally systematic throughout the domain, so their influence on gradients was small. Changes could be reduced substantially if the last preliminary estimates were obtained by using the full retrieval scheme instead of the "quick" scheme. In retrospect it appears that the additional full retrievals would have been worth the extra computer cost for this case. Given the size of the model grid and the resolution of the satellite data the extra cost would have been about fifteen percent of the cost of the model integrations.

A surface temperature extrapolation method was needed so that the model run with satellite-derived values could be extended beyond 10 MST. The chosen method allowed the satellite-retrieved gradients to be maintained while time changes were determined through energy balance computations. At 10 MST the retrieved and energy balance-determined temperatures were differenced at each grid point, and thereafter the differences were added to the energy balance results at each time step. A drawback of this approach is that it is slightly unstable since each energy balance result depends (weakly) on previous surface temperatures.

5.3.3 Surface Temperature Results

Two things should be kept in mind when intercomparing surface temperatures. First, the gridded surface temperatures apply to the exposed ground surfaces, whereas the conventional surface observations were air temperatures at about 2 m above the ground. Second, the satellite-based values presented here are from the final retrievals; preliminary retrievals also were used as model input.

At 04 MST the energy balance values (Fig. 5.13) generally followed the terrain elevations. There was a prominent cool tongue on the northern Palmer Divide, which was roughly consistent with the surface observations. The satellite-based values deviated more from the terrain elevations and generally had weaker gradients over the mountain slopes. On the plains there was a significant gradient from north to south, as was present in the surface observations. A cool spot ($< 14°C$) in the upper Arkansas Valley appeared to be caused by insufficient screening for clouds (see Fig. 5.9a). Neither the energy balance nor the satellite-

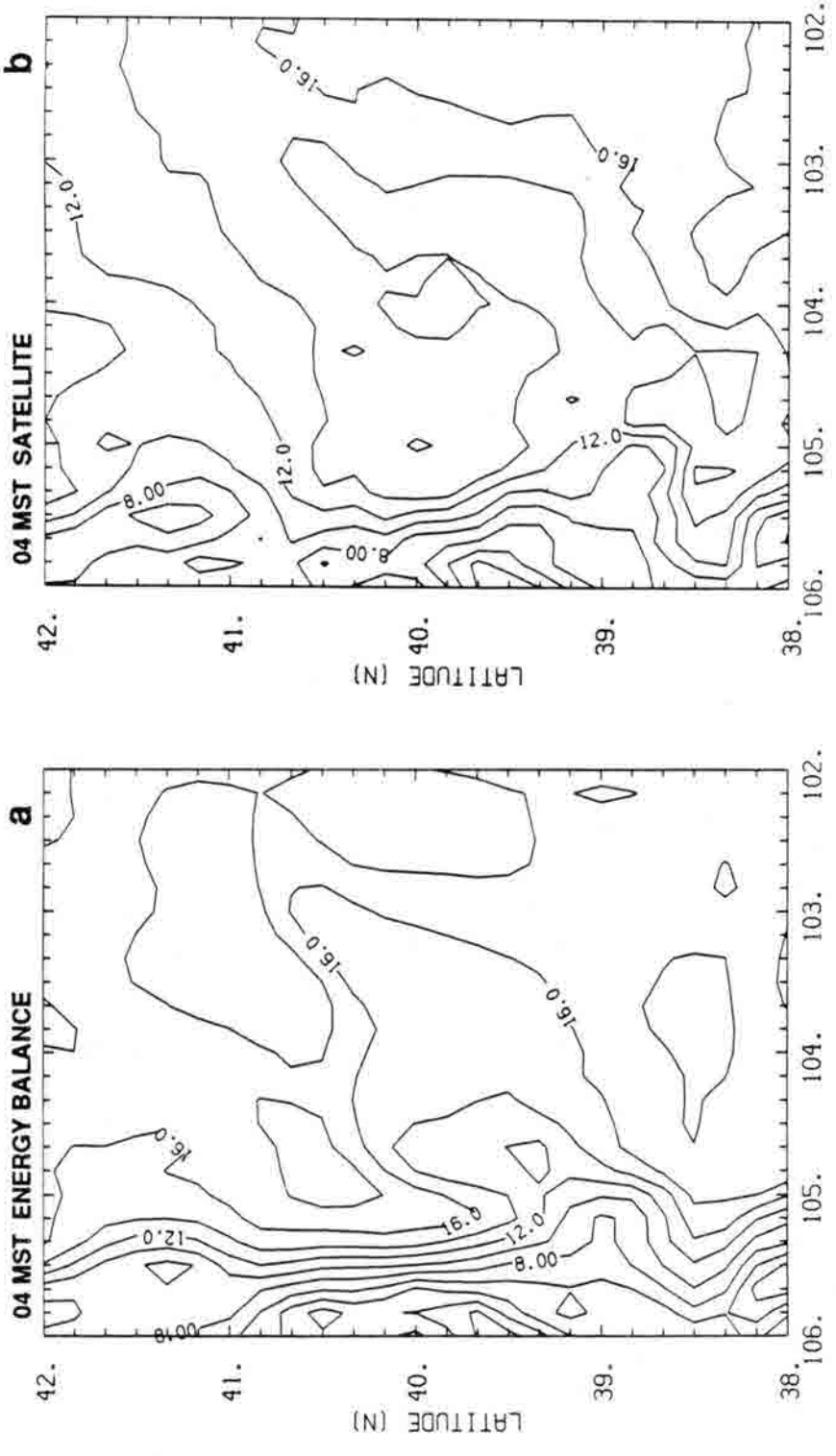

Figure 5.13 Ground surface temperatures at 04 MST from the two model runs with coupled water vapor analyses: a) energy balance-based and b) satellite retrieval-based. Contours are at 2°C intervals.

based values were systematically different from the surface observations by a large amount, but the satellite-based values tended to be cooler on the plains.

At 07 MST the energy balance values had warmed substantially (Fig. 5.14), but followed terrain elevations closely. In the satellite results there was a distinct warm region in the southeast and a warm band along the plains just east of the continental divide ($> 20°C$). Both of these features were well supported by the surface observations. Surface observational density was not great enough to verify several other features in the retrievals. Domain-wide the differences between retrievals and surface observations were small, whereas the energy balance values were generally 6 to 8°C warmer.

At 10 MST the energy balance temperatures diverged somewhat from the terrain-following pattern (Fig. 5.15). In regions with very light winds (shown in the next subsection) heat fluxes to the atmosphere were reduced and the ground surface warmed especially strongly. In the satellite-based results there were very strong gradients at this time even over relatively flat terrain. Between a hot region in the southeast and a cool band to the north there was a difference of more than 12°C over a 70-km distance. The features in the satellite-derived data are very similar to those resolved by the surface observations, although the magnitudes are very different. Among these features is the series of warm, cool, and warm regions in the South Platte Valley, the cool areas on the northern Palmer and Cheyenne ridges, and the hot Arkansas Valley. Surface temperatures from both sources were substantially warmer than the observed air temperatures at this time, but energy balance values were generally still warmer than satellite values.

By 13 MST the energy balance-based temperatures (Fig. 5.16) had been strongly influenced by wind speed variations. Temperatures were particularly high in the upper river valleys. Interestingly, the wind speed effects resulted in a gradient between the Arkansas Valley and the Palmer Divide that was similar to the observed air temperature gradient. It appears that this was a fortuitous coincidence since the observed winds over the Arkansas Valley were far from calm (Fig. 5.5d). The time-extrapolated retrieval field contained the same major features as the 10 MST field, but they were distorted somewhat since energy balance computations did not result in the same time change at every grid point. As expected, the correspondence between satellite-based values and surface observations decreased from

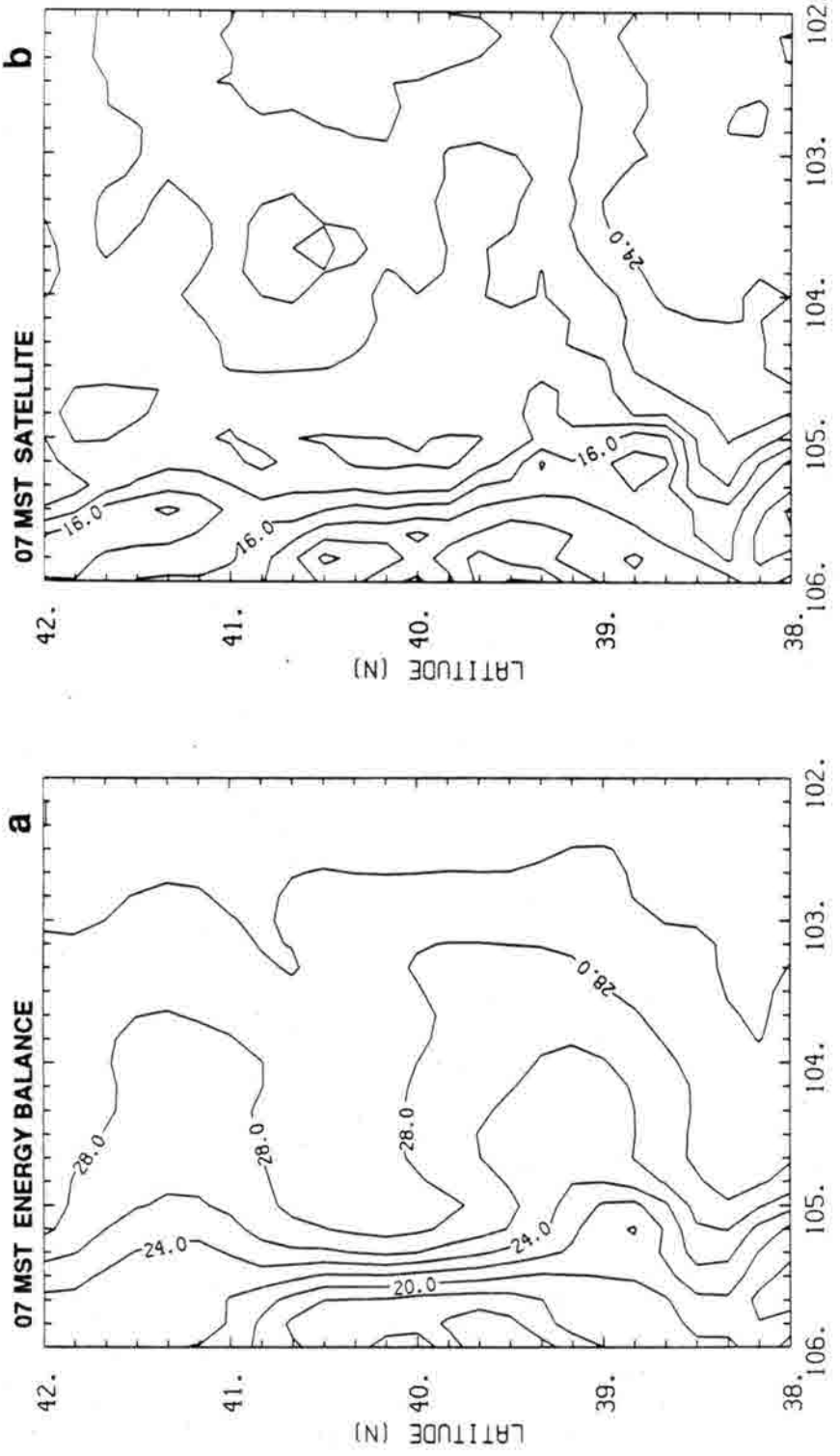

Figure 5.14 As in Fig. 5.13, but at 07 MST.

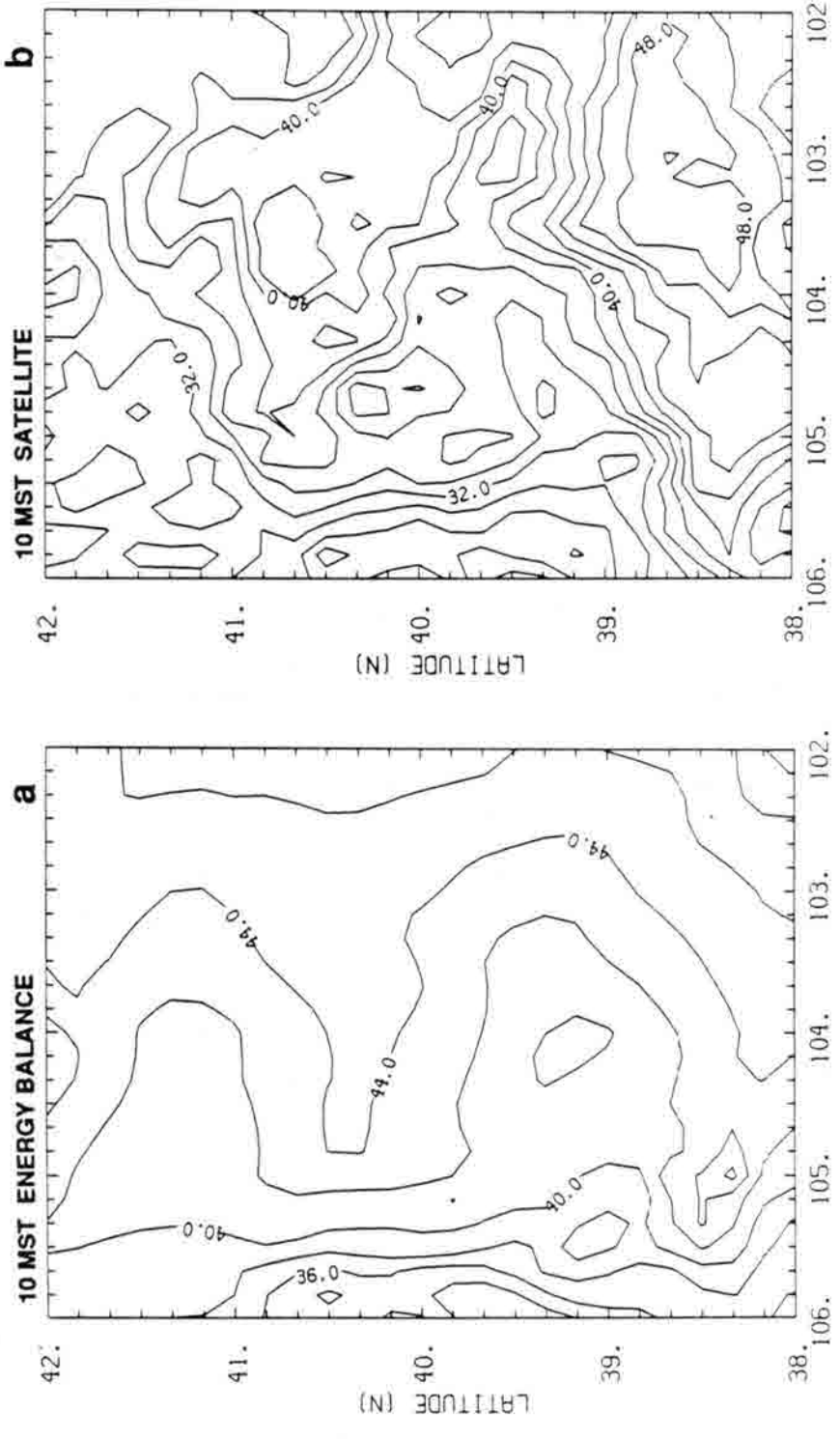

Figure 5.15 **As in Fig. 5.13, but at 10 MST.**

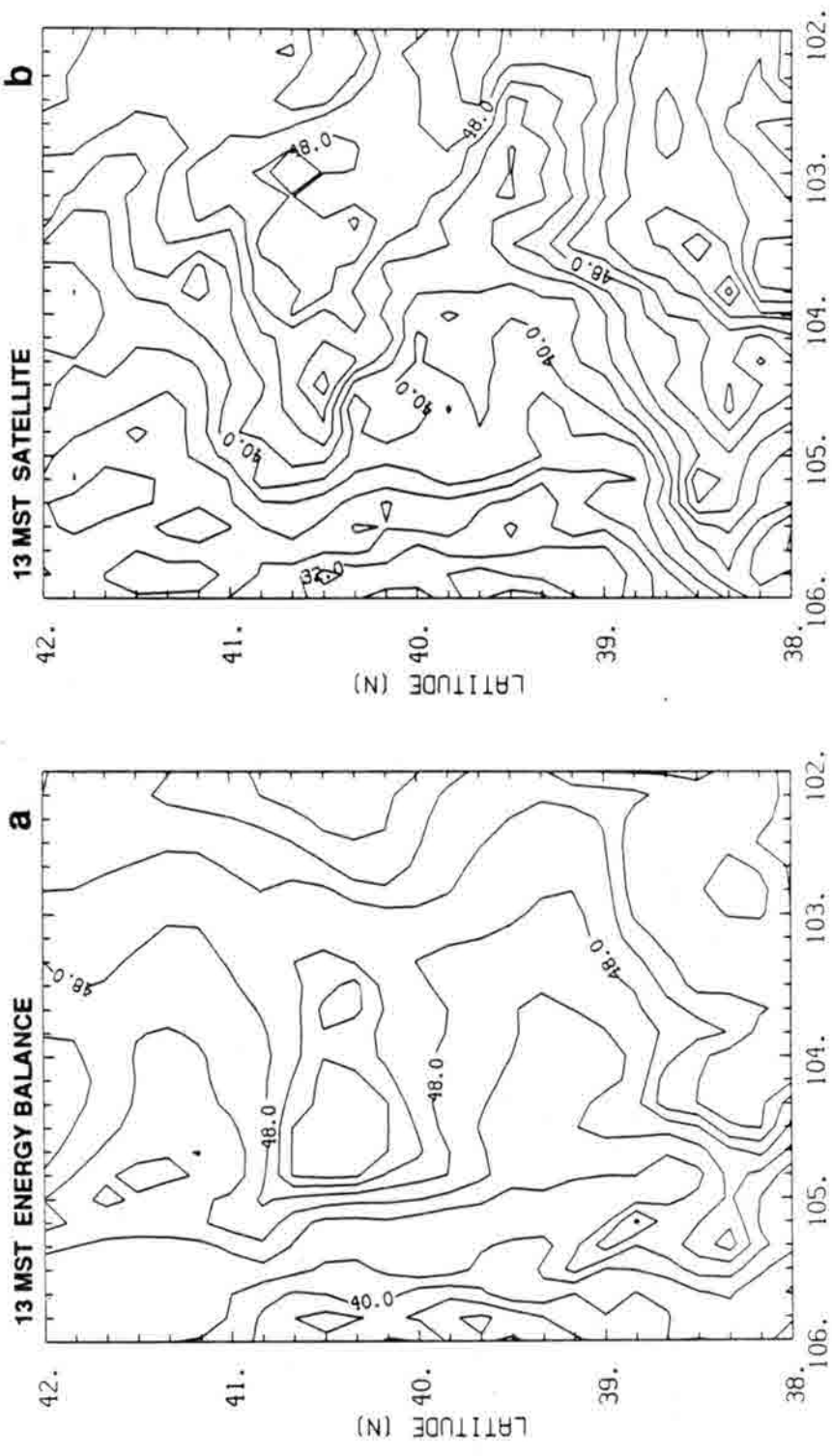

Figure 5.16 **As in Fig. 5.13, but at 13 MST. The satellite-based values are extrapolations from 10 MST.**

10 to 13 MST. The observations reflected the influence of convective cloud development, which the extrapolated values did not account for.

The surface observations were also compared with air temperatures from the model's lowest grid level for thermodynamic parameters. The height offset was large (2 m versus 15 m), but it is implicit in the model's surface-layer parameterization that the temperature at 2 m is somewhere between the surface and 15-m values. Temperatures at heights within the surface layer cannot be directly retrieved, in general, since the formulation includes empirical adjustments that are not valid very near the ground.

At 04 MST the temperatures from the energy balance and satellite-based runs were very similar (Fig. 5.17). They tended to be warmer than the surface observations, which is reasonable given that a thermal inversion was present. The satellite-based data field had relatively cool values from the South Platte Valley northward and had a weaker gradient along the mountain slopes than the energy balance field. Both fields had a cool tongue extending northeast from the upper Palmer Divide and a warm band close to the central mountains. These features were likely caused by the interaction of nocturnal drainage flow with a mountain wave forced by the westerlies aloft (see Appendix B). The features were not present in the 04 MST surface observations, but at 07 MST they appeared strongly in the surface observations and the satellite-based results and weakly in the energy balance-based results (Fig. 5.18). The satellite-derived field also contained a north to south gradient in the eastern region at 07 MST that was roughly consistent with the observations. Given that the 0- to 15-m modeled layer was about isothermal at this time, there should be little temperature bias between the model values and the observed values. The energy balance values were about 2–8°C too warm and the satellite values were generally within about 2°C of the surface observations.

At 10 MST the satellite-derived 15-m temperatures (Fig. 5.19) corresponded very closely with the surface observations, although the series of warm, cool, and warm spots did not penetrate to the this level despite the forcing from the ground surface. Given that the temperature lapse rate was strong, the satellite values were too warm for an ideal match. The energy balance values were about 2–6°C warmer yet, with particularly large discrepancies in the northern region. The two model fields had about the same gradient between the upper

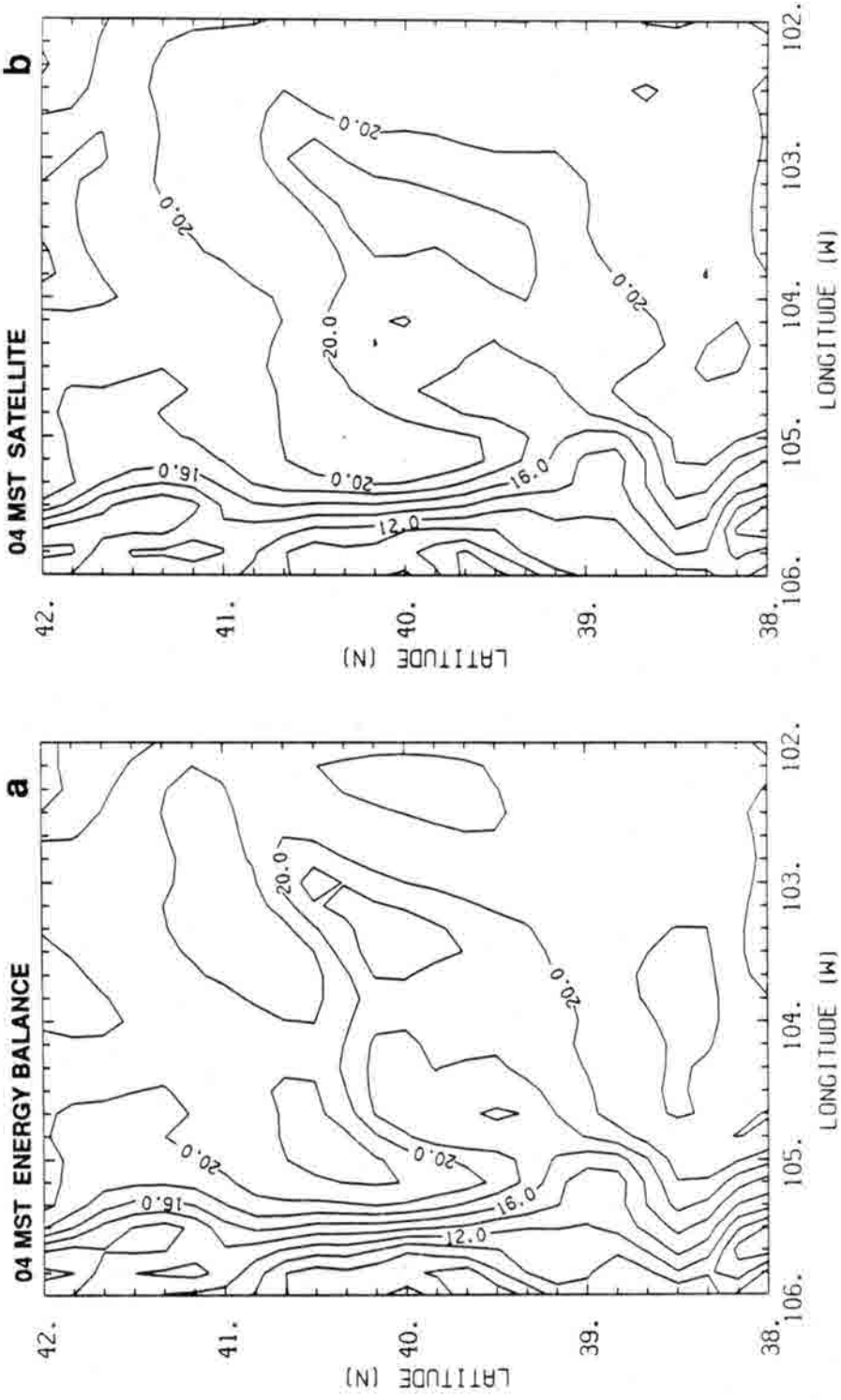

Figure 5.17 Air temperatures at 15 m above ground at 04 MST from the two model runs with coupled water vapor analyses: a) energy balance-based and b) satellite retrieval-based ground surface temperatures. Contours are at 2°C intervals.

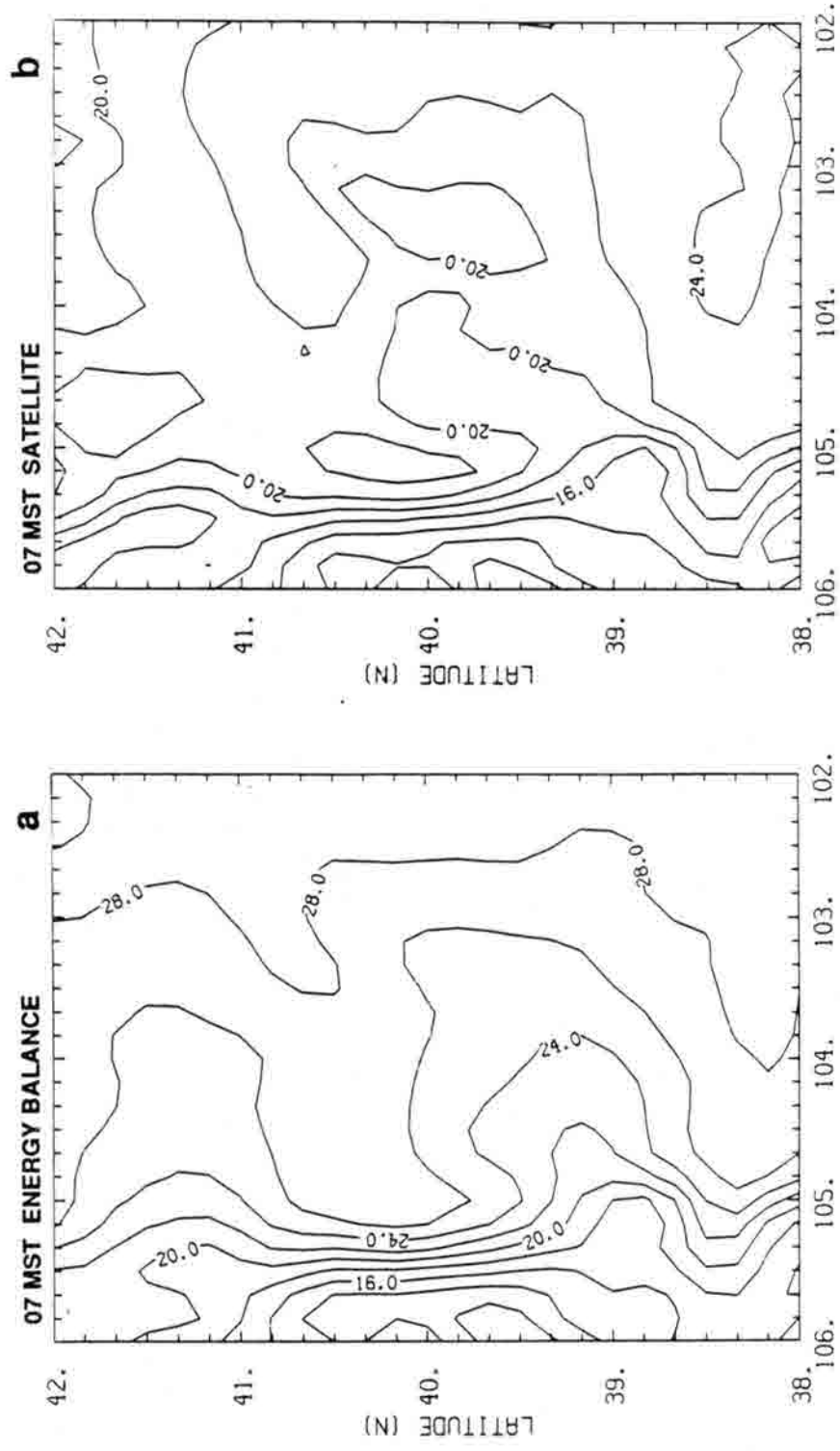

Figure 5.18 As in Fig. 5.17, but at 07 MST.

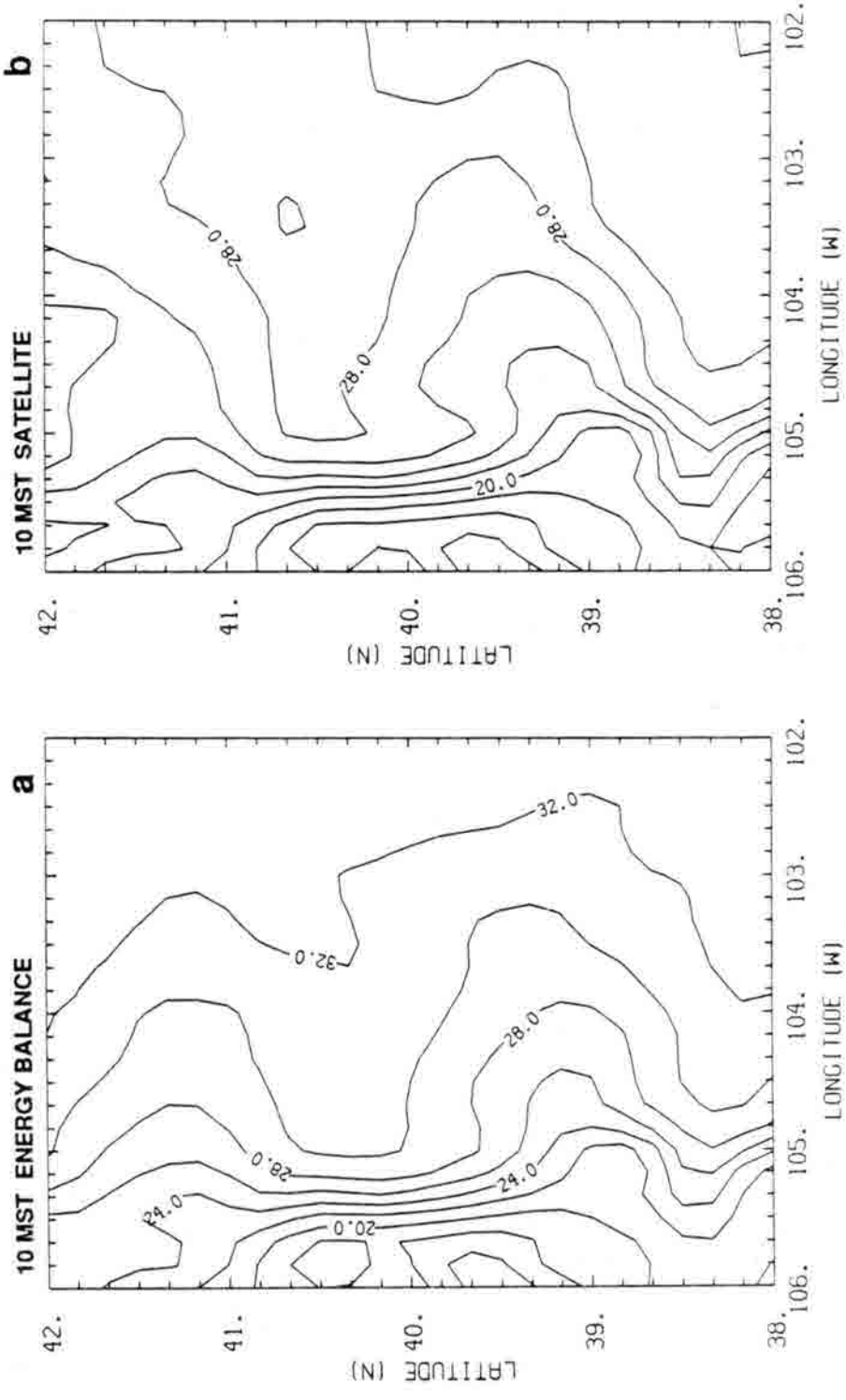

Figure 5.19 As in Fig. 5.17, but at 10 MST.

Palmer Divide and the southeast corner, but it was more compact in the satellite-based field.

In general the satellite retrievals appeared to provide more realistic surface temperatures than the energy balance computations. The match of satellite-derived gradients with observed gradients lends strong support to the value of the retrievals, but the lack of large biases is not particularly significant. For example, the satellite-based air temperatures would have been warmer at 10 MST had it been possible to use the final 10 MST retrievals instead of preliminary values in the 07 to 10 MST spline (see Fig. 5.12). In addition, retrieved surface temperatures are somewhat sensitive to the estimate of the spectral surface emittance, which is subject to estimation errors.

5.3.4 Wind Results

Modeled and observed winds were readily compared. The lowest wind level in the model was at a 10-m height, about the same as the surface observations.

At 04 MST winds in the two model runs were very similar to each other (Fig. 5.20). The 10-m modeled winds generally followed the pattern of the surface observations, but there were significant differences. The modeled winds were stronger over the plains, with speed maxima on the lee side of the Palmer and Cheyenne ridges that were not supported by observations. The observed region of southwesterly drainage flow was reproduced by the model, but over a smaller region than observed. Above the surface the winds generally were weaker, except for a jet of northwesterlies centered about 400 m above the high plains (Fig. 5.21). A weaker version of this feature was present in the Denver radiosonde report from one hour later (Fig. 5.3a). The evolution of the modeled jet is discussed further in Appendix B.

By 07 MST there was an important difference between the two modeled wind fields (Fig. 5.22). The energy balance-based winds no longer included a zone of southwesterly drainage, but the feature persisted in both the satellite-based results and the observations (Fig. 5.5b). Over much of the domain the satellite-based winds were slightly stronger and more westerly than the energy balanced-based values. This is consistent with the cooler surface temperatures and consequent weaker boundary layer mixing. Both model fields

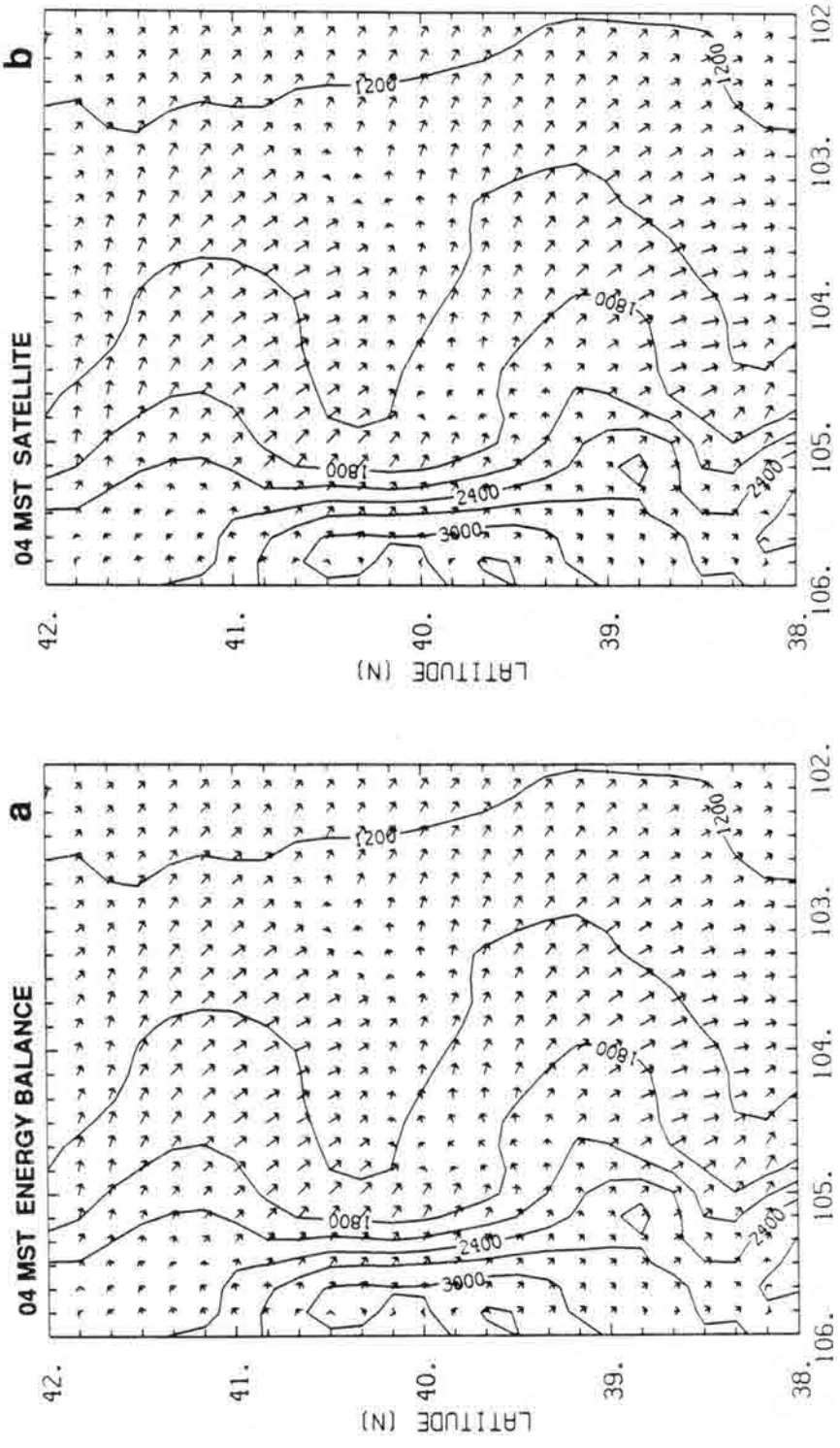

Figure 5.20 Horizontal winds at 10 m above ground at 04 MST from the two model runs with coupled water vapor analyses: a) energy balanced-based and b) satellite retrieval-based ground surface temperatures. Vector scaling is as in Fig. 5.5.

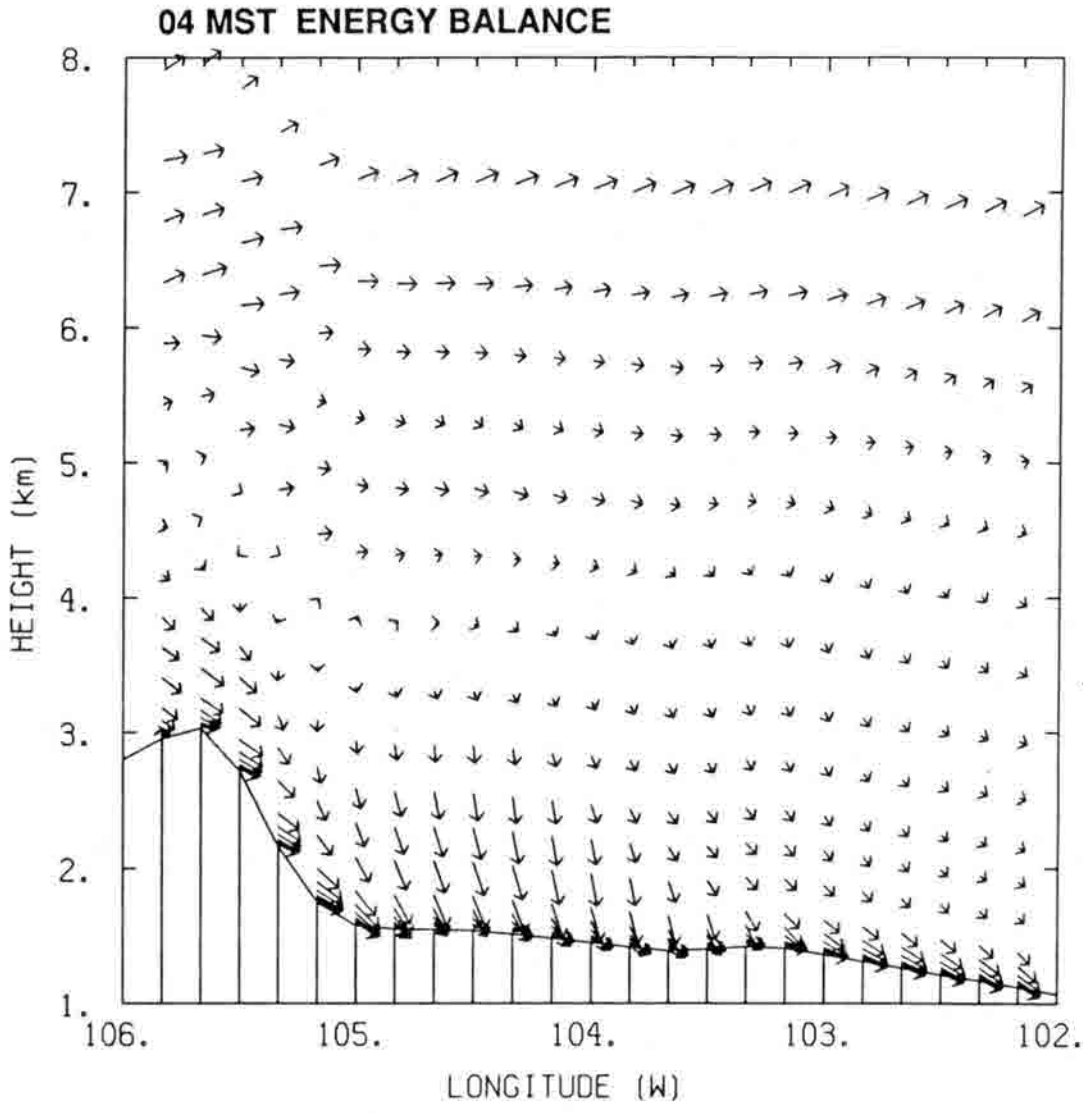

Figure 5.21 An east/west cross section through 40°N of horizontal winds at 04 MST from the model run with coupled water vapor analysis and energy balanced-based surface temperatures (vectors were very similar in the run with satellite-based surface temperatures). Vector scaling is as in Fig. 5.5.

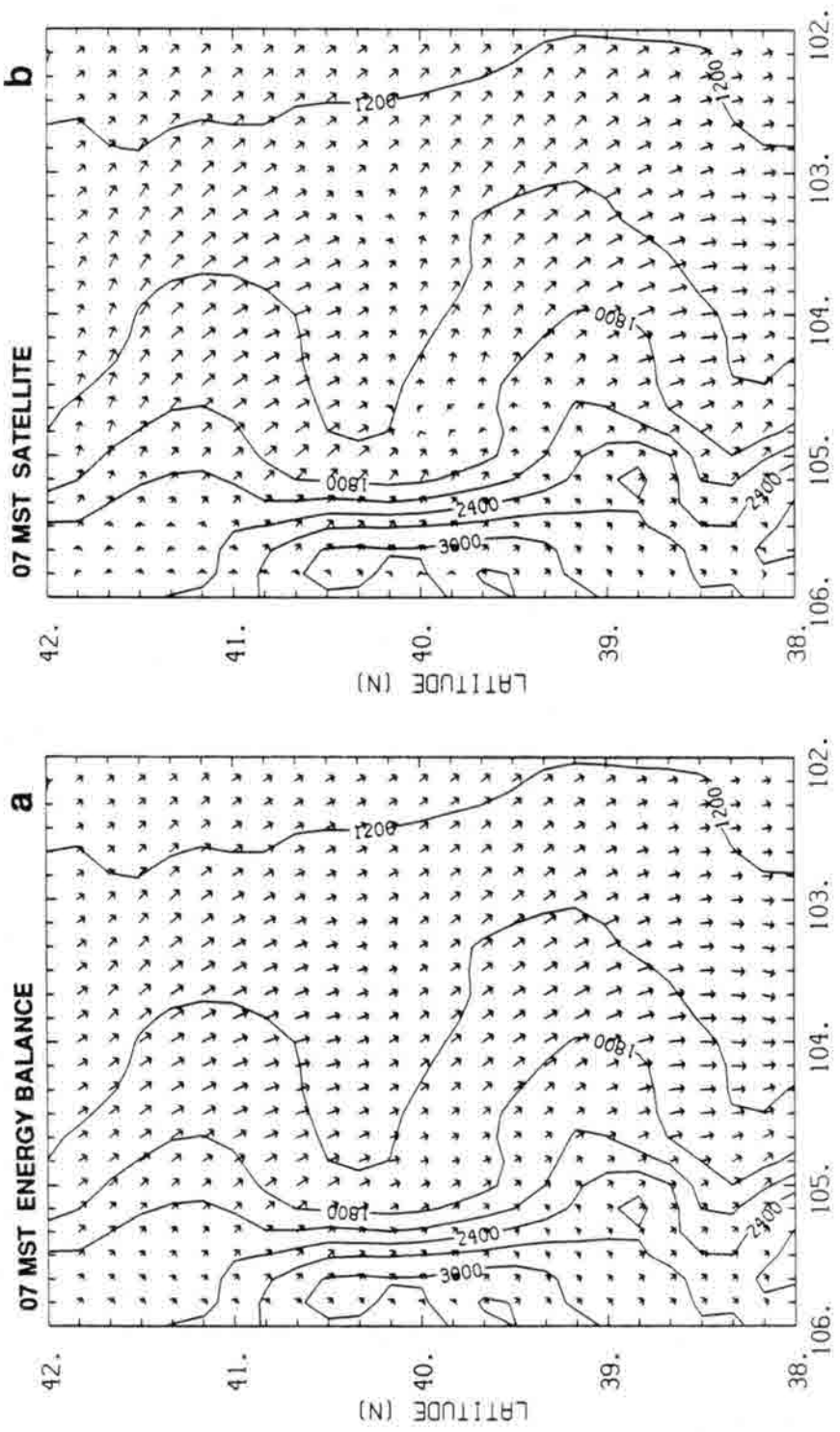

Figure 5.22 As in Fig. 5.20, but at 07 MST.

agreed well with the observations over the eastern plains in both direction and speed. There was an exception in the Arkansas Valley, where the direction was off by about 90°. This discrepancy probably resulted in part from the model's limited domain. The Raton Mesa, which is just south of the Arkansas River, could be expected to divert the flow eastward as did the Palmer and Cheyenne ridges.

The low-level winds were strongest just above the surface at 07 MST. At the 250-m level the flow was north-northwesterly at about 10 m/s over much of the domain (Fig. 5.23), with the satellite-based winds being slightly stronger.

The 250-m vertical velocities at 07 MST were dominated by the interaction of the horizontal background flow with the terrain (Fig. 5.24). The lee side downslope sinking was stronger in the satellite-based run, but the patterns of rising and sinking were very similar.

By 10 MST the modeled 10-m winds had turned to upslope east of the continental divide (Fig. 5.25). The rotation was not as great as in the observations (Fig. 5.5c), which included stations with a southerly component. In addition, easterly components were present over a wider area in the observations. Both model runs included a mountain/valley breeze front on the eastern slope of the continental divide, but it occurred at a lower elevation and was weaker in the satellite-based run. Over the plains the satellite-based winds were stronger, and both fields matched well with most of the observations. There were not enough observing stations to verify the model fields' speed maxima along the Cheyenne and Palmer ridges.

As the modeled boundary layers grew, differences in surface forcing affected flow at successively higher levels. At 10 MST both runs included north-northwesterlies at 500 m (Fig. 5.26), but the satellite-based winds were the stronger of the two. There was also a difference in the position of the mountain/valley convergence line at that level.

The vertical velocities were far more sensitive than horizontal winds to the surface temperature differences (Fig. 5.27). In the energy balance-based results at 10 MST there was strong rising at 500 m just east of the mountain peaks and compensating sinking further eastward. In the satellite-based results the mountain circulations were much weaker and there was still evidence of lee-side downsloping. The satellite-based velocities were relatively strong over the plains, with upward motion downwind of the surface hot spots. The effect

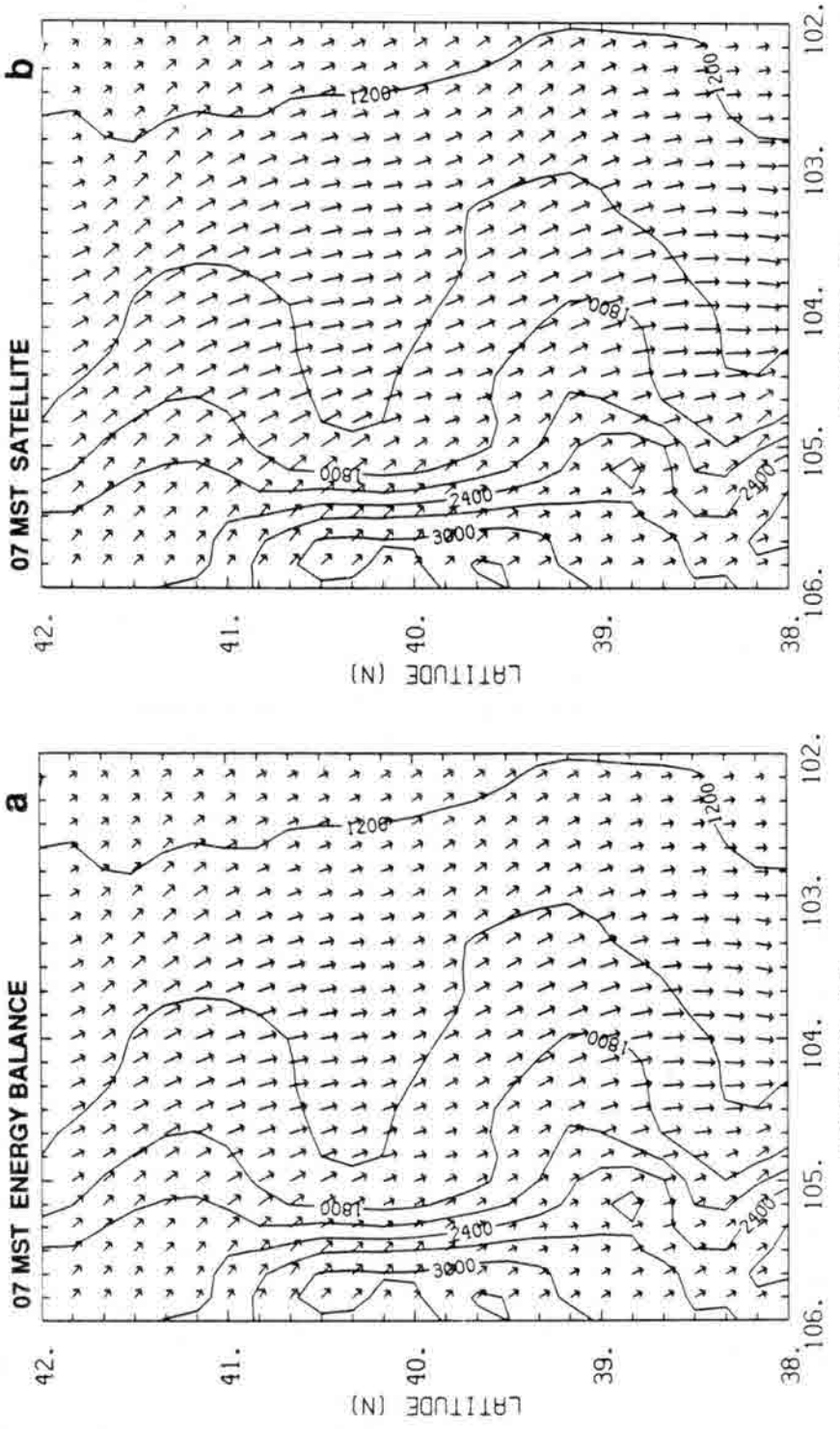

Figure 5.23 Horizontal winds, as in Fig. 5.20, but at 250 m above ground and at 07 MST.

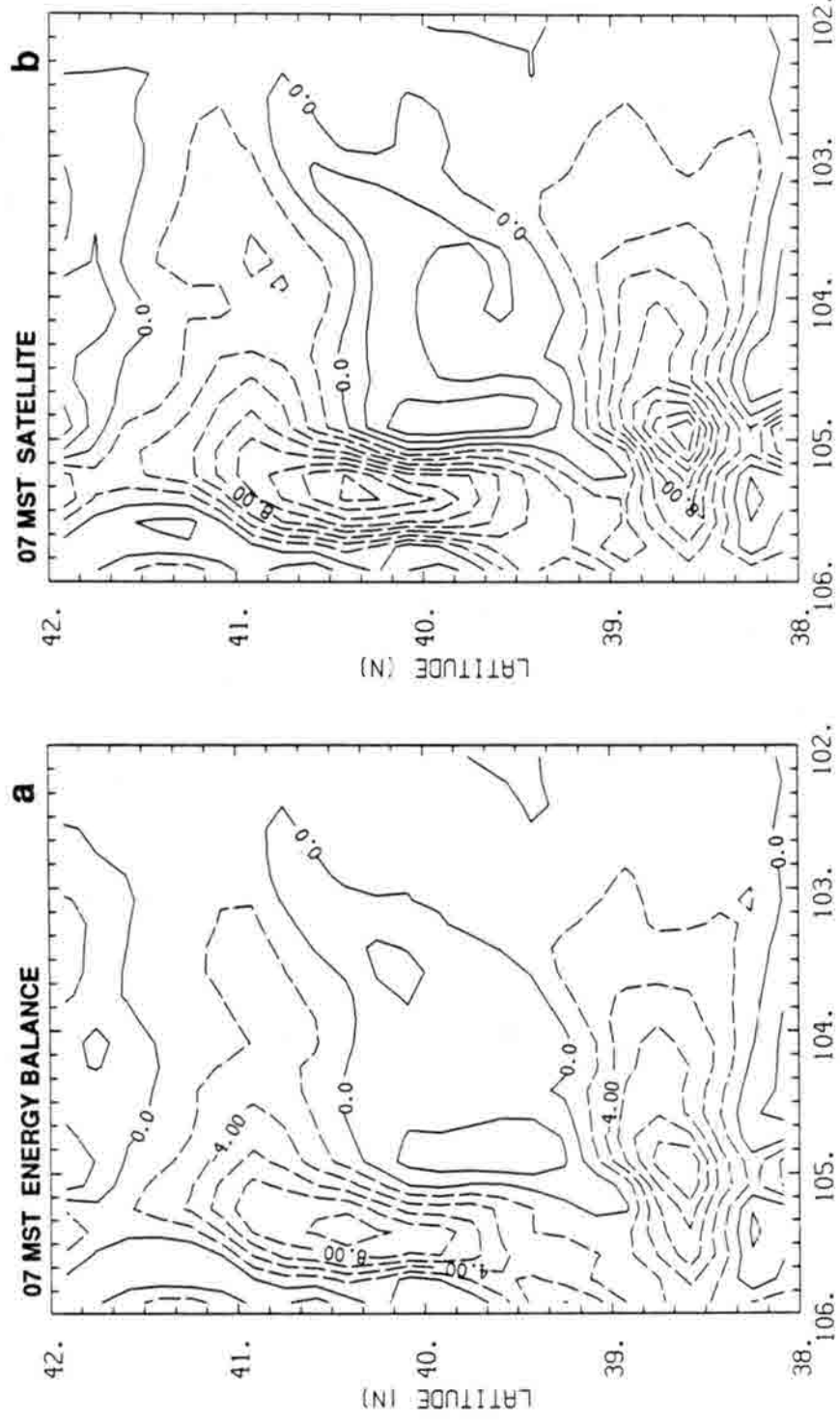

Figure 5.24 Vertical velocities at 250 m above ground at 07 MST from the a) energy balance-based and b) satellite retrieval-based model runs. Contours are at 2-cm/s intervals.

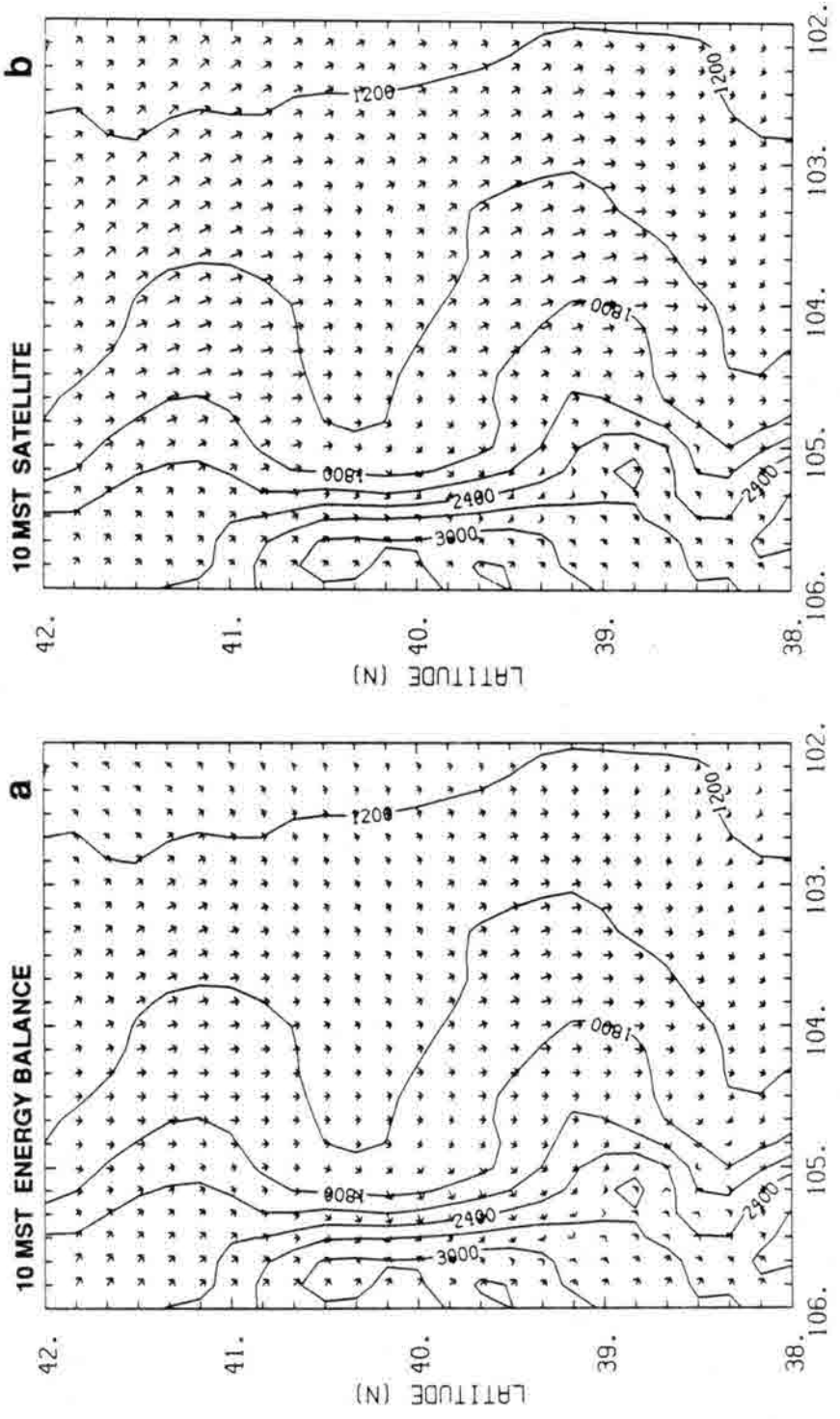

Figure 5.25 As in Fig. 5.20, but at 10 MST.

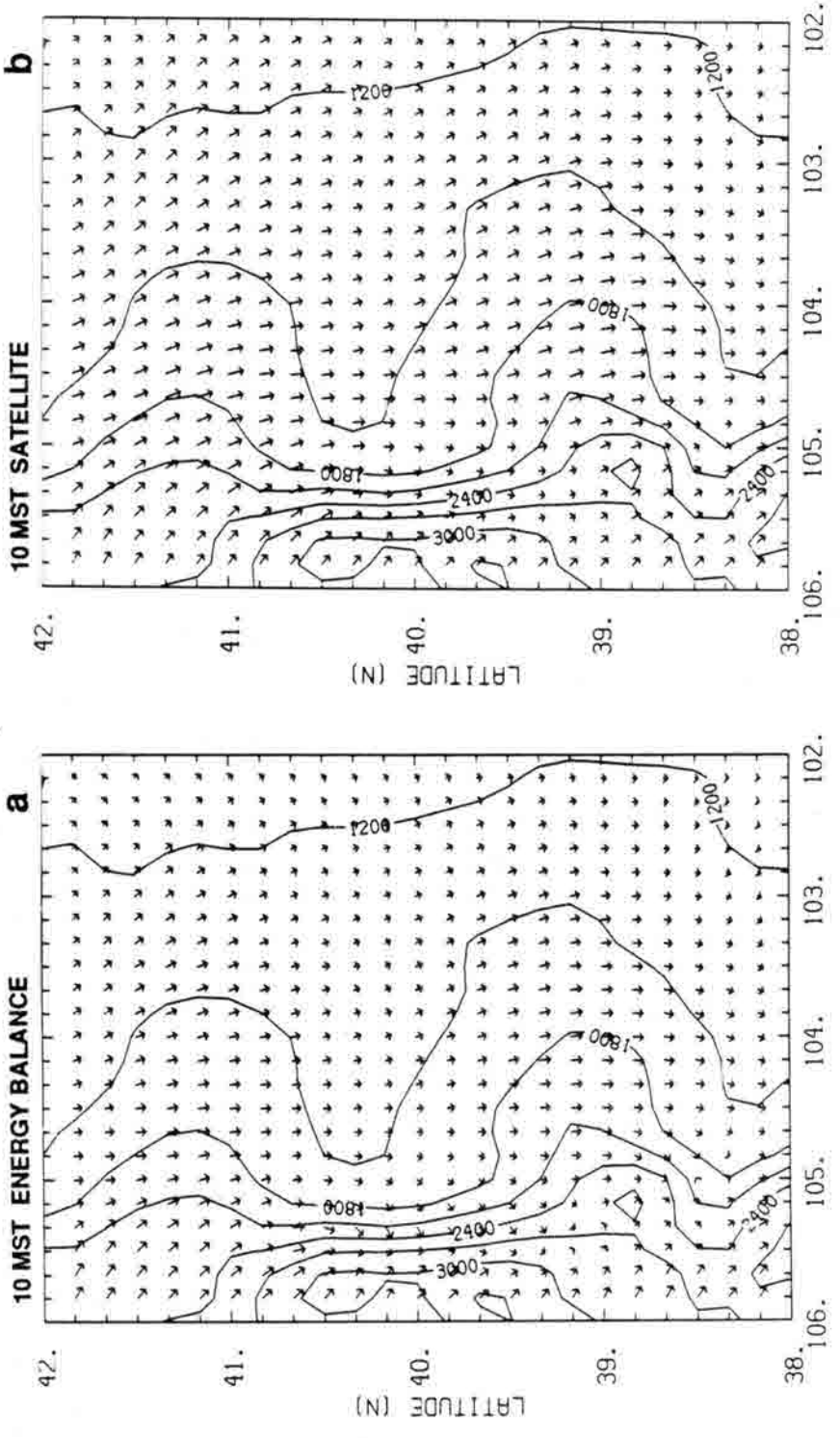

Figure 5.26 Horizontal winds, as in Fig. 5.20, but at 500 m above ground and at 10 MST.

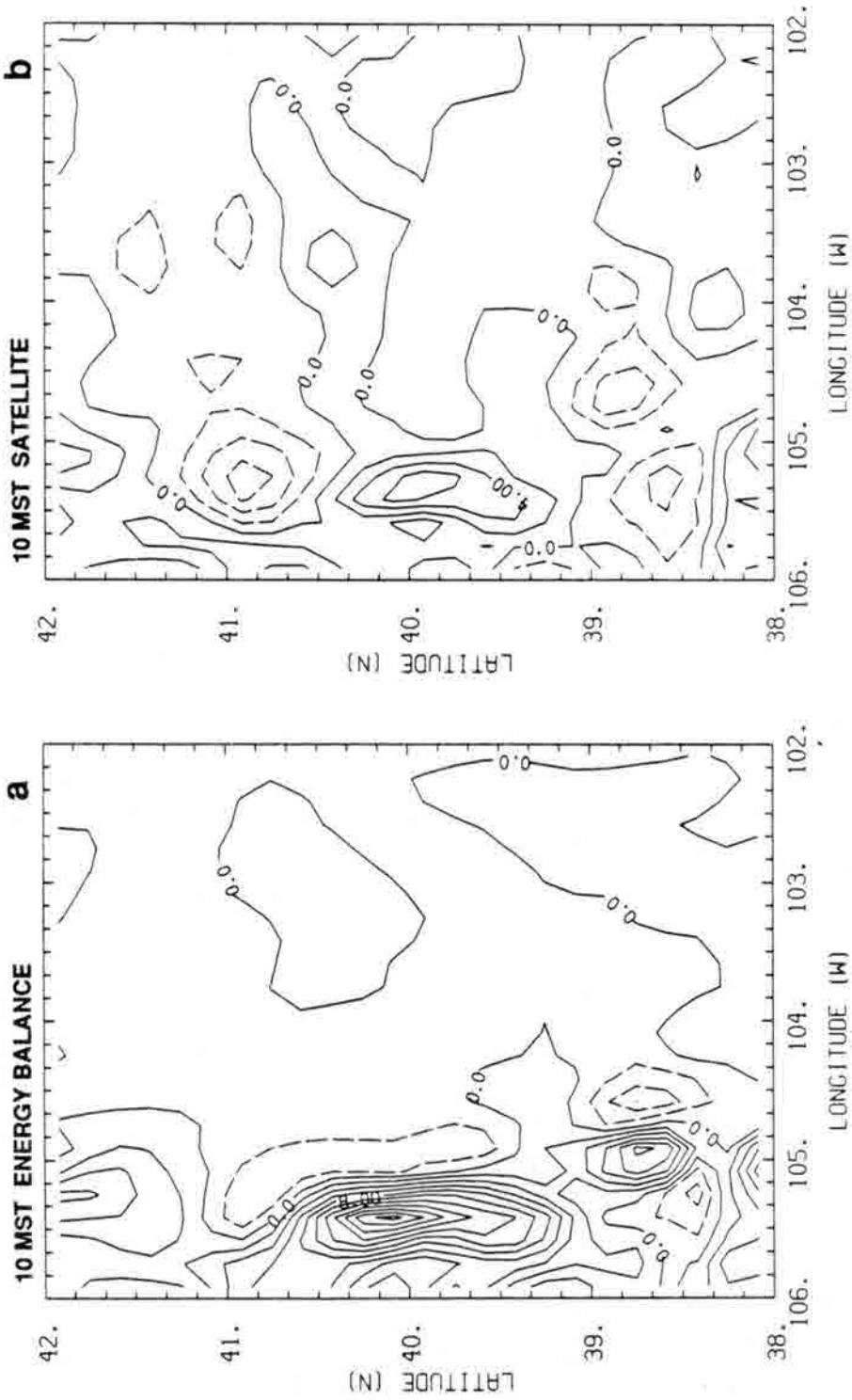

Figure 5.27 Vertical velocities, as in Fig. 5.24, but at 500 m above ground and at 10 MST.

of surface temperature features is clear in the vertical motion differences between the two runs (Fig. 5.28).

At 13 MST the local influences on modeled low-level winds were obvious (Fig. 5.29). Both model fields included easterlies on the primary mountain slope that matched the observations well. However, the eastward extent of the easterlies was not nearly as great in the model fields as in the observations. There was a particularly large discrepancy along the southern Cheyenne Ridge where the satellite-based winds were northerly and the observed winds were southeasterly. The two model fields were very different in the Arkansas Valley region. There was strong convergence in the satellite-based winds over the hot surface, including southerlies along the southern border where the observed wind (station LHX) was in the opposite direction. This difference suggests that the extrapolation of satellite-retrieved surface temperatures may have resulted in an over-estimation of gradients. It is also likely that cloud development had a substantial impact on the observed winds.

The vertical winds accelerated greatly in the hours leading up to 13 MST (Fig. 5.30). The energy balance-based velocities were strongly positive over the eastern mountain slopes and relatively weak elsewhere. A noticeable feature is the slot of sinking air east of the mountains, where there was a clear zone in the satellite imagery. The satellite-based velocities were strongly upward over the mountains and over the hottest regions of the plains. There was sinking east of the mountains and over the tongue of cool ground on the eastern Palmer Ridge (see Fig. 5.16).

It had been expected that surface conditions would have a substantial impact on modeled circulations (e.g. Segal, *et al.*, 1988a) and that was true in the satellite/energy balance comparisons. Nevertheless, the comparisons of modeled and observed winds throughout the morning do not lead to any strong conclusions about the relative accuracy of the two methods of determining ground surface temperatures. Some of the modeled/observed differences suggest that the background geostrophic northwesterlies at low levels may have been over-estimated.

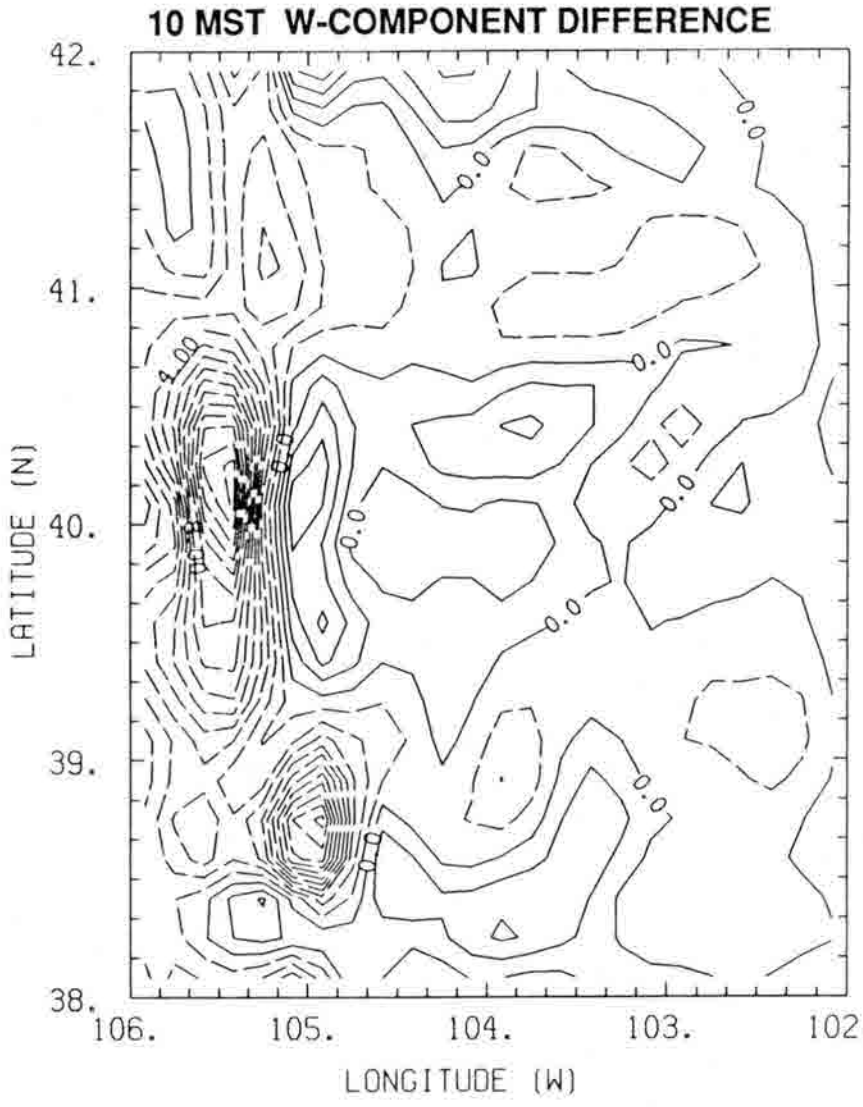

Figure 5.28 Vertical velocity differences at 500 m above ground at 10 MST from the two model runs: satellite-based run minus energy balance-based run. Contours are at intervals of 1 cm/s.

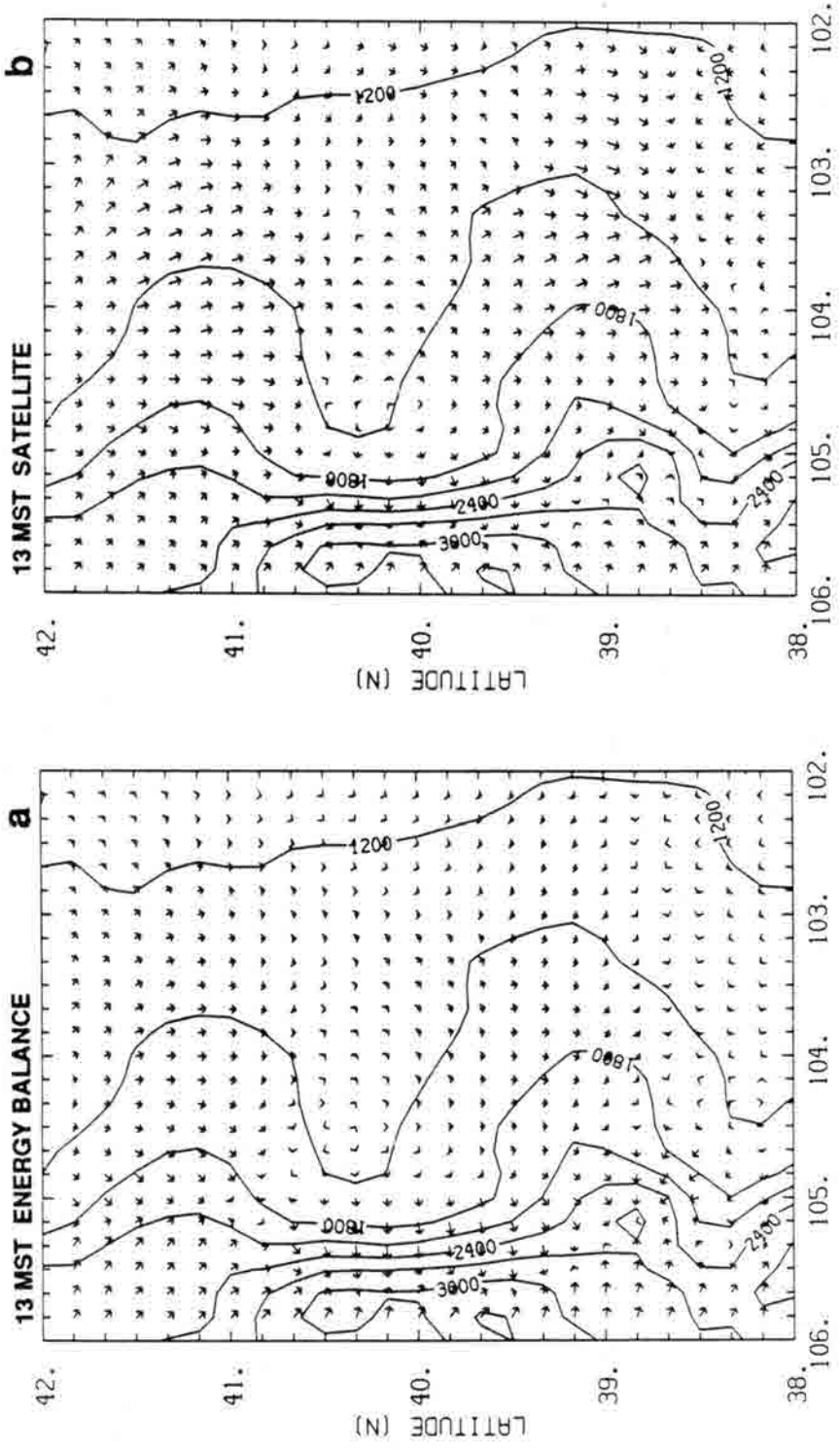

Figure 5.29 As in Fig. 5.20, but at 13 MST.

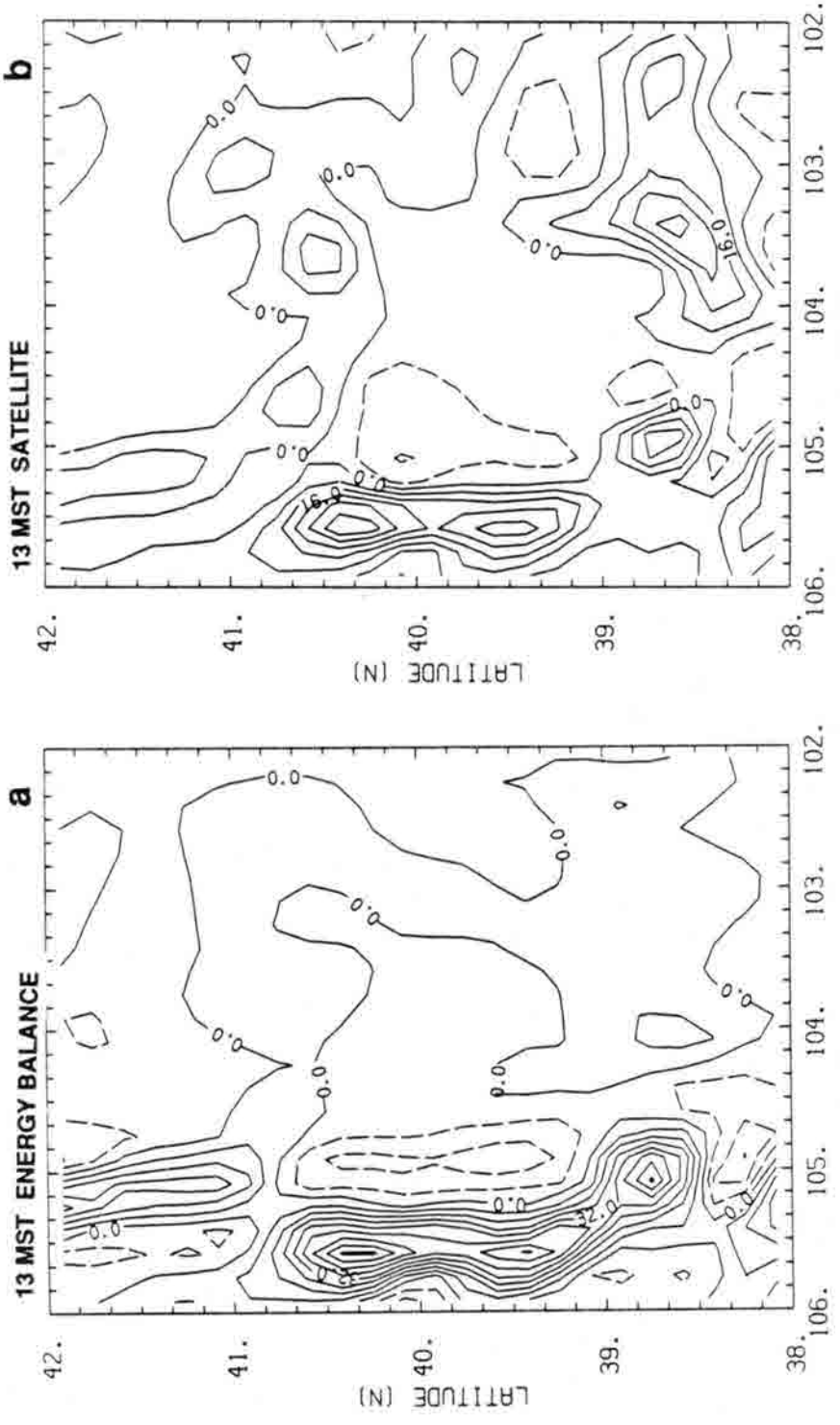

Figure 5.30 Vertical velocities at 1350 m above ground at 13 MST from the a) energy balanced-based and b) satellite retrieval-based model runs. Contours are at 8-cm/s intervals.

5.4 Water Vapor Analyses

Several water vapor analyses were intercompared in detail to evaluate the relative strengths and weaknesses of the various analysis methods. A secondary purpose of the analyses was to verify modeled winds. Errors in advecting winds were one possible cause of discrepancies whenever satellite-retrieved water vapor changes disagreed with model-simulated changes.

5.4.1 Conventional Results

The first task was to prepare the best possible three-dimensional gridded analyses based solely on conventional (*in situ*) data. Analyses were made at 04, 07 and 10 MST. For each surface observation (Fig. 5.4a-c) the 05 MST Denver radiosonde profile of dewpoint temperature was altered so that it would match the observed value at the level of the station's surface pressure. For stations lower than the 84-kPa level the radiosonde profile was extrapolated before adjustment. The adjustment decreased linearly from the surface up to about 61 kPa (about 4400 m elevation). The adjusted profiles were extrapolated downward to facilitate horizontal interpolation to a grid with varying surface elevations. The Lipton and Hillger (1982) method was used for horizontal interpolation, and then the values were linearly interpolated to the model's vertical grid levels. Surface observations that were considered to be non-representative (including all the mountain station reports) were eliminated from this procedure. The gridded surface (10-m level) mixing ratio analyses are presented in Fig. 5.31.

5.4.2 Stand-Alone Retrieval Results

The conventional water vapor analyses were used as initial guess data for the stand-alone retrievals. The 05 MST Denver temperature sounding, with the surface inversion removed, was the temperature initial guess at all sounding locations at each of the three analysis times. The initial guess field was adjusted throughout the analysis domain, regardless of cloud coverage, based on the cloud-free fields of view.

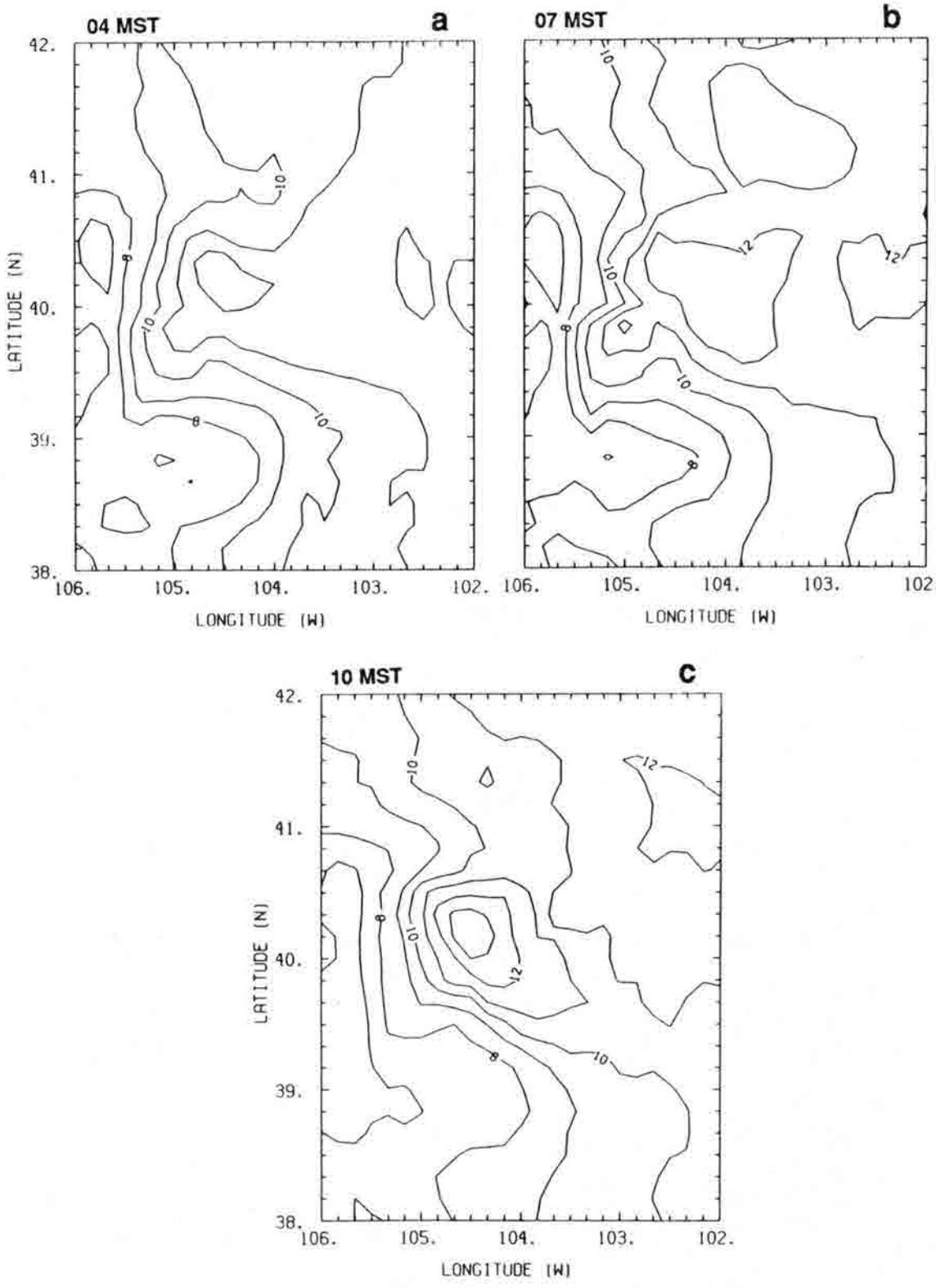

Figure 5.31 Mixing ratios at 10 m above the ground from the analysis of conventional data for a) 04, b) 07, and c) 10 MST. Contours are at 1-g/kg intervals.

The 04 MST stand-alone surface analysis, in Fig. 5.32, is much different from the conventional analysis. A prominent feature is a band of very high mixing ratios cutting across the domain from the south to the northeast. At mid-levels (about 5 km) the southeast corner of the domain is relatively moist, as revealed by the cross-sections. This feature shows up clearly in the image from VAS channel 10 at 0430 MST (Fig. 5.33).

There are several reasons to believe that the low-level water vapor retrievals at 04 MST are not reliable. First, the conventional/stand-alone analysis differences are larger than would be expected solely on the basis of differences in data source and coverage. Second, in the very moist regions the retrievals produced temperature profiles that were unrealistic; they had diverged from accurate initial guesses through the iterative process in response to increasing low-level moisture. Third, the features in the 04 MST analysis are not consistent with features in the 07 and 10 MST analyses.

The likely cause of the poor results is the ill-posedness of the water vapor retrieval problem under the circumstances present at 04 MST. The average lapse rate of the lower troposphere was very small due to a surface-based inversion. When the lapse rate is small the radiances detected by satellite sounders become insensitive to changes in water vapor concentrations. Retrievals based on the radiances are unstable, such that small errors in estimates of atmospheric transmittances or surface emittances can have a large impact on retrieved concentrations. Undetected clouds may have also been a culprit, but they could not have been the sole cause of the differences. According to results of radiative transfer computations clouds could not have lead to the water vapor increases without having an obvious impact on surface temperature retrievals.

The 07 MST stand-alone analysis (Fig. 5.34) is similar to the conventional analysis at the surface. The most notable difference is that the retrievals indicated the northern plains region was relatively moist. The cross-sections show this to be a shallow feature. There is also a dry spot (<10 g/kg) on the Northeastern Palmer Divide.

The 10 MST analysis (Fig. 5.35) is consistent with the conventional data in indicating that the upper South Platte Valley was relatively moist, but it has increasing moisture toward the northeast. The retrievals implied higher mixing ratios than the observations

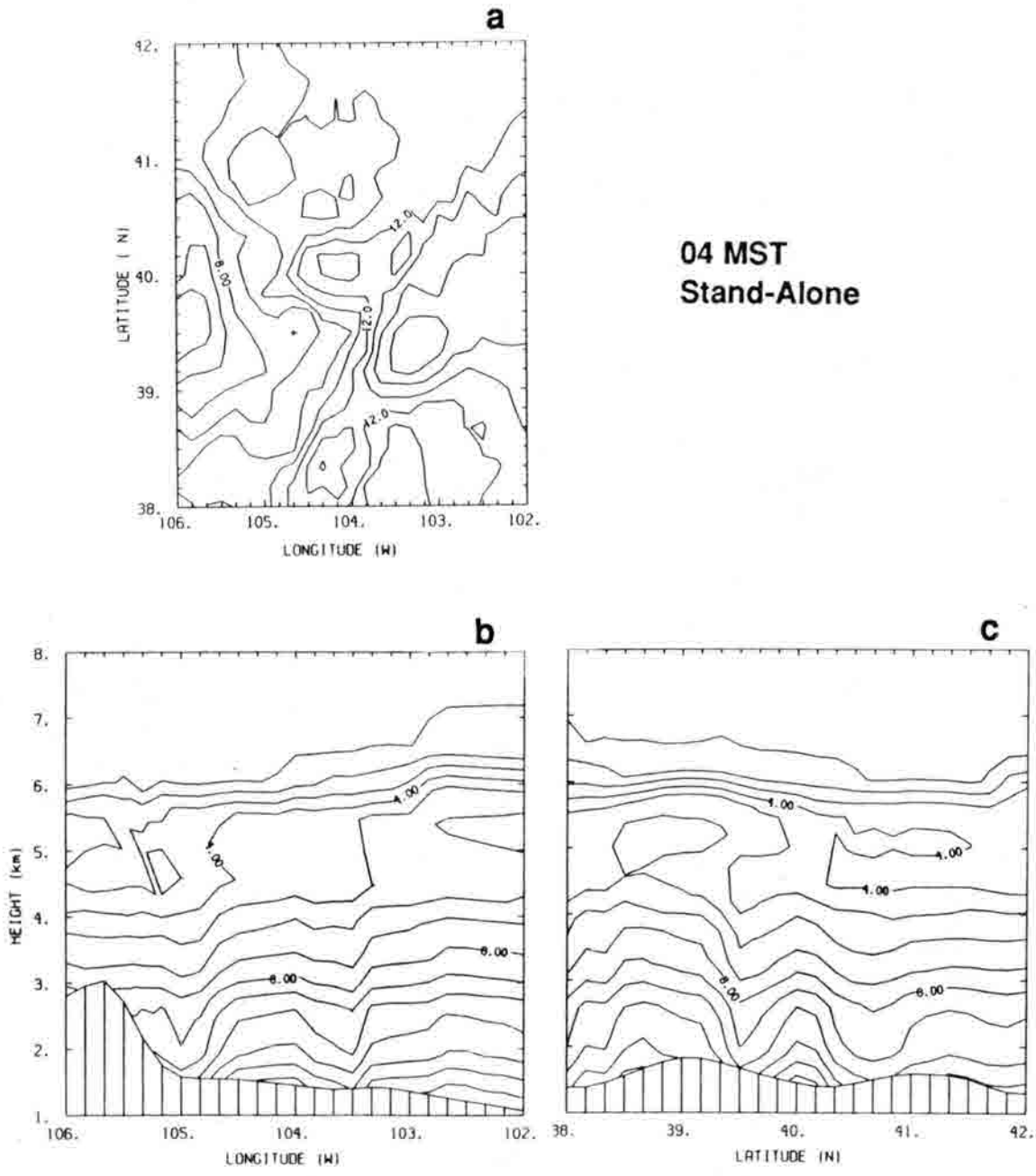

Figure 5.32 Mixing ratios at 04 MST from the stand-alone analysis: a) at 10 m above the ground, b) cross-section along 40°N, c) cross-section along 104°W. Contours are at 1-g/kg intervals.

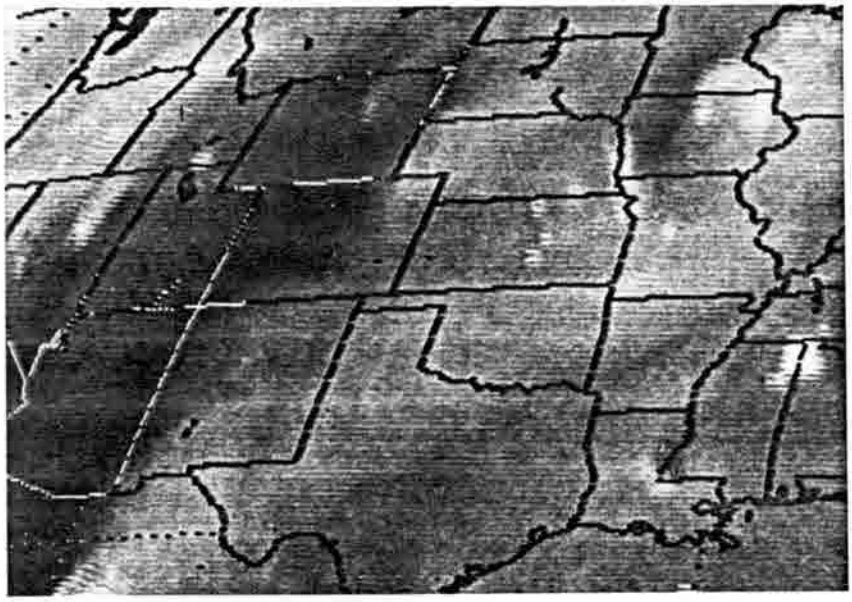

Figure 5.33 The GOES-5 water vapor channel (channel 10) image from 0430 MST 21 Aug 1983. State boundaries are denoted by dotted lines.

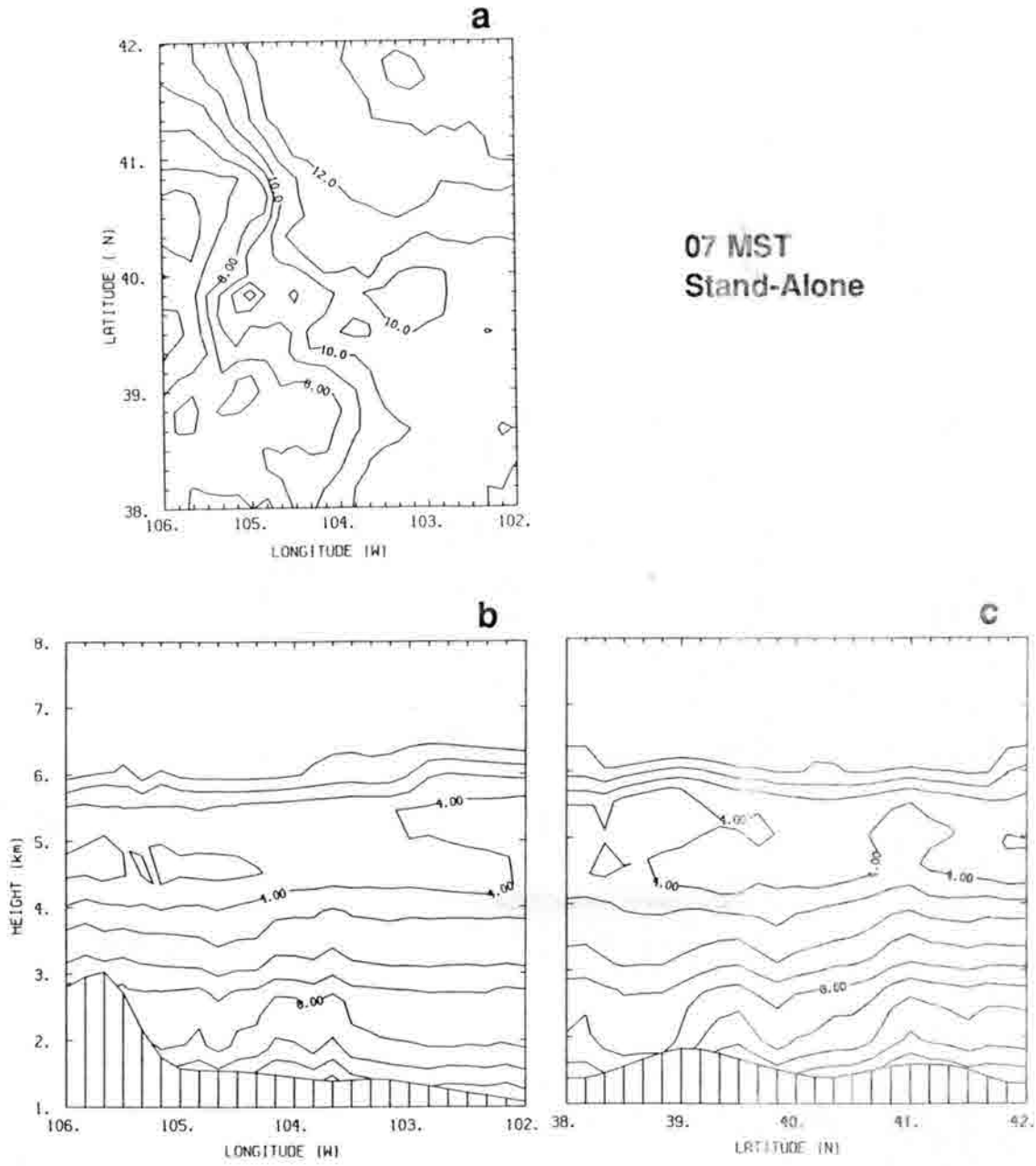

Figure 5.34 As in Fig. 5.32, but at 07 MST.

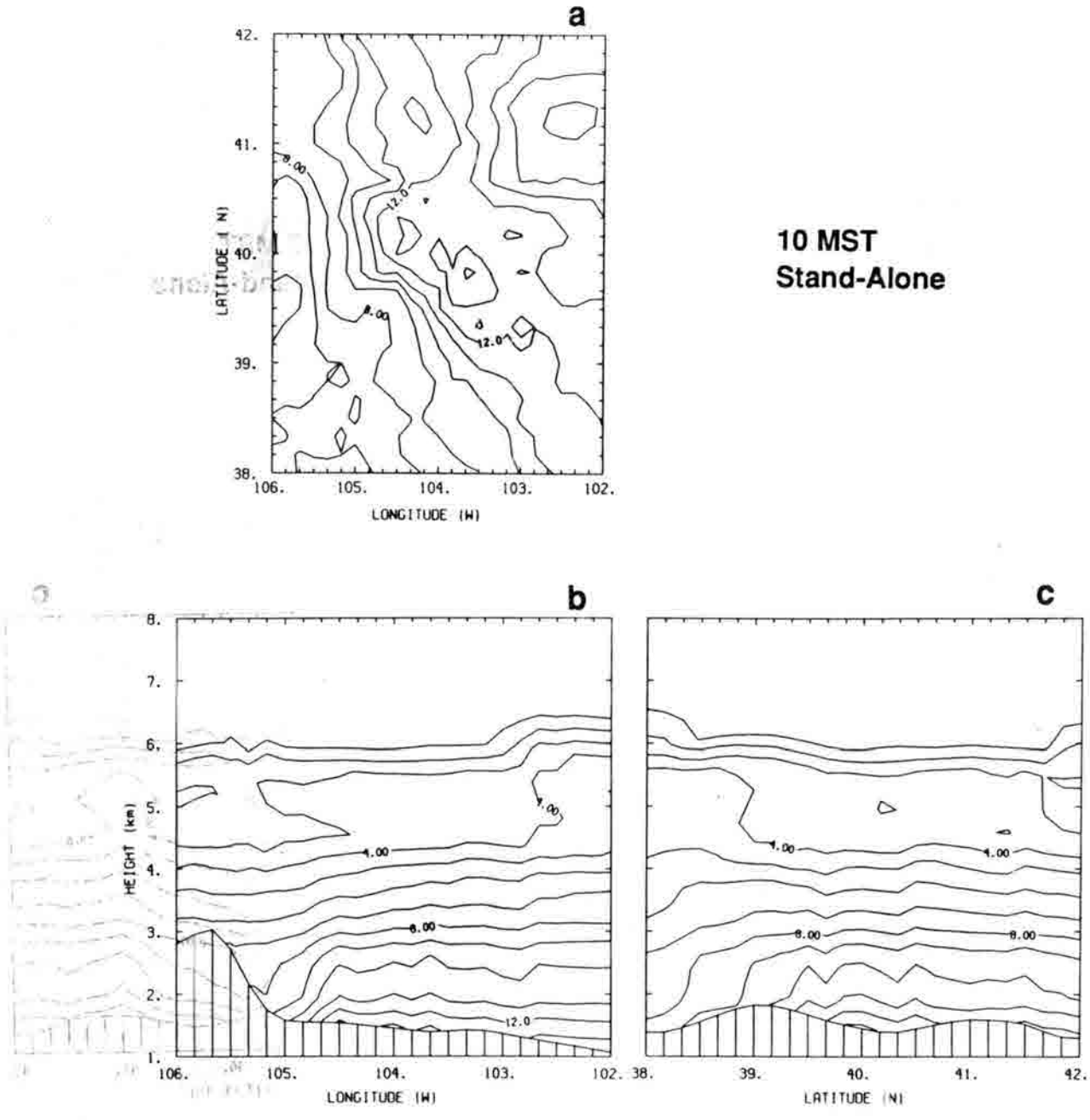

Figure 5.35 As in Fig. 5.32, but at 10 MST.

over most of the plains. The cross-sections indicate a relatively uniform vertical gradient throughout the lower troposphere and an eastward propagation of the mid-level moist region.

5.4.3 Initialized Model Run Results

For this analysis, the initial guesses for the 04 MST retrievals were composed of model values of air and ground temperatures and the conventional 04 MST water vapor analysis. Only one analysis sequence was done, using the energy balance-based model. There was little value in doing a second sequence with satellite retrieval-based surface temperature input, given that the initializing water vapor retrievals were unreliable.

As expected, the 04 MST analysis (Fig. 5.36) differed little from the stand-alone analysis. After three hours of integration the features were smoothed and displaced by advection (Fig. 5.37). There is little similarity between the stand-alone and initialized-model-run analyses at 07 MST, further supporting the contention that the 04 MST retrievals were erroneous. Nevertheless, an interesting effect of the model circulations showed up in the cross-sections. Near the mountains downsloping gave rise to water vapor inversions. By 10 MST (Fig. 5.38) there were prominent effects of mixing in the boundary layer and upsloping over the mountains.

5.4.4 Modeled Initial Guess Results

Two sequences of analysis were prepared with a modeled initial guess, one set for each method of determining surface temperatures. In both cases the model water vapor concentrations were initialized at 04 MST using the conventional analysis and then the model integration proceeded to 10 MST.

For the energy balance-based sequence the 04 MST analysis is the same as in the initialized-model-run sequence. The 07 MST analysis (Fig. 5.39) differs substantially from the corresponding stand-alone analysis despite being based on the same satellite data. The modeled-initial-guess analysis is moist at low levels in a band along the Palmer Divide, as well as in the northeast. It also lacks the anomalous local maximum centered on station LAK in both the conventional and stand-alone surface analyses, replacing it with a dry

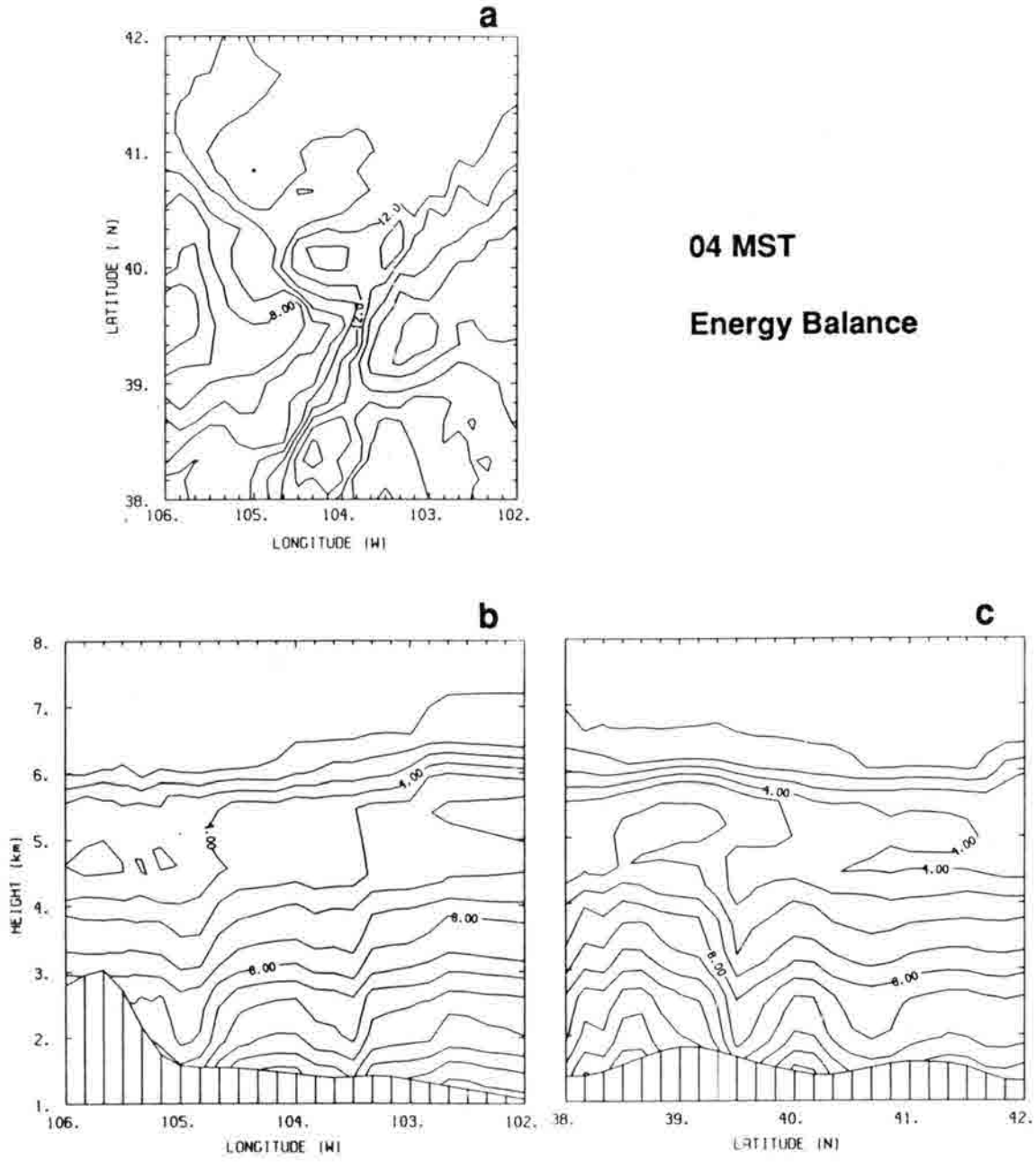

Figure 5.36 Mixing ratios at 04 MST that apply to the initialized-model-run, modeled-initial-guess, and coupled analysis sequences with energy balance-based surface temperatures. Sections and contours are as in Fig. 5.32.

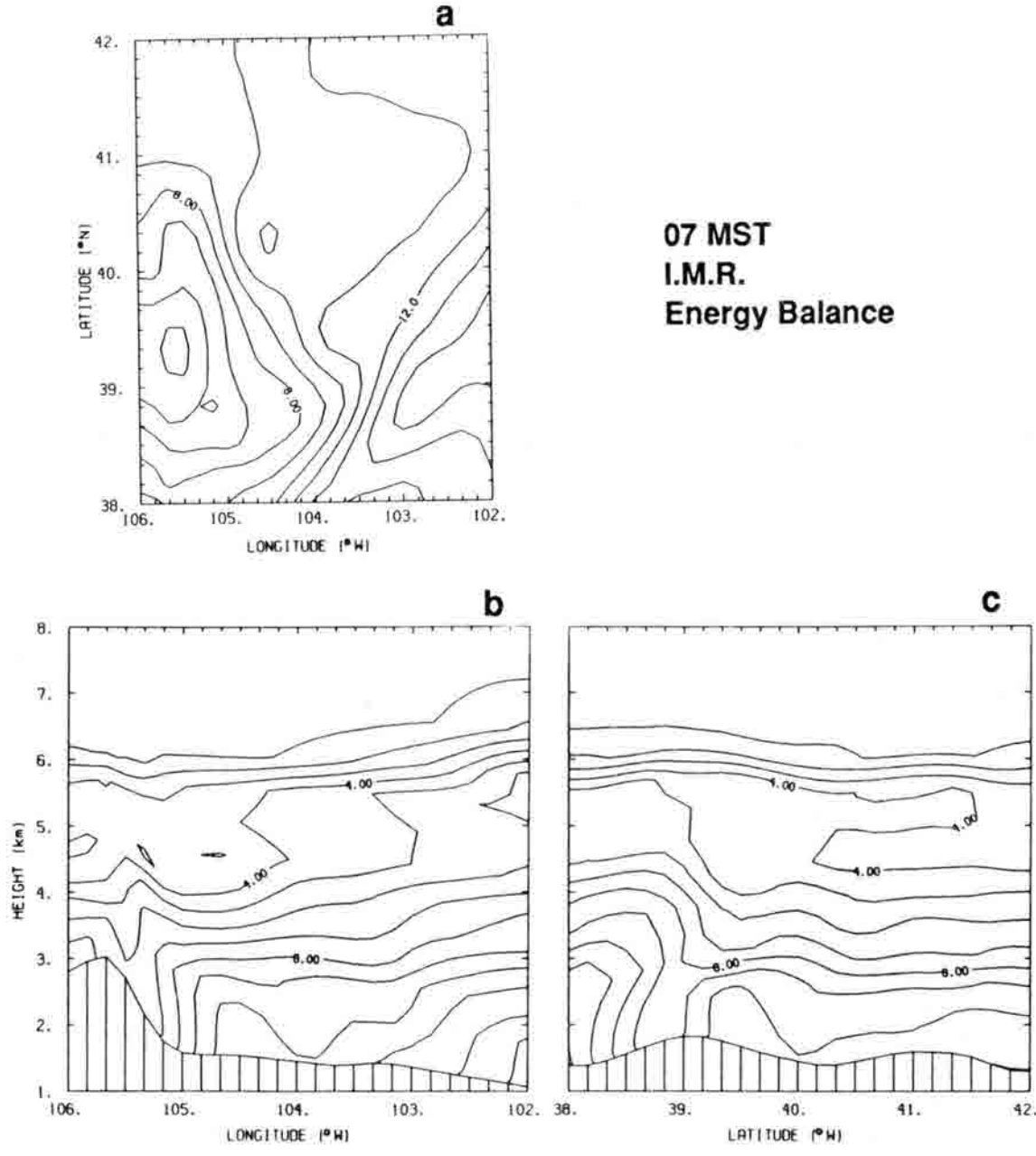

Figure 5.37 Mixing ratios at 07 MST from the initialized-model-run analysis. Sections and contours are as in Fig. 5.32.

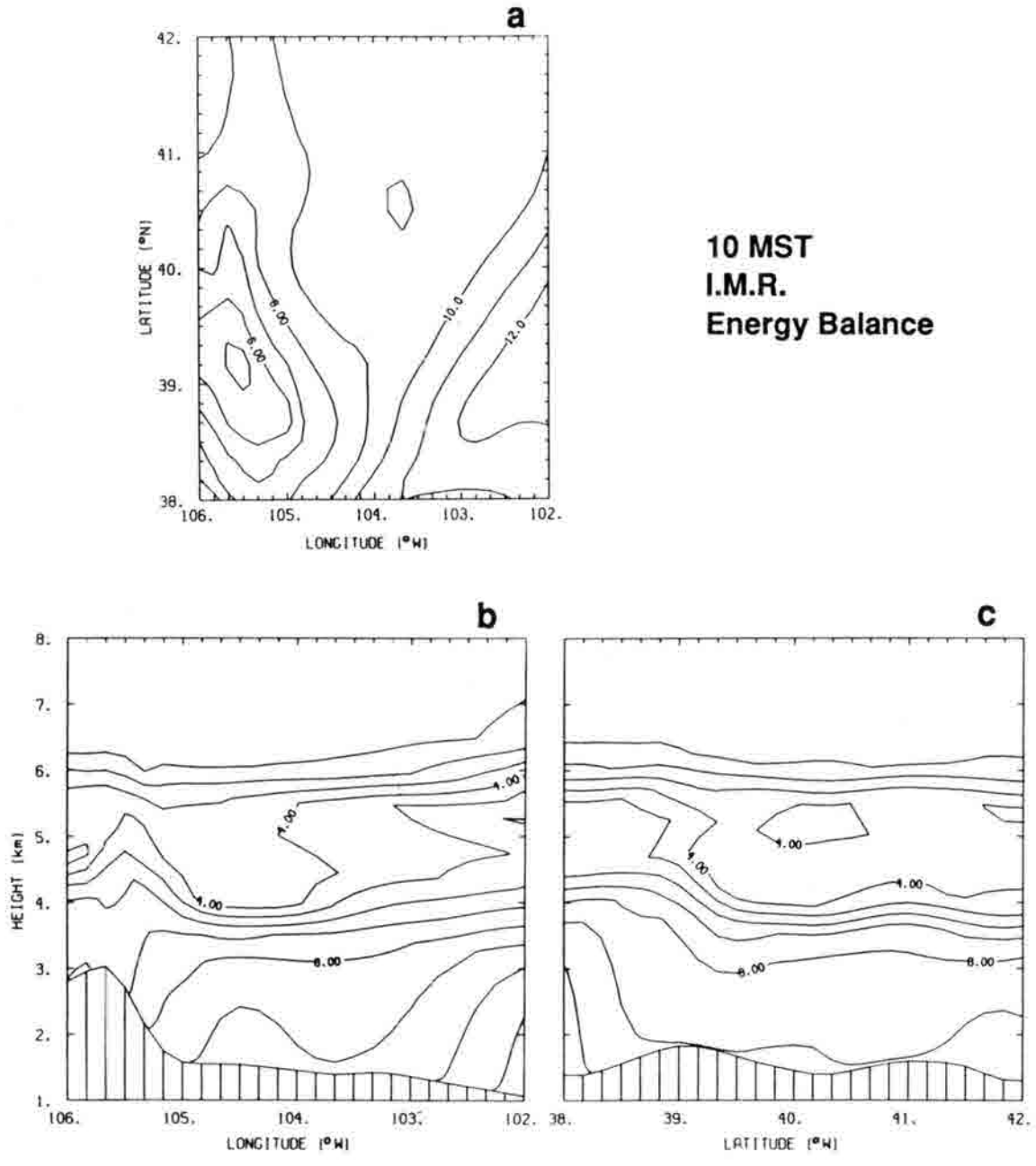

Figure 5.38 As in Fig. 5.37, but at 10 MST.

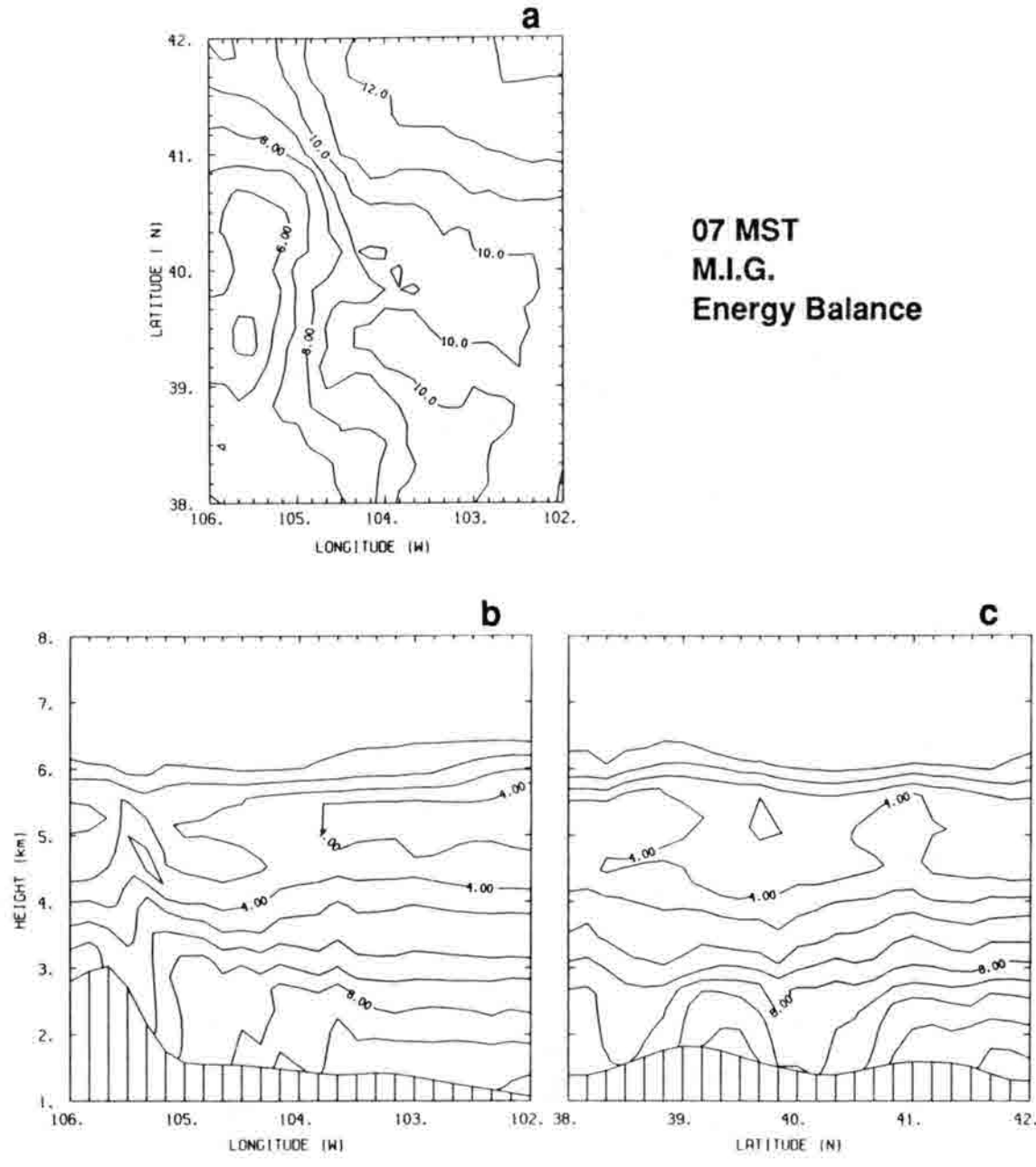

Figure 5.39 Mixing ratios at 07 MST from the modeled-initial-guess analysis with energy balance-based surface temperatures. Sections and contours are as in Fig. 5.32.

surface and deep moisture above (Fig. 5.39b). The 10 MST modeled-initial-guess analysis (Fig. 5.40) had lesser mixing ratios at low levels than the corresponding stand-alone analysis due to modeled vertical mixing. There were also differences in the positions of the local maximum near the domain center. At both 07 and 10 MST the impact of the model circulations is evident in the distinct vertical water vapor structure over the mountains and the contrast between boundary-layer and free-atmosphere gradients over the plains.

The sequence of analyses based on the model with satellite-determined surface temperatures (Figs. 5.41–43) is generally similar to the energy balance-based sequence. At 07 MST the concentrations over the high plains reflected the more persistent downsloping in the satellite-based run (Fig. 5.42b). Due to lower surface temperatures the mixing of water vapor occurred over a shallower layer in the satellite-based run. The resulting differences were particularly apparent at 10 MST.

In general, the differences between the stand-alone and modeled-initial-guess analyses demonstrate that prominent characteristics of the analyses depend heavily on the fine-scale vertical structure of the initial guess profiles.

5.4.5 Coupled Results

For coupled analyses at 07 and 10 MST the adjustments to initial guess fields were suppressed in cloudy regions. The level of suppression was based on the radius of consideration at each grid point, which is a product of the objective analysis program. Suppression decreased linearly from total at radii greater than 164 km to none at radii less than 64 km. The objective analysis routine treated a grid point as if it were in a data gap for radii greater than 64 km, as applied to this data set. The purpose of the suppression was to retain water vapor information from previous retrievals wherever no new data were available.

The coupled analyses at 04 MST were the same as those from the modeled-initial-guess series'. For the later times the energy balance-based results will be addressed first.

The 07 MST analysis (Fig. 5.44) includes some remnants of the unreliable 04 MST retrievals, including the moist band in the southeast. It is also drier than the modeled-initial-guess analysis in the northeast corner due to suppression of adjustment. Those two analyses were similar near the center of the domain although the orientation of surface

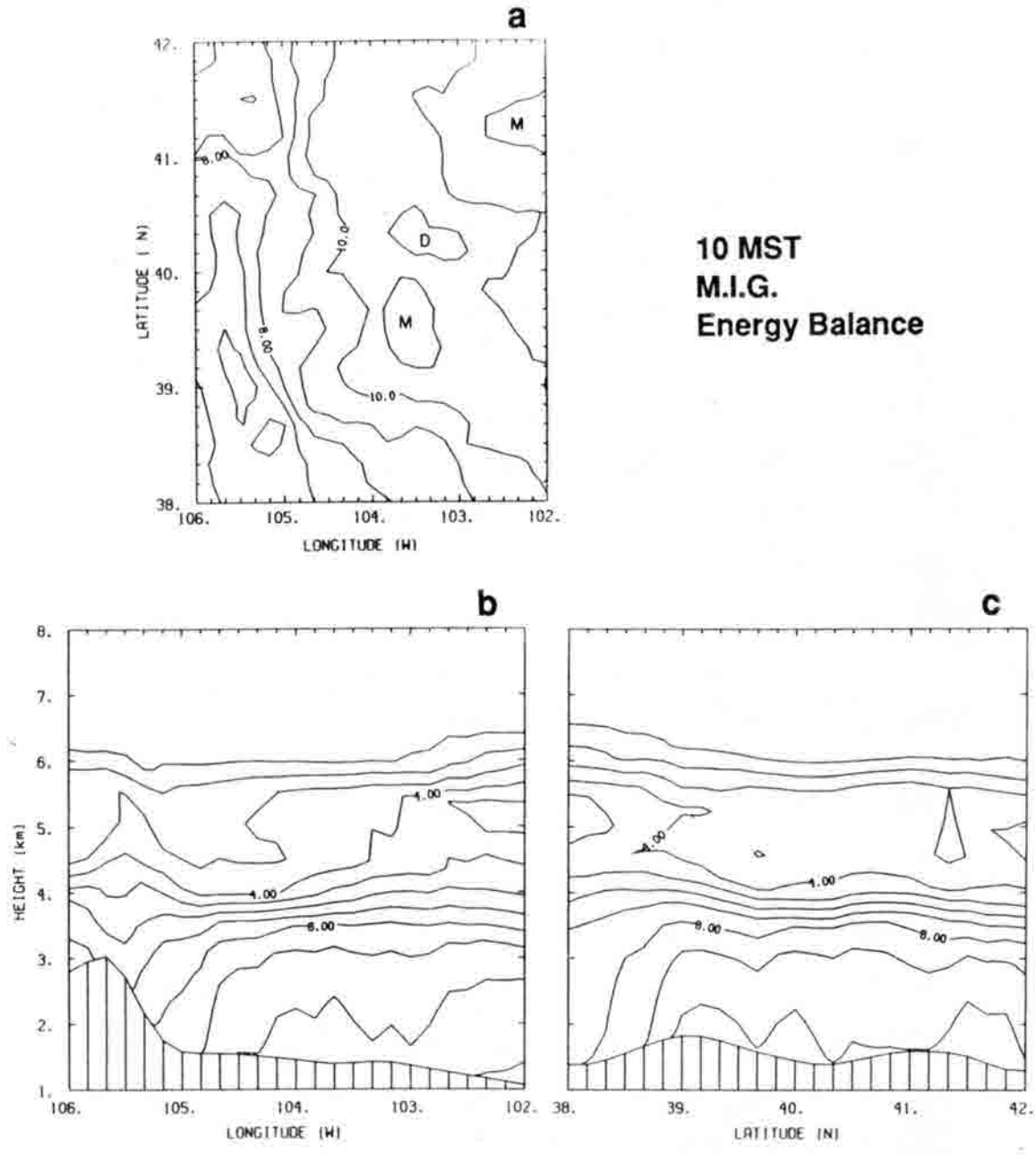

Figure 5.40 As in Fig. 5.39, but at 10 MST. The M and D indicate local areas of relatively moist and dry air, respectively.

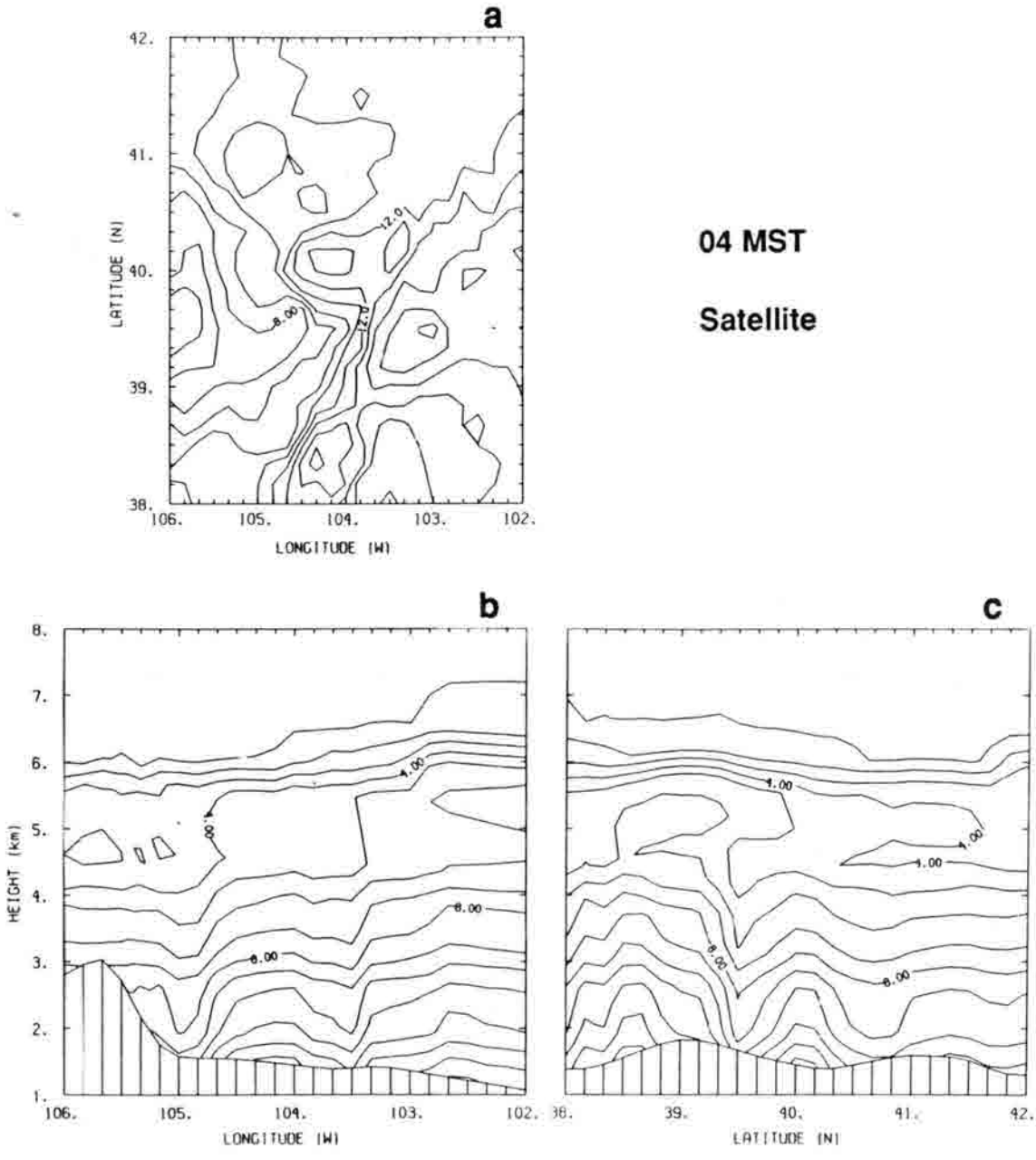

Figure 5.41 Mixing ratios at 04 MST that apply to the modeled-initial-guess and coupled analysis sequences with satellite retrieval-based surface temperatures. Sections and contours are as in Fig. 5.32.

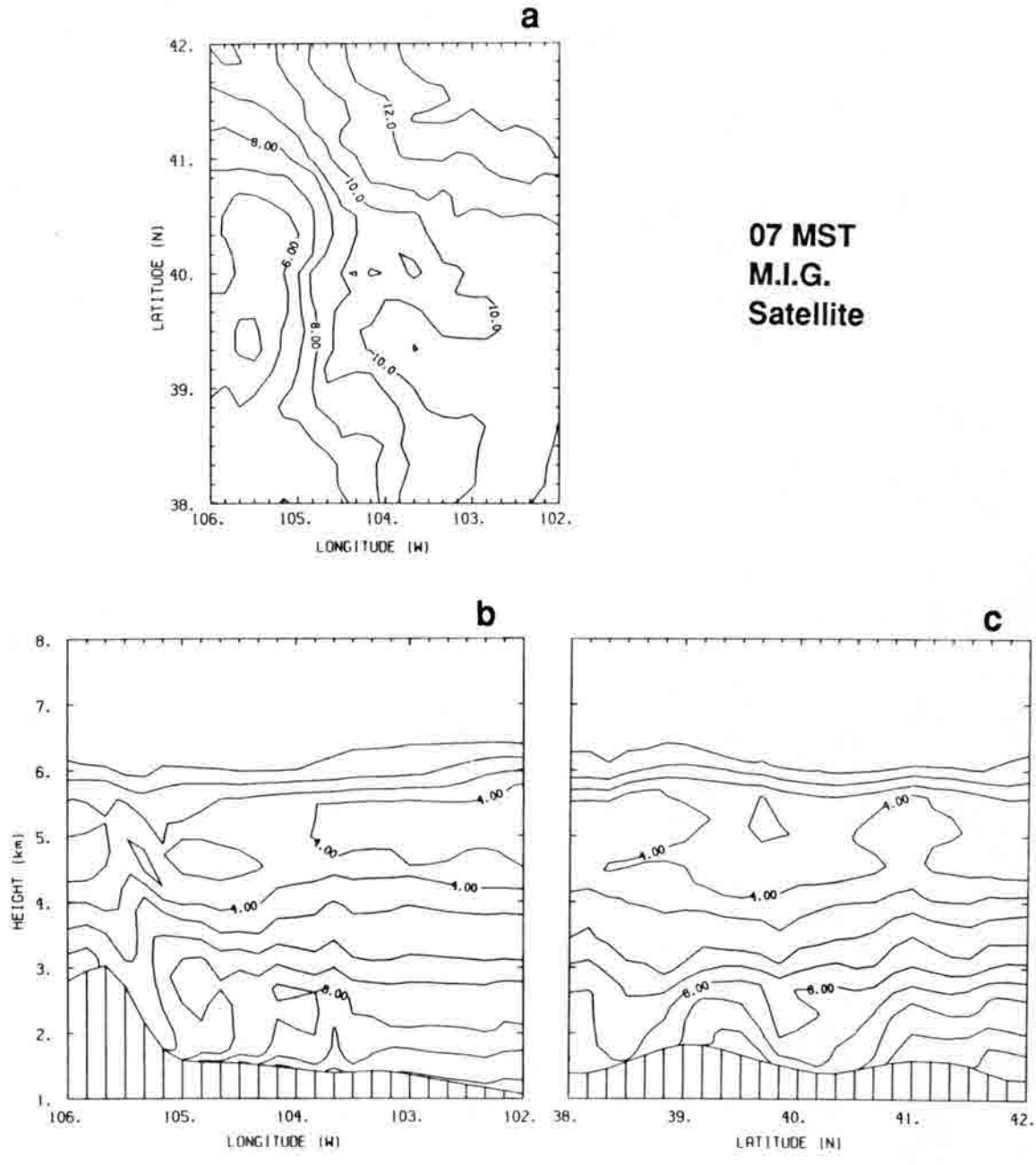

Figure 5.42 As in Fig. 5.39, but with satellite retrieval-based surface temperatures.

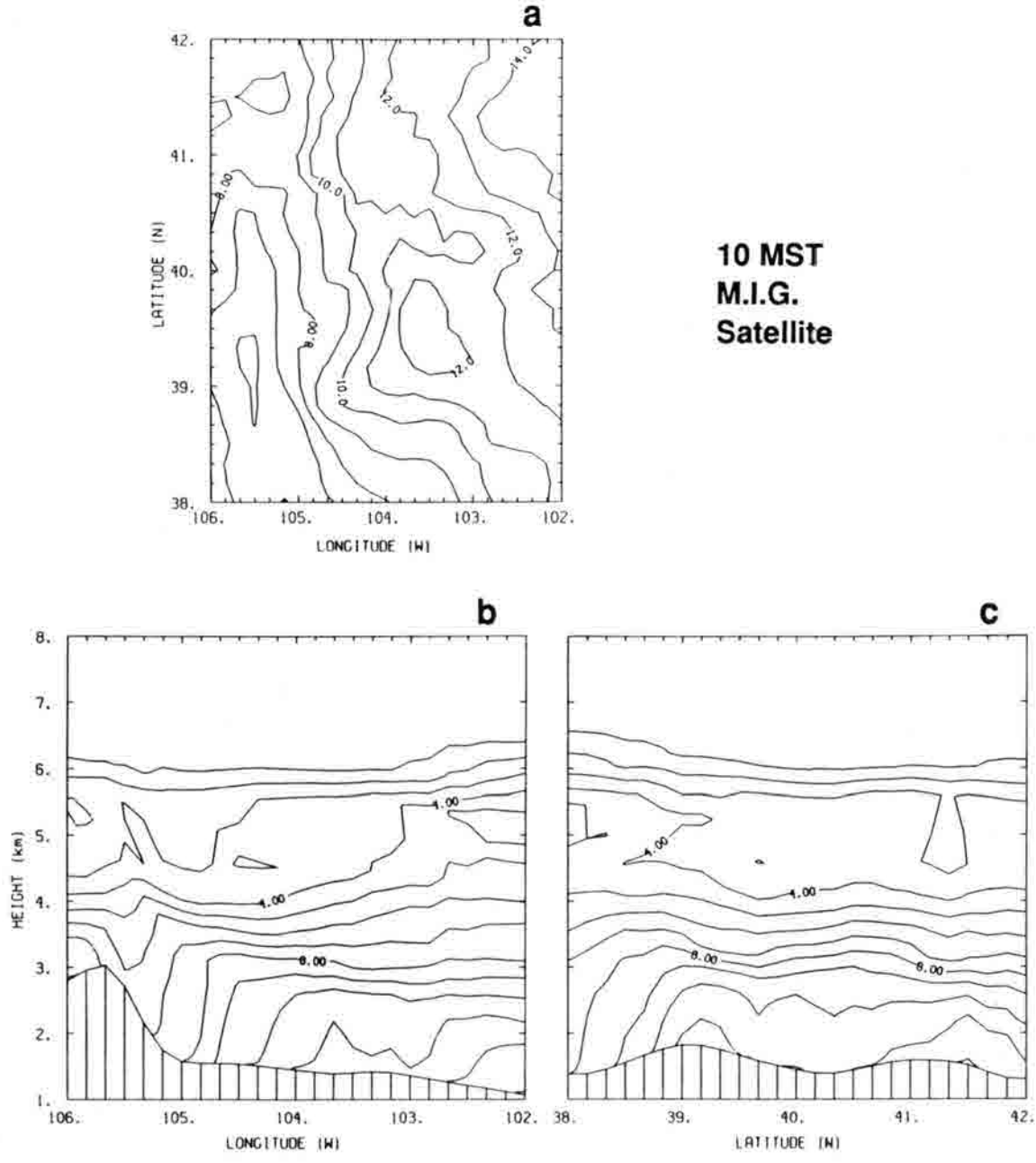

Figure 5.43 As in Fig. 5.40, but with satellite retrieval-based surface temperatures.

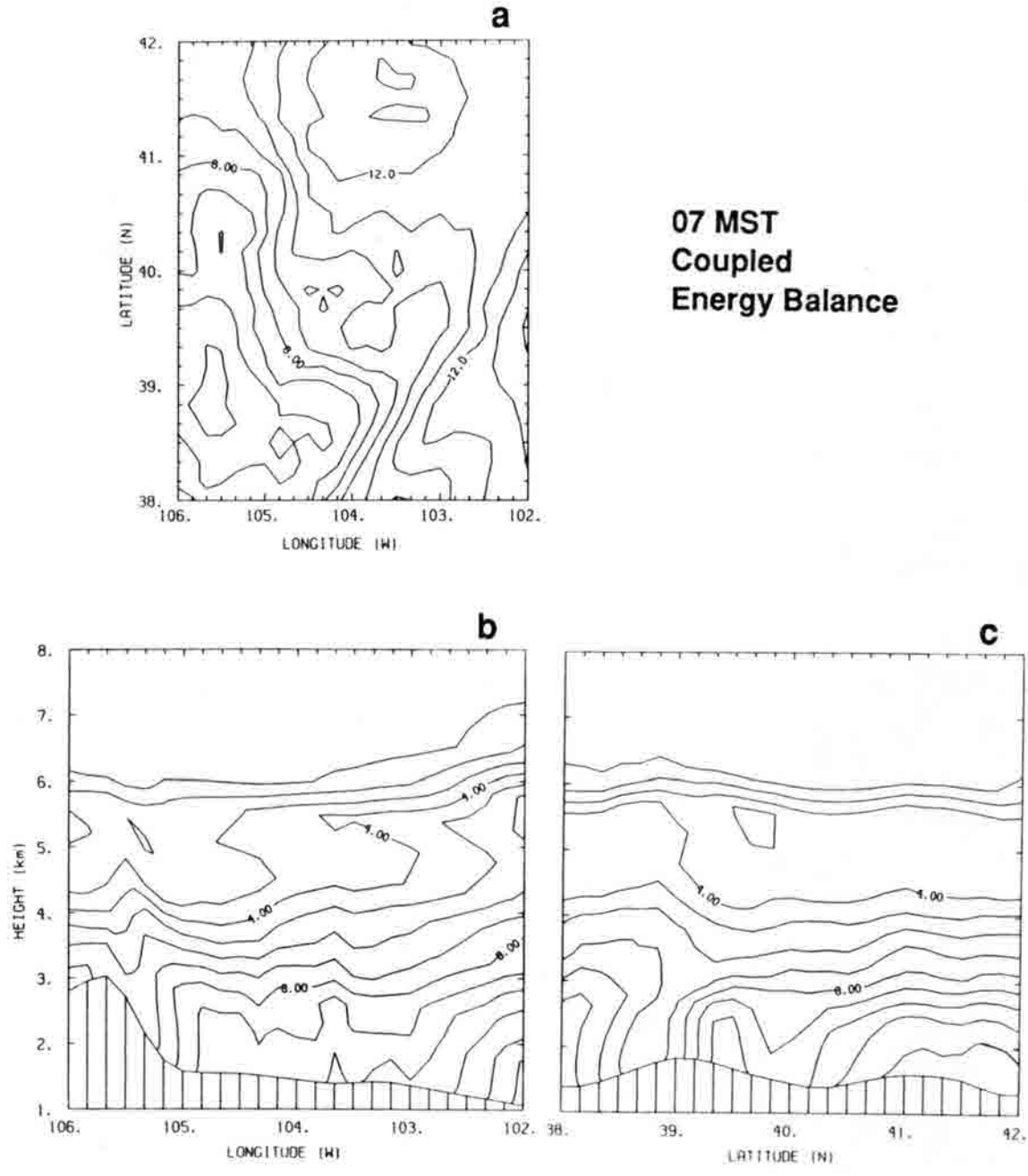

Figure 5.44 Mixing ratios at 07 MST from the coupled analysis with energy balance-based surface temperatures. Sections and contours are as in Fig. 5.32.

contours is different. By 10 MST (Fig. 5.45) the effects of the 04 MST retrievals had reduced as data coverage expanded. The central arc of surface mixing ratios over 11 g/kg is similar to a feature in the modeled-initial-guess analysis, but here the local maximum is shifted northwestward. The differences correspond with variations in the depth of the mixed layer, as depicted in the cross-sections. In the "forecast" for 13 MST (Fig. 5.46) the mixed layer is very deep, particularly over the eastern mountain slope. Superimposed on the east-west gradient there are relative maxima just south of the Palmer and Cheyenne ridges and east of the continental divide. These features correspond to regions of low-level convergence and upward motion.

The 07 MST coupled analysis with satellite-based surface temperatures (Fig. 5.47) is very similar to the energy balance-based analysis. The primary distinguishing feature of the 10 MST analysis is the sharp contrast between the moist spot near the center of the domain and the dry tongue to the southeast (Fig. 5.48). The two analyses for 13 MST are substantially different. In the analysis from the satellite-based run there is a low-level local maximum near the center of the domain and the zones of deep mixing appear further south in the north–south cross-section (Fig. 5.49).

The coupled analyses were particularly useful at assessing the consistency of the three sets of satellite data and the reliability of the modeled winds.

At mid-levels there was an overall decrease in moisture from 04 to 07 MST, while the change was small from 07 to 10 MST. This suggests that problems with the 04 MST retrievals extended well above the surface.

At an elevation of 5-km the modeled wind, based on the geostrophic wind initialization, was about 3 m/s from the west. The observed wind over Denver at 05 MST was 7 m/s from just south of west (about 250°), so its westerly component was about 6.6 m/s. Given that the mid-level water vapor gradient was oriented roughly parallel to the wind (see Fig. 5.33), its movement indicates time-averaged wind speed. In the coupled results the 4-g/kg contour moved east about 50 km from 07 to 10 MST, implying a wind speed of about 5 m/s. The same computation from the initialized-model-run analysis gave a value of about 3 m/s, which agrees with the modeled winds as expected. These results indicate that the geostrophic wind estimate was substantially weaker than the actual wind on this day.

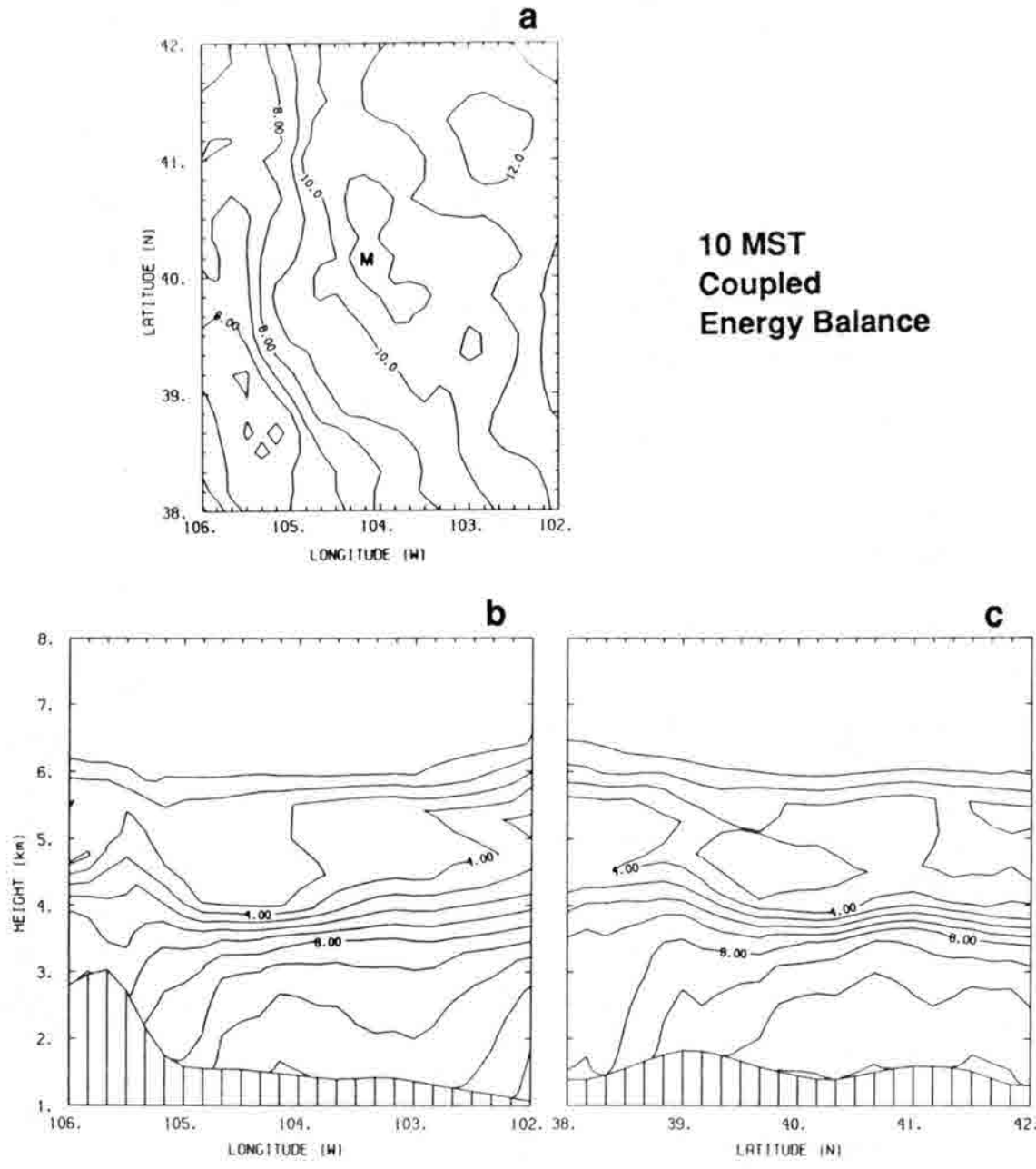

Figure 5.45 As in Fig. 5.44, but at 10 MST. The M indicates a local maximum of moisture.

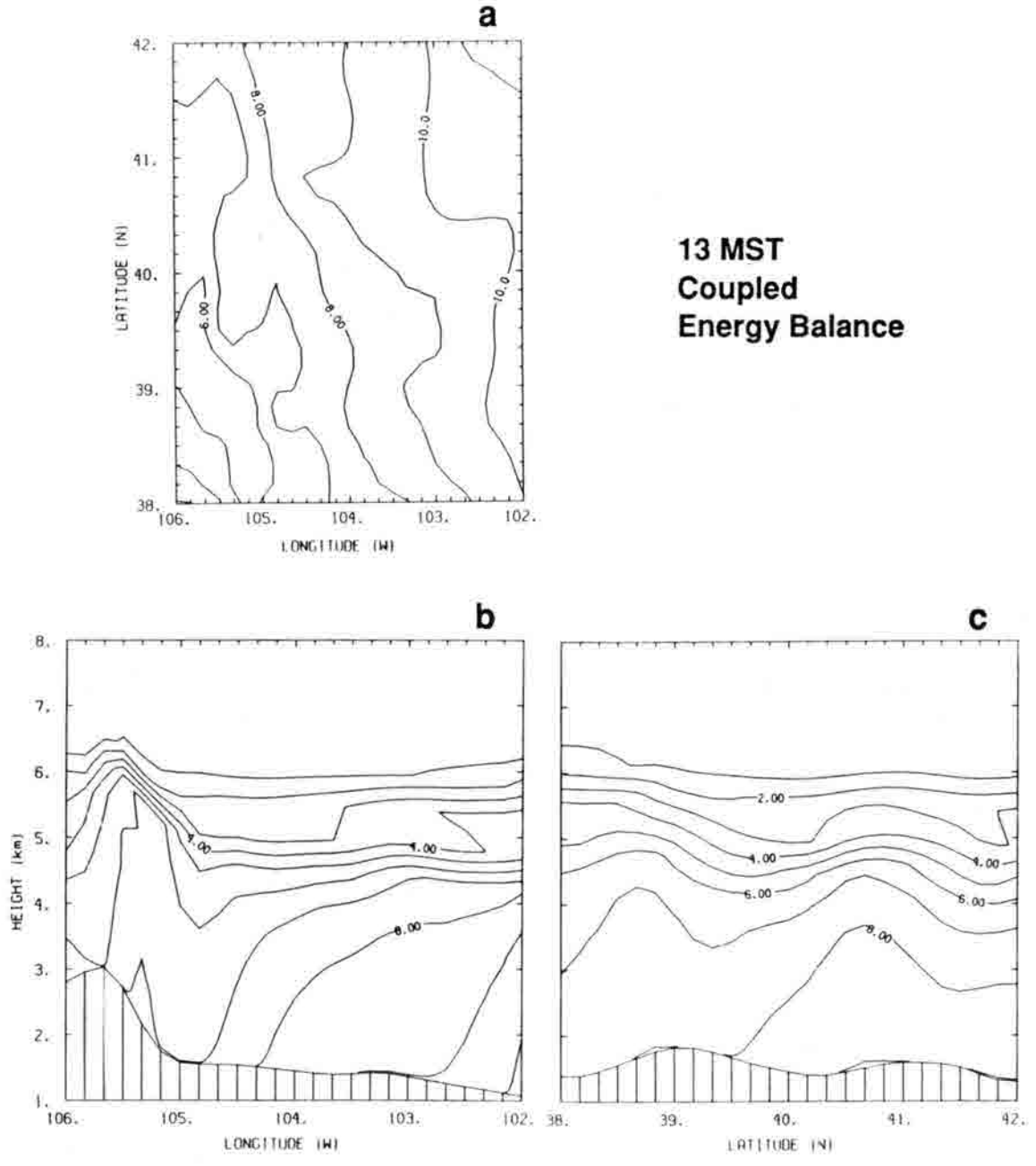

Figure 5.46 As in Fig. 5.44, but from the 13 MST "forecast."

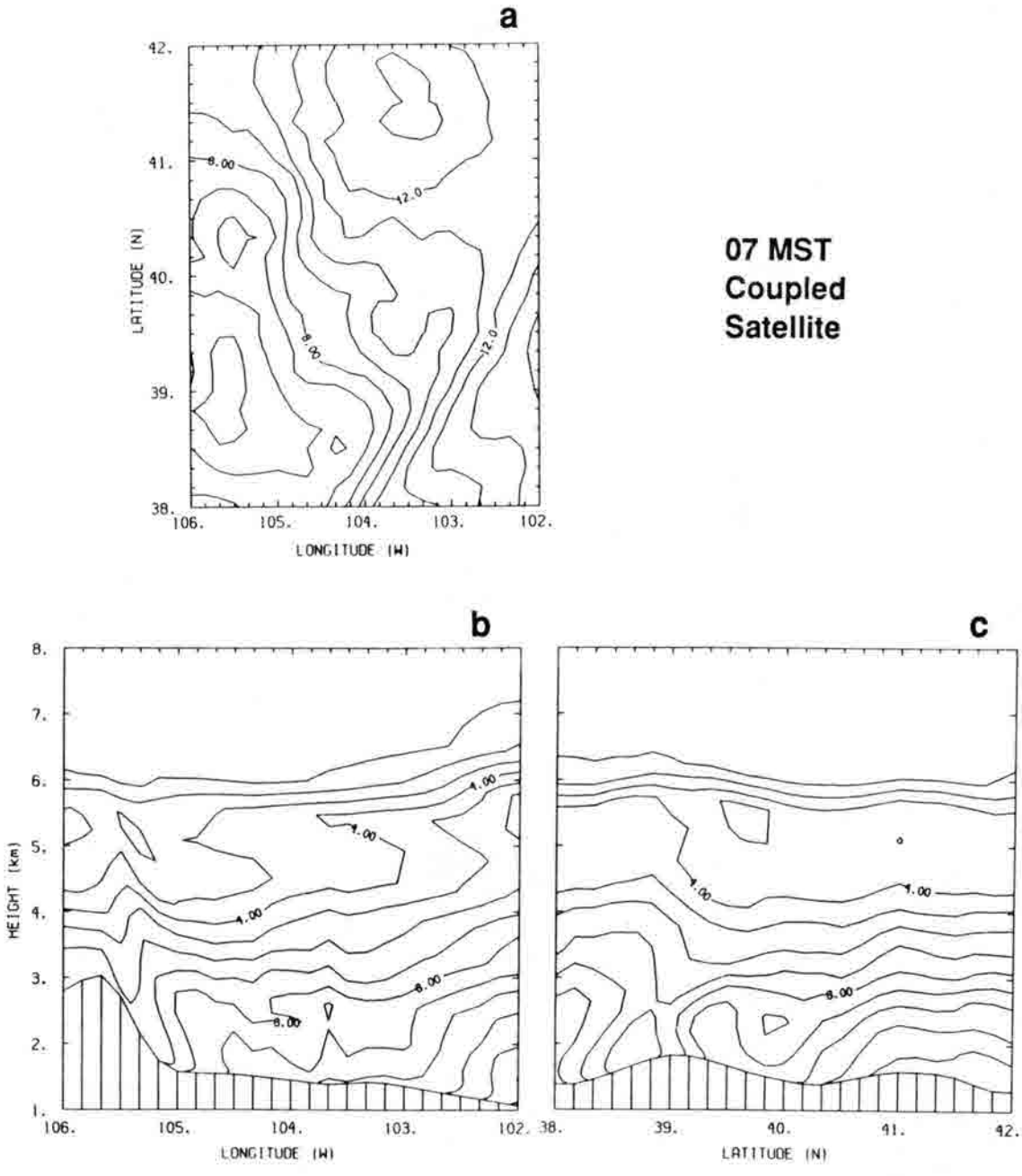

Figure 5.47 As in Fig. 5.44, but with satellite retrieval-based surface temperatures.

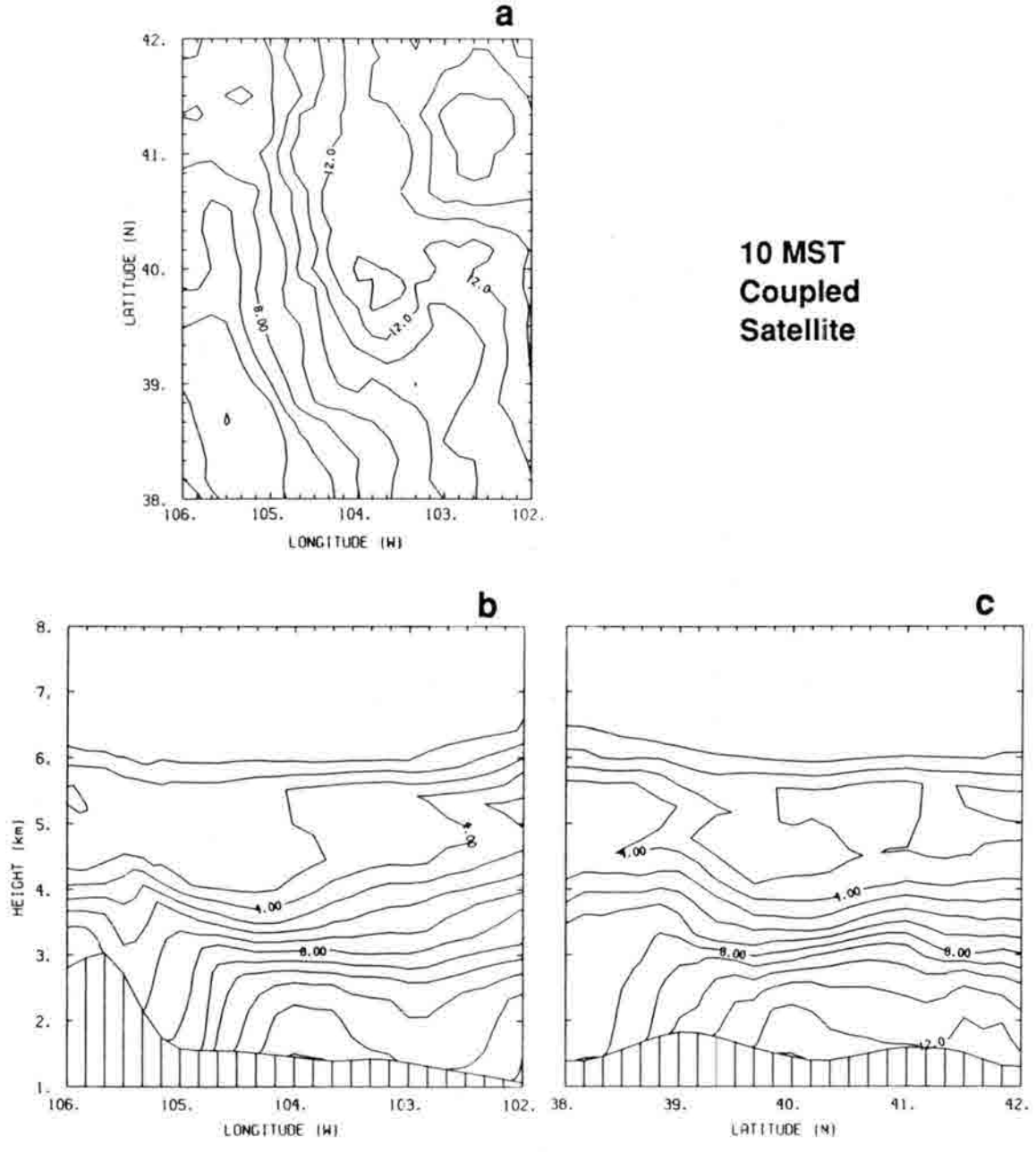

Figure 5.48 As in Fig. 5.45, but with satellite retrieval-based surface temperatures.

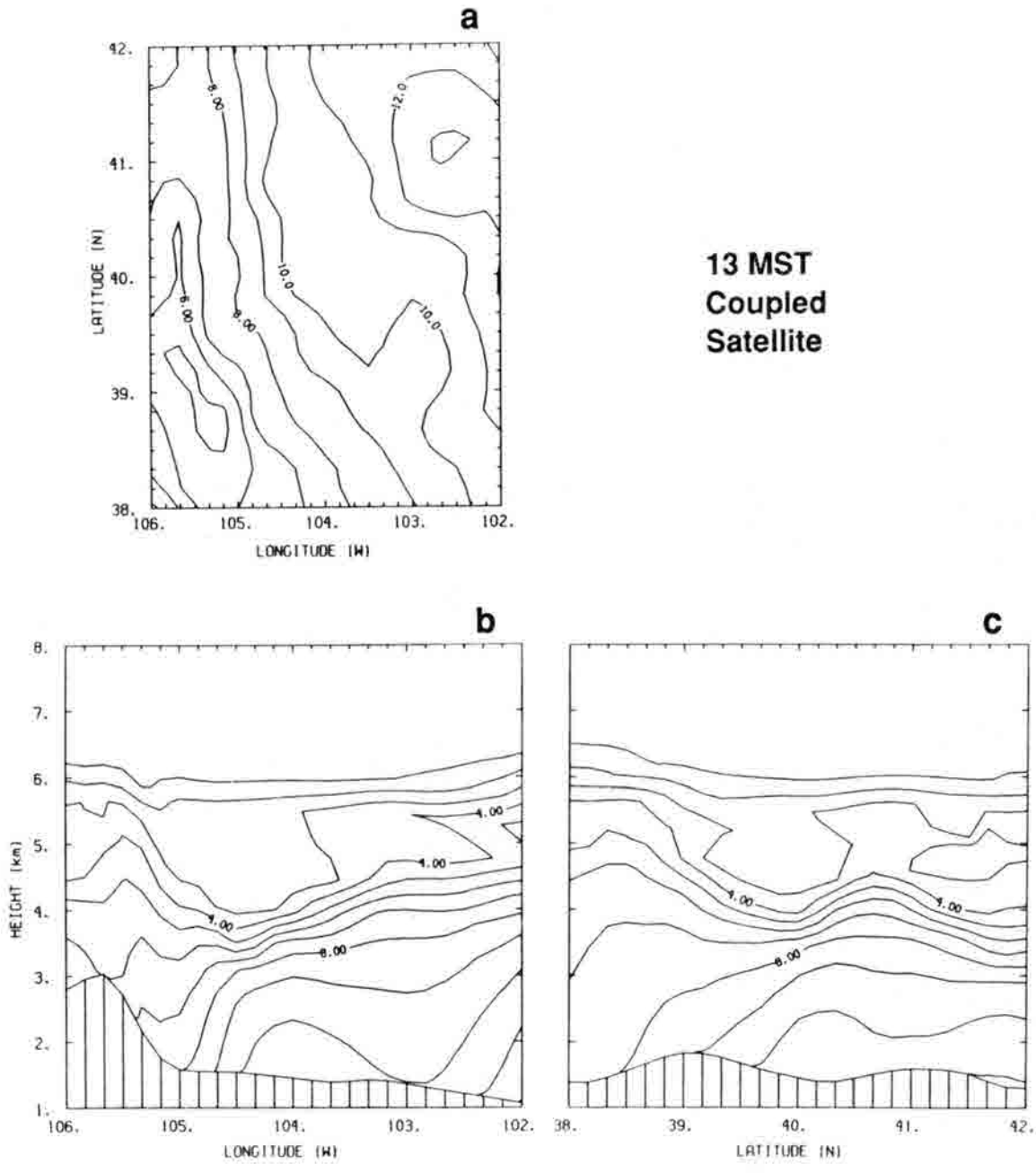

Figure 5.49 As in Fig. 5.46, but with satellite retrieval-based surface temperatures.

It was found that integrated water vapor from 60 kPa to the surface was a very useful quantity to consider in assessing the reliability of low-level fields. For example, the water vapor retrievals at 04 MST were further discredited by plotting the adjustment to integrated water in the 07 MST retrieval step (Fig. 5.50). This showed that the 07 MST retrievals contradicted the 04 MST retrievals since the adjustments opposed the primary features of the pre-adjustment field (Fig. 5.50a). The 10 MST adjustments were small by comparison indicating that the 07 and 10 MST retrievals were generally consistent (Fig. 5.51). There was a general tendency for increased concentrations at 10 MST. One possible explanation for this is if the southwesterly component of the mean lower tropospheric wind was too strong in the 07–10 MST model run. Other possibilities are time-dependent retrieval biases, cloud contamination, or excess evaporation from the ground. The local increase near the domain center was too large to be explained solely by wind errors of a reasonable magnitude. The 10 MST adjustments for the energy balance-based and satellite-based experiments were so similar that no conclusions could be drawn regarding the relative accuracies of their winds.

5.5 Water Vapor Kinematics

The evaluation of water vapor kinematics was limited to the analysis features that appeared to be most reliable. All of the analysis sequences were considered to some degree.

Water vapor changes over the mountains were determined primarily by the model since no low-level retrievals were used over high terrain. Between 04 and 07 MST there was drying just above the eastern slopes of the mountains (Figs. 5.44b, 5.47b) caused by downslope flow, giving rise to a water vapor "front" at the base of the mountains. The position of the front was further east in the satellite-based run than in the energy balance-based run because the downsloping was more persistent in the former case. Another aspect of the mountains' effect on the wind was upward motion and high mixing ratios just above the dry zone. The 07 MST features only indicate the trends of water vapor features because there is no assurance that it was accurate to initialize the field as horizontally flat at 04 MST.

From 07 to 10 MST the low-level winds turned easterly at the mountain base, reversing the mixing ratio trend just about the ground. But the moistening at higher levels was not

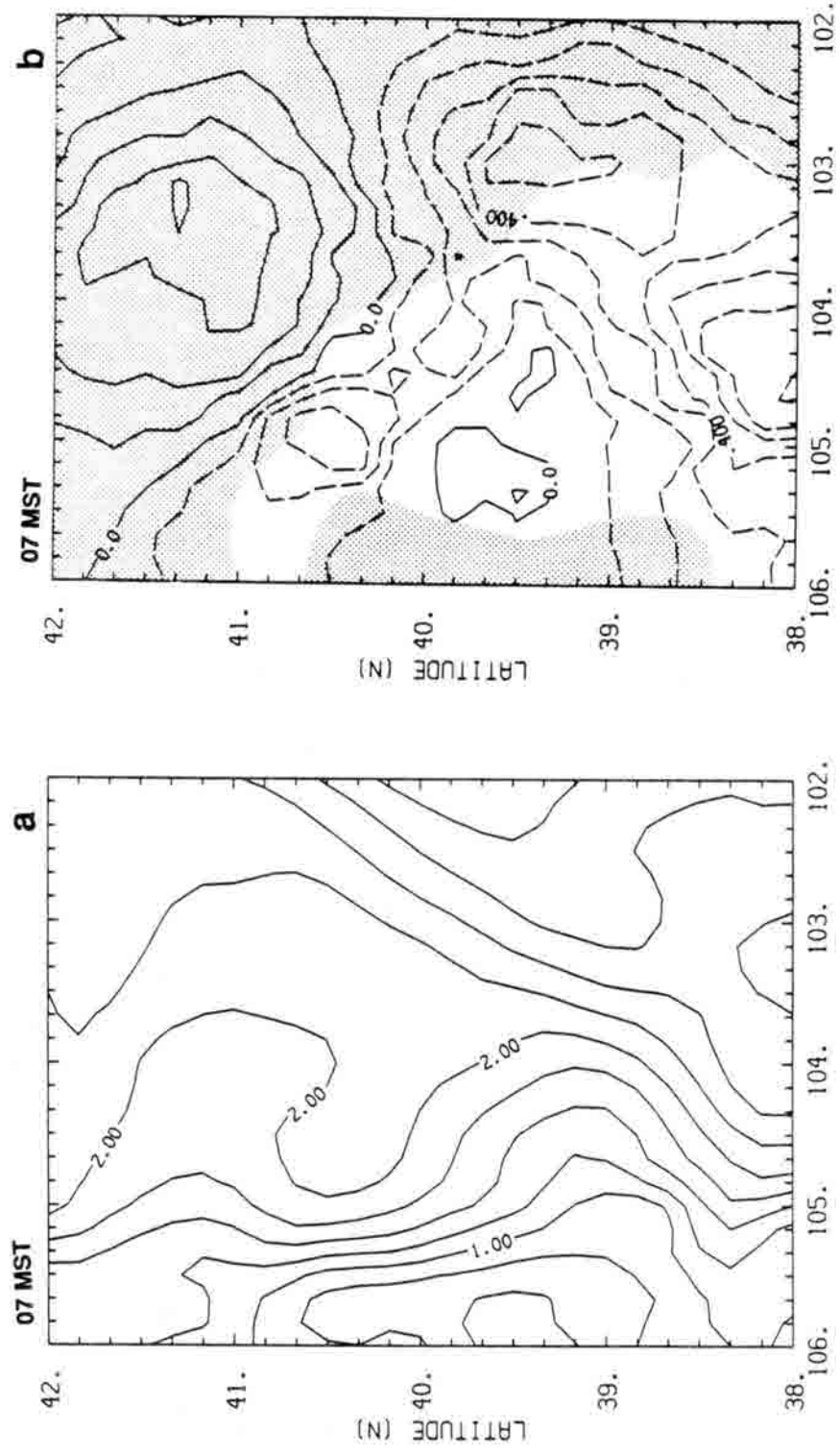

Figure 5.50 a) Integrated water vapor from 60 kPa to the surface just before the 07 MST coupled adjustment, with contours at 0.25-cm intervals; and b) the integrated water vapor adjustment at 07 MST, with contours at 0.1-cm intervals. Plots are from the run with satellite retrieval-based surface temperatures. Values were similar for the run with energy balance-based surface temperatures. Stippled areas were cloudy at either 07 or 10 MST.

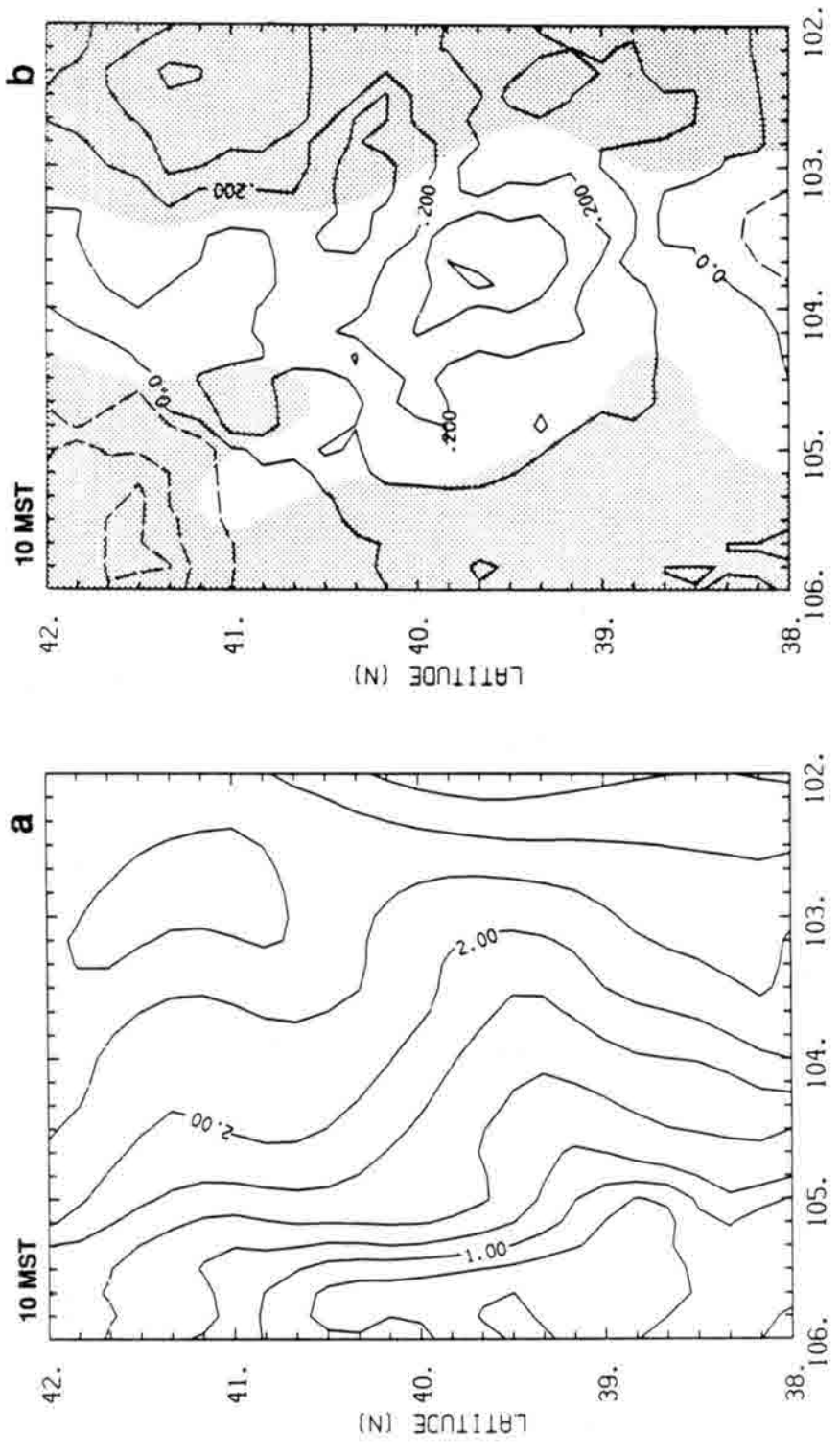

Figure 5.51 As in Fig. 5.50, but at 10 MST.

reversed. It persisted because convergence at low levels fed an updraft above the slope. This effect was far stronger in the energy balance-based analysis (Fig. 5.45b) than in the satellite-based analysis (Fig. 5.48b), and it can play an important role in intensification of convective clouds (Tripoli, 1986). In both analyses there was a suppression of the moist layer over the high plains, resulting in particularly strong vertical gradients.

The analyses were unanimous in indicating a flow of dry air southeastward from the upper Palmer Divide into the Arkansas Valley over the 07–10 MST period. Near the center of the domain the situation is not so clear cut. Both of the coupled analyses have a northwestward shift of the local surface mixing ratio maximum from 07 to 10 MST, in opposition to the modeled advection. These surface values were not representative of the integrated low-level water vapor, in which a moist tongue moved southward during that period (Fig. 5.52). The surface features can be explained in part by the relatively shallow mixed layer at 10 MST in the South Platte Valley (Figs. 5.45c, 5.48c). It is also likely that evaporation from the ground played a role in moistening this area, since the greatest moistening occurred over a band of relatively cool ground (Fig. 5.15b). Further evidence are reports of 11 mm (Hoyt) and 22 mm (Byers) rainfall totals near the domain center during the previous four days (NCDC, 1983), although it is uncertain whether the evaporation rate remained high on 21 August.

In the upper South Platte Valley the only analysis with large surface values through 10 MST was the stand-alone, which had the 10 MST conventional data as initial guesses. This was apparently a shallow, evaporation-related feature that could not be resolved in the retrieval process.

The highest mixing ratios in the domain were in the northeast corner and appeared to drift southeastward over the 07–10 MST period. Changes in magnitude and position of the maximum cannot be estimated with high reliability because satellite data coverage was incomplete.

During the period leading up to 10 MST convergence appeared to play no more than a minor role in water vapor changes over the plains. From 10 to 13 MST convergence effects appeared to dominate changes throughout the domain. In the energy balance-based run precipitable water values increased greatly over the mountains, where convergence was

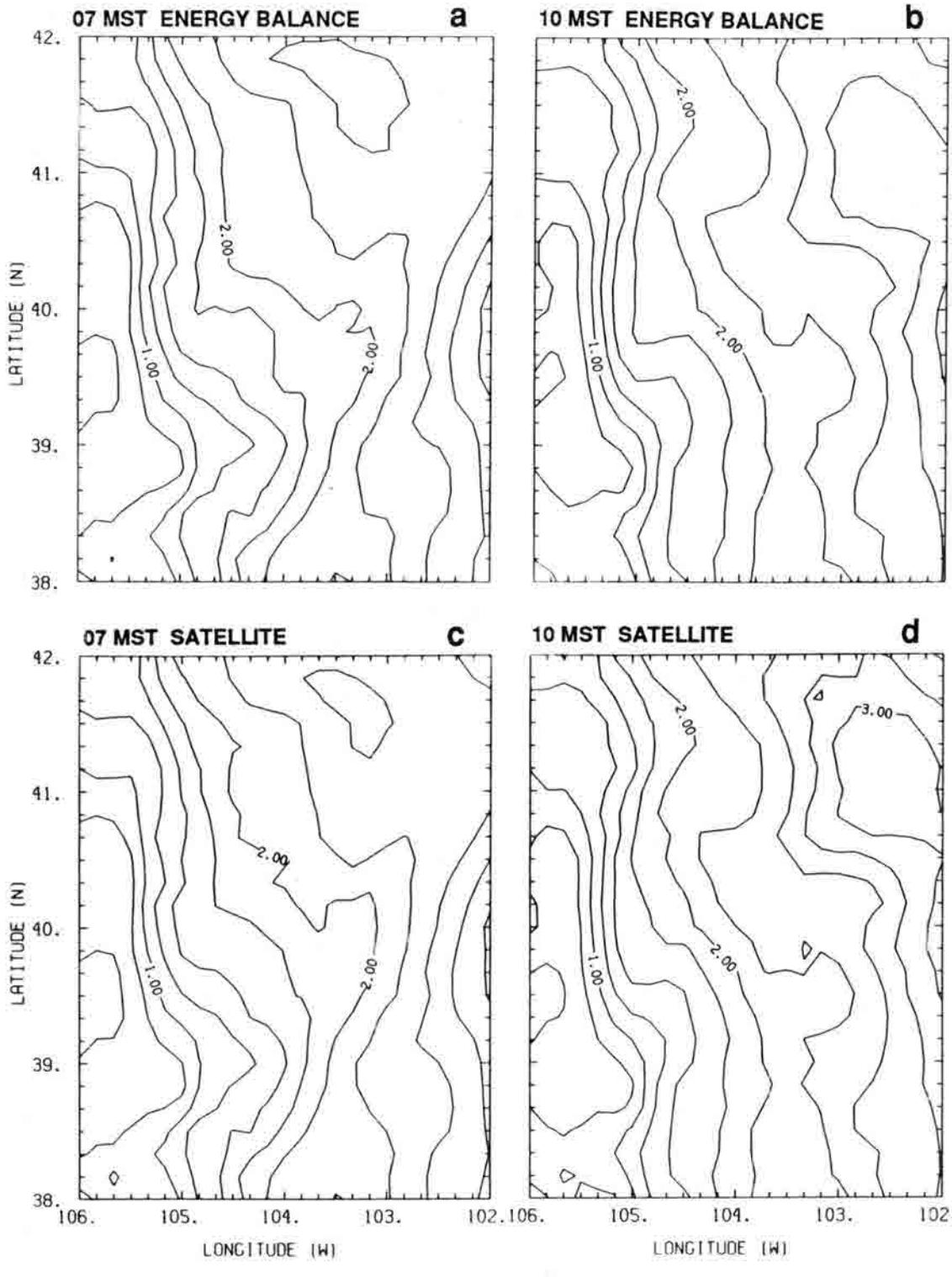

Figure 5.52 Integrated water vapor from 60 kPa to the surface from the coupled analyses with energy balance-based (a and b) and satellite-based (c and d) surface temperatures. Times are 07 MST for a and c, and 10 MST for b and d.

strong, and by small amounts just south of the Palmer and Cheyenne ridges (Fig. 5.53a). In the run with satellite retrieved surface temperatures there were comparable increases over the mountains and the convergent regions on the plains (Fig. 5.53b). The satellite-based run implies that low-level mixing ratios were enhanced in the upper South Platte Valley by local suppression of mixing (Fig. 5.49). One result is a strong north/south gradient along the Palmer Divide.

5.6 Factors in Convective Development

Some of the cloud features depicted in the satellite imagery can be readily related to the evolution of water vapor concentrations. The first convection was near the mountain peaks during the 07–10 MST period. Later, there was a clear slot where water vapor mixing was suppressed. In addition, convection initiated early along the southern Cheyenne Ridge, where low-level moisture was abundant and increasing, and mixing was deep. The other plains region with early convection was the upper Palmer Divide. Modeled upward mixing extended higher just south of the divide axis but there was far more low-level moisture just north of the axis. At the mesoscale, initiating clouds could not be exclusively associated with either upward vertical motion or abundant low-level water vapor. It is uncertain, however, that the model runs had the rising air in the right place.

By the end of the numerical "forecast" period (13 MST) the mountain convection was decaying, so it is very likely that the upward flow of water vapor in that region was overestimated by the energy balance-based run. The intensifying convection on the Palmer Divide was in a region of relatively low precipitable water (Fig. 5.54), but there appears to have been a strong southward flux of low-level water vapor into that region (Figs. 5.29b,49c). The most intense convection in the northern part of the domain was in a region of deep moisture and rising motion just south of the Cheyenne Ridge.

It is interesting that the two primary convective regions propagated differently after 13 MST. The Cheyenne clouds moved almost straight eastward, toward the water vapor maximum, before dying out. The Palmer clouds first moved east-northeastward and then southeastward, steering away from a relatively dry zone in the the 13 MST low-level water

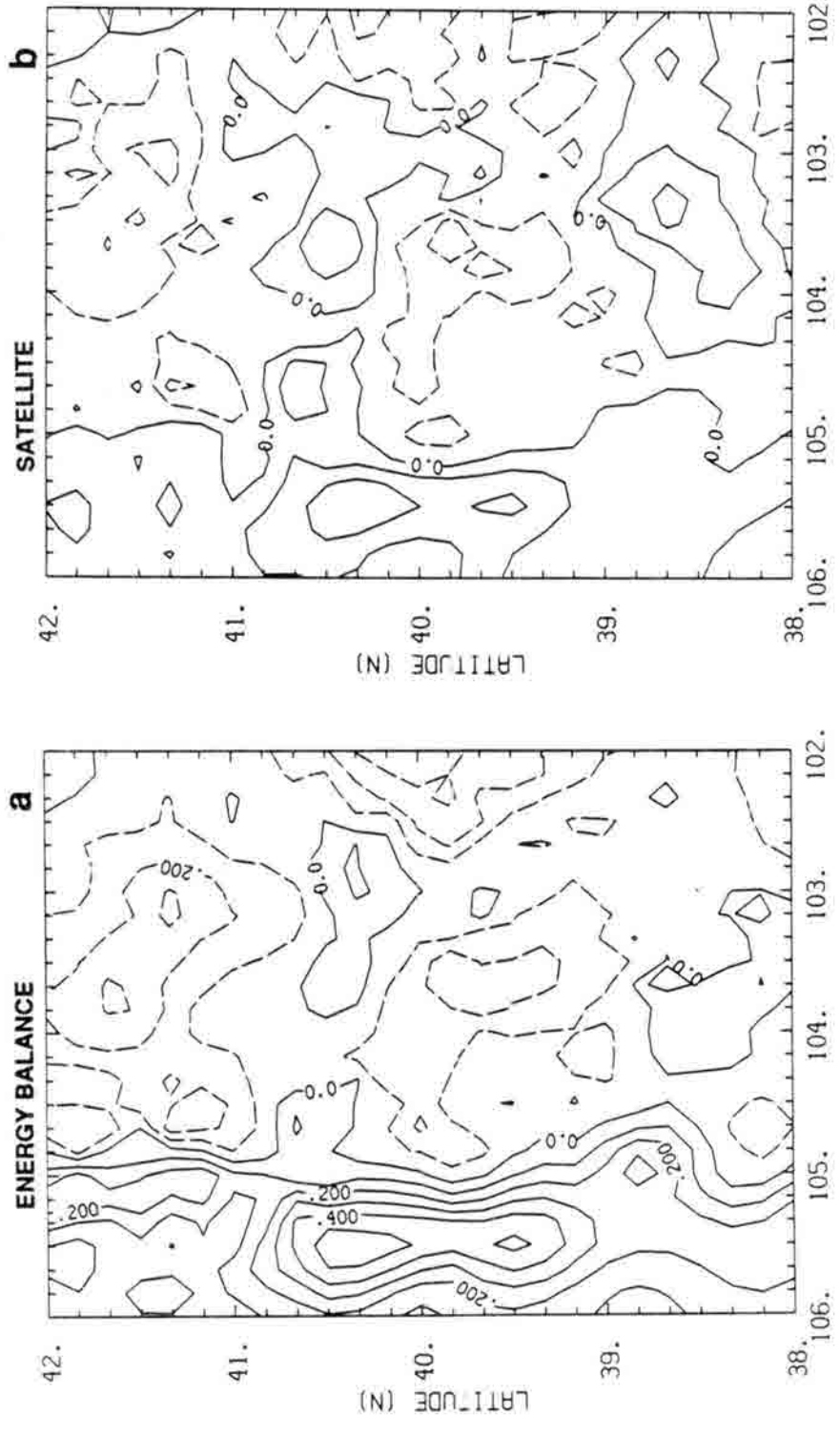

Figure 5.53 The change in total precipitable water from 10 to 13 MST from the runs with a) energy balance-based and b) satellite retrieval-based surface temperatures. Contours are at 0.1-cm intervals.

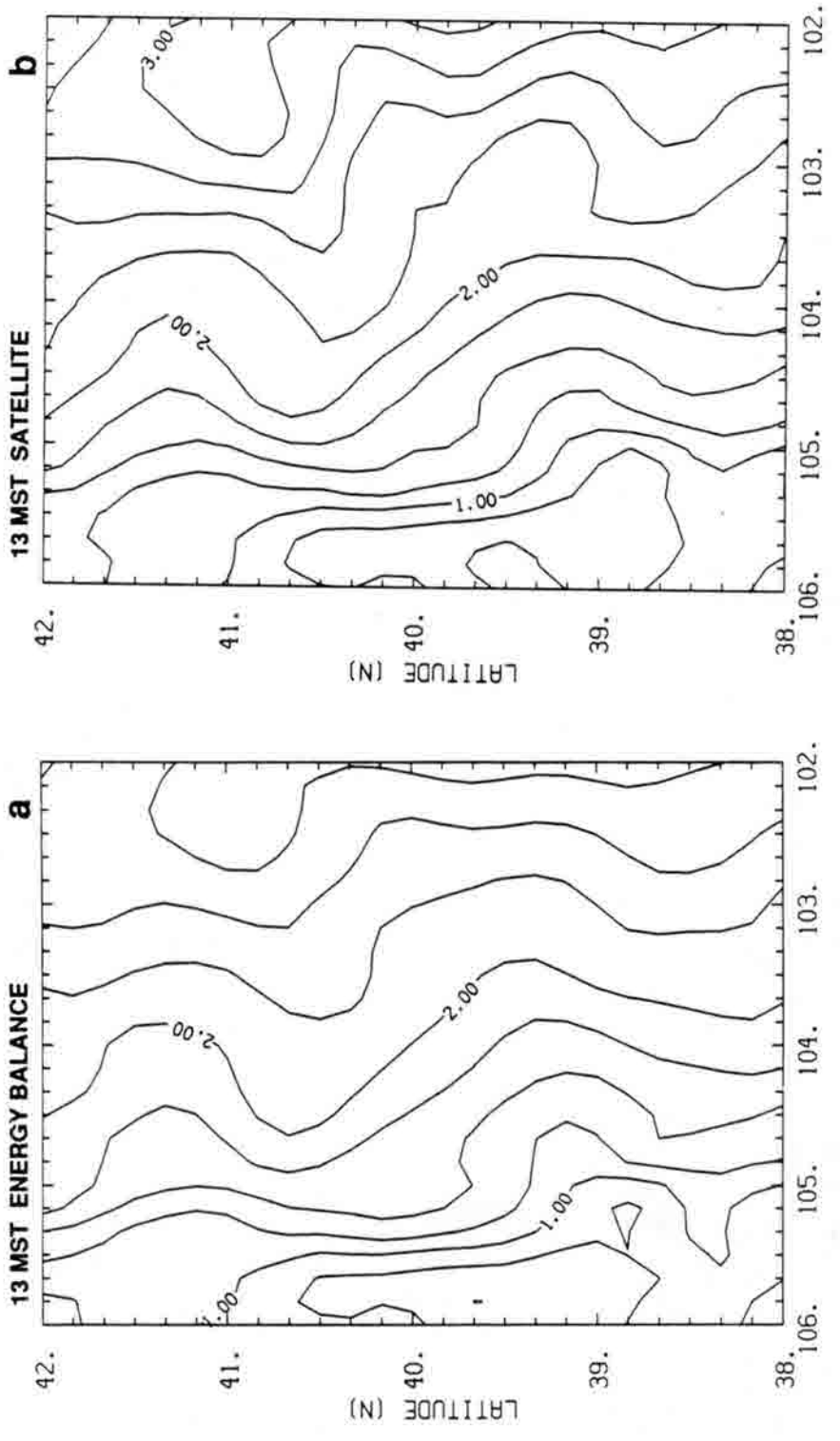

Figure 5.54 Integrated water vapor from 60 kPa to the surface at 13 MST from the coupled analyses with a) energy balance-based and b) satellite-based surface temperatures.

vapor field (Fig. 5.49), as convection intensified. This pattern of motion may be largely coincidental since storm dynamics are also important to storm propagation.

Since water vapor is not the only factor in convective instability, parcel buoyancies were computed also (Darkow, 1986). Buoyancies account for convergence and vertical motion effects on both the temperature lapse rate and the low-level water vapor distribution. The origins of lifted parcels were assumed to be at 375 m above ground, beyond the strong surface-based gradients. The buoyant energy was integrated from 375 m to the level of free convection (negative buoyancy) and from the LFC to the equilibrium level (positive buoyancy). At 10 MST none of the energy balance-based simulated atmospheres had significant negative buoyancy anywhere in the domain. That does not jive with the observed degree of cloud development at that time. In the satellite retrieval-based runs the negative buoyancy was smallest over the mountains and just south of the Cheyenne and Palmer ridges (except where there was not a LFC) in close correspondence with the initial pattern of convective clouds (Figs. 5.55a,56a). The distribution of positive buoyancy was similar in the energy balance-based and satellite retrieval-based runs (Figs. 5.55b,56b,57,58), although values tended to be higher in the latter. There were substantial differences in distribution between the modeled-initial-guess and coupled results, generally corresponding to differences in low-level water vapor.

The modeled initial guess satellite based run had positive buoyancies that matched particularly well with the pattern of convective development. Most notable is the local maximum in the region where the Palmer storm intensified from 10–13 MST. These results imply that the coupled analysis was less accurate, presumably because of lingering contamination by the 04 MST retrievals. This possibility was checked by doing a second coupled analysis with satellite-based surface temperatures, doing the first water vapor adjustment with the 07 MST satellite data in this case. The results were generally similar to those of the analysis that started at 04 MST, but they indicated that the tongue of low positive buoyancies on the eastern Palmer Divide had been misrepresented — there was not really such a prominent minimum (Fig. 5.59b). The results were consistent with those of the modeled-initial-guess analysis with regard to the tongue of high positive buoyancies along the southern Palmer Divide.

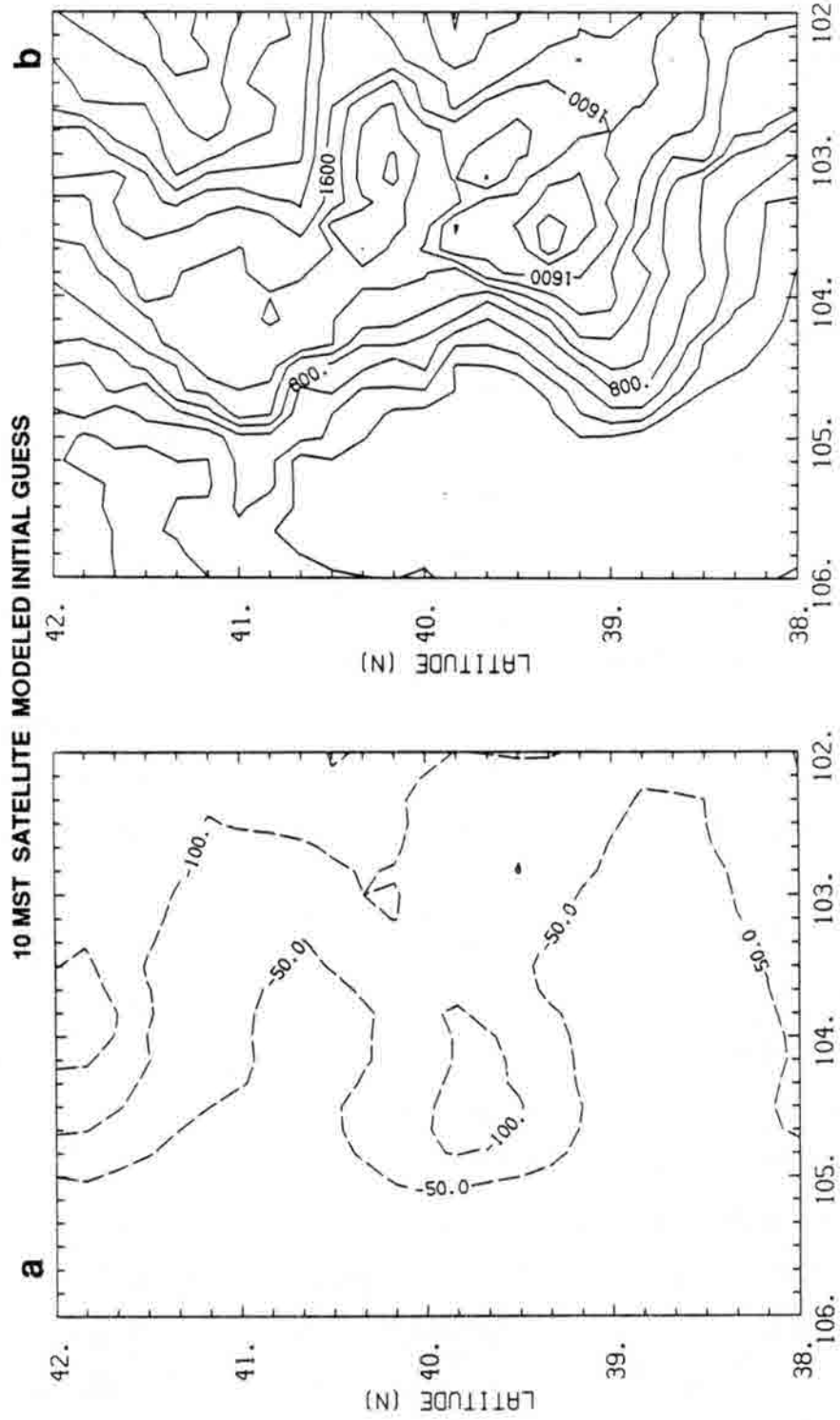

Figure 5.55 Integrated buoyant energies from the modeled-initial-guess analysis with satellite-based surface temperatures at 10 MST: a) negative buoyancy and b) positive buoyancy. Contours are at intervals of 50 and 200 J/kg, respectively.

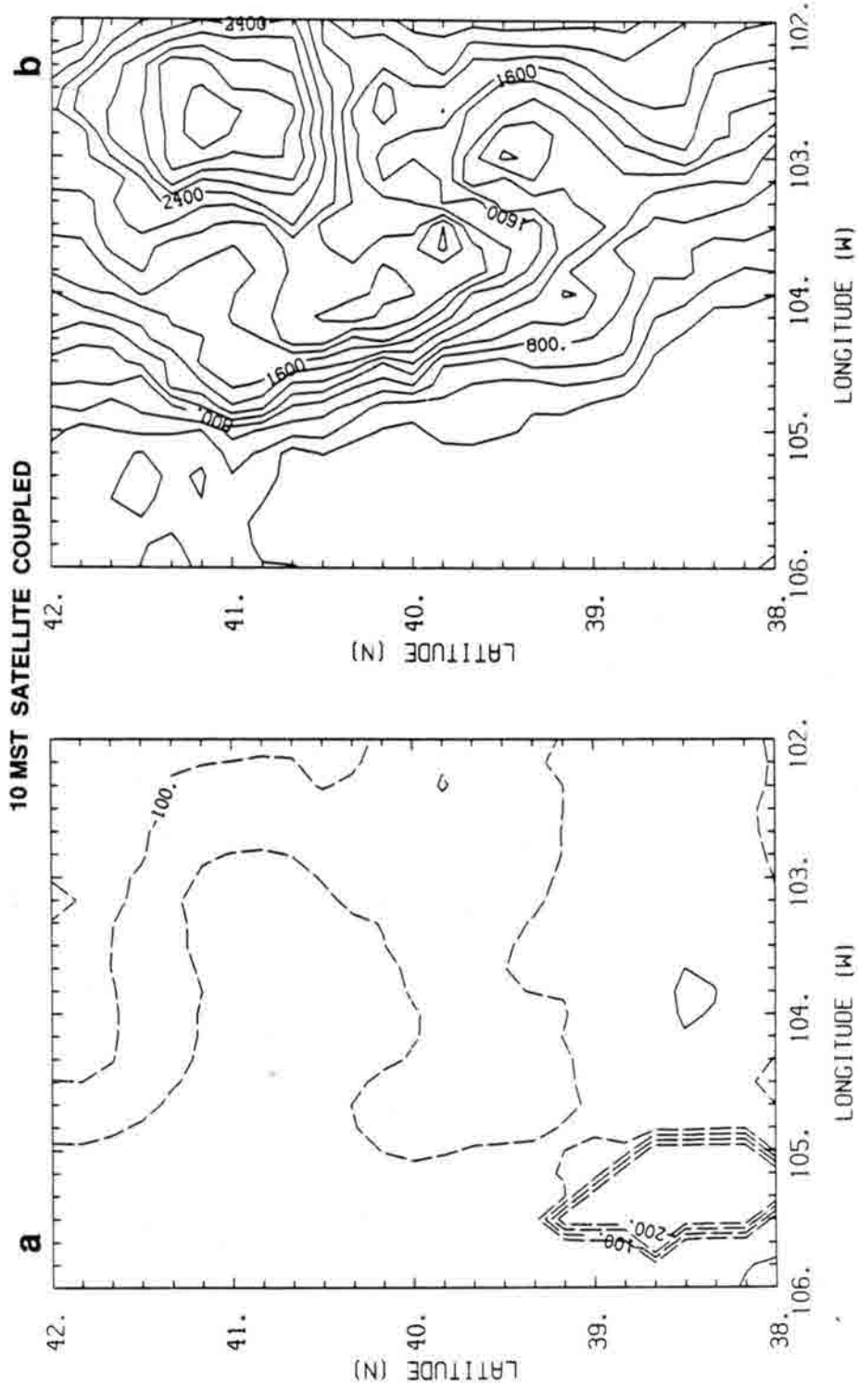

Figure 5.56 As in Fig. 5.55, but from the coupled analysis. Negative buoyancies less than -200 J/kg denote points where there was no level of free convection. Values greater than zero (solid contour) denote points where the stratification was essentially neutral from the surface to the lifting condensation level.

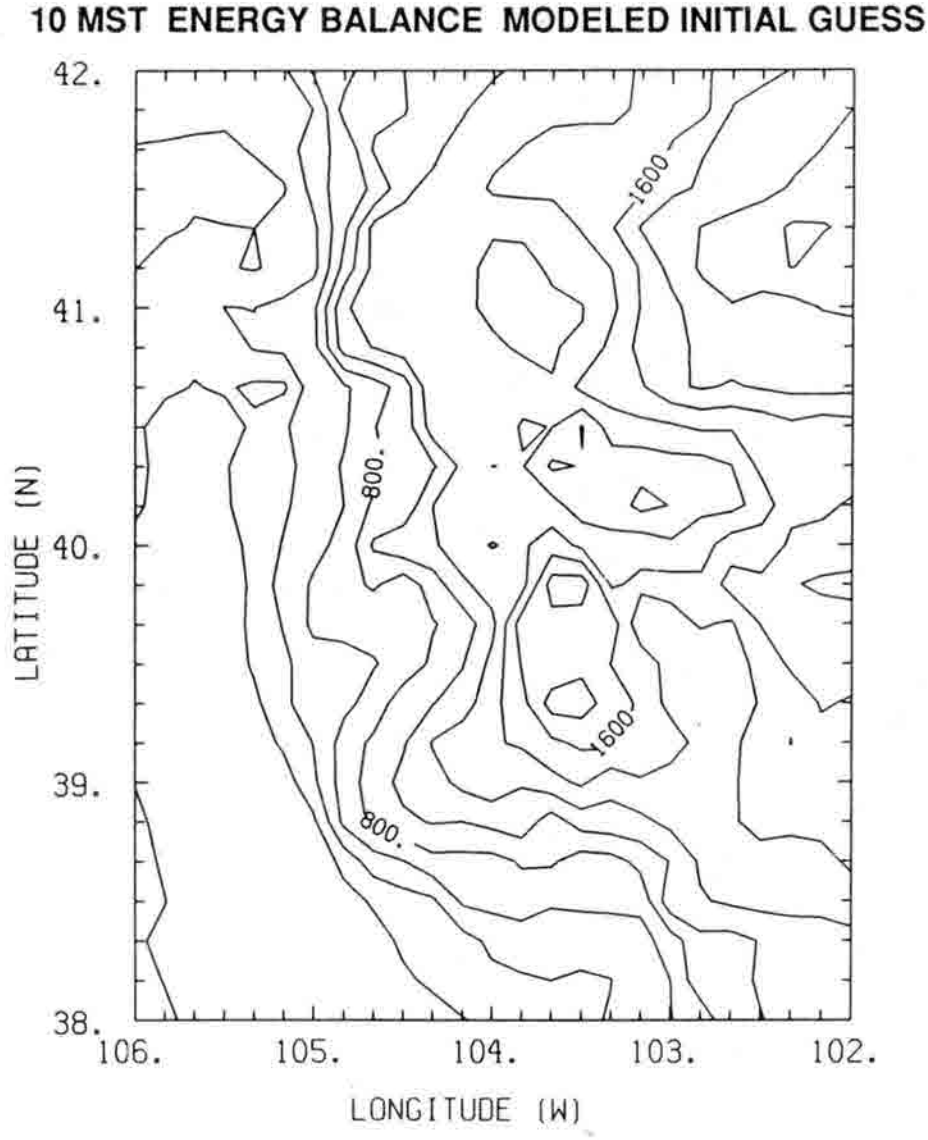

Figure 5.57 Positive buoyancy from the modeled-initial-guess analysis with energy balance-based surface temperatures at 10 MST. Contours are at 200-J/kg intervals.

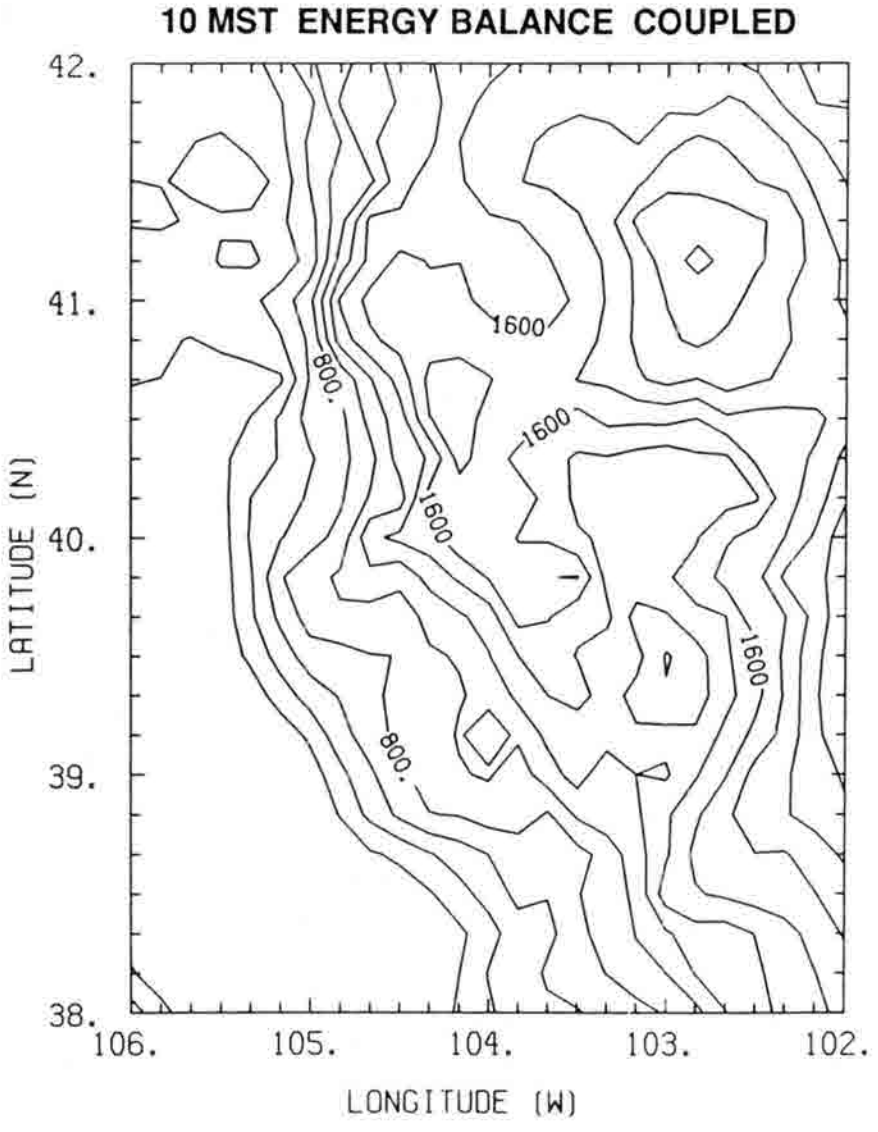

Figure 5.58 As in Fig. 5.57, but from the coupled analysis.

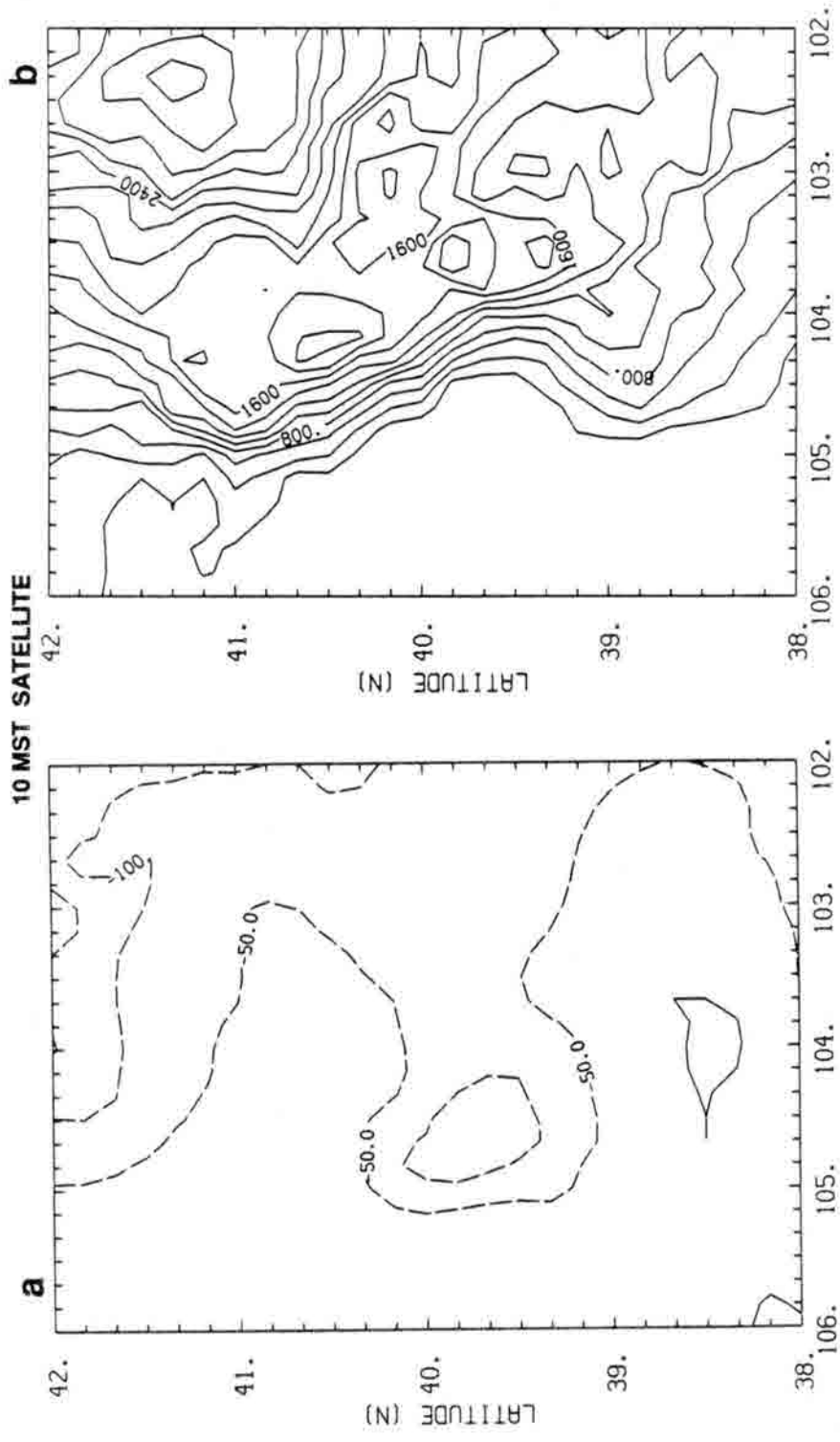

Figure 5.59 As in Fig. 5.55, but from the coupled analysis that began with 07 MST water vapor retrievals.

Upward movement of moisture led to large changes in positive buoyancies from 10 to 13 MST in the original coupled analyses (Figs. 5.60,61). There were increases over the mountains and relatively small decreases just south of the Palmer and Cheyenne ridges in the energy balance-based forecast. The changes in the satellite retrieval-based forecast were similar but smaller. A prominent difference was that the South Platte Valley maximum and the misrepresented Eastern-Palmer minimum mixed out only in the energy balance case.

5.7 Summary

Many of the analyses prepared in this case study were useful in assessing the relative accuracies of the two methods for determining surface temperatures. In almost every comparison the independent observations were matched better by the satellite/coupled results than energy balance results.

For the water vapor analyses there were no direct, mesoscale measurements to use as ground truth in comparisons, so inferences about quality are less conclusive than for surface temperatures. Satellite images were sources of proxy data. Cloud development corresponded most closely with results from the coupled and modeled-initial-guess methods, as compared with derived buoyant energies. The coupled analysis results were particularly useful in demonstrating that both terrain elevation and surface temperature gradients were important to the movement of water vapor during the pre-convective period.

There were significant differences among the series' of water vapor analyses despite that fact that the VAS data were the same for every satellite-based series. Among the stand-alone, modeled-initial-guess and coupled results the differences were due mostly to differences in retrieval initial guesses at fine vertical scales — scales below the resolution of satellite sounders. This illustrates that for mesoscale applications it is particularly important to use whatever means may be available (e.g. a numerical model) to improve the initial guess data.

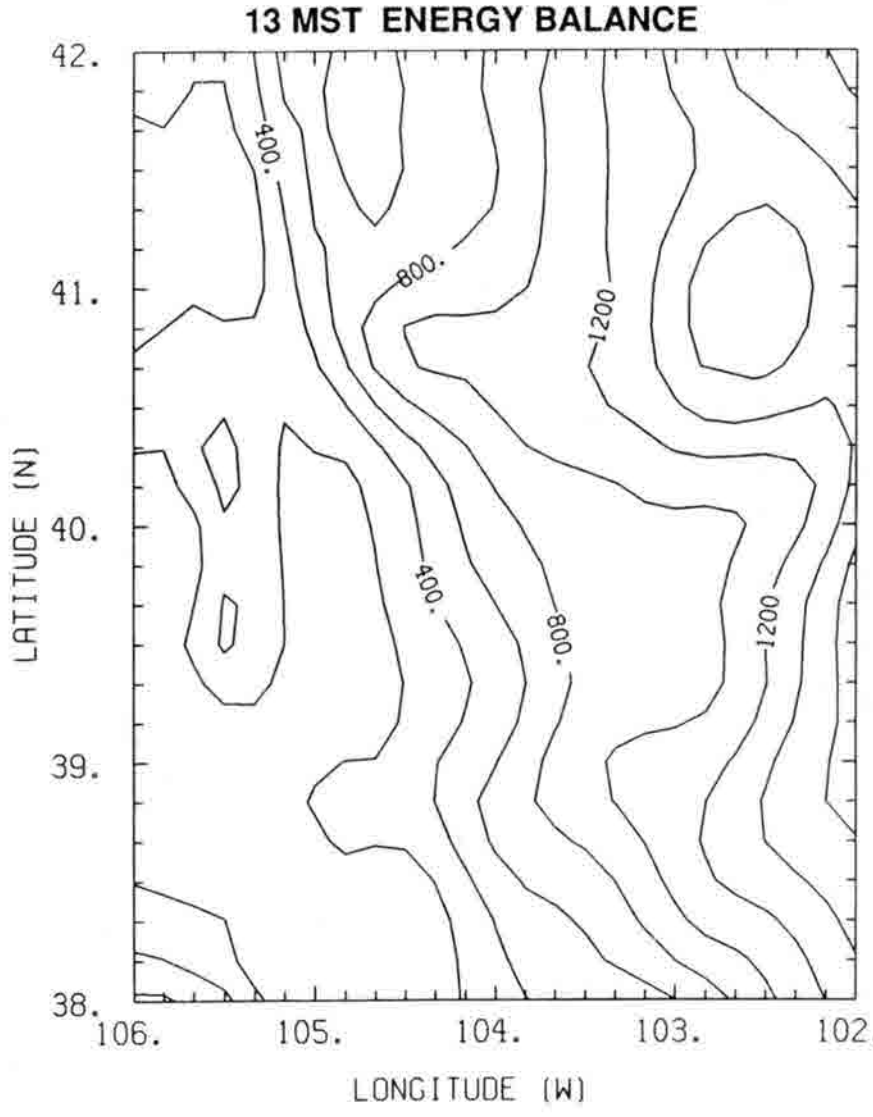

Figure 5.60 As in Fig. 5.57, but from the coupled analysis at 13 MST.

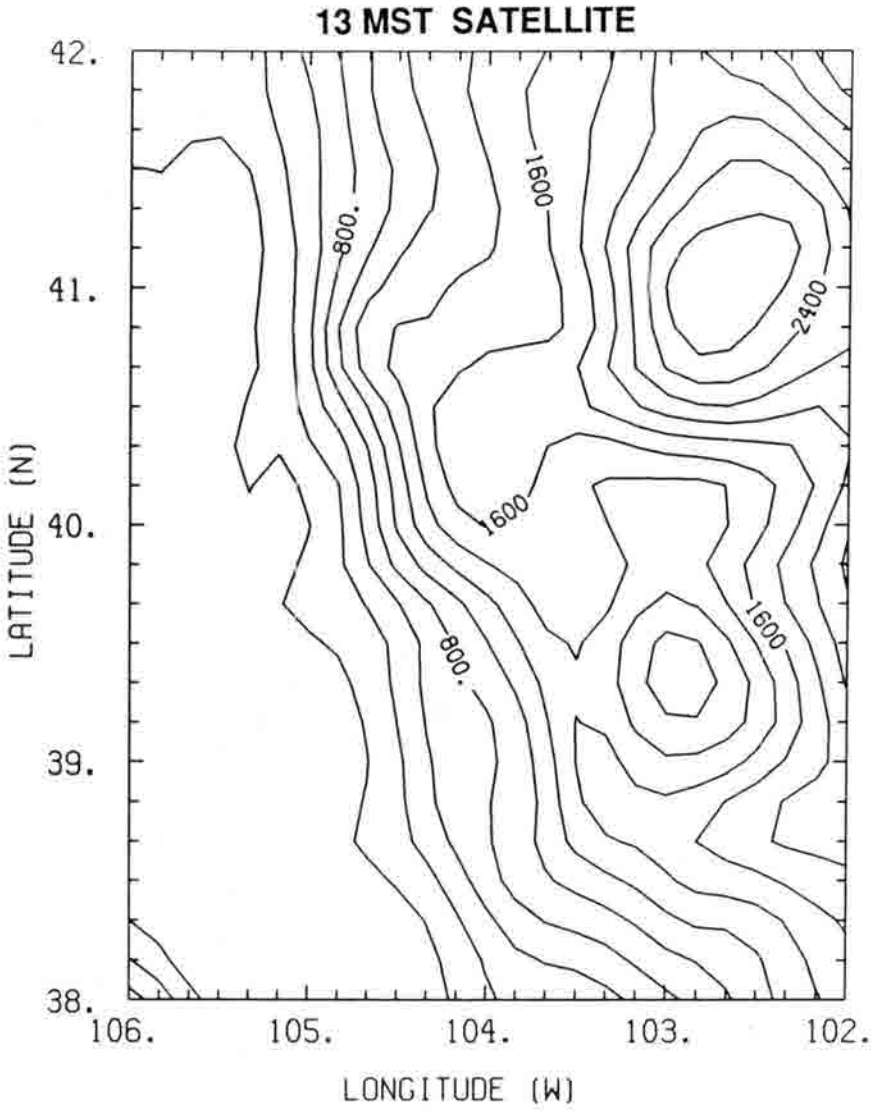

Figure 5.61 Positive buoyancy from the coupled, satellite-based analysis at 13 MST.

6.0 CONCLUSION

6.1 Sensitivity of Modeled Circulations

Two-dimensional model sensitivity experiments demonstrated the response of modeled circulations to the perturbations arising in a coupled analysis, under Northeastern Colorado summertime conditions. For water vapor mixing ratios, variations that might be caused by analysis errors had very little impact on circulations when phase changes were not a factor. This allowed time-continuous water vapor analysis methods to be compared without any need to account for feedback to the dynamics of the pre-convective flow at the mesoscale. Differences in estimates of water vapor concentrations become important to the dynamics only when the analyses are used to make forecasts of cloud development and associated phase changes.

Ground surface temperature variations, in contrast, were shown to have a large impact on circulations, so analysis errors are very relevant to pre-convective dynamics. When a relatively small contrast in surface temperature (2 K) was added to a basic plateau/plains gradient there was a very noticeable distortion of the basic circulation, about 12% of the unperturbed circulation strength. For reference, a moderate contrast of soil wetness (0.04 *vs.* 0.2) gave rise to a 7 K contrast in surface temperature at the end of a nine-hour daytime simulation. Sensitivity of winds to a domain-wide alteration of surface temperatures was smaller; a change of 2 K caused a wind speed change of about 5%. Systematic biases of this kind had an additional impact on boundary layer deepening, and are thus directly relevant to convective instability. Unsystematic surface temperature perturbations, in the form of random noise with 1-K standard deviation at 15-km resolution, resulted in substantially distorted flows. However, VAS-based surface temperature retrievals have random noise levels considerably below 1 K, so in simulated and real-data analysis the noise was small enough that its effect was very minor.

Sensitivity tests also addressed the modeling of changes in surface temperatures over time, since satellite data for making retrievals were available only at three-hour intervals for this study. It was found that three-hourly data fit with cubic splines could very accurately account for the diurnal cycle of surface temperatures.

6.2 Analysis Method Performance

Several time-continuous mesoscale analysis methods, including the coupled approach developed in the present study, were intercompared by means of two-dimensional simulations and a three-dimensional case study for 21 August 1983. Quantitative and qualitative intercomparisons lead to a number of the primary results of this dissertation as follows.

Simulated surface temperature analysis experiments were used to compare the use of satellite retrievals with the alternative of relying on energy balance computations. The energy balance computations were so sensitive to soil characteristics, which were simulated as unknown, that the satellite retrieval method gave better results even with cloud contamination.

In the case study the horizontal and time variations of satellite-retrieved surface temperatures closely corresponded to the conventional shelter temperature observations, but had much greater detail. Time-independent systematic biases were kept small by tuning some of the coefficients used in retrieval. In contrast, the energy balance-based temperatures tended to increase too quickly during the morning and lacked some of the observed gradients. According to the retrievals, there can be very large mesoscale gradients in temperatures at the ground surface even without the effects of mountain slopes, water bodies, or cloud shading.

The source of surface temperature data (energy balance or satellite) turned out to be important in evaluating some aspects of the case study circulations. Regardless of the source, the modeled horizontal winds matched most of the observed flow features, with some errors in areal coverages and intensities of features. It was inferred from the errors that the modeled background geostrophic wind was too strong and that topographical features beyond the model domain were relevant to the modeled flow. Surface temperature-related differences were more apparent in the vertical winds. In the energy balance-based case

vertical velocities were closely tied to terrain features, whereas in the satellite-based case the terrain-related updrafts were not much greater than updrafts related to ground surface temperature gradients. Thus, the results of the present study reinforce other findings that ground surface temperature gradient information is very important in mesoscale analysis and forecasting.

In water vapor analysis comparisons, no single satellite-based method was superior in every application. Stand-alone retrievals had poor vertical resolution, but resolved horizontal gradients within deep layers. The vertical resolution was much better when a model run provided time-varying initial guesses for retrievals, accounting for development of a deep mixed layer. Under some circumstances, an accurate time-continuous analysis could be derived from initializing the model with retrieved concentrations at the start of the analysis period and then integrating forward. This works well provided that the initialization data are not contaminated by clouds or other problems and that the model describes the flow very accurately. This initialized-model-run method worked poorly in the case study because the initialization data turned out to be unreliable due to a sensitivity problem. Those results illustrated a hazard of relying on a single set of satellite data.

A characteristic of the coupled analysis method that distinguishes it from the aforementioned methods is that its final result is dependent on several sets of satellite data. In the simulations it was shown that repeated insertion of data can result in smoothing of model-induced gradients, but that problem is avoided with the adjustment approach used in the coupled method. With repeated adjustment, analysis features that stem from data noise show up as inconsistencies and tend to be damped, while true features become more coherent. A drawback is that repeated adjustment tends to amplify any systematic biases stemming from the data or the retrieval process.

Contamination of retrieved data, by cloudiness or some other problem, highlights some of the pros and cons of the coupled method. When the first set of data is less reliable than the later sets (as in the case study) then some of the contamination lingers throughout the analysis period. In this situation the analyses at later times may not be as accurate as those produced by the modeled initial guess method. However, in pre-convective studies it is common for contamination to increase over time as small cumulus clouds form. When this

situation was simulated, coupled analyses were superior at the later times to those based on a modeled initial guess. This is significant because it suggests that the coupled method offers some relief from a substantial problem in applying infrared retrievals to pre-convective mesoscale analysis and to forecasting.

The coupled approach to mesoscale analysis provides a method for quality control. Some unreliable water vapor features were easily recognized as such in the case study analyses. The results also gave independent verification that modeled winds at mid-levels were weaker than the true winds. Coupling may be most useful when its capabilities for quality control are fully exploited. A preliminary analysis could be used to detect and correct any data problems through computer/person interaction, and then the final analysis could be made. Hollingsworth *et al.* (1986) advocated a similar kind of quality control feedback as a result of their data assimilation studies with a global scale model.

In general, the coupled method appeared to be the most valuable of the water vapor analysis methods considered in this study. It exploited the major strengths of the numerical model and the satellite data while making it relatively easy to recognize the impacts of their weaknesses.

6.3 Application of Analysis Results

In the case study, the results of the various analysis methods would tend to give a meteorologist a variety of impressions about the mesoscale distribution of water vapor, particularly when looking at surface values. The first-order effect was that the analyses with deeper mixing had much lower mixing ratios at the surface. A second effect was that mesoscale variations in low-level mixing ratios were tied to mesoscale variations in mixing depth. It was common for tongues of relatively high mixing ratios to have different locations and orientations in analyses generated by different methods. It could be quite deceptive, in terms of assessing convective potential, to know mixing ratio values at the surface but not be aware of mesoscale variations in the depth of the moist layer. These effects were most evident in comparing conventionally observed values to satellite-retrieved values and, among the satellite-based analyses, in comparing results of the stand-alone method to results of the other methods. The effects were also apparent when the only difference in preparing the

analyses was the source of surface temperature data. These findings further confirm that the usefulness of satellite sounder data at the mesoscale depends heavily on the method of interpretation.

Despite the differences between the analyses, some conclusions could be drawn regarding the water vapor kinematics in the case study. Mixing ratios near the mountains were strongly affected by interaction of mountain wave effects and slope flow. By late morning there was deep moisture just downwind of the main mountain range and the other prominent ridges, while moisture depth was suppressed in a band along the westernmost part of the plains. Water vapor movement resulted primarily from horizontal advection early on, but by the end of the morning vertical advection had a prominent effect. Evaporation from the ground also appeared to be a significant factor. These results support the hypothesis that both ground surface temperatures and terrain variations can play important roles in pre-convective water vapor kinematics.

The development of convective clouds, as revealed in satellite imagery, corresponded largely with the convergence and deepening of low-level water vapor depicted by the satellite/model system. Cloud formation and intensification corresponded very well with stability parameters from two of the analysis series' with satellite-derived surface temperatures. Cloud initiation was retarded in regions where subsidence gave rise to relatively large negative buoyant energies, and intensification was greatest in regions with relatively large positive buoyant energies. This information was very useful for understanding convective potential on the studied day, but it alone would not have given an unambiguous forecast.

6.4 Principal Results and Implications for Future Research

This dissertation has taken the merger of satellite sounding and mesoscale modeling beyond hopeful speculation and into practice. The research involved overcoming a number of practical problems, including the tendency for degradation of modeled gradients whenever satellite retrievals are inserted.

The results of the analysis experiments indicate that the coupled method of mesoscale analysis will be highly valuable in future applications because:

1. The results of the coupled method differ from results of other contemporary satellite-based methods in ways that are significant for weather forecasting. One positive difference is better definition of horizontal water vapor gradients.

2. The satellite/model combination produces more accurate water vapor analyses than the satellite alone. The advantage was large when the model's description of the flow was essentially perfect (in the simulations), but even with imperfect modeling (in the case study) the advantage was evident.

3. The coupled method allowed pre-convective water vapor kinematics to be described in greater detail than would have been possible with either the model or the satellite data alone.

4. The results demonstrated the great potential of using satellite-based retrievals of surface temperatures in analysis of individual mesoscale weather events.

5. The coupling framework provides checks of consistency on both the model performance and the satellite data.

Some guidance regarding future applications of the coupled method can be inferred from the relative strengths and weaknesses of analysis methods, as came to light in this research. An alternative to the fully coupled approach should be used when clouds are dissipating or breaking up during the pre-convective period, or when there is some other reason to believe that the early satellite data are relatively unreliable. On the other hand, the coupled method will be particularly advantageous when cloudiness increases during the analysis period. The surface temperature analysis results prompt a warning that models relying solely on energy balance computations will in some cases have significantly erroneous winds and boundary layer depths. This can happen even when cloud cover is not an issue. In general it will be best to stay flexible in applying the coupled method. Variations on the method may be used in response the given conditions.

Future research on coupled analysis should include application of the method to cases similar to the one studied in this dissertation. The experience would allow refinement of the method and would lead to a better understanding of the kinematics of the pre-convective

environment. Other types of meteorological situations could also be profitably studied with this approach. For some situations it would be necessary to use a model that includes synoptic scale forcing, cloud processes, or other factors.

There are many possibilities for further exploiting ground surface temperature information from satellites within the coupled system. Detailed comparisons of satellite- and energy balance-based surface temperatures may be highly profitable. In the case studied here, for example, it appeared that the energy balance-based temperatures warmed too quickly because soil wetnesses were too low. Quantitative comparisons and adjustments might give rise to improved estimates of evaporative fluxes. Numerical forecasts might also be improved since it is necessary to rely on energy balance computations for model integration beyond the time of the last satellite observations.

The basic framework of coupled analysis is general enough that a wide variety of atmospheric parameters and/or sources of data could be considered, not just ground surface temperatures and water vapor mixing ratios. Remotely sensed air temperatures and cloud characteristics would likely be very useful to include in this type of mesoscale analysis.

It will only be possible to fully assess the value and quality of coupled analysis products by comparing them with thorough mesoscale *in situ* observational data sets, which are rare. This would require several corresponding sets of VAS data and mesoscale upper air and surface measurements under conditions in which mesoscale data are relevant to a forecast of convective development. It would be important that ground surface skin temperatures are among the measured quantities.

REFERENCES

Abbs, D. J., and R. A. Pielke, 1986: Thermally forced surface flow and convergence patterns over northeast Colorado. *Mon. Wea. Rev.*, **114**, 2281–2296.

Anthes, R. A., 1984: Enhancement of convective precipitation by mesoscale variations in vegetative covering in semiarid regions. *J. Climate Appl. Meteor.*, **23**, 541–554.

Anthes, R. A., Y. M. Kuo, and J. R. Gyakum, 1983: Numerical simulations of a case of explosive marine cyclogenesis. *Mon. Wea. Rev.*, **111**, 1174–1188.

Aune, R. M., L. W. Uccellini, R. A. Petersen, and J. J. Tuccillo, 1987: A VAS-numerical model impact study using the Gal-Chen variational approach. *Mon. Wea. Rev.*, **115**, 1009–1035.

Austin, J. M, 1948: A note on cumulus growth in a nonsaturated environment. *J. Meteor.*, **5**, 103–107.

Baker, W. E., S. C. Bloom, J. S. Woollen, M. S. Nestler, E. Brin, T. W. Schlatter, and G. W. Branstator, 1987: Experiments with a three-dimensional statistical objective analysis scheme using FGGE data. *Mon. Wea. Rev.*, **115**, 272–296.

Banta, R. M., 1982: An Observational and Numerical Study of Mountain Boundary-Layer Flow. Ph.D. thesis and Atmospheric Science Paper No. 350, Dept. of Atmos. Sci., Colorado State Univ., Fort Collins, CO 80523, 203 pp.

Barnes, S. L., and D. K. Lilly, 1975: Covariance analysis of severe local storm environments. Preprints, Ninth Conf. on Severe Local Storms, Amer. Meteor. Soc., Boston, MA, 301–306.

Bates, J. J., and W. L. Smith, 1985: Sea surface temperature observations from geostationary satellites. *J. Geophys. Res.*, **90**, 11 609–11 618.

Beebe, R. G., and F. C. Bates, 1955: A mechanism for assisting in the release of convective instability. *Mon. Wea. Rev.*, **83**, 1–10.

Beran, D. W., and C. G. Little, 1979: Prototype Regional Observing and Forecasting Service: From concept to implementation. *Natl. Wea. Dig.*, **4**, No. 3, 2–5.

Bonner, W. D., and J. Paegle, 1970: Diurnal variations in boundary layer winds over the south-central United States in summer. *Mon. Wea. Rev.*, **98**, 735–744.

Braham, R. R., Jr., and M. Draginis, 1960: Roots of orographic cumuli. *J. Meteor.*, **17**, 214–226.

Chen, C.-H., and H. D. Orville, 1980: Effects of mesoscale convergence on cloud convection. *J. Appl. Meteor.*, **19**, 256–274.

Chesters, D., A. Mostek, and D. A. Keyser, 1986: VAS sounding images of atmospheric stability parameters. *Wea. Forecasting*, **1**, 5–22.

Chesters, D., and W. D. Robinson, 1983: Performance Appraisal of VAS Radiometry for GOES-4, -5 and -6. NASA Tech. Memo. 85125, Goddard Space Flight Center, Greenbelt, MD 20771.

Chesters, D., L. W. Uccellini, and A. Mostek, 1982: VISSR Atmospheric Sounder (VAS) simulation experiment for a severe storm environment. *Mon. Wea. Rev.*, **110**, 198–216.

Cho, H.-R., and Y. Ogura, 1974: A relationship between cloud activity and the low-level convergence as observed in Reed-Recker's composite easterly waves. *J. Atmos. Sci.*, **31**, 2058–2065.

Clark, T. L., and W. R. Peltier, 1977: On the evolution and stability of finite-amplitude mountain waves. *J. Atmos. Sci.*, **34**, 1715–1730.

Cram, J. M., and M. L. Kaplan, 1985: Variational assimilation of VAS data into a mesoscale model; assimilation method and sensitivity experiments. *Mon. Wea. Rev.*, **113**, 467–484.

Darkow, G. L., 1986: Basic thunderstorm energetics and thermodynamics. In *Thunderstorm Morphology and Dynamics*, 2nd ed., E. Kessler, ed., Univ. Oklahoma Press, 59–73.

de Vries, D. A., 1963: Thermal properties of soils. In *Physics of Plant Environment*, W. R. van Wijk, ed., North–Holland Publ., Amsterdam, 382 pp.

Defant, F., 1949: Zur Theorie der Hangwinde, nebst Bemerkungen zur Theorie der Berg-und Talwinde. *Archiv fur Meteorologie Geophysik und Bioklimatologie*, Ser. A, **1**, 421–450. English translation "A theory of slope winds, along with remarks on the theory of mountain winds and valley winds." In Alpine Meteorology: Translations of Classic Contributions by A. Wagner, E. Ekhart, and F. Defant. Report PNL-5141 ASCOT-84-3, C. D. Whiteman and E. Dreiseitl, 1984, Pacific Northwest Lab., Richland, WA, 95–121.

Defant, F., 1951: Local winds. In *Compendium of Meteorology*, T. F. Malone, ed., Amer. Meteor. Soc., Boston, MA, 655–672.

Dirks, R. A., 1969: A Climatology of Central Great Plains Mesoscale Convective Systems. Tech. Rep. Contract E-10-68G, Dept. of Atmos. Sci., Colorado State Univ., Fort Collins, CO 80523, 60 pp.

Dirks, R. A., J. D. Mahlman and E. R. Reiter, 1967: Evidence of a Mesoscale Wave Phenomenon in the Lee of the Rocky Mountains. Atmospheric Science Paper No. 115, Dept. of Atmos. Sci., Colorado State Univ., Fort Collins, CO 80523, 51 pp.

Douglas, S. G., and T. T. Warner, 1987: Utilization of VAS satellite data in the initialization of an oceanic cyclogenisis simulation. *Mon. Wea. Rev.*, **115**, 2996–3012.

Durran, D. R., 1986: Mountain waves. In *Mesoscale Meteorology and Forecasting*, P. S. Ray, ed., Amer. Meteor. Soc., Boston, MA, 472–492.

Fleming, H. E., and L. M. McMillin, 1977: Atmospheric transmittance of an absorbing gas 2: A computationally fast and accurate transmittance model for slant paths at different zenith angles. *Appl. Opt.*, **16**, 1366–1370.

Fuchs, M., and C. B. Tanner, 1966: Infrared thermometry of vegetation. *Agron. J.*, **58**, 597–601.

Gal-Chen, T., B. D. Schmidt, and L. W. Uccellini, 1986: Simulation experiments for testing the assimilation of geostationary satellite temperature retrievals into a numerical prediction model. *Mon. Wea. Rev.*, **114**, 1213–1230.

Haltiner, G. J. and R. T. Williams, 1980: *Numerical Prediction and Dynamic Meteorology*, 2nd ed., Wiley & Sons, 477 pp.

Hayden, C. M., 1973: Experiments in the four-dimensional assimilation of Nimbus 4 SIRS data. *J. Appl. Meteor.*, **12**, 425–436.

Henz, J. R., 1974: Colorado High Plains Thunderstorm Systems — A Descriptive Radar-Synoptic Climatology. M.S. thesis, Depart. of Atmos. Sci., Colorado State Univ., Fort Collins, Colorado 80523, 82 pp.

Hillger, D. W., 1984: Spatial and temporal variations in mesoscale water vapor retrieved from TOVS infrared radiances in a nocturnal inversion situation. *J. Climate Appl. Meteor.*, **23**, 704–723.

Hillger, D. W., and T. H. Vonder Haar, 1981: Retrieval and use of high-resolution moisture and stability fields from Nimbus-6 HIRS radiances in pre-convective situations. *Mon. Wea. Rev.*, **109**, 1788–1806.

Hillger, D. W., and T. H. Vonder Haar, 1988: Estimating noise levels of remotely-sensed measurements from satellites using spatial structure analysis. *J. Atmos. Ocean. Tech.*, **5**, 206–214.

Hoke, J. E., and R. A. Anthes, 1976: The initialization of numerical models by a dynamic-initialization technique. *Mon. Wea. Rev.*, **104**, 1551–1556.

Hollingsworth, A., D. B. Shaw, P. Lönnberg, L. Illari, K. Arpe, and A. J. Simmons, 1986: Monitoring of observation and analysis quality by a data assimilation system. *Mon. Wea. Rev.*, **114**, 861–879.

Holton, J. R., 1967: The diurnal boundary layer wind oscillation above sloping terrain. *Tellus*, **19**, 199–205.

Klemp, J. B., and D. K. Lilly, 1975: The dynamics of wave-induced downslope winds. *J. Atmos. Sci.*, **32**, 320–339.

Klemp, J. B., and D. K. Lilly, 1978: Nonlinear numerical simulation of hydrostatic mountain waves. *J. Atmos. Sci.*, **35**, 78–107.

Klitch, M. A., J. F. Weaver, F. P, Kelly, and T. H. Vonder Haar, 1985: Convective cloud climatologies constructed from satellite imagery. *Mon. Wea. Rev.*, **113**, 326–337.

Kreitzberg, C. W., 1976: Interactive applications of satellite observations and mesoscale numerical models. *Bull. Amer. Meteor. Soc.*, **57**, 679–685.

Link, L. E., 1979: Thermal modeling of battlefield scene components. Miscellaneous Paper EL-79-5, U.S. Army Engineer Waterways Experiment Station, CE, Vicksburg, MS.

Lipton, A. E., and D. W. Hillger, 1982: Objective analysis of discontinuous satellite-derived data fields for grid point interpolation. *J. Appl. Meteor.*, **21**, 1571–1581.

Liu, W.–Y., R. T. Field, R. G. Gantt, and V. Klemas, 1987: Measurement of the surface emissivity of turbid waters. *Rem. Sens. Envir.*, **21**, 97–109.

Mahrer, Y., and R. A. Pielke, 1977: A numerical study of the air flow over irregular terrain. *Con. Atmos. Phy.*, **50**, 98–113.

Mahrer, Y., and R. A. Pielke, 1978: A test of an upstream spline interpolation technique for the advective terms in a numerical mesoscale model. *Mon. Wea. Rev.*, **106**, 818–830.

Mahrt, L., 1977: Influence of low-level environment on severity of high-plains moist convection. *Mon. Wea. Rev.*, **105**, 1315–1329.

McCumber, M. C., and R. A. Pielke, 1981: Simulation of the effects of surface fluxes of heat and moisture in a mesoscale numerical model. Part I: Soil layer. *J. Geophys. Res.*, **86**, 9929–9938.

McMillin, L. M., and H. E. Fleming, 1976: Atmospheric transmittance of an absorbing gas: A computationally fast and accurate transmittance model for absorbing gases with constant mixing ratios in homogeneous atmospheres. *Appl. Opt.*, **15**, 358–363.

McNider, R. T., and R. A. Pielke, 1981: Diurnal boundary layer development over sloping terrain. *J. Atmos. Sci.*, **38**, 2198–2212.

Menzel, W. P., W. L. Smith, G. S. Wade, L. D. Herman, and C. M. Hayden, 1983: Atmospheric sounding from a geostationary satellite. *Appl. Opt.*, **22**, 2686–2689.

Modahl, A. C., 1979: Synoptic parameters as discriminators between hailfall and less significant convective activity in northeast Colorado. *J. Appl. Meteor.*, **18**, 671–681.

Mostek, A., L. W. Uccellini, R. A. Petersen, and D. Chesters, 1986: Assessment of VAS soundings in the analysis of a preconvective environment. *Mon. Wea. Rev.*, **114**, 62–87.

National Climate Data Center, 1983: Hourly Precipitation Data, Colorado, **33**, No. 8. NCDC, Federal Bldg., Asheville, NC 28801.

Njoku, E. G., T. P. Barnett, R. M. Laurs and A. C. Vastano, 1985: Advances in satellite sea surface temperature measurements and oceanographic applications. *J. Geophys. Res.*, **90**, 11 573–11 586.

O'Lenic, E. A., 1986: The effect of VISSR Atmospheric Sounder data on some LFM analyses and forecasts. *MonẆea. Rev.*, **114**, 1832–1846.

Ookouchi, Y., M. Segal, R. C. Kessler and R. A. Pielke, 1984: Evaluation of soil moisture effects on the generation and modification of mesoscale circulations. *MonẆea. Rev.*, **112**, 2281–2292.

Orville, H. D., 1964: On mountain upslope winds. *J. Atmos. Sci.*, **21**, 622–633.

Orville, H. D., 1965: A numerical study of the initiation of cumulus clouds over mountainous terrain. *J. Atmos. Sci.*, **22**, 684–699.

Orville, H. D., 1968: Ambient wind effects on the initiation of development of cumulus clouds over mountains. *J. Atmos. Sci.*, **25**, 385–403.

Peltier, W. R., and T. L. Clark, 1979: The evolution and stability of finite-amplitude mountain waves. Part II: Surface wave drag and severe downslope windstorms. *J. Atmos. Sci.*, **36**, 1498–1529.

Pielke, R. A., 1974: A three dimensional numerical model of the sea breeze over south Florida. *Mon. Wea. Rev.*, **102**, 115–134.

Pielke, R. A., 1984: *Mesoscale Meteorological Modeling*, Academic Press, Orlando, FL, 455–495.

Pielke, R. A., and M. Segal, 1986: Mesoscale circulations forced by differential terrain heating. In *Mesoscale Meteorology and Forecasting*, P. S. Ray, ed., Amer. Meteor. Soc., Boston, MA, 516–548.

Purdom, J. F. W., 1982: Subjective interpretation of geostationary satellite data for nowcasting. In *Nowcasting*, K. A. Browning, ed., Academic Press, 149–166.

Scorer, R., 1949: Theory of waves in the lee of mountains. *Quart. J. Roy. Meteor. Soc.*, **75**, 41–56.

Schwalb, A., 1985: GOES-Next Overview. Envirosat–2000 Report, NOAA/National Satellite, Data and Information Service, Washington, DC.

Segal, M., R. Avissar, M. C. McCumber, and R. A. Pielke, 1988a: Evaluation of vegetation effects on the generation and modification of mesoscale circulations. *J. Atmos. Sci.* (in press).

Segal, M., and R. A. Pielke, 1981: Numerical model simulation of human biometeorological heat load conditions — Summer day case study for the Chesapeake Bay area. *J. Appl. Meteor.*, **20**, 735–749.

Segal, M., W. E. Schreiber, G. Kallos, J. R. Garratt, A. Rodi, J. Weaver, and R. A. Pielke, 1988b: The impact of crop areas in Northeast Colorado on mid-summer mesoscale thermal circulations. *Mon. Wea. Rev.* (under review).

Smith, D. L., F. L. Zuckerberg, J. T. Schaefer and G. E. Rasch, 1986: Forecast problems: The meteorological and operational factors. In *Mesoscale Meteorology and Forecasting*, P. S. Ray, ed., Amer. Meteor. Soc., Boston, MA, 36–49.

Smith, W. L., 1970: Iterative solution of the radiative transfer equation for temperature and absorbing gas profiles of an atmosphere. *Appl. Opt.*, **9**, 1993–1999.

Smith, W. L., 1983: The retrieval of atmospheric profiles from VAS geostationary radiance observations. *J. Atmos. Sci.*, **40**, 2025–2035.

Smith, W. L., H. M. Woolf, P. G. Abel, C. M. Hayden, M. Chalfant, and N. Grody, 1974: Nimbus-5 Sounder Data Processing System, Part I: Measurement Characteristics and Data Reduction Procedures. NOAA Tech. Memo. NESS 57, 99 pp.

Taylor, S. E., 1979: Measured emissivity of soils in the southeast United States. *Rem. Sens. Envir.*, **8**, 359–364.

Toth, J. J., and R. H. Johnson, 1985: Summer surface flow characteristics over northeast Colorado. *Mon. Wea. Rev.*, **113**, 1458–1469.

Tripoli, G. J, 1986: A Numerical Investigation of an Orogenic Mesoscale Convective System. Ph.D. thesis and Atmospheric Science Paper No. 401, Dept. of Atmos. Sci., Colorado State Univ., Fort Collins, CO 80523, 290 pp.

Ulanski, S. L., and M. Garstang, 1978: The role of surface divergence and vorticity in the life cycle of convective rainfall. Part I: Observation and Analysis. *J. Atmos. Sci.*, **35**, 1047–1062.

U. S. Standard Atmosphere, 1976. Published by NOAA, NASA, USAF. U. S. Govt. Printing Office, Washington, DC 20402.

Wagner, A., 1938: Theorie und Beobachtung der periodischen Gebirgswind. *Gerlands Beitrage zur Geophisik*, **52**, 408–449. English translation "Theory and observation of periodic mountain winds" in Alpine Meteorology: Translations of Classic Contributions by A. Wagner, E. Ekhart, and F. Defant. Report PNL-5141 ASCOT-84-3, C. D. Whiteman and E. Dreiseitl, 1984, Pacific Northwest Lab., Richland, WA, 95–121.

Weinreb, M. P., and A. C. Neuendorffer, 1973: Method to apply homogeneous path transmittance models to inhomogeneous atmospheres. *J. Atmos. Sci.*, **30**, 662–666.

Yan, H., and R. A. Anthes, 1988: The effect of variations in surface moisture on mesoscale circulations. *Mon. Wea. Rev.*, **116**, 192–208.

Zhang, D., and R. A. Anthes, 1982: A high-resolution model of the planetary boundary layer – Sensitivity tests and comparisons with SESAME-79 data. *J. Appl. Meteor.*, **21**, 1594–1609.

APPENDIX A

RETRIEVAL MECHANISMS

A.1 VAS Channel Usage

In the simulation experiments (Chap. 4) it was assumed that the earth's surface behaved as a black body at infrared wavelengths and thus there was no reflected solar radiation. Therefore, it was straightforward to use every VAS channel for retrieval, using each for its principal purpose (Table 2.1).

In the case study (Chap. 5) it was necessary to account for the spectral variation of the earth's emittance and for solar radiation. There was also the practical consideration that channel 11 was out of operation. There are significant amounts of solar radiation only at the relatively short wavelengths, so most of the channels are unaffected by it. The affected channels (6 and 12) were omitted from daytime case study retrievals because of the large uncertainties involved in computing solar reflection. Channel 12 was also omitted from nighttime retrievals because its radiances are very sensitive to the surface emittance, which cannot be accurately estimated at that wavelength. Channel 8 was used for retrieving air temperatures as well as surface temperatures. The assumed emmittance values are in Table A.1.

Table A.1 Surface emittances for case-study retrievals

Channel	Emittance	Channel	Emittance
1	0.98	6	0.90
2	0.98	7	0.98
3	0.98	8	0.95
4	0.98	9	0.98
5	0.98	10	0.98

These values are appropriate for terrestrial surfaces (Taylor, 1979; Fuchs and Tanner, 1966) and were chosen so that radiances computed from the Denver morning radiosonde would agree with the corresponding observed radiances.

A.2 Temperature Profile Adjustment

The temperature adjustment formula given by Smith (1983) was used with two minor modifications. The temperature at pressure level p_k at iteration $n+1$ is

$$T^{n+1}(p_k) = T^n(p_k) + \frac{\sum_{j=1}^{M_t} W^n(\nu_j, p_k, \theta)[T_B(\nu_j) - T_B^n(\nu_j)]Z^n(\nu_j,\theta)^{-1}}{\sum_{j=1}^{M_t} W^n(\nu_j, p_k, \theta)} \qquad \text{(A.1)}$$

where W is a weighting function, ν_j is the representative wavenumber for channel j, θ is the local zenith angle of the satellite, T_B is an observed VAS brightness temperature, T_B^n is a computed VAS brightness temperature at iteration n, Z is a response factor, and M_t is the number of channels used for temperature retrieval. The choice of W was

$$W^n(\nu, p, \theta) = \left[\frac{\partial B(\nu, T^n)/\partial T}{\partial B(\nu, T_B^n)/\partial T}\right] \delta\tau^n(\nu, p, \theta), \qquad \text{(A.2)}$$

where B is the Plank radiance and τ is the transmittance, each integrated over the spectral response of a VAS channel.

The response factor is

$$Z^n(\nu,\theta) = \left[\frac{\partial B(\nu, T_s^n)/\partial T}{\partial B(\nu, T_B^n)/\partial T}\right] \tau^n(\nu, p_s, \theta) + \sum_{k=1}^{K} \left[\frac{\partial B(\nu, T^n)/\partial T}{\partial B(\nu, T_B^n)/\partial T}\right] \delta\tau^n(\nu, p_k, \theta), \qquad \text{(A.3)}$$

where the subscript s refers to values at the ground surface, and K is the number of atmospheric levels. Division of the brightness temperature difference by Z takes account of the responsiveness of the brightness temperature in a given channel to changes in atmospheric temperature, and it arises because the Plank function is non-linear with respect to temperature.

A.3 Surface Temperature Adjustment

Formula (A.1) is based on the assumption that the brightness temperature difference in a given channel arises from an error in temperature that is constant over the depth that the channel senses. A similar assumption is possible in deriving a surface temperature adjustment formula, but it would be inappropriate under some circumstances. During the first iteration it is likely that the surface temperature guess (T_s^n, $n = 1$) is less accurate than the atmospheric temperature profile guess since surface temperature varies greatly in space and time. The assumption can be quantified through

$$T(p) - T^n(p) = x\,[T_s - T_s^n] \quad (0 \le x), \tag{A.4}$$

where true values have no superscript, and x indicates relative expected errors.

The surface temperature adjustment formula incorporated (A.4) such that

$$T_s^{n+1} = T_s^n + \frac{\sum_{j=1}^{M_s} W_s^n(\nu_j,\theta)\,[T_B(\nu_j) - T_B^n(\nu_j)]\,F^n(\nu_j,\theta)^{-1}}{\sum_{j=1}^{M_s} W_s^n(\nu_j,\theta)}, \tag{A.5}$$

where the weighting factors were

$$W_s^n(\nu,\theta) = \left[\frac{\partial B(\nu,T_s^n)/\partial T}{\partial B(\nu,T_B^n)/\partial T}\right] \tau^n(\nu,p_s,\theta), \tag{A.6}$$

and

$$F^n(\nu,\theta) = \left[\frac{\partial B(\nu,T_s^n)/\partial T}{\partial B(\nu,T_B^n)/\partial T}\right] \{\tau^n(\nu,p_s,\theta) + x[\,1 - \tau^n(\nu,p_s,\theta,]]\}\,. \tag{A.7}$$

The choices of x were $x = 0.5$ on the first iteration and $x = 1.0$ on subsequent iterations. The bracketed ratio in (A.7) accounts for the responsiveness of each channel to surface temperature changes.

A.4 Water Vapor Profile Adjustment

The formula used for water vapor profile adjustment is from Smith (1970), and can be written

$$q^{n+1}(p_k) = q^n(p_k)\left\{1 + \frac{\sum_{j=1}^{M_v} W_v^n(\nu_j,p_k,\theta)\,[L(\nu_j) - L^n(\nu_j)]\,S^n(\nu_j,\theta)^{-1}}{\sum_{j=1}^{M_v} W_v^n(\nu_j,p_k,\theta)}\right\}, \tag{A.8}$$

where q is water vapor mixing ratio, W_v is a weighting function, L is a radiance, and S is a response factor. The W_v are

$$W_v^n(\nu,p,\theta) = \left[\frac{\partial\tau^n(\nu,p,\theta)}{\partial U^n(p)}\right] dB\left[\nu,T^n(p)\right], \tag{A.9}$$

where

$$U^n(p) = \frac{1}{g}\int_0^p q^n(p)dp \tag{A.10}$$

is the precipitable water. In addition,

$$S^n(\nu,\theta) = \int_{B[\nu,T^n(p_t)]}^{B[\nu,T_s^n]} U^n(p)\left[\frac{\partial\tau^n(\nu,p,\theta)}{\partial U^n(p)}\right] dB(\nu,T), \tag{A.11}$$

where t denotes the top of the atmosphere.

Problems can arise with the use of (A.8) when the part of the atmosphere sensed by a given channel is nearly isothermal. As $\frac{dB}{dp}$ approaches zero S also approaches zero and the adjustment to q becomes very sensitive to small radiance differences, including differences cause by noise. To avoid this problem a limit was put on S such that

$$\hat{S} = \begin{cases} S & |S| \geq S_c \\ \pm\ S_c & |S| < S_c \end{cases}, \tag{A.12}$$

where $\hat{S}$ was substituted for S in (A.8). The cutoff value S_c was chosen such that the adjustment of q caused by a radiance difference equal to the expected radiance noise would not exceed 5% per iteration. The derivation of S_c began with

$$q^{n+1} = q^n\left[1 + \frac{(L-L^n)}{S^n}\right], \tag{A.13}$$

which gives the adjustment to q specified for a single channel (in analogy with eq. A.8). Rewriting (A.13) in terms of a proportional change yields

$$Q \equiv \frac{q^{n+1}-q^n}{q^n} = \frac{L-L^n}{S^n}. \tag{A.14}$$

The specified condition was that (A.14) be satisfied for $Q = Q_c = 0.05$, $L - L^n = \epsilon_L$, and $S^n = S_c$, so

$$S_c = \frac{\epsilon_L}{Q_c}, \tag{A.15}$$

where ϵ_L is an expected noise value, as given in Table 2.1.

A.5 Retrieval Procedures

The basic steps in retrieval were:

1. Specify initial guesses of surface temperature and profiles of atmospheric temperature and water vapor.

2. Compute transmittances and T_B^n for the surface temperature channels.

3. Compute W_S^n and F^n for the surface channels, and compute a new estimate of surface temperature.

4. Compute transmittance and T_B^n for the longwave atmospheric temperature channels using the updated surface temperature T_S^{n+1}.

5. Compute W^n and Z^n for the temperature channels, and compute a new estimate of atmospheric temperature at each level in the vertical.

6. Compute transmittances and L^n for the water vapor channels using the updated temperatures T^{n+1}.

7. Compute U^n, W^n, and S^n for the water vapor channels, and compute a new estimate of mixing ratio at each level.

8. Recompute transmittances and compute T_B^{n+1} for all channels, using the updated mixing ratios q^{n+1}.

9. Go back to step 3, unless any one convergence criterion is satisfied.

The convergence criteria were intended to emphasize accuracy in the water vapor profile, and were based on root-mean-square residuals

$$R_t^n = \left\{ \sum_{j=1}^{M_t} [T_B^n(\nu_j) - T_B(\nu_j)]^2 \right\}^{1/2},$$

$$R_s^n = \left\{ \sum_{j=1}^{M_s} [T_B^n(\nu_j) - T_B(\nu_j)]^2 \right\}^{1/2}, \text{ and}$$

$$R_v^n = \left\{ \sum_{j=1}^{M_v} [T_B^n(\nu_j) - T_B(\nu_j)]^2 \right\}^{1/2},$$

as compared with root-mean-square noise estimates

$$E_t = \left[\sum_{j=1}^{M_t} \epsilon_T(\nu_j)^2 \right]^{1/2}$$

$$E_s = \left[\sum_{j=1}^{M_s} \epsilon_T(\nu_j)^2 \right]^{1/2}$$

$$E_v = \left[\sum_{j=1}^{M_v} \epsilon_T(\nu_j)^2 \right]^{1/2}.$$

The criteria were:

1. Stop if at least three iterations have been done and

$$R_t^n - R_t^{n+1} < -E_t/5 \text{ and } R_t^{n+1} > E_t$$

or

$$R_s^n - R_s^{n+1} < -E_s/5 \text{ and } R_s^{n+1} > E_s.$$

This checks for significant divergence of the temperature profile and surface temperature residuals, and indicates poor performance of the retrieval procedure.

2. Stop if

$$R_t^n - R_t^{n+1} < E_t/10 \text{ and } R_v^n - R_v^{n+1} < E_t/10$$

or if

$$R_t^n - R_t^{n+1} \geq E_t/10 \text{ and } R_v^n - R_v^{n+1} < -(R_t^n - R_t^{n+1}).$$

This checks for water vapor profile convergence, with the stipulation that iteration stops if water vapor residuals are not decreasing fast enough to compensate for any simultaneous increase in temperature residuals.

3. Stop if

$$R_v^{n+1} < E_v \text{ and } R_t^{n+1} < E_t \text{ and } R_s^{n+1} < E_s.$$

There were options to ignore criterion 3, or to retrieve only surface temperature by halting the retrieval procedure after step 3 on the first iteration ("quick" surface temperature retrieval).

The retrieval procedure could be manipulated to allow retrieving surface temperatures at double the resolution of the atmospheric retrievals. First, surface temperatures and atmospheric parameters (temperatures and water vapor concentrations) were retrieved at low resolution using the 9-step iterative method. Then a crude scheme was used to interpolated the full retrieval results to the high-resolution sites. At each high-resolution site the interpolated surface temperatures were taken to be simple averages of any low-resolution surface temperature retrievals within a distance of one high-resolution line or element. The same interpolation scheme was used for atmospheric parameters except over the mountains, where atmospheric retrievals were unreliable. Over mountains (surface pressure < 79 kPa) the interpolated atmospheric parameters were averages from at least three of the nearest non-mountain low-resolution retrievals. Finally, the interpolated data were used as initial guesses for "quick" surface temperature retrievals at the high-resolution sites.

APPENDIX B

EXPERIMENTS WITH INITIAL/BOUNDARY CONDITIONS IN CASE-STUDY MODELING

The model initial and boundary conditions were tested in two-dimensional runs before any three-dimensional runs were attempted. The purpose was to find the most appropriate input values for the particular case being studied, without consuming much computer time. The domain was a vertically oriented east/west cross section passing roughly through Denver, Colorado.

Within the two-dimensional experiments, changes in the surface roughness length (z_0) over the mountains produced some interesting changes in the circulations. Runs were made with $z_0 = 3$ cm throughout the domain (bare mountain), and with $z_0 = 100$ cm at terrain elevations above 2300 m, $z_0 = 3$ cm below 1800 m, and a linear interpolation for intermediate elevations (forested mountain). The handling of z_0 for the forested mountain was intended to simulate eastern Colorado conditions, where the plains are largely rolling grassland and at about 1800 m elevation there is a shift toward more rugged terrain and denser stands of trees with heights up to about 10 m. All other model input parameters were the same as in the three-dimensional runs, except for a small difference in the initial temperature profile. In both the bare and forested mountain simulations, six hours of dynamic initialization led up to 17 MST, and the simulations continued for another six hours with radiative forcing.

At 17 MST the westerly wind components (Fig. B.1a,b) had a mountain wave structure with a maximum near the surface of the downwind slope and a local minimum above it. The north/south wind components (Fig. B.1c,d) had a northerly jet just eastward of the westerly wind maximum. The northerlies appeared to result from turning of the westerlies in response to the Coriolis force. The difference in surface roughness affected both the magnitude and position of the wind maxima and minima. They were displaced upward and westward and were weakened with the increase in roughness. The roughness change

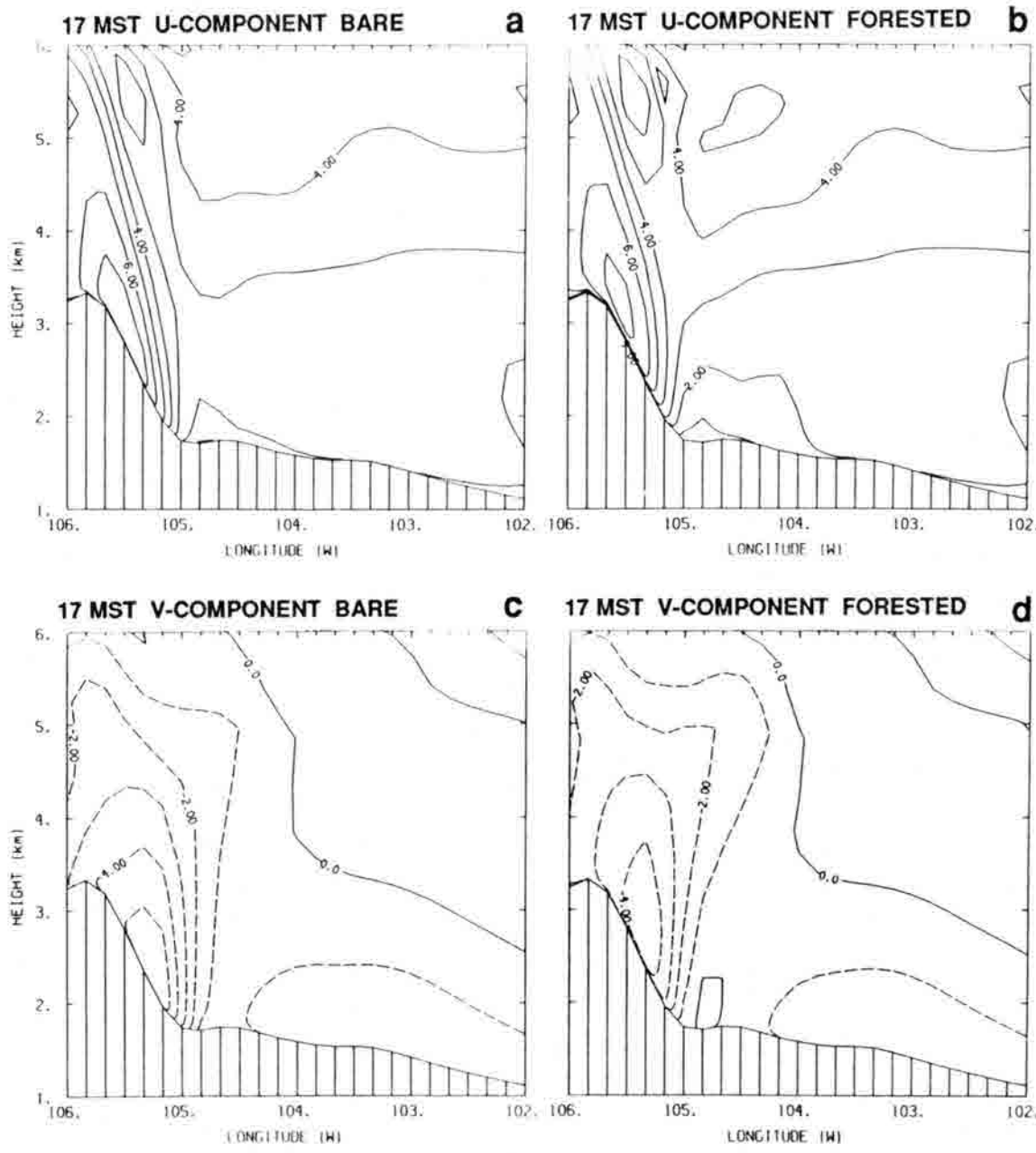

Figure B.1 Wind components of two-dimensional initialization parameter tests at 17 MST. Frames are a) westerly component, bare mountain, b) westerly component, forested mountain, c) southerly component, bare mountain, d) southerly component, forested mountain. Heights are relative to mean sea level. Contours are at intervals of 0.5 m/s.

had a bigger impact on the northerlies than on the westerlies. This is reasonable since the westerlies must move a prescribed amount of mass across the mountain (via the boundary conditions), whereas the northerlies are just a response to the local forcing.

The difference in westerly winds between the bare and forested cases was greater by 23 MST (Fig. B.2a,b), when nocturnal drainage was active. However, the northerlies (Fig. B.2b,c) were more similar at 23 MST than at 17 MST. In general, wind differences were confined to the lowest 1 km above ground.

After sunset the forcing of the northerly jet changed greatly. Surface drag was vastly reduced, allowing the northerlies to be controlled by the local pressure gradient, the Coriolis force and momentum advection. It appears that those forces differed little between the two simulations at the position of the jet maximum. With reference to the westerlies, it appears that the surface roughness plays an important role in the interaction of the mountain wave with the drainage flow.

Other two-dimensional experiments were conducted in which the mountain wave effect was eliminated by reducing the background geostrophic flow to 0.5 m/s from the south. The differences in westerly winds at 23 MST (Fig. B.3a,b) were not as great as the differences with mountain wave effects (Fig. B.2a,b), but it is difficult to compare the two since the frictional forces themselves depend on wind speed. One outstanding feature of the north/south wind plots (Fig. B.3c,d) is the position and intensity of the maxima and minima, relative to those resulting from a mountain wave influence (Fig. B.2c,d). Without the wave effect the northerlies were weak and confined to a very shallow layer overlaid by southerlies. Figures B.1c and d represent the pure wave effect, since no drainage was present at 17 MST. A three-way comparison of frames c and d between figures B.1, 2, and 3 reveals that the characteristics of the northerly jet are very sensitive to the interaction of the mountain wave with the drainage effect.

The background geostrophic winds also had a significant influence on nocturnal low-level air temperatures. In a thin layer over the upper plains the air was more than 4 K warmer when the mountain wave was present than when it was not (Fig. B.4), regardless of the z_0 value. The cause of the warming appeared to be turbulent mixing, since a cool layer

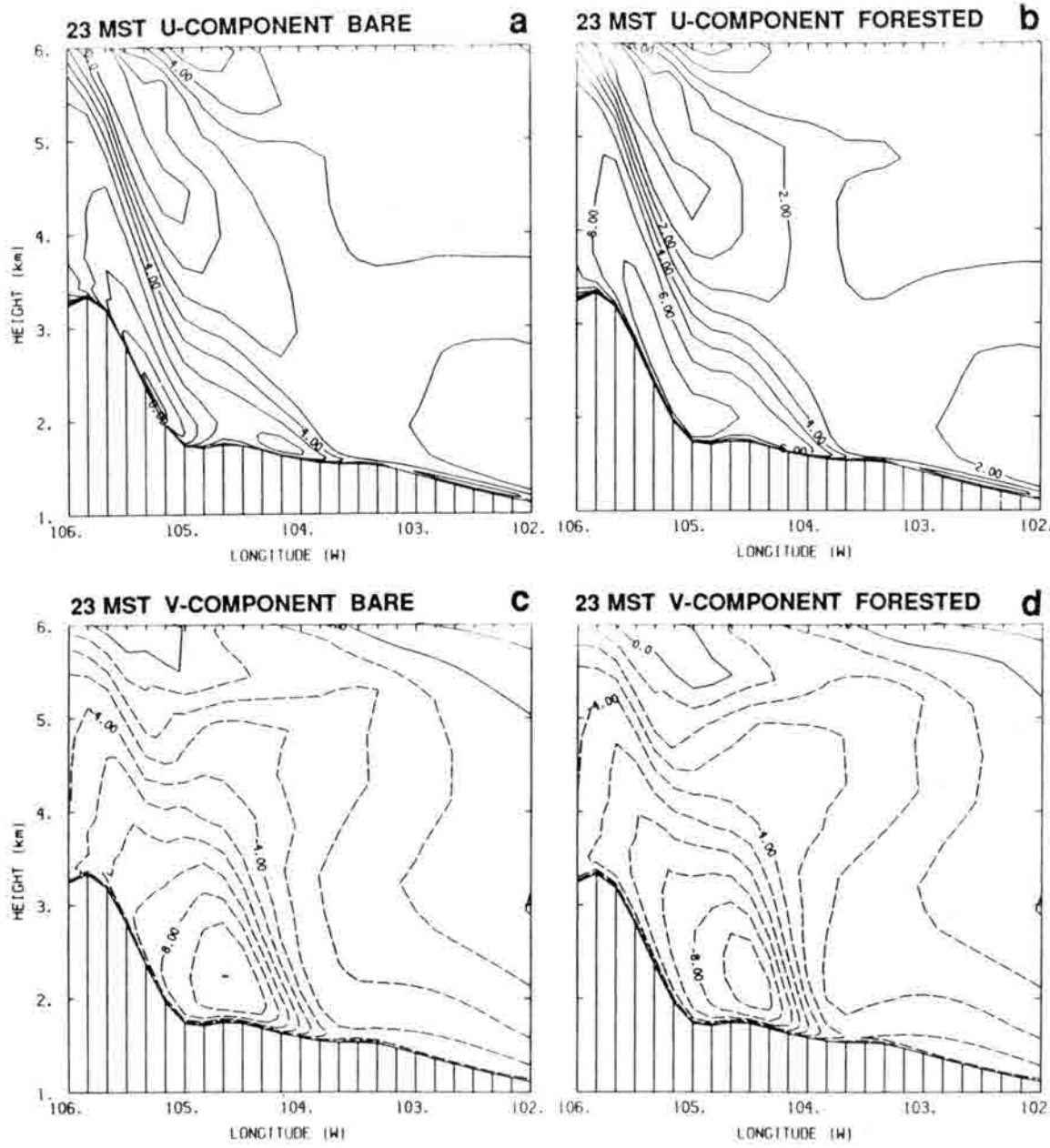

Figure B.2 As in B.1, but for 23 MST.

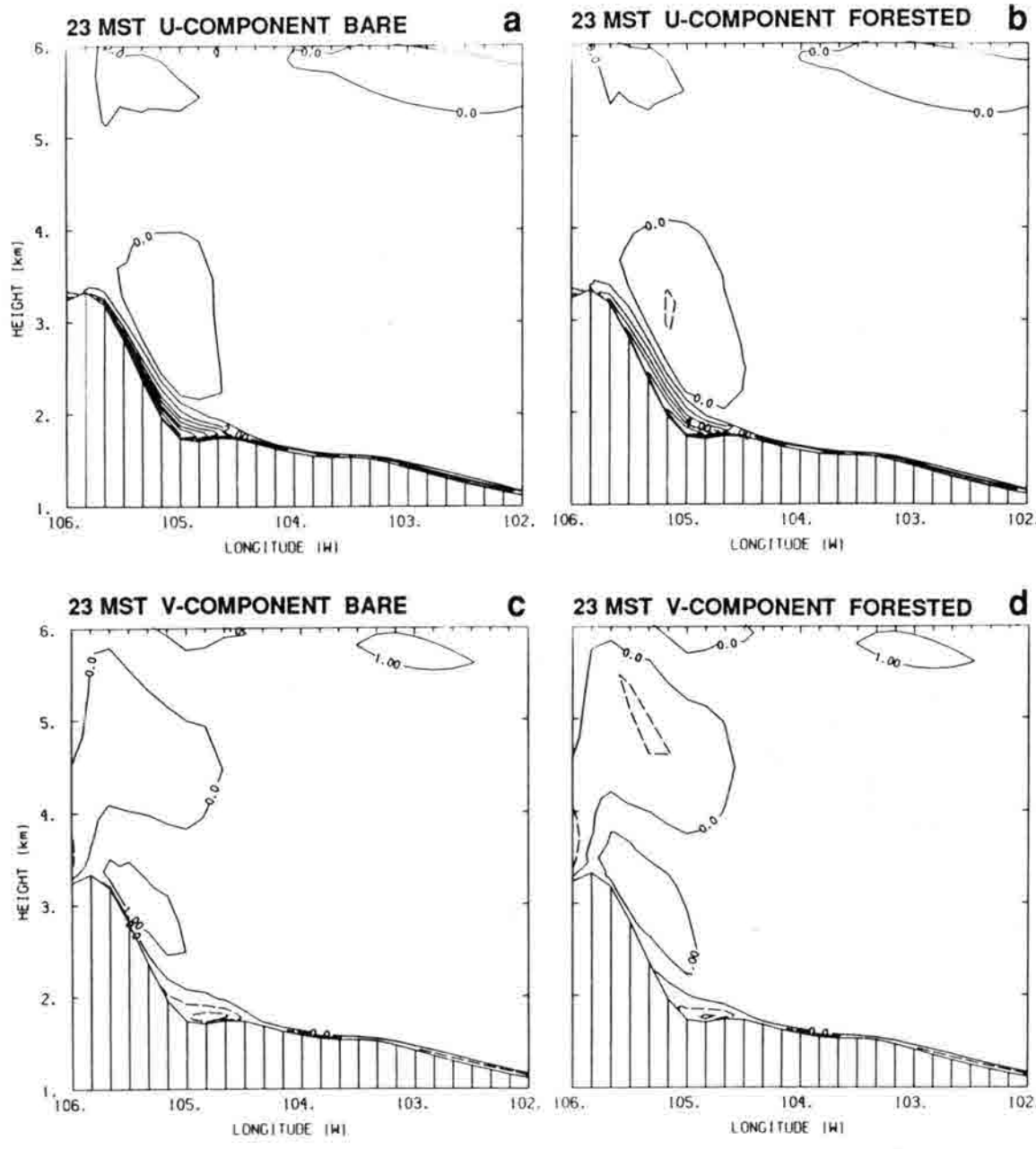

Figure B.3 As in B.2, but for a case with background geostrophic winds of 0.5 m/s from the south.

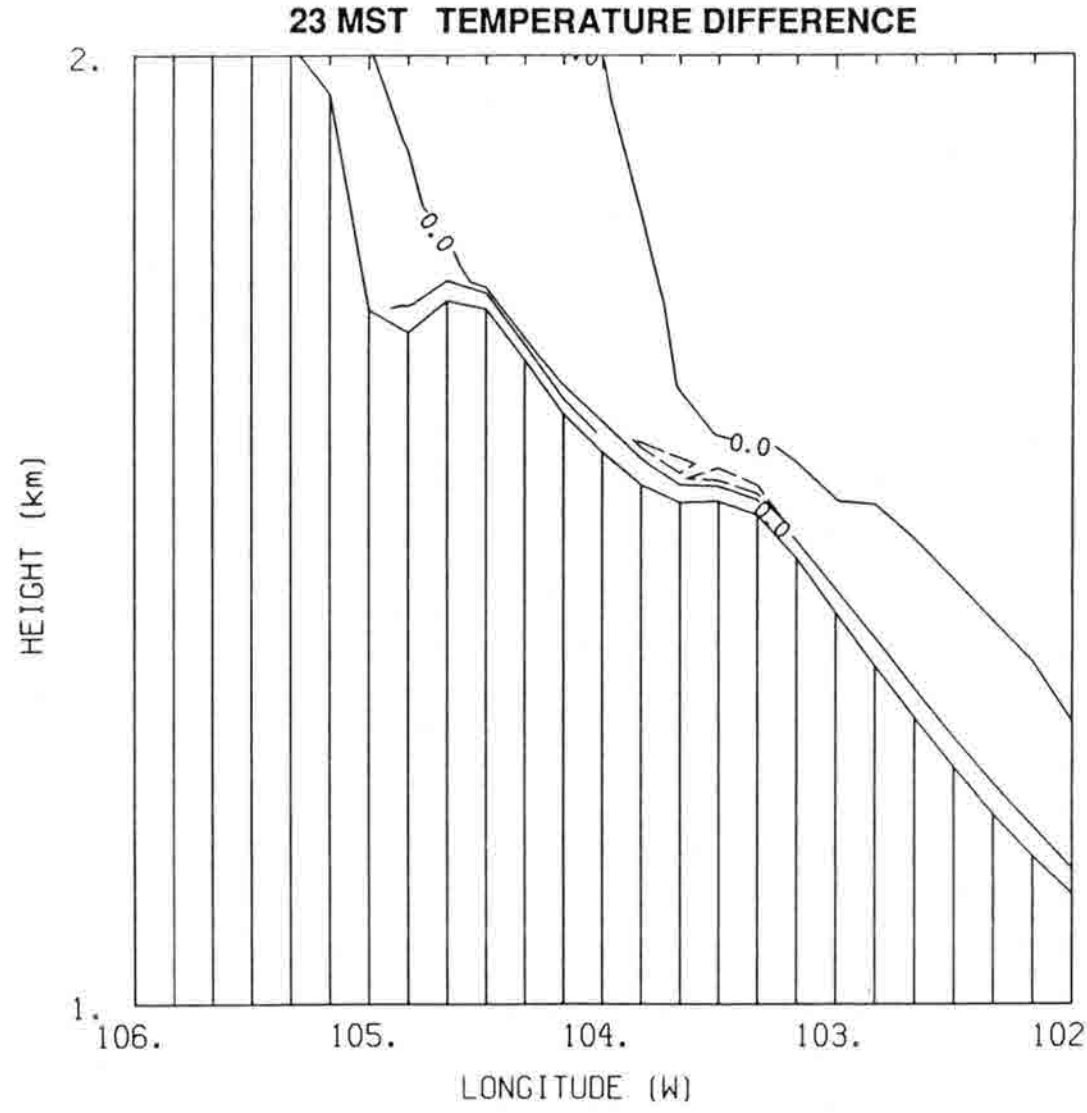

Figure B.4 A microscopic view of temperature differences at 23 MST caused by differing background geostrophic winds: the "strong" wind (case study) values minus the weak wind values. Differences are from the experiments with a forested mountain, while the bare-mountain values were very similar. The vertical scale is exaggerated relative to Figs. B1-3. Contours are at 4 K intervals.

overlaid the warm one and there was a substantial wind speed difference in the region (Fig. B.2b,d *vs.* B.3b,d).